School of Earth and Planetary Sciences

Extracting Martian Meteorite Mineral Spectra for Remote Sensing of the Surface Geology of Mars

Kenneth James Orr

0000-0002-8421-3091

This thesis is presented for the Degree of
Doctor of Philosophy - Geology
of
Curtin University

September 2021

Declaration

To the best of my knowledge and belief this thesis contains no material previously published by any other person except where due acknowledgement has been made.

This thesis contains no material which has been accepted for the award of any other degree or diploma in any university.

Signature: …….

Date: ……...

Abstract

Martian meteorites are the only direct samples from Mars that we can analyse on Earth. They offer the opportunity to develop our understanding of the geology and evolution of Mars. However, a key piece of missing information are the source craters of the Martian meteorites. We only know they originate from Mars, but exactly where on the planet remains elusive. One way to find a potential source crater is to match compositional similarities of the surface geology to the meteorites through mid-infrared (MIR) spectroscopy. This method has been hampered because the matches to whole meteorite spectra are not found in global composition maps of the surface. This PhD focuses on extracting pyroxene spectra directly from the shergottites to supplement the current spectral libraries in modelling of Martian surface MIR spectra. By undertaking a detailed mineralogical and geochemical analysis of the shergottites and using a suite of in-situ scanning electron microscopic techniques, I measured eleven meteorite-derived pyroxene spectra. These were then used to linearly model bulk spectra to evaluate their usefulness in deconvolution results. Models using planet-representative spectral end members improves the spectral fit of the modelling, and the accuracy of the mineral abundance determination. Overall, these new spectra fill the compositional hole of the currently available pyroxene spectra. In tandem with other remote sensing techniques, they can help constrain the locations of the source craters of the Martian meteorites.

Acknowledgements

Firstly, I would like to thank my supervisor, Gretchen, for her continuous help and support throughout my PhD. Without her this research would not have been possible. I would also like to thank my other supervisors Lucy, Mark and Vicky who provided valuable expertise and knowledge in the various areas of this research. Additionally, I would like to thank Malcolm, Chappy, Hugo, Tommo, Brad, and Kai for helping me carry out and process my analyses.

I would like to thank all my family in the UK and here in Australia for supporting me during my PhD, especially my fiancé Morgan and our dog Freya. Also, thanks to Morgan's family who have offered their continuous support during my PhD and while being away from my family during the Covid pandemic.

Acknowledgement of Country

We acknowledge that Curtin University works across hundreds of traditional lands and custodial groups in Australia, and with First Nations people around the globe. We wish to pay our deepest respects to their ancestors and members of their communities, past, present and to their emerging leaders. Our passion and commitment to work with all Australians and peoples from across the world, including our First Nations peoples are at the core of the work we do, reflective of our institutions' values and commitment to our role as leaders in the Reconciliation space in Australia.

Attribution Tables

Table i Attribution statement table for Chapter 3: *Geochemical and Mineralogical Classification of Four New Shergottites: NWA 10441, NWA 10818, NWA 11043 and NWA 12335.*

	Conception and Design	Acquisition of Data and Method	Data Processing and Manipulation	Interpretation and Discussion	Total % Contribution
Co-Author 1 Kenneth Orr	70	80	70	60	72
Co-Author 1 Acknowledgement: I acknowledge that these represent my contribution to the above research output.				Signed:	
Co-Author 2 Lucy Forman	-	5	10	5	2
Co-Author 2 Acknowledgement: I acknowledge that these represent my contribution to the above research output.				Signed:	
Co-Author 3 Kai Rankenburg	-	-	10	5	2
Co-Author 3 Acknowledgement: I acknowledge that these represent my contribution to the above research output.				Signed	
Co-Author 4 Noreen Evans	-	-	-	5	2
Co-Author 4 Acknowledgement: I acknowledge that these represent my contribution to the above research output.				Signed:	
Co-Author 5 Brad McDonald	-	10	-		1
Co-Author 5 Acknowledgement: I acknowledge that these represent my contribution to the above research output.				Signed:	
Co-Author 6 Belinda Godel	-	5	10		1
Co-Author 6 Acknowledgement: I acknowledge that these represent my contribution to the above research output.				Signed:	
Co-Author 7 Gretchen Benedix	30	-	-	25	20
Co-Author 7 Acknowledgement: I acknowledge that these represent my contribution to the above research output.				Signed:	
Total %	**100**	**100**	**100**	**100**	**100**

Table ii Attribution statement table for Chapter 4: *Application of μ-FTIR Spectroscopy to the Measurement of Pigeonite in Martian Shergottites*.

	Conception and Design	Acquisition of Data and Method	Data Processing and Manipulation	Interpretation and Discussion	Total % Contribution
Co-Author 1 Kenneth Orr	50	90	85	60	71
Co-Author 1 Acknowledgement: I acknowledge that these represent my contribution to the above research				Signed:	
Co-Author 2 Lucy Forman	-	5	5	-	2
Co-Author 2 Acknowledgement: I acknowledge that these represent my contribution to the above research				Signed:	
Co-Author 3 Mark Hackett	-	5	5	5	2
Co-Author 3 Acknowledgement: I acknowledge that these represent my contribution to the above research				Signed:	
Co-Author 4 Victoria Hamilton	-	-	-	15	5
Co-Author 4 Acknowledgement: I acknowledge that these represent my contribution to the above research				Signed:	
Co-Author 5 Gretchen Benedix	50	-	5	20	20
Co-Author 5 Acknowledgement: I acknowledge that these represent my contribution to the above research				Signed:	
Total %	**100**	**100**	**100**	**100**	**100**

Table iii Attribution statement table for Chapter 5: *Linear Modelling of Basaltic Shergottites using Martian Composition-Specific Mineral Spectra*.

	Conception and Design	Acquisition of Data and Method	Data Processing and Manipulation	Interpretation and Discussion	Total % Contribution
Co-Author 1 Kenneth Orr	80	95	80	60	74
Co-Author 1 Acknowledgement: I acknowledge that these represent my contribution to the above research				Signed:	
Co-Author 2 Victoria Hamilton	-	-	10	20	8
Co-Author 2 Acknowledgement: I acknowledge that these represent my contribution to the above research				Signed:	
Co-Author 3 Mark Hackett	-	5	-	-	2
Co-Author 3 Acknowledgement: I acknowledge that these represent my contribution to the above research				Signed:	
Co-Author 4 Lucy Forman	-	-	-	-	1
Co-Author 4 Acknowledgement: I acknowledge that these represent my contribution to the above research				Signed:	
Co-Author 5 Gretchen Benedix	20	-	10	20	15
Co-Author 5 Acknowledgement: I acknowledge that these represent my contribution to the above research				Signed:	
Total %	**100**	**100**	**100**	**100**	**100**

Table of Contents

Chapter 1: Introduction

Mars has long fascinated humans. From the Romans looking at a red planet and naming it after their god of war to popular culture such as Tim Burton's Mars Attacks! featuring lots of little green men invading Earth. This enthusiasm for Mars and the possibility of life has fuelled decades of space exploration to the planet. With the recent inclusion of countries like China, India and the United Arab Emirates into the small Mars exploration club (members including the European Space Agency, USA and USSR/Russia), and private industry, such as SpaceX, nobly taking it upon themselves to save the human race, now is a great time for research and innovation. Just this past year, even with the Covid-19 pandemic raging across the world, NASA still managed to successfully land their most advanced rover to date, Perseverance, at Jezero Crater, and China became the third country to successfully land on the surface with their Tianwen-1 satellite/lander/rover. Across the world, future Mars missions are being planned and developed. The most ambitious of which is NASA's Mars Sample Return program. Culminating in a multi-year inter-space agency collaboration, samples will be gathered by Perseverance and stored on the Martian surface to be returned later and analysed by future researchers here on Earth (around 2030). However, until then, the only samples from Mars that we have on Earth are meteorites.

Martian meteorites are pieces of rock that have been ejected into space from the planet's surface through large, crater-forming, asteroid impacts. These impact events must be sufficiently large to generate enough energy for the ejecta to reach over the escape velocity of Mars (5 km/s) (Fritz et al., 2005). After millions of years (exact time identified by cosmic ray exposure ages, e.g., Nyquist et al., 2001) of intra-solar system space travel, some of those rocks are captured by Earth's gravity. Provided they survive the destructive atmospheric entry, the rocks land on the surface (or ocean) of Earth. The achondrites, Shergotty and Zagami, were the first meteorites proposed to originate from Mars (McSween and Stolper, 1980). It was only after matching the composition of the Martian atmosphere (measured by Viking) to gas pockets in Elephant Moraine (EETA) 79001 that these were confirmed to originate on Mars (Bogard and Johnson, 1983). Since then, the number of Martian meteorites has significantly risen. Now there are approximately 150 known pairing groups, with over 260 individual meteorites recovered (Meteoritical Bulletin Database,

https://www.lpi.usra.edu/meteor). Although meteorite investigations have yielded a wealth of previously unknown information about Mars, we still do not know one fundamental piece of geological information; specifically, precisely from where they come on the Martian surface.

Establishing the exact location from which the meteorites originate would provide essential geological context from which more detailed geological histories and a broader evolution of Mars could be derived. Tying a meteorite (with a known crystallization age) to a specific location would also allow for crater counting to be calibrated at Mars, increasing the accuracy of surface chronology. Given these benefits, the source craters of the Martian meteorites have been the subject of a number of studies attempting to compositionally match one or more groups of meteorites to a specific crater (i.e., Mouginis-Mark, et al., 1992; Hamilton et al., 2003b; McFadden et al., 2005; Tornabene et al., 2006; Werner et al., 2014; Ody et al., 2015; Kereszturi and Chatzitheodoridis, 2016). So far, none of the postulated craters have been internationally accepted as one of the source craters of the Martian meteorites. Although notoriously difficult to identify, some constraints can be placed on possible source craters. Based on ejection ages (combining cosmic ray exposure and terrestrial age) of the Martian meteorites, 11 separate events (separate source craters) have been suggested (Herd et al., 2018). The craters are likely >3 km wide, as this was found to be the minimum size of impact that could generate escape velocity ejecta (Head et al., 2002; Artemieva and Ivanov, 2004). Due to the largely Amazonian age of the meteorites, the source craters are likely to be found in similarly aged terranes on the Martian surface. This potentially restricts the source craters to younger volcanic regions of Mars, such as Tharsis or Elysium (Mouginis-Mark et al., 1992). However, not all the craters fitting these conditions will be a source crater of the Martian meteorites, the surface geology also needs to compositionally match that of the meteorites.

Determining the geological composition of the Martian surface is primarily accomplished using a range of spectrometers and instruments. Among these, thermal (or mid-infrared, 5-50 μm) infrared spectrometers are especially useful at unravelling the geological composition of silicate rocks (similar to the Martian meteorites) (i.e., Christensen et al., 2001). By using the principal that an infrared spectrum of an area is

equal to the areal abundances of its constituents, the modal mineralogy of remote surfaces can be calculated (Ramsey and Christensen, 1998). By comparing known mineral spectra (from a spectral library) to the unknown spectrum of the target surface, a best fit linear combination of mineralogy can be found (Christensen et al., 2000). To accurately model the unknown spectrum of an area, the spectral library needs to be as representative of that area as possible, as missing compositions (spectral end members) will increase the error of the modelling. The major mineralogy of the Martian meteorites are primarily pyroxene, olivine and plagioclase (often shock deformed to maskelynite) (i.e., McSween, 2015). Therefore, ensuring the range in compositions of these minerals in the meteorites are fully represented in the spectral libraries is essential. A number of studies have measured and analysed the full compositional range in olivine (Koeppen and Hamilton, 2008; Hamilton, 2010) and plagioclase (e.g., Nash and Salisbury, 1991), including shocked infrared spectra of plagioclase to use for modelling (Johnson et al., 2002; Johnson et al., 2003). The same is true for pyroxene, with a number of clino- and orthopyroxene spectra available (Christensen et al., 2000; Hamilton, 2000, 2003a). However, the composition of pyroxene in the Martian meteorites is predominantly pigeonite and low-Ca augite (Udry et al., 2020). These compositions are rare on Earth, often pigeonite has exsolved or cannot be isolated abundantly in pure form (as a particulate) for an infrared spectrum to be measured. Currently, there are eight synthetic pigeonite spectra available (there was only one available until 2019) covering new pyroxene compositions, however, these still do not cover the range found in the Martian meteorites (Hamilton, 2000; Lindsley et al., 2019). This is problematic, as pyroxene spectra change based on their composition (Hamilton, 2000; Hamilton, 2003a). Therefore, using non-representative composition pyroxene spectra in modelling mineralogy can lead to inaccurate results (i.e., Hamilton et al., 1997). Overcoming this problem and producing pyroxene spectra that are more representative of true Martian meteorite compositions is the overarching aim of this PhD.

Chapter 2 details the samples and different methods used in this PhD. Each technique and corresponding data are described, with a particular focus on micro-Fourier transform infrared spectroscopy.

Chapter 3 is focused on a detailed classification of new Martian meteorites. The purpose is to establish a strong foundation of the mineralogy and geochemistry of the Martian meteorites, from which the infrared spectra will be measured.

Chapter 4 uses a number of non-destructive analytical techniques to produce pyroxene spectra from the Martian meteorites. Using the data of the previous chapter, the extensive geochemical zoning and associated issues with acquiring pigeonite infrared spectra from the meteorites were overcome.

Chapter 5 is the final manuscript associated with this PhD. Here I apply the new Martian pyroxene spectra (from chapter 4) to linearly model bulk Martian meteorite spectra to observe any improvement over previous modelling. By testing these spectra on known samples, we can fully evaluate their effectiveness for future surface spectral modelling.

1.1 References

Artemieva, N. & Ivanov, B. (2004) Launch of martian meteorites in oblique impacts. *Icarus 171*, 84-101. doi.org/10.1016/j.icarus.2004.05.003

Bogard, D. D., & Johnson, P. (1983). Martian Gases in an Antarctic Meteorite? *Science*, *221*(4611), 651–654. https://doi.org/10.1126/science.221.4611.651

Christensen, P. R., Bandfield, J. L., Hamilton, V. E., Howard, D. A., Lane, M. D., Piatek, J. L., et al. (2000). A thermal emission spectral library of rock-forming minerals. *Journal of Geophysical Research: Planets*, *105*(E4), 9735–9739. https://doi.org/10.1029/1998je000624

Christensen, P. R., Bandfield, J. L., Hamilton, V. E., Ruff, S. W., Kieffer, H. H., Titus, T. N., et al. (2001). Mars Global Surveyor Thermal Emission Spectrometer experiment: Investigation description and surface science results. *Journal of Geophysical Research: Planets*, *106*(E10), 23823–23871. https://doi.org/10.1029/2000je001370

Fritz, J., Artemieva, N., & Greshake, A. (2005). Ejection of Martian meteorites. *Meteoritics & Planetary Science*, *40*(9–10), 1393–1411. https://doi.org/10.1111/j.1945-5100.2005.tb00409.x

Hamilton, V. E., Christensen, P. R., & McSween, H. Y. (1997). Determination of Martian meteorite lithologies and mineralogies using vibrational spectroscopy. *Journal of Geophysical Research: Planets*, *102*(E11), 25593–25603. https://doi.org/10.1029/97je01874

Hamilton, V. E. (2000). Thermal infrared emission spectroscopy of the pyroxene mineral series. *Journal of Geophysical Research: Planets*, *105*(E4), 9701–9716. https://doi.org/10.1029/1999je001112

Hamilton, V. E. (2003a). Thermal infrared emission spectroscopy of titanium-enriched pyroxenes. *Journal of Geophysical Research: Planets (1991–2012)*, *108*(E8). https://doi.org/10.1029/2003je002052

Hamilton, V. E., Christensen, P. R., McSween, H. Y., & Bandfield, J. L. (2003b). Searching for the source regions of Martian meteorites using MGS TES: Integrating Martian meteorites into the global distribution of igneous materials on Mars. *Meteoritics & Planetary Science*, *38*(6), 871–885. https://doi.org/10.1111/j.1945-5100.2003.tb00284.x

Hamilton, V. E. (2010). Thermal infrared (vibrational) spectroscopy of Mg–Fe olivines: A review and applications to determining the composition of planetary surfaces. *Chemie Der Erde - Geochemistry*, *70*(1), 7–33. https://doi.org/10.1016/j.chemer.2009.12.005

Head, J. N., Melosh, H. J., & Ivanov, B. A. (2002). Martian Meteorite Launch: High-Speed Ejecta from Small Craters. *Science*, *298*(5599), 1752–1756. https://doi.org/10.1126/science.1077483

Herd, C. D. K., Tornabene, L. L., Bowling, T. J., Walton, E. L., Sharp, T. G., Melosh, H. J., et al. (2018, March). Linking Martian Meteorites to their Source Craters: New Insights. In *Lunar and Planetary Science Conference* (No. 2083, p. 2266).

Johnson, J. R., Hörz, F., Lucey, P. G., & Christensen, P. R. (2002). Thermal infrared spectroscopy of experimentally shocked anorthosite and pyroxenite: Implications for remote sensing of Mars. *Journal of Geophysical Research: Planets (1991–2012)*, *107*(E10), 3-1-3–14. https://doi.org/10.1029/2001je001517

Johnson, J. R., Hörz, F., & Staid, M. I. (2003). Thermal infrared spectroscopy and modeling of experimentally shocked plagioclase feldspars. *American Mineralogist*, *88*(10), 1575–1582. https://doi.org/10.2138/am-2003-1020

Kereszturi, A., & Chatzitheodoridis, E. (2016). Searching for the Source Crater of Nakhlite Meteorites. *Origins of Life and Evolution of Biospheres*, *46*(4), 455–471. https://doi.org/10.1007/s11084-016-9498-x

Koeppen, W. C., & Hamilton, V. E. (2008). Global distribution, composition, and abundance of olivine on the surface of Mars from thermal infrared data. *Journal of Geophysical Research: Planets (1991–2012)*, *113*(E5). https://doi.org/10.1029/2007je002984

Lindsley, D. H., Nekvasil, H., & Glotch, T. D. (2019). Synthesis of pigeonites for spectroscopic studies. *American Mineralogist*, *104*(4), 615–618. https://doi.org/10.2138/am-2019-6869ccbyncnd

McFadden, L. A., & Cline, T. P. (2005). Spectral reflectance of Martian meteorites: Spectral signatures as a template for locating source region on Mars. *Meteoritics & Planetary Science*, *40*(2), 151–172. https://doi.org/10.1111/j.1945-5100.2005.tb00372.x

McSween, H. Y., & Stolper, E. M. (1980). Basaltic meteorites. *Scientific American*, *242*(6), 54-63.

McSween, H. Y. (2015). Petrology on Mars. *American Mineralogist*, *100*(11–12), 2380–2395. https://doi.org/10.2138/am-2015-5257

Mouginis-Mark, P. J., McCoy, T. J., Taylor, G. J., & Keil, K. (1992). Martian parent craters for the SNC meteorites. *Journal of Geophysical Research: Planets, 97*(E6), 10213-10225. https://doi.org/10.1029/92jeoo612

Nash, D. B., & Salisbury, J. W. (1991). Infrared reflectance spectra (2.2–15 μm) of plagioclase feldspars. *Geophysical Research Letters*, *18*(6), 1151-1154.

Nyquist, L. E., Bogard, D. D., Shih, C.-Y., Greshake, A., Stöffler, D., & Eugster, O. (2001). Ages and Geologic Histories of Martian Meteorites. *Space Science Reviews*, *96*(1/4), 105–164. https://doi.org/10.1023/a:1011993105172

Ody, A., Poulet, F., Quantin, C., Bibring, J.-P., Bishop, J. L., & Dyar, M. D. (2015). Candidates source regions of Martian meteorites as identified by OMEGA/MEx. *Icarus*, *258*, 366–383. https://doi.org/10.1016/j.icarus.2015.05.019

Ramsey, M. S., & Christensen, P. R. (1998). Mineral abundance determination: Quantitative deconvolution of thermal emission spectra. *Journal of Geophysical Research: Solid Earth*, *103*(B1), 577–596. https://doi.org/10.1029/97jb02784

Tornabene, L. L., Moersch, J. E., McSween, H. Y., McEwen, A. S., Piatek, J. L., Milam, K. A., & Christensen, P. R. (2006). Identification of large (2–10 km) rayed craters on Mars in THEMIS thermal infrared images: Implications for possible Martian meteorite source regions. *Journal of Geophysical Research: Planets (1991–2012)*, *111*(E10). https://doi.org/10.1029/2005je002600

Udry, A., Howarth, G. H., Herd, C. D. K., Day, J. M. D., Lapen, T. J., & Filiberto, J. (2020). What Martian Meteorites Reveal About the Interior and Surface of Mars. *Journal of Geophysical Research: Planets*, *125*(12). https://doi.org/10.1029/2020je006523

Werner, S. C., Ody, A., & Poulet, F. (2014). The Source Crater of Martian Shergottite Meteorites. *Science*, *343*(6177), 1343–1346. https://doi.org/10.1126/science.1247282

Chapter 2: Samples and Methodology

2.1 Introduction

The samples and methods used in this PhD project comprise of Martian meteorites, a number of laboratory analytical techniques, linear modelling and the utilization of advanced analytical processes and methods to help answer the outlying research questions. This chapter seeks to describe and explain more broadly each method or technique and includes information not pertinent to the focused methodology sections in the following chapters. These specific methodology sections will focus on the corresponding chapters specific analytical conditions and associated error analyses.

The samples were all acquired from meteorite collections from around the world including the Institute of Meteoritics, University of New Mexico, USA and the National Institute for Polar Research, Japan. Before any other analysis or sample processing, all the samples were analysed using high-resolution X-ray computed tomography (HRXCT) at CSIRO. The other analytical instruments used are part of the John de Laeter Centre (TIMA and EBSD) at Curtin University, the Centre for Microscopy, Characterisation and Analysis (EPMA) at the University of Western Australia, the GeoHistory Facility (LA-ICP-MS) in the John de Laeter Centre at Curtin University and at the School of Molecular and Life Science (μ-FTIR) at Curtin University. These instruments were used to analyse qualitative and quantitative geochemistry (TIMA and EPMA), crystallographic orientations of the meteorites (EBSD), rare earth element (REE) compositions (LA-ICP-MS) of specific minerals and to measure infrared spectra (μ-FTIR) of the meteorites and constituent mineralogy. The linear modelling used the infrared spectra and a linear least squares algorithm to predict the mineralogy and modal abundance of the Martian meteorites. This chapter will systematically explain the approach and methodologies associated with each technique, and contribution to the overarching research questions.

2.2 Samples: Martian meteorites

The first Martian meteorite identified as such was the achondrite Elephant Moraine 79001 (a shergottite). Bogard and Johnson (1983) found tiny gas pockets trapped

inside impact melt glasses of the meteorite. The composition of these gas pockets matched the composition of the Martian atmosphere measured by the Viking landers (Owen et al., 1977). The only way for trapped Martian atmosphere to be inside a rock was for it to be from Mars. This really kick started the identification of Martian meteorites. Now there are an additional two modes of Martian meteorite identification: (1) the oxygen isotope ratio and (2) the Fe/Mn ratio in pyroxene (e.g., Ali et al., 2016). Both have values unique to Mars that can be used to distinguish against other planetary bodies and asteroid populations. Since the identification of the first Martian meteorite, there are now over 150 confirmed Martian meteorite pairs on Earth (Udry et al., 2020). They represent <0.5% of the total population of confirmed meteorites on the planet. So far, they are the only samples from Mars that we can directly study. They can be split up into three major groups: chassignites, nakhlites, shergottites (Bridges and Warren, 2006; Fig. 2.1). There are an additional two groups comprising only a single meteorite each: an orthopyroxenite and a sedimentary breccia (Mittlefehldt, 1994; Agee et al., 2013).

Martian meteorites were traditionally grouped into 3 classes, collectively known as the SNCs. The **C**hassignites, named after the first in this group called Chassigny, are cumulate dunites, primarily comprised of olivine (e.g., Treiman et al., 2007). They are the smallest (major) group of Martian meteorites, with only ~3 confirmed thus far. The **N**akhlites, again named after the first in this group Nakhla, are clinopyroxenites composed of predominantly augite with minor olivine and maskelynite (shocked-metamorphosed plagioclase) (e.g., Treiman, 2005; Jambon et al., 2016). There are 8 confirmed meteorites in this class. It has been suggested, based on the crystallisation age and geochemically similar rare earth element (REE) patterns, that the chassignites and nakhlites likely were ejected from the same impact crater (McCubbin et al., 2013; Udry and Day, 2018). The single orthopyroxenite, Alan Hills (ALH) 84001, is the oldest of the Martian meteorites (~4.5 Ga) comprised of predominantly orthopyroxene (Mittlefehldt, 1994; Barrat and Bollinger, 2010). It is famously remembered for being suggested to harbour evidence of past life on Mars in the form of odd-looking worm shaped minerals (McKay et al., 1996). This has since been discredited by numerous studies explaining the appearance and composition of these features through other processes such as alteration (e.g., Harvey et al., 1996; Shaheen et al., 2015). Northwest Africa (NWA) 7034 and pairs represents the only sedimentary Martian meteorite

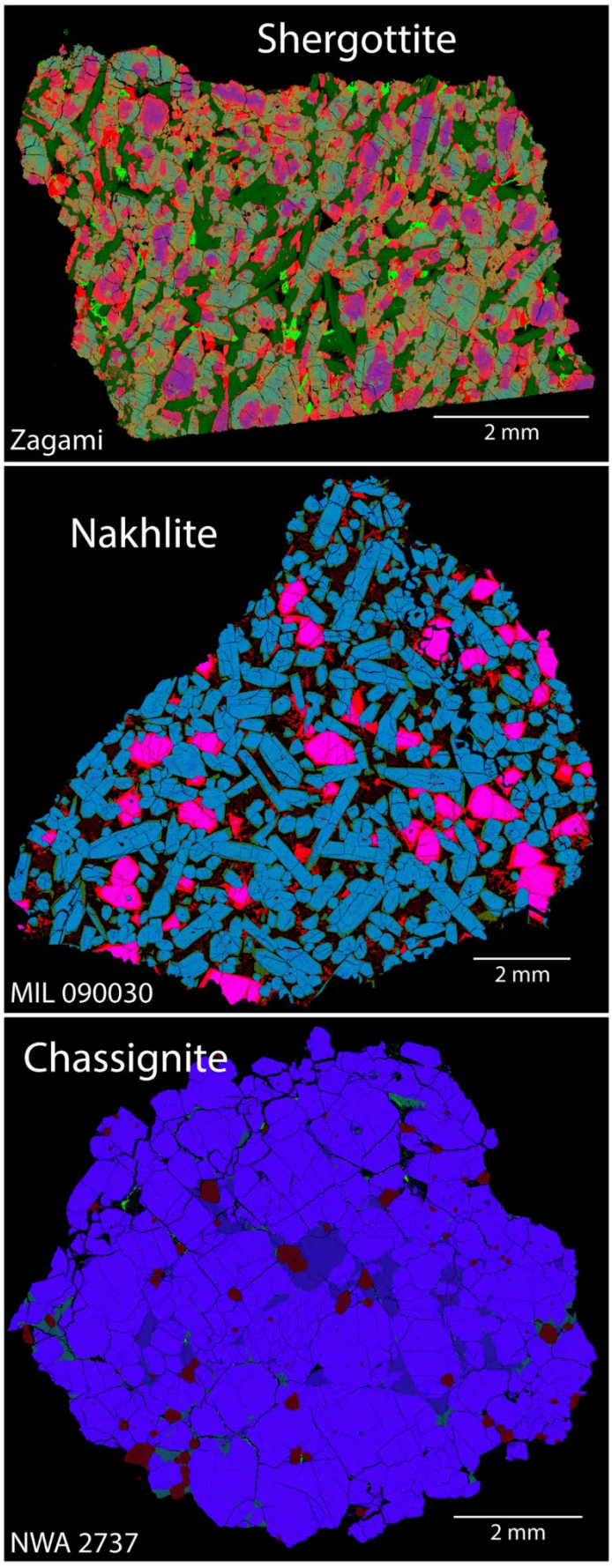

Figure 2.1 *TIMA combined element maps illustrating the compositional and textural differences between the shergottites (basaltic), nakhlites (clinopyroxenites) and chassignites (dunites). Fe = red, Ca = green, Mg = blue.*

(Agee et al., 2013). It is a volcanic-derived polymict regolith breccia, formed from a number of impact and subsequent brecciation events (McCubbin et al., 2016; MacArthur et al., 2018). Containing some of the oldest Martian zircons (~4.5 Ga), this rock has a long history stretching back to the early accretion of Mars (~4.6 Ga) (Cassata et al., 2018). By far the most abundant group of Martian meteorites are the shergottites, named after the first meteorite in this class Shergotty (Smith and Hervig, 1979; Bridges and Warren, 2006). There are over 150 meteorites in this group. As all the samples used in this PhD project are shergottites, they will be the focus of the rest of this sample section.

The **S**hergottites are largely near-surface intrusion or surface extrusion ultramafic to mafic lavas, forming (mostly) in the Late Amazonian period of Mars (~600 Ma) (e.g., Nyquist et al., 2001; Jambon et al., 2002; Taylor et al., 2002; Lin et al., 2005; Bouvier et al., 2009). Most likely due to their abundance, they are broadly split up into three major sub-groups: basaltic, olivine-phyric and poikilitic (Fig. 2.2). The basaltic shergottites are predominantly composed of augite, pigeonite and plagioclase (often in the form of maskelynite), including minor phases such as phosphate, ilmenite, and magnetite (e.g., McCoy et al., 1992; Warren et al., 2004; Howarth et al., 2018). The pyroxene is often complexly zoned, with Mg-rich cores to Fe-rich rims (e.g., He et al., 2015; Cao et al., 2018). In some cases, Fe-dominant pyroxferroite, a triclinic pyroxenoid, can also be present on the rims of the pyroxene grains (McSween et al., 1996; Kring et al., 2003). The maskelynite is similarly zoned with Ca-rich cores to Na-rich rims. Although largely comprised of the same mineralogy, the basaltic shergottites can be split up into several groups based on texture and/or other factors such as age or composition. Based on texture, there are three groups of basaltic shergottites: fine grained, diabasic and gabbroic. As the name suggests, fine grained basaltic shergottites (i.e., Zagami) have a finer grain size compared to diabasic (i.e., Los Angeles) which are generally coarser (e.g., McCoy et al., 1992; Walton and Spray, 2003). Gabbroic shergottites (i.e., NWA 6963) are coarse-grained anhedral cumulates, composed predominantly of pigeonite (Udry et al., 2017; Filiberto et al., 2018). The grain size differences reflect the crystallisation history of the rocks. The finer grained rocks likely crystallised rapidly in a lava flow while the coarser grained gabbroic rocks cooled more slowly trapped in a hypabyssal magmatic system (e.g., Filiberto, 2017). There is

also a group of basaltic shergottites (i.e., NWA 7635 and NWA 8159) that are augite-rich and still contain plagioclase that has not been fully shocked to form

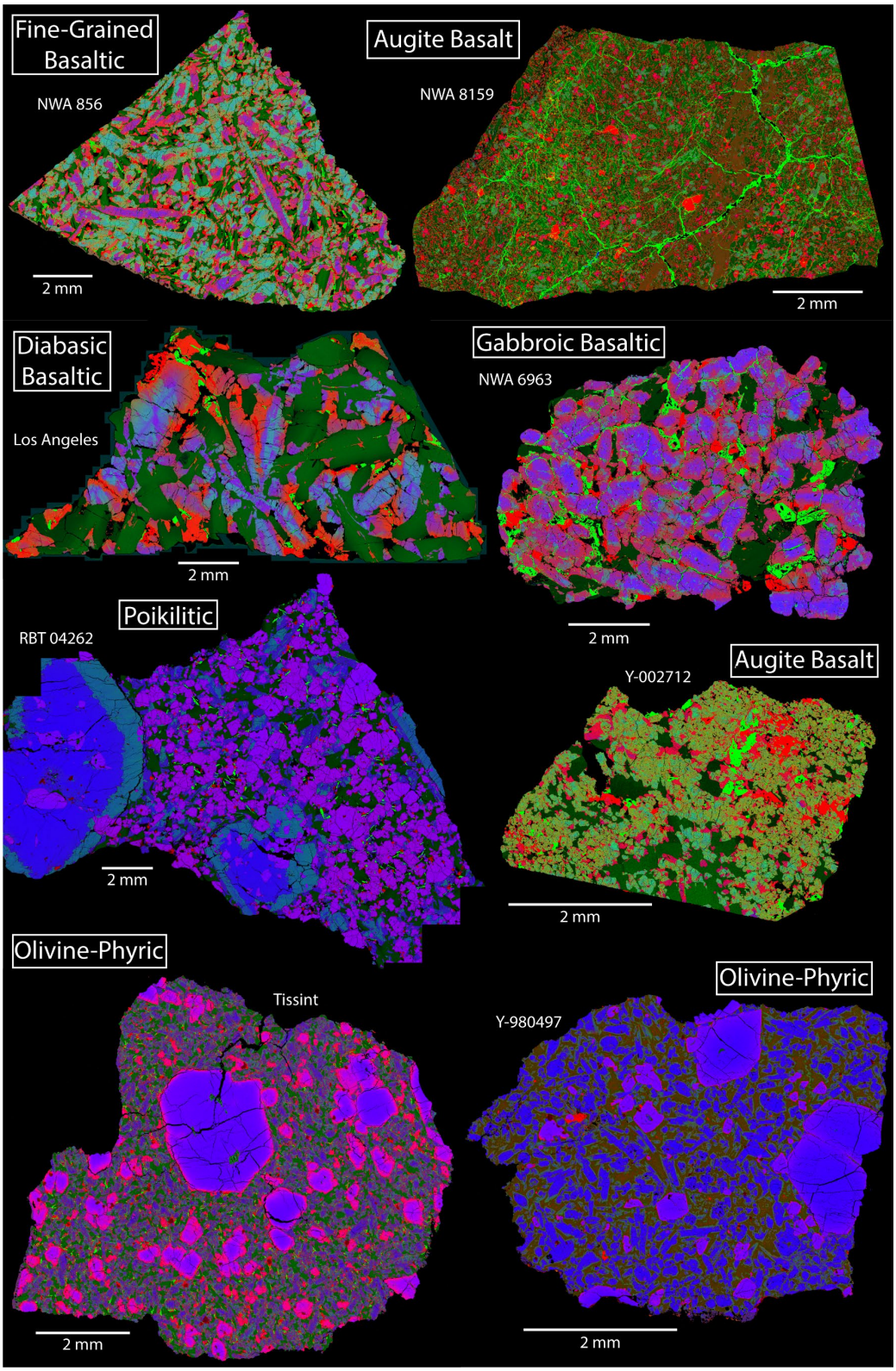

Figure 2.2 *TIMA combined element maps of the mineralogical and textural diversity in the shergottites (3 µm spatial resolution). Fe = red, Ca = green and Mg = blue. The basaltic shergottites are primarily composed of zoned pyroxene (augite and pigeonite) and maskelynite. The poikilitic shergottites are comprised of mostly olivine and pyroxene with minor maskelynite. Similarly, the olivine-phyric shergottites contain olivine, pyroxene (orthopyroxene, pigeonite and augite) and maskelynite (or in some cases devitrified glass).*

maskelynite (Lapen et al., 2017; Herd et al., 2017). Both these rocks have ages of ~2.5 Ga, making them the oldest formed shergottites.

The olivine-phyric shergottites are porphyritic lavas composed of olivine phenocrysts surrounded by a pyroxene and maskelynite groundmass (e.g., Goodrich, 2002; Usui et al., 2008; Sarbadhikari et al., 2009). The olivine grains are zoned with Fe-rich rims and the pyroxene are zoned with Mg-rich cores to Fe-rich rims (e.g., Gross et al., 2011). There is a gradual phase transition in the pyroxene, from orthopyroxene in the core (though in some cases this step is not observed), to pigeonite, then augite and finally Fe-rich pigeonite rims (e.g., Filiberto et al., 2012). Maskelynite, similarly to the basaltic shergottites, is zoned with Ca-rich cores to Na-rich rims. In some cases, devitrified glass or mesostasis is observed instead of maskelynite (e.g., Usui et al., 2008; Gross et al., 2011; First and Hammer, 2016). The crystallisation history of the olivine-phyric shergottites may be connected to that of the basaltic shergottites (Filiberto et al., 2012; Treiman and Filiberto, 2015; Collinet et al., 2017). The magmatic evolution of the basaltic shergottites includes an olivine fractionation event from the magma (e.g., Jones, 2015). The remaining magma then ascends to the surface and crystallises the basaltic shergottites, without olivine. Similarly, the olivine-bearing magma then undergoes polybaric crystallisation as the magma ascends towards the surface, finally crystallising the olivine-phyric shergottites as lavas (e.g., Balta et al., 2013).

The poikilitic shergottites are composed of large pyroxene (pigeonite cores and augite rims) oikocrysts enclosing smaller olivine and chromite chadacrysts (e.g., Mikouchi et al., 2008; Usui et al., 2010). The non-poikilitic areas comprise smaller grains of olivine, complexly zoned pyroxene (augite and pigeonite) and chromite (e.g., Riches et al., 2011; Kizovski et al., 2019). The poikilitic shergottite parent magma is less evolved than the basaltic and olivine-phyric parents magmas, with the highest Mg# of all the shergottites (e.g., Udry et al., 2020). This suggests the magma experienced few melting or fractionation events prior to crystallisation (Rahib et al., 2019). Similarly to the olivine-phyric shergottites, the poikilitic shergottites underwent polybaric crystallisation during ascension towards the surface, finally crystallising near the surface in a hypabyssal system (e.g., Howarth et al., 2014; Combs et al., 2019).

Aside from the mineralogy and petrology, the shergottites can be split based on incompatible trace elements (ITE), including rare earth element (REE) patterns and radiogenic isotopes (i.e., $^{87}Sr/^{86}Sr$ and $^{187}Os/^{188}Os$) (e.g., Bridges and Warren, 2006; Udry et al., 2020). The shergottites can either be enriched, where the REE pattern is flat, intermediate, where there is a slight depletion in the light rare earth elements (LREE) or depleted, where there is a significant depletion in the LREE (e.g., Filiberto, 2017). The REE patterns and radiogenic isotope ratios are used to constrain the magma sources of the shergottites, as in theory, if a rock has a different REE pattern or isotope ratio then that would suggest a different magmatic source (e.g., Borg and Draper, 2003). However, there is considerable debate for the cause of these different REE patterns and isotope ratios, all of which are centred on the Martian mantle. One theory is that the mantle is heterogeneous with separate enriched, intermediate, and depleted REE source regions (e.g., Rahib et al., 2019). The shergottite parent magmas are derived from these regions and then, during their ascension through the Martian crust, there is little to no crustal assimilation (e.g., Herd, 2003; Debaille et al., 2008; Ferdous et al., 2017; Armytage et al., 2018). This is unlike Earth, where crustal contamination is a major geological process. The opposing theory claims the Martian mantle is relatively homogenous and depleted in LREE; all the shergottite parent magmas were derived from this depleted source and were subsequently enriched through crustal assimilation processes during the magma's ascension to the surface (e.g., Nyquist et al., 2001; Borg et al., 2002; Humayun et al., 2013; Usui et al., 2012; Peters et al., 2015). Both theories have major implications for how the Martian mantle mixed and the role of the crust, and therefore the geological evolution of the planet.

2.3 High-Resolution X-Ray Computed Tomography (HRXCT)

The first step in the analysis protocol was to use non-destructive HRXCT to map the 3D characteristics of the mineralogy and textures in the Martian meteorites. This was carried out with a Zeiss Versa XRM520 X-ray microscope fitted with a flat panel 136 detector at the Australian Resources Research Centre (ARRC), CSIRO Mineral Resources in Kensington, Perth. Varying X-ray energies allows complex materials (rocks) to be accurately analysed. In geological samples, the density differences between the minerals, and hence how they react to X-rays (attenuation), can be used

to generate a 3D model of the samples (e.g., Mees et al., 2003; Ketcham, 2005; Godel et al., 2013).

Initially the sample is placed on a sample holder, with no prior sample preparation required (Fig. 2.3). The sample is then scanned with an X-ray emitter, with the sample rotating so the whole sample can be analysed. The X-rays pass through the sample and out to the detector. Once the X-ray projections (X-rays that have passed through the sample) are detected, mathematical processing creates 2D slices of the sample, which can then be stacked together to create a 3D model. The exact processing steps are detailed in Godel et al. (2013). The spatial resolution of the analysis, the voxel size (i.e., a 3D pixel), is related to specimen size, X-ray energy and acquisition time. The samples in this study were all ~0.5g chips and analysed with a voxel size of 12 µm. Typical grain sizes of major mineralogy in the basaltic shergottites ranges from 1-3 mm or up to 5 mm for coarse grained samples. Poikilitic shergottite grain sizes range from ~0.5-1 mm for non-poikilitic regions and up to 5-6 mm for the oikocrysts. A 12 µm voxel size is adequate to distinguish the major mineralogy. Although this voxel size is considerable larger than the other analyses (see below), it provided a 3D detailed view of each sample, providing essential context for future analyses. For more detail, see Chapter 3: Methods.

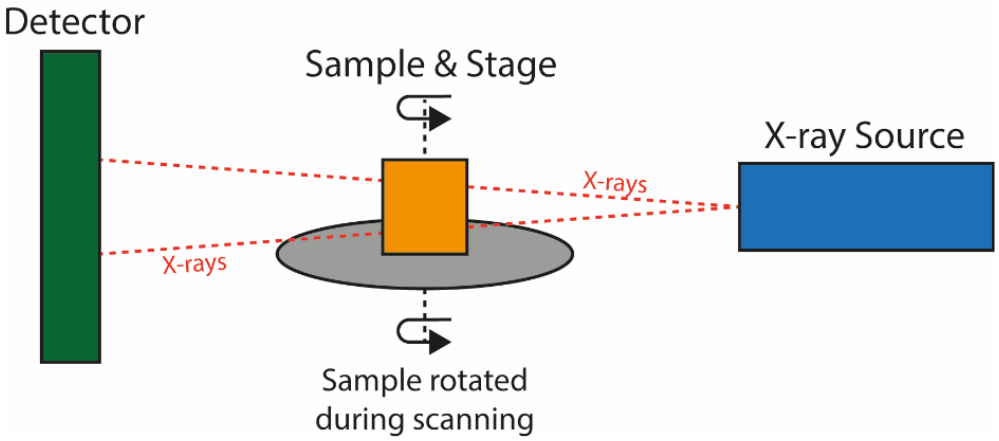

Figure 2.3 *Schematic diagram of HRXCT. The X-ray source emits the X-rays which pass through the rotating sample and then on to the detector. The varying densities of the mineralogy of the rock interact with the X-rays, from which mathematical processes can generate 2D slices of the whole rock. Combining all the 2D slices can create an accurate 3D model of the sample.*

2.4 Scanning Electron Microscopy

Several techniques use a scanning electron microscope (SEM) as the base instrument, with configurations and/or additional detectors as required. Unlike a light microscope, a SEM directs a focused electron beam onto the surface of a sample (Goldstein et al., 2003, Fig. 2.4). Compared to light, electrons have much shorter wavelengths, and therefore can achieve considerably higher magnification. On interactions with the sample surface, they also generate a number of different signals, such as backscattered electrons and characteristic X-rays. These signals can be detected using the corresponding detector to provide images or information about the surface topography and composition of the sample. The following techniques are all either adaptations of a SEM system or a new detector inside a SEM.

2.4.1 Tescan Integrated Mineral Analyser (TIMA)

The TIMA, located in the John de Laeter Centre at Curtin University, is a specifically designed scanning electron microscope (SEM), utilising four X-ray detectors using energy dispersive spectroscopy (EDS), to map the elemental distribution in the samples (e.g., Hrstka et al., 2018; Fig. 2.4).

EDS analyses all the characteristic energies of the emitted X-rays (e.g., K, L and M) from the sample by the electron beam. This produces a plot of intensity (corresponding to the relative abundance) vs X-ray energy. The major elements and likely mineral are then identified. The TIMA was utilised to generate element maps (of the major elements), which were then combined using Adobe Photoshop to produce RGB images of the meteorites. The RGB images were the combination of three different element maps. Due to the flexibility of this approach, any combination of three elements could be achieved, highlight various minerals or textures at my discretion. Geochemical analysis of samples, especially the Martian meteorites which are generally quite small, is essential for fully understanding the mineralogical and petrological complexities of the samples, and for providing context to future analyses with other instruments.

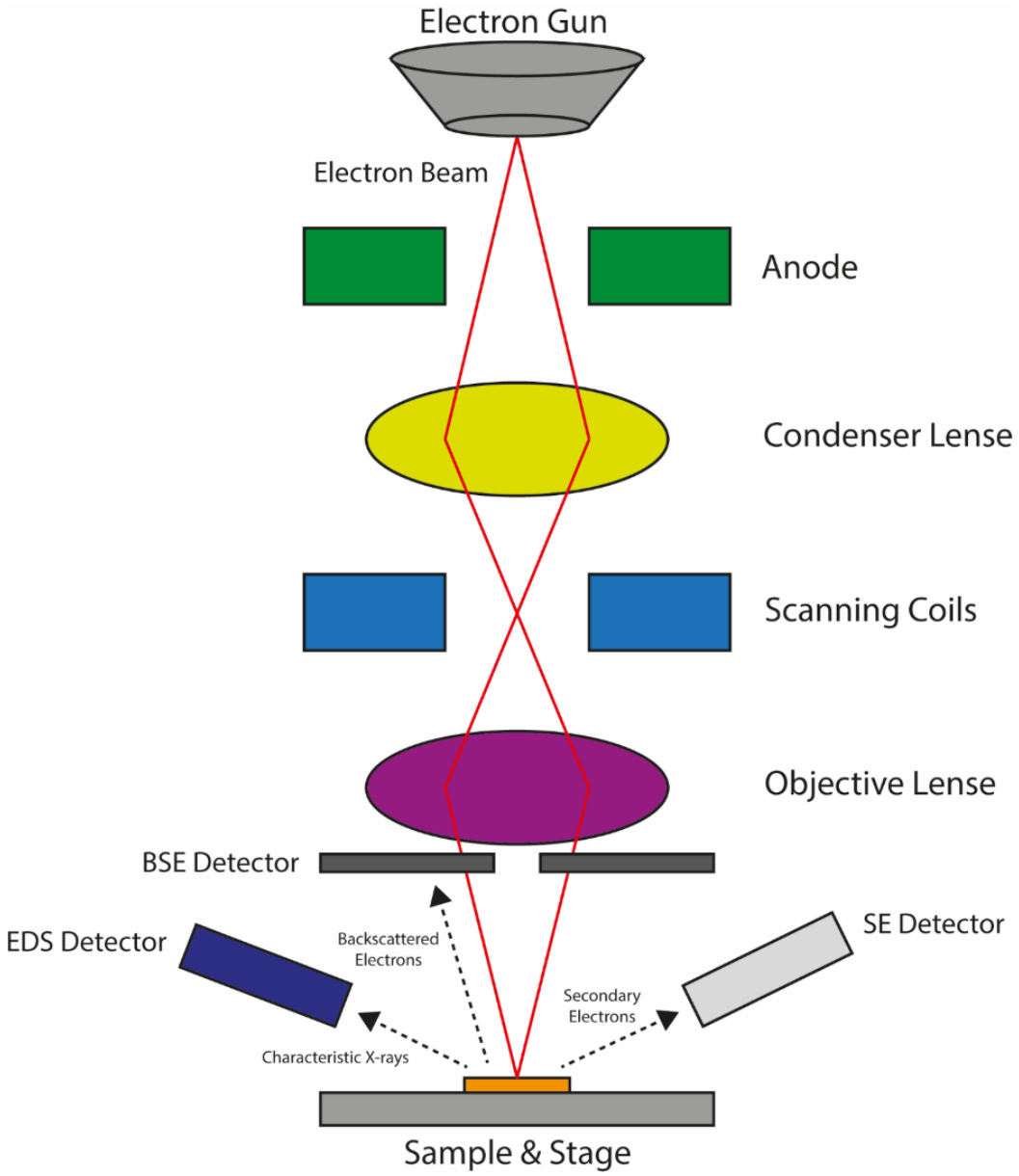

Figure 2.4 *Schematic diagram of a scanning electron microscope (SEM), variants of which are used in the TIMA, EPMA and EBSD analytical techniques. The gun generates an electron beam which is then accelerated by the anode down a column of lenses (and apertures) which focus the electron beam onto the sample. The scanning coils enable the rastering or scanning of the sample with the now focused electron beam. The various interactions of the high energy electron beam with the sample generates a number of products, such as backscattered electrons, secondary electrons and characteristic X-rays, which are identified using their corresponding detectors. In the TIMA system, there are four EDS detectors positions equally around the sample to enable fast and accurate X-ray detection.*

The TIMA has a number of operational modes that can be used for mapping samples. Initially, I used the dot mapping mode, where an EDS spectrum would only be collected when a new phase was encountered. Dot mapping generally produces low-resolution maps, used for basic identification of mineralogy. However, due to the zoning and complex geochemistry of the Martian meteorites, I found this mode to be

insufficient for my needs. Next, I tried high-resolution mapping. This mapping mode takes an EDS spectrum at each step, for the majority of the samples this was done at 3 μm spatial resolution. This significantly improved the resolution and accuracy of the elemental distribution across the samples. Using these maps, I observed a number of features not available using dot mapping, for example the complex zoning in the pyroxenes of the basaltic shergottites and the distribution of accessory phases. For a minority of samples, 3 μm was still too coarse. These relatively fine-grained samples (i.e. NWA 7034 and NWA 8159) were mapped at 1 μm resolution. This improved the resolution 9-fold (Fig. 2.5). By increasing the resolution, the much higher detail of these samples could be observed. Using these maps as the benchmark for 1 μm elemental mapping, I analysed four other, coarser samples (see Chapter 2) to explore any improvements. The images were much sharper, but also features such as exsolution in the pyroxene and complex weathering patterns could be observed. Overall, the TIMA high-resolution elemental maps set the important foundation for my understanding of Martian meteorites and helped constrain specific locations in the samples for future analyses.

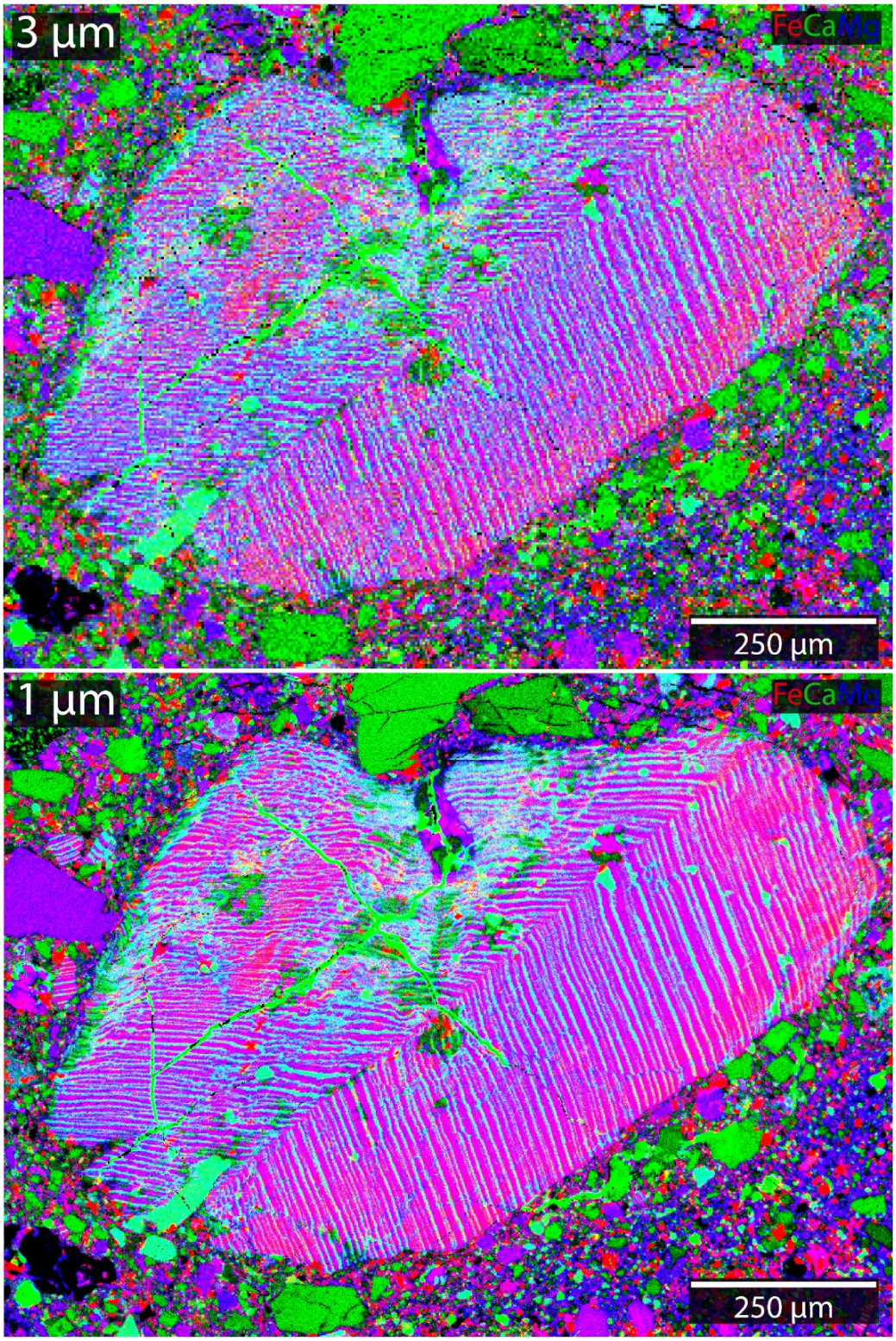

Figure 2.5 *TIMA combined element maps of a pyroxene mineral clast in NWA 7034. Fe = red, Ca = green and Mg = blue. The maps demonstrate the observable differences between 3 and 1 µm high-resolution mapping. The 1 µm map increases the spatial resolution by 9-fold, allowing identification of smaller features such as minor faulting offsetting exsolution lamellae in the pyroxene mineral clast.*

2.4.2 Electron Probe Micro Analyser (EPMA)

The electron probe micro analyser (EPMA), in the Centre for Microscopy, Characterisation and Analysis at the University of Western Australia, was utilised for in-situ quantitative geochemical analysis of the mineralogy in the samples (e.g., Lanari et al., 2019). Unlike the TIMA (EDS), the EPMA uses crystal spectrometers with wavelength dispersive spectroscopy (WDS) to quantitatively analyse material (Goldstein et al., 2003; Fig. 2.6). The electron beam hits the sample to generate characteristic X-rays. X-rays (e.g., K, L and M) are reflected by the analytical crystals (based on Braggs Law) and passed on to the X-ray detector. The elements that are analysed have fixed wavelengths. Using a crystal(s) with fixed d-spacing at a fixed angle, characteristic X-rays can be quantified. Commonly, EPMA instruments comprise of five crystal spectrometers, which, in turn, allow for up to five different elements to be analysed at a time. In most cases, the EPMA analyses the same spot twice, to produce results for ten target elements (i.e., all the major elements).

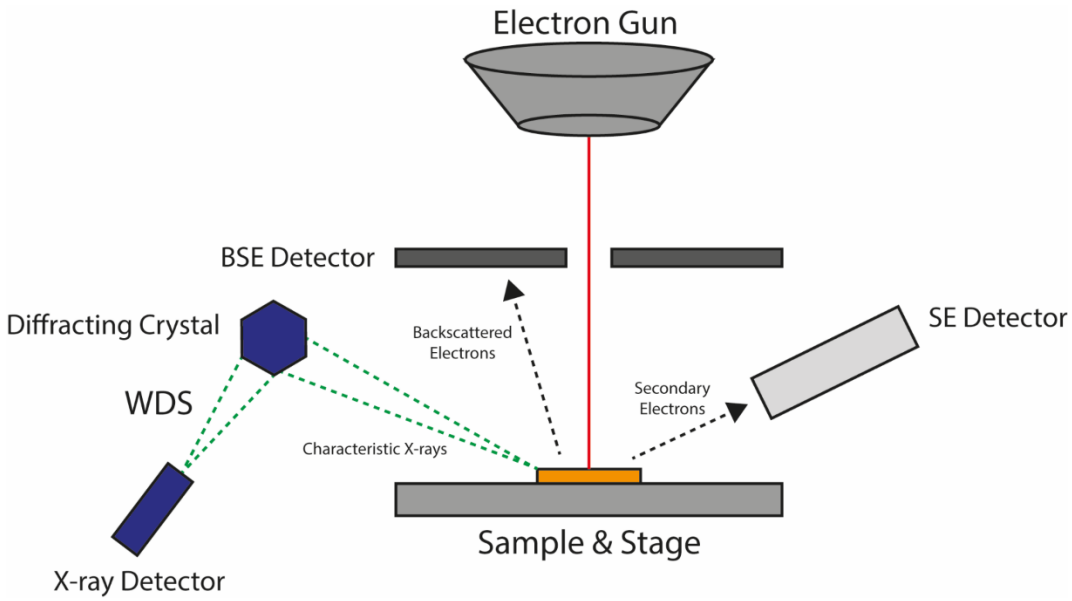

Figure 2.6 *Schematic diagram of EPMA, with the SEM part (Fig. 4) omitted. Unlike the TIMA, the EPMA uses WDS and crystal spectrometers (the EPMA used in this study utilised five spectrometers) to detect target element X-rays to accurately quantify the composition of the sample.*

There are a number of operational modes that can be used for geochemical analysis with an EPMA, such as spot or line analyses. I used the quantitative mapping mode. Similarly, to mapping with the TIMA, quant mapping with the EPMA analyses each step individually. All the maps were acquired with a 2 µm step size with most maps acquiring in the region of 2.5 million individual quantitative geochemical analysis

points. As far as EPMA analyses goes, that is not a small number. To acquire so many points, each point was only analysed for 40 ms, which is significantly less than the normal dwell time. The rapidness of the acquisition leads to larger errors associated with each point. However, these errors are significantly reduced through the sheer numbers of analyses. By averaging or plotting upwards of a million individual spots, errors are kept at a minimum. There are a number of benefits to using quantitative mapping, especially in complexly zoned samples. They can reveal patterns and geochemical distributions not before seen, but also demonstrate how just taking spot analysis of minerals may not elucidate the true geochemical detail that they hold.

To accurately extract the data from a quantitative element map, specifically of a target mineral or phase, the CalcImage package of the Probe for Windows EPMA control software was utilized. Through this program, spots, lines or polygons of the element map could be extracted. To accurately retrieve the data, filters were used. For example, these filters could be the totals of the data or specific elemental percentages. For example, use of data with analysis total between 98.5 and 101% enabled an easy first pass to ensure no major elements were missed. More detailed filters such as Fe% or Al% were used to distinguish between the mineralogy.

2.4.3 Electron Back-Scattered Diffraction (EBSD)

For crystallographic orientation analyses, a TESCAN MIRA variable pressure scanning electron microscope (VP-SEM) fitted with an Oxford Instruments Symmetry electron backscatter diffraction (EBSD) detector was utilized (e.g., Humphreys et al., 2004; El-Dasher and Torres, 2009). For electron backscattered diffraction (EBSD) analysis, a specific sample preparation protocol must be followed to ensure that any relatable and accurate data can be collected. The samples not only need to be polished, but ‘EBSD polished’. This is an extra polishing step, using very fine polishing mats with colloidal silica (in a Buehler Vibromet II Polisher) to achieve the best possible polish (not usually required for other techniques). Once polished to the right standard, the samples then need to be carbon coated with only a 5 nm thickness. Just thick enough to avoid charging of the sample, but not too thick as to prevent the back-scatter electrons from being detected. Once this protocol has been completed, the sample is ready for EBSD analysis. EBSD determines the crystallographic orientation of mineral grains through detecting back-scattered electrons from the electron-beam hitting the

sample (Fig. 2.7). To detect these back-scattered electrons, the sample must be tilted 70^{o} and ideally, the detector brought as close to the sample as possible (to ensure maximum detection). To distinguish between different phases, crystallographic structures and the grain orientation, the software uses a Hough transform to calculate kikouchi patterns of the minerals from the back-scattered electrons. The kikouchi patterns act almost like fingerprints for minerals and their orientations. The patterns comprise an array of bands and nodes that can be identified to relate to a specific mineral and structure or match unit. Through the use of match units, the majority of minerals can be identified and indexed to reveal their crystallographic orientations. The majority of EBSD analyses in the PhD project was large area mapping (LAM). The whole area of each sample was mapped, to provide a conclusive crystallographic orientation atlas of all the grains. This worked for all the major and minor mineralogy except for maskelynite. As a diaplectic glass, maskelynite did not index during EBSD analyses. However, there is some debate as to the crystallographic form of maskelynite and its mode of formation, with the possibility of direct analyses in the future (e.g., Jaret et al., 2015; Fritz et al., 2019).

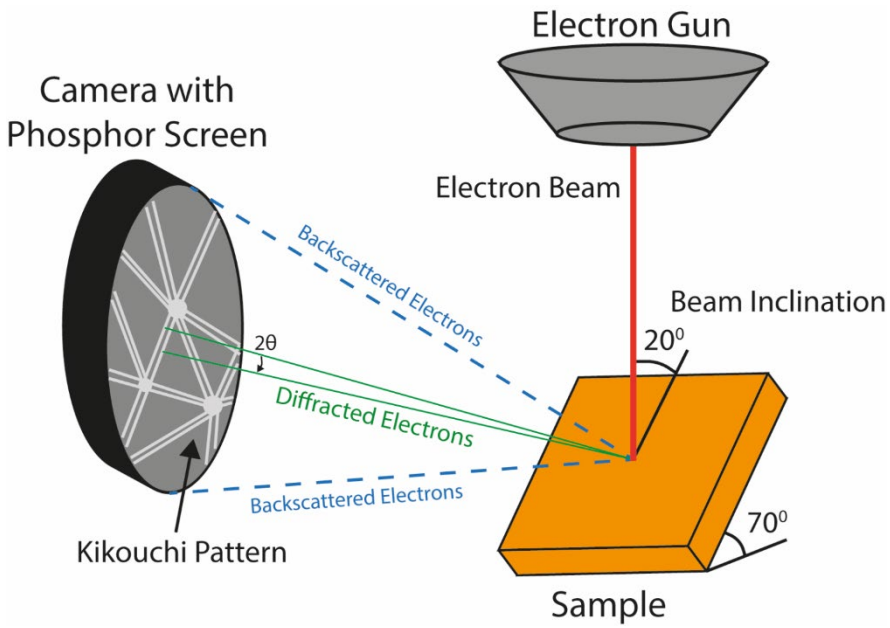

Figure 2.7 *Schematic diagram representing EBSD in a SEM system. Unlike the previous SEM techniques, the sample is tilted 70o with the EBSD detector close enough to detect the diffracted electrons of the sample. This technique provides crystallographic and structural information of the sample. EBSD is often combined with an EDS detector, so both techniques can be utilised to analyse the sample.*

2.5 Laser Ablation Inductively Coupled Plasma Mass Spectrometry (LA-ICP-MS)

In-situ trace element analysis was conducted using a RESOlution-SE excimer laser and an Agilent 8900 QQQ ICP-MS at the GeoHistory Facility in the John de Laeter Centre at Curtin University (e.g., Günther and Hattendorf, 2005; Koch and Günther, 2011; Fig. 2.8). This analysis relates to Chapter 2, for determining the REE element abundances of four new Martian meteorites. The benefit of laser ablation inductively coupled plasma mass spectrometry (LA-ICP-MS) is that the mineralogy of the meteorites can be analysed in situ, and destruction is limited to micron-sized pits (which require further polishing to remove).

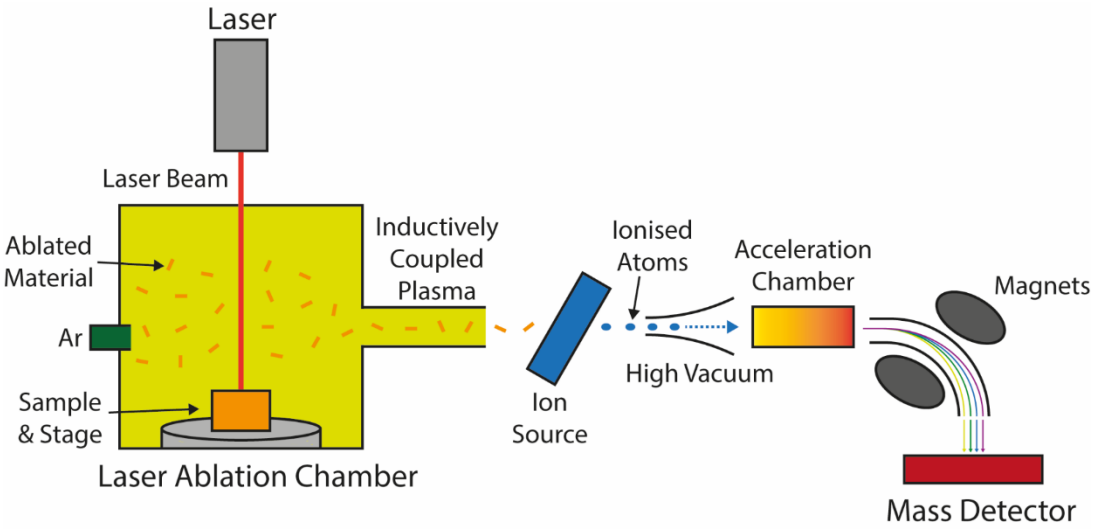

Figure 2.8 *Schematic diagram of the LA-ICP-MS system. The laser ablates the material of the sample away, which is transported through to the plasma source with argon gas. Once ionised, the atoms are accelerated into the mass spectrometer, which can distinguish between the elements and/or isotopes mass-to-charge ratio using a magnetic field. Aside from a small proportion of material that is ablated, this techniques is largely non-destructive.*

Preparation for analysis only included removing the carbon coat of the samples, as this would affect the results during ablation. Once the samples were placed in the instrument, target selection could begin. To aid with finding the target mineral grains, the instrument itself had an in-built light microscope. Additionally, the TIMA combined RGB element maps of the samples, could be electronically overlain on top of the sample images in the instrument software. This enabled targets to be selected based on the light microscope sample image and the TIMA compositional maps, significantly improving target identification. The minimum size of any grain and/or phase that could be accurately analysed needed to be larger than the laser analytical

diameter of 50 μm. During analysis, for each individual spot, two cleaning pulses were initially used to remove any excess carbon or other material that may contaminate the results. Then laser ablation was conducted on each spot for 40s. As the material is ablated away, the constant flow of an inert gas, in this case argon, is required to transport the ablated particles to the inductively coupled plasma. Once reaching the plasma source (which is kept at temperature of ~10,000 K) the ablated particles become ionised. This process tears the neutral molecules apart to become charged ions. These ions then are separated based on their mass-to-charge ratio in the mass spectrometer using a magnetic field, which can differentiate between the different elemental ions and isotopes of the sample. With this technique, elemental abundances in the part per billion (ppb) range may be detected.

2.6 Micro-Fourier Transform Infrared Spectroscopy (μ-FTIR)

Infrared spectroscopy is an adaptable technique used to non-destructively analyse the geochemical composition of samples. It is widely used in the laboratory and in remote sensing of planetary surfaces (e.g., Thompson and Wadsworth, 1957; Kieffer et al., 1972; Hanel et al., 1972; Chabal, 1988; Yamaguchi et al., 1998; Christensen et al., 2001; Christensen et al., 2004; Stuart, 2005; Siesler et al., 2008; Hamilton et al., 2019). Infrared spectroscopy of materials in the laboratory relies on detecting vibrations between the chemical bonds in the material, which corresponds to absorptions (analysing in reflection) in their infrared spectra at specific wavelengths (e.g., Salisbury et al., 1987). These absorptions represent the fingerprint of the material in the infrared. Varying compositions and bonds will produce different infrared spectra, and utilising this assumption enables accurate determination of the composition of whichever material is being analysed. For determining major mineralogical composition of rocks, the mid-infrared (MIR, 5-50 μm) is a very useful wavelength range to use. This range covers all the major rock forming mineral bonds such as Si-O (silicates), C-O (carbonates), S-O (sulphides) and M(metal)-O (oxides) (Lane and Bishop, 2019). In the MIR, the absorptions (alternatively known as bands) of the silicate minerals correspond to stretching, bending and rotating of the Si-O bonds in the crystal lattices of the minerals, causing molecular vibrations. The other major elements in the minerals, for example Fe, Mg or Ca, add another layer of complexity, by changing positions (and number) of the bands of the minerals based on elemental

abundance and charge of the ions. Because of the influence of the major cations, detailed silicate mineralogy can be determined from rocks. Not only can pyroxene be distinguished from olivine, but the composition or end members of both minerals can be identified. The primary method to identifying mineralogy is to compare the spectra of the target to known spectral end members. These are spectra measured from minerals with a known compositions (like using standards in other analytical processes). Spectral end members enable a comprehensive identification of mineral spectra in unknown samples.

The advance in infrared spectrometer technology is one the primary reasons this PhD research can be undertaken. Dispersive infrared spectrometers were the first instruments to be able to analyse material in the infrared (Diem et al., 1988; Hamid and Prichard, 1988; Stuart, 2005). Historically, they used a series of mirrors and a prism to analyse the sample and then direct, individually, each wavelength of light through a slit to the detector. This process can be extremely slow and with no internal wavelength calibration (unlike a FTIR), comparison between spectra from different analytical runs can be problematic. The FTIR instrument, first introduced in 1969, was a significant improvement over dispersive spectrometers (Faix, 1992; Griffiths and Haseth, 2007). It has several major advantages. It can measure all the wavelengths of light, within the spectral range of the instrument, simultaneously (and can combine scans). With fewer mirrors and no slit to limit the light reaching the detector, more energy reaches the sample and detector in a FTIR instrument, improving the signal-to-noise, and therefore sensitivity. Finally, the laser in the instrument acts as a wavelength calibration source, enabling direct comparisons between different analytical runs and/or from different FTIR instruments. In effect, standardising infrared analysis. The micro-FTIR (μ-FTIR) increases the capability of traditional FTIR instruments (Hook and Kahle, 1996). These instruments include a light microscope, which enables in-situ targeted analysis of samples. For example, a traditional FTIR instrument would analyse bulk particulate materials, but with the microscope upgrade, individual grains in a thin section can now be analysed.

To analyse the Martian meteorites, I used a μ-FTIR which is principally a Michelson interferometer (Fig. 2.9) consisting of a stationary and a moving mirror, the radiation from the infrared source in split evenly (as close to 50/50 as possible) by a

beamsplitter, to both mirrors (reflected to the stationary mirror and transmitted to the moving mirror). The light is reflected off the mirrors and recombined at the beamsplitter, then focused onto the sample, from which it reflects (in reflection mode) and finally directed into the detector. The resulting interferogram represents the radiation/light intensity as a function of the optical path differences (the difference in optical distances of the light beams between the moving and stationary mirrors). The maximum and minimum intensities are set based on the constructive (in phase) and destructive (out of phase) nature of the recombined light from the different mirrors. The moving mirror ensures the recombined light varies between these extremes. The interferogram is measured in the time domain. To convert it to the traditional infrared spectrum (in the frequency domain), a Fourier transform must be applied. Fourier analysis is conducted on the background interferogram (taken before sample acquisition) and then on the sample interferogram. This produces an infrared spectrum of each, with which the sample spectrum is divided by the background spectrum to produce the final infrared spectrum of the sample.

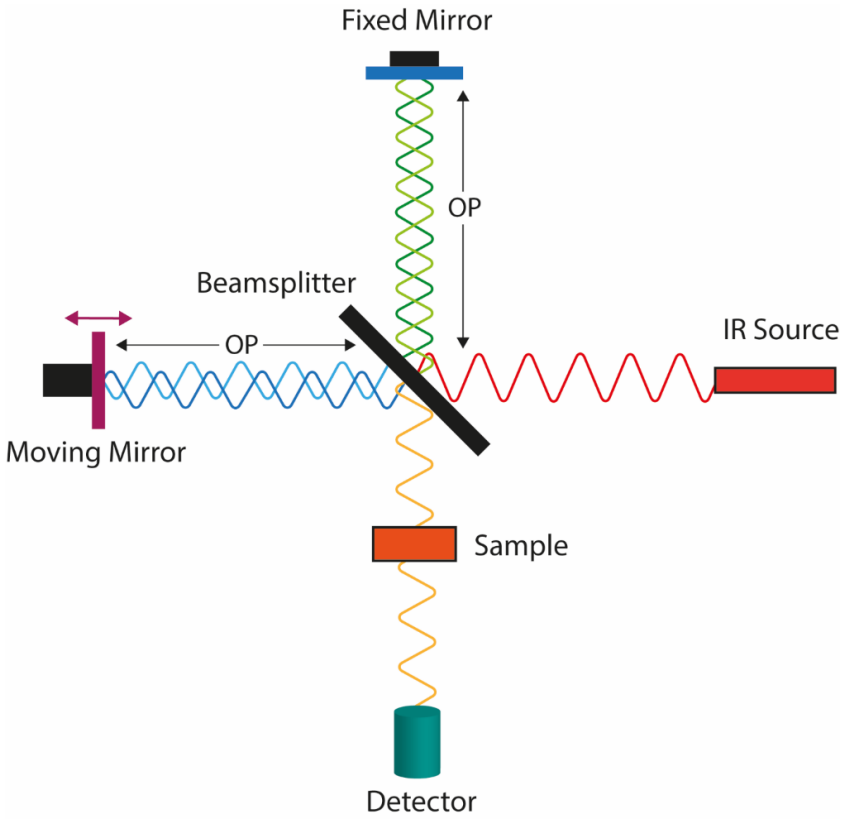

Figure 2.9 *Schematic diagram of a FTIR instrument. The IR source generates broad spectrum light that is split at the beamsplitter to the fixed and moving mirrors. The light is then reflected off the mirrors and recombined at the beamsplitter to pass and reflect off the sample into the detector. From which, a Fourier transform in used on the resulting interferogram (based on the optical path differences of the different mirrors) to produce the traditional frequency based infrared spectrum. OP = optical path.*

A Thermo Scientific Nicolet iN10MX infrared imaging microscope at Curtin University was used for mid-infrared (5-15 μm) analysis. In the μ-FTIR spectrometer, the primary detector was a Mercury Cadmium Telluride (MCT) liquid-N_2 cooled A detector (MCT/A). MCT/A, as opposed to an MCT/B, is a slightly narrower band infrared detector operating in the 5-15 μm wavelength region, as compared to 5-25 μm for the MCT/B. This narrower wavelength range improves infrared response of the samples, increasing the speed of acquisition and signal-to-noise ratio. The MCT/A detector is limited to 15 μm, but by sacrificing wavelength range, the potential spatial resolution of the data greatly increases. This is essential for acquiring targeted spectra of complexly zoned minerals. On Mars, the CO2 (atmosphere) prevents any spectral data between ~12-20 μm from being acquired. Between 20-50 μm (up to the wavelength range of TES) include absorptions that relate to longer-wavelength reststrahlen features (mainly Si(T)-O bending). Hamilton (2000) suggests longer wavelength features are not as susceptible to changing based on the geochemistry of the pyroxenes. The main impact of missing these features will be in the identification of pyroxene in TES surface spectra of Mars. Unlike the previous instruments, the μ-FTIR spectrometer was predominantly used for biomedical research. Therefore, a number of tests had to be conducted to evaluate the optimal conditions and methodologies for geological sample analysis.

There are three essential conditions to any geological IR analysis: (1) the aperture (spot) and step size, in my analysis these were always the same, (2) the scan rate, which is equivalent to the dwell time and (3) the polished gold background sample. As with most analyses, the higher the spatial (spot and step size) resolution the noisier the data. To mitigate these effects, scan rates can be increased. The longer the same spot is being measured, the higher the signal-to-noise ratio will be. However, by increasing the spatial resolution and scan rate, the speed of acquisition can be significantly reduced. This is a limiting factor, as due to the requirement for liquid-N_2 to keep the detector cool, maximum mapping time is ~20 hours. Thereby, higher spatial resolutions are directly proportional to mapping smaller areas. Lastly, a background acquisition of a polished gold standard removes any outlying atmospheric interference from the measured infrared spectra. The principal aim of the tests was to find the optimal conditions that will provide infrared spectra of the Martian meteorites with a high enough signal-to-noise while mapping a large enough area for further analysis (Table

2.1). To match spectra in the extant spectral libraries and to provide extra detail for spectral analysis, 4 cm^{-1} spectral resolution was chosen. For courser data, such as TES surface spectra, the 4 cm^{-1} spectra can be convolved to 10 cm^{-1}. The spatial resolutions tested were 25, 50, 100, 300 and 400 µm, at 4, 64, 128, 256 scans. For the fine-grained meteorites, such as NWA 7034 and NWA 8159, 25 µm resolution at 128 scans was found to be optimal. Below 25 µm, the resolution hits the diffraction limit at ~20 µm. Above, it become too coarse to identify the various mineral grains effectively. 128 scans kept the noise at a minimum to identify all the details (band centres etc.) in the spectra. Any higher would not be worth the time, and at lower scan rates, the noise becomes quite a lot worse. 50 µm was the optimal spatial resolution for large area spectra maps (LASM) of the basaltic shergottites (Fig. 2.10). Due to the complex geochemical zoning, the resolution needed to be high enough to limit contamination to the spectra between different zones (as the spectra of pyroxene will vary based on geochemical composition). Lower resolution, such as 25 µm, would improve this 4-fold. However, the LASM produced at 25 µm is much smaller than at 50 µm, as the maximum analytical time does not change (~20 hours). This is compounded by the need of only 64 scans with 50 µm (128 scans were required at 25 µm), which kept the noise to very minimal levels. The lower required scans meant a higher number of spectra could be analysed. Infrared mapping of the poikilitic shergottites, which comprise relatively coarse pyroxene oikocrysts with much more distinct geochemical zoning, was conducted at 100 µm resolution. This enabled larger areas to be covered, while still being adequately high enough resolution to distinguish between the major mineralogy and phases. These parameters were suitable when mineral grains were the target. In the case when a bulk (averaged) spectrum of a whole sample was required, high resolution spectral detail was not necessary. Therefore, the largest spatial resolution size of 400 µm was used, at only 4 scans. Due to the spot size, only 4 scans were required to ensure the highest signal to noise in the spectra. These parameters allowed for rapid acquisition of the Martian meteorite spectra.

Table 2.1 *Acquisition time trials for a 900 μm² area using the MCT/A detector on the μ-FTIR.*

Step and Spot Size (μm	Scan Rate	Number of Spectra	Time
300	4	16	1 mins 15
300	64	16	7 mins 30
300	128	16	12 mins 30
300	256	16	24 mins 30
100	4	100	4 mins 10
100	64	100	39 mins
100	128	100	1 hour 16 mins
100	256	100	2 hours 30 mins
50	4	361	24 mins
50	64	361	6 hours 24 mins
50	128	361	12 hours 48 mins
50	256	361	25 hours 42 mins
25	4	1369	1 hours 30 mins
25	64	1369	24 hours 18 mins
25	128	1369	48 hours 42 mins
25	256	1369	97 hours 24 mins

The purpose of using infrared analysis of the Martian meteorites is to be able directly compare these spectra to the emissivity spectra often used in planetary remote sensing. Measuring directly in emissivity in the laboratory requires temperature controls of the sample and instrument, as the sample must be heated for analysis to be conducted. Heating and maintaining certain temperatures are not possible with the currently available off the shelf μ-FTIR spectrometers. And this PhD project requires the high-resolution in-situ targeting of a μ-FTIR to pinpoint specific grains. Therefore, for our infrared analyses, the samples were measured in reflectance, which using Kirchhoff's Law of E = 1 – R (E = emissivity, R = reflectance), we can calculate effective emissivity (Salisbury et al., 1994: Hamilton et al., 2010). In terms of band centre positions of mineral (and rock) spectra, effective emissivity is directly comparable to true emissivity. The only major difference is in the band depths of the mineral spectra. When measuring polished surfaces for infrared analysis, the signal received is much greater than that of measuring particulate samples (and remote surfaces) for emissivity. Therefore, a blackbody is included in any processing, which uniformly increases or reduces the spectral contrast differences across multiple datasets, allowing for direct comparisons.

Once the infrared analyses were completed, they were saved as ENVI files and imported into the Arizona State University's open source Davinci program (http://davinci.asu.edu). This program was specially designed to handle and process the data acquired with the Thermal Emission Spectrometer (TES), Miniature-Thermal Emission Spectrometer (Mini-TES) and the Thermal Emission Imaging System (THEMIS) instruments sent to Mars onboard various spacecraft. Hence, this program was ideally suited to manipulate and then test any of the infrared spectra data. Once imported, the infrared maps were flipped and normalised to an effective emissivity of one (1). This normalisation procedure prevents any meaningful quantitative spectral contrast or emissivity from being investigated, however, as stated previously, this does not affect the band centres of the mineral spectra. Once this was completed, the spectra were ready for interpretation and modelling.

2.7 Linear Modelling

The final step in the methodology is to use the infrared spectra measured from the Martian meteorites, in combination with other spectra, to model target infrared spectra (i.e., bulk Martian meteorites) using linear modelling. This is because in MIR wavelengths, the infrared spectrum of an area is the linear combination of its constituents (e.g., Aronson et al., 1966; Salisbury and Eastes, 1985; Sabol et al., 1992; Ramsey and Christensen, 1998). For example, the bulk infrared spectrum of a rock will be a linear combination of its mineralogy and their respective abundances. Using this process, we can infer the composition of rocks by using linear least squares (LLS)

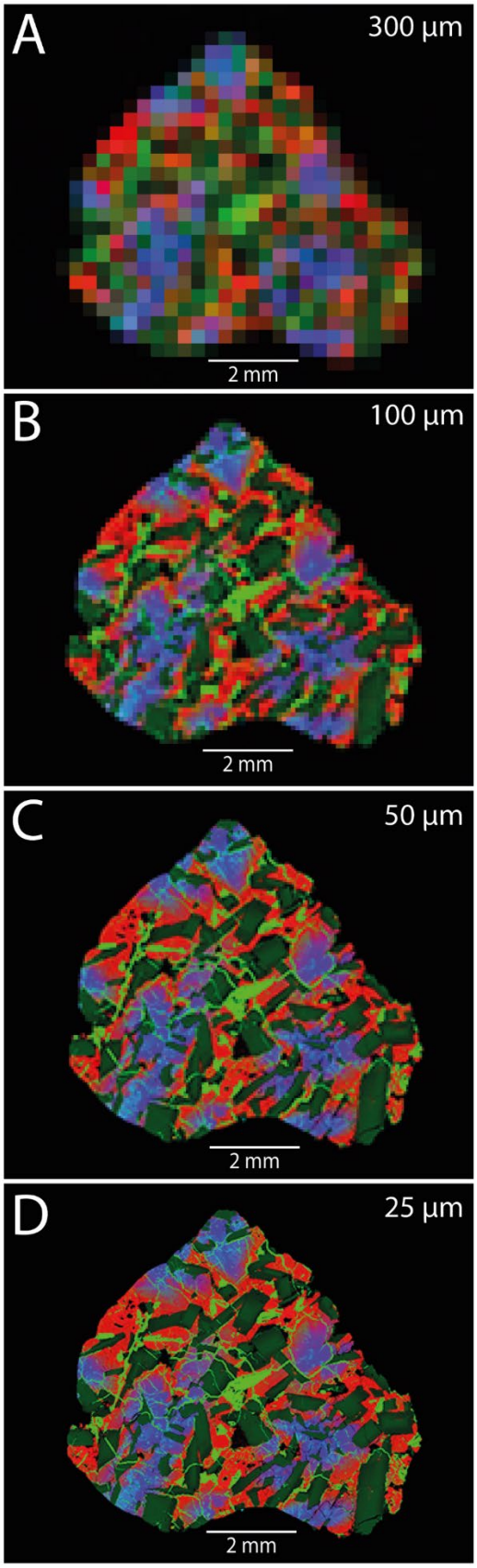

Figure 2.10 *TIMA combined element maps of basaltic shergottite NWA 12335 at different spatial resolutions (replicating reproducibility in the µ-FTIR system). Fe = red, Ca = green and Mg = blue. 50 µm was selected as the optimal spatial resolution that could distinguish the complex zoning in the basaltic shergottites and still produce LASMs within the liquid-N_2 cooling time constraints.*

modelling of infrared spectra (Adams, 1993; Ramsey and Christensen, 1998). This is an iterative mathematical algorithm that attempts to match the best combination and abundance of spectral end members to the target spectrum. The goodness of fit of the algorithm can be measured by subtracting the model from the measured spectrum, giving the residual error. This indicates the specific wavelengths where there is a mismatch (or not), which may indicate missing compositions or that the spectral library being used may need to be revised. With each iteration of the LLS modelling, spectral end members that resulted in a negative abundance are removed. When using large spectral libraries (>30 spectral end members) this can remove spectral end members that may actually be present in the target rock (Rogers and Christensen, 2007). To avoid unnecessary removal of spectral end members, this project uses a non-negative least squares (NNLS) algorithm, which does not remove spectral end members with negative abundances (Lawson and Hanson, 1974; Rogers and Aharonson, 2008). All the end members of the spectral library are available to the algorithm until the final iteration, where the non-negative solution is found. This improves the accuracy of the final modelling result by removing the possibility of discarding a true spectral end member. To enable comparison between differently sourced spectra, for example between thin section or particulate measured spectra, a blackbody spectral end member is used (e.g., Hamilton et al., 1997; Bandfield et al., 2000). A blackbody spectrum equals unity at all wavelengths, and therefore can uniformly increase or decrease spectral contrast of infrared spectra. This is quite important when using thin section measured spectra as they tend to have a large spectral contrast due to the high signal detected from the polished surfaces.

2.8 Conclusion

The number of techniques in this project were used to characterise the mineralogical and geochemical composition of the shergottites and use that information to examine infrared spectra of the major mineralogy, especially the pyroxenes, in thin section. As Martian meteorites are exceptionally rare, all the techniques are (mostly) non-destructive. This has enabled cross-examination of the same areas of the samples with multiple techniques. For example, in Chapter 2, the bulk rare-earth element (REE) patterns of the samples were inferred by combining the modal mineralogy determined by HRXCT and TIMA with the trace element compositions (LA-ICP-MS) of the

mineralogy. And in Chapter 3, TIMA, EBSD, EPMA and μ-FTIR were all used on the same areas/grains to produce infrared spectra of the shergottites, with a known geochemistry and crystallography. The final linear modelling (Chapter 4) utilises the results of the previous two chapters to model Martian meteorite infrared spectra.

2.9 References

Adams, J. B. (1993). Imaging spectroscopy: Interpretation based on spectral mixture analysis. *Remote geochemical analysis: Elemental and mineralogical composition*, 145-166.

Agee, C. B., Wilson, N. V., McCubbin, F. M., Ziegler, K., Polyak, V. J., Sharp, Z. D., et al. (2013). Unique Meteorite from Early Amazonian Mars: Water-Rich Basaltic Breccia Northwest Africa 7034. *Science*, *339*(6121), 780–785. https://doi.org/10.1126/science.1228858

Ali, A., Jabeen, I., Gregory, D., Verish, R., & Banerjee, N. R. (2016). New triple oxygen isotope data of bulk and separated fractions from SNC meteorites: Evidence for mantle homogeneity of Mars. *Meteoritics & Planetary Science*, *51*(5), 981–995. https://doi.org/10.1111/maps.12640

Armytage, R. M. G., Debaille, V., Brandon, A. D., & Agee, C. B. (2018). A complex history of silicate differentiation of Mars from Nd and Hf isotopes in crustal breccia NWA 7034. *Earth and Planetary Science Letters*, *502*(Science 339 2013), 274–283. https://doi.org/10.1016/j.epsl.2018.08.013

Aronson, J. R., Emslie, A. G., & McLinden, H. G. (1966). Infrared spectra from fine particulate surfaces. *Science*, *152*(3720), 345-346.

Balta, J. B., Sanborn, M., McSween, H. Y., & Wadhwa, M. (2013). Magmatic history and parental melt composition of olivine-phyric shergottite LAR 06319: Importance of magmatic degassing and olivine antecrysts in Martian magmatism. *Meteoritics & Planetary Science*, *48*(8), 1359–1382. https://doi.org/10.1111/maps.12140

Bandfield, J. L., Hamilton, V. E., & Christensen, P. R. (2000). A Global View of Martian Surface Compositions from MGS-TES. *Science*, *287*(5458), 1626–1630. https://doi.org/10.1126/science.287.5458.1626

Barrat, J., & Bollinger, C. (2010). Geochemistry of the Martian meteorite ALH 84001, revisited. *Meteoritics & Planetary Science*, *45*(4), 495–512. https://doi.org/10.1111/j.1945-5100.2010.01042.x

Bogard, D. D., & Johnson, P. (1983). Martian Gases in an Antarctic Meteorite? *Science*, *221*(4611), 651–654. https://doi.org/10.1126/science.221.4611.651

Borg, L. E., Nyquist, L. E., Wiesmann, H., & Reese, Y. (2002). Constraints on the petrogenesis of Martian meteorites from the Rb-Sr and Sm-Nd isotopic systematics of the lherzolitic shergottites ALH77005 and LEW88516. *Geochimica et Cosmochimica Acta*, *66*(11), 2037-2053.

Borg, L. E., & Draper, D. S. (2003). A petrogenetic model for the origin and compositional variation of the martian basaltic meteorites. *Meteoritics & Planetary Science*, *38*(12), 1713–1731. https://doi.org/10.1111/j.1945-5100.2003.tb00011.x

Bouvier, A., Blichert-Toft, J., & Albarède, F. (2009). Martian meteorite chronology and the evolution of the interior of Mars. *Earth and Planetary Science Letters*, *280*(1–4), 285–295. https://doi.org/10.1016/j.epsl.2009.01.042

Bridges, J. C., & Warren, P. H. (2006). The SNC meteorites: basaltic igneous processes on Mars. *Journal of the Geological Society*, *163*(2), 229–251. https://doi.org/10.1144/0016-764904-501

Cao, T., He, Q., & Xue, Z. (2018). Petrogenesis of basaltic shergottite NWA 8656. *Earth and Planetary Physics*, *2*(5), 384–397. https://doi.org/10.26464/epp2018036

Cassata, W. S., Cohen, B. E., Mark, D. F., Trappitsch, R., Crow, C. A., Wimpenny, J., et al. (2018). Chronology of martian breccia NWA 7034 and the formation of the

martian crustal dichotomy. *Science Advances*, *4*(5), eaap8306. https://doi.org/10.1126/sciadv.aap8306

Chabal, Y. J. (1988). Surface infrared spectroscopy. *Surface Science Reports*, *8*(5-7), 211-357.

Christensen, P. R., Bandfield, J. L., Hamilton, V. E., Ruff, S. W., Kieffer, H. H., Titus, T. N., et al. (2001). Mars Global Surveyor Thermal Emission Spectrometer experiment: Investigation description and surface science results. *Journal of Geophysical Research: Planets*, *106*(E10), 23823–23871. https://doi.org/10.1029/2000je001370

Christensen, P. R., Jakosky, B. M., Kieffer, H. H., Malin, M. C., Jr, H. Y. M., Nealson, K., et al. (2004). The Thermal Emission Imaging System (THEMIS) for the Mars 2001 Odyssey Mission. *Space Science Reviews*, *110*(1/2), 85–130. https://doi.org/10.1023/b:spac.0000021008.16305.94

Collinet, M., Charlier, B., Namur, O., Oeser, M., Médard, E., & Weyer, S. (2017). Crystallization history of enriched shergottites from Fe and Mg isotope fractionation in olivine megacrysts. *Geochimica et Cosmochimica Acta*, *207*(Philos. Trans. Roy. Soc. B: Biol. Sci. 361 2006), 277–297. https://doi.org/10.1016/j.gca.2017.03.029

Combs, L. M., Udry, A., Howarth, G. H., Righter, M., Lapen, T. J., Gross, J., et al. (2019). Petrology of the enriched poikilitic shergottite Northwest Africa 10169: Insight into the martian interior. *Geochimica et Cosmochimica Acta*. https://doi.org/10.1016/j.gca.2019.07.001

Debaille, V., Yin, Q.-Z., Brandon, A. D., & Jacobsen, B. (2008). Martian mantle mineralogy investigated by the 176Lu–176Hf and 147Sm–143Nd systematics of shergottites. *Earth and Planetary Science Letters*, *269*(1–2), 186–199. https://doi.org/10.1016/j.epsl.2008.02.008

Diem, M., Roberts, G. M., Lee, O., & Barlow, A. (1988). Design and performance of an optimized dispersive infrared dichrograph. *Applied spectroscopy*, *42*(1), 20-27.

El-Dasher, B. S., & Torres, S. G. (2009). Electron Backscatter Diffraction in Materials Science, 339–344. https://doi.org/10.1007/978-0-387-88136-2_25

Faix, O. (1992). Fourier transform infrared spectroscopy. In *Methods in lignin chemistry* (pp. 83-109). Springer, Berlin, Heidelberg.

Ferdous, J., Brandon, A. D., Peslier, A. H., & Pirotte, Z. (2017). Evaluating crustal contributions to enriched shergottites from the petrology, trace elements, and Rb-Sr and Sm-Nd isotope systematics of Northwest Africa 856. *Geochimica et Cosmochimica Acta*, *211*(Science 339 2013), 280–306. https://doi.org/10.1016/j.gca.2017.05.032

Filiberto, J., Chin, E., Day, J. M. D., Franchi, I. A., Greenwood, R. C., Gross, J., et al. (2012). Geochemistry of intermediate olivine-phyric shergottite Northwest Africa 6234, with similarities to basaltic shergottite Northwest Africa 480 and olivine-phyric shergottite Northwest Africa 2990. *Meteoritics & Planetary Science*, *47*(8), 1256–1273. https://doi.org/10.1111/j.1945-5100.2012.01382.x

Filiberto, J. (2017). Geochemistry of Martian basalts with constraints on magma genesis. *Chemical Geology*, *466*(Earth Planet. Sci. Lett. 224 3-4 2004), 1–14. https://doi.org/10.1016/j.chemgeo.2017.06.009

Filiberto, J., Gross, J., Udry, A., Trela, J., Wittmann, A., Cannon, K. M., et al. (2018). Shergottite Northwest Africa 6963: A Pyroxene-Cumulate Martian Gabbro. *Journal of Geophysical Research: Planets*, *123*(7), 1823–1841. https://doi.org/10.1029/2018je005635

First, E., & Hammer, J. (2016). Igneous cooling history of olivine-phyric shergottite Yamato 980459 constrained by dynamic crystallization experiments. *Meteoritics & Planetary Science*, *51*(7), 1233–1255. https://doi.org/10.1111/maps.12659

Fritz, J., Fernandes, V. A., Greshake, A., Holzwarth, A., & Böttger, U. (2019). On the formation of diaplectic glass: Shock and thermal experiments with plagioclase of

different chemical compositions. *Meteoritics & Planetary Science*, *54*(7), 1533–1547. https://doi.org/10.1111/maps.13289

Goldstein, J. I., Newbury, D. E., Echlin, P., Joy, D. C., Lyman, C. E., Lifshin, E., et al. (2003). Scanning Electron Microscopy and X-ray Microanalysis, Third Edition. https://doi.org/10.1007/978-1-4615-0215-9

Goodrich, C. A. (2002). Olivine-phyric martian basalts: A new type of shergottite. *Meteoritics & Planetary Science*, *37*(S12), B31–B34. https://doi.org/10.1111/j.1945-5100.2002.tb00901.x

Griffiths, P. R., & De Haseth, J. A. (2007). *Fourier transform infrared spectrometry* (Vol. 171). John Wiley & Sons.

Gross, J., Treiman, A. H., Filiberto, J., & Herd, C. D. K. (2011). Primitive olivine-phyric shergottite NWA 5789: Petrography, mineral chemistry, and cooling history imply a magma similar to Yamato-980459. *Meteoritics & Planetary Science*, *46*(1), 116–133. https://doi.org/10.1111/j.1945-5100.2010.01152.x

Günther, D., & Hattendorf, B. (2005). Solid sample analysis using laser ablation inductively coupled plasma mass spectrometry. *TrAC Trends in Analytical Chemistry*, *24*(3), 255–265. https://doi.org/10.1016/j.trac.2004.11.017

Hamid, S. H., & Prichard, W. H. (1988). Application of infrared spectroscopy in polymer degradation. *Polymer-Plastics Technology and Engineering*, *27*(3), 303-334.

Hamilton, V. E., Christensen, P. R., & McSween, H. Y. (1997). Determination of Martian meteorite lithologies and mineralogies using vibrational spectroscopy. *Journal of Geophysical Research: Planets*, *102*(E11), 25593–25603. https://doi.org/10.1029/97je01874

Hamilton, V. E. (2010). Thermal infrared (vibrational) spectroscopy of Mg–Fe olivines: A review and applications to determining the composition of planetary

surfaces. *Chemie Der Erde - Geochemistry*, *70*(1), 7–33. https://doi.org/10.1016/j.chemer.2009.12.005

Hamilton, V. E., Simon, A. A., Christensen, P. R., Reuter, D. C., Clark, B. E., Barucci, M. A., et al. (2019). Evidence for widespread hydrated minerals on asteroid (101955) Bennu. *Nature Astronomy*, *3*(4), 332-340.

Hanel, R., Conrath, B., Hovis, W., Kunde, V., Lowman, P., Maguire, W., et al. (1972). Investigation of the Martian environment by infrared spectroscopy on Mariner 9. *Icarus*, *17*(2), 423-442.

Harvey, R. P., & McSween, H. Y. (1996). A possible high-temperature origin for the carbonates in the Martian meteorite ALH84001. *Nature*, *382*(6586), 49-51.

He, Q., Xiao, L., Balta, J. B., Baziotis, I. P., Hsu, W., & Guan, Y. (2015). Petrography and geochemistry of the enriched basaltic shergottite Northwest Africa 2975. *Meteoritics & Planetary Science*, *50*(12), 2024–2044. https://doi.org/10.1111/maps.12571

Herd, C. D. K. (2003). The oxygen fugacity of olivine-phyric martian basalts and the components within the mantle and crust of Mars. *Meteoritics & Planetary Science*, *38*(12), 1793–1805. https://doi.org/10.1111/j.1945-5100.2003.tb00015.x

Herd, C. D. K., Walton, E. L., Agee, C. B., Muttik, N., Ziegler, K., Shearer, C. K., et al. (2017). The Northwest Africa 8159 martian meteorite: Expanding the martian sample suite to the early Amazonian. *Geochimica et Cosmochimica Acta*, *218*(Science 339 2013), 1–26. https://doi.org/10.1016/j.gca.2017.08.037

Hook, S. J., & Kahle, A. B. (1996). The micro Fourier transform interferometer (μFTIR)—a new field spectrometer for acquisition of infrared data of natural surfaces. *Remote Sensing of Environment*, *56*(3), 172-181.

Howarth, G. H., Pernet-Fisher, J. F., Balta, J. B., Barry, P. H., Bodnar, R. J., & Taylor, L. A. (2014). Two-stage polybaric formation of the new enriched, pyroxene-

oikocrystic, lherzolitic shergottite, NWA 7397. *Meteoritics & Planetary Science*, *49*(10), 1812–1830. https://doi.org/10.1111/maps.12357

Howarth, G. H., Udry, A., & Day, J. M. D. (2018). Petrogenesis of basaltic shergottite Northwest Africa 8657: Implications for fO2 correlations and element redistribution during shock melting in shergottites. *Meteoritics & Planetary Science*, *53*(2), 249–267. https://doi.org/10.1111/maps.12999

Hrstka, T., Gottlieb, P., Skála, R., Breiter, K., & Motl, D. (2018). Automated mineralogy and petrology - applications of TESCAN Integrated Mineral Analyzer (TIMA). *Journal of Geosciences*, 47–63. https://doi.org/10.3190/jgeosci.250

Humayun, M., Nemchin, A., Zanda, B., Hewins, R. H., Grange, M., Kennedy, A., et al. (2013). Origin and age of the earliest Martian crust from meteorite NWA 7533. *Nature*, *503*(7477), 513–516. https://doi.org/10.1038/nature12764

Humphreys, F. J. (2004). Characterisation of fine-scale microstructures by electron backscatter diffraction (EBSD). *Scripta Materialia*, *51*(8), 771–776. https://doi.org/10.1016/j.scriptamat.2004.05.016

Jambon, A., Barrat, J. A., Sautter, V., Gillet, P., Göpel, C., Javoy, M., et al. (2002). The basaltic shergottite Northwest Africa 856: Petrology and chemistry. *Meteoritics & Planetary Science*, *37*(9), 1147–1164. https://doi.org/10.1111/j.1945-5100.2002.tb00885.x

Jambon, A., Sautter, V., Barrat, J.-A., Gattacceca, J., Rochette, P., Boudouma, O., et al. (2016). Northwest Africa 5790: Revisiting nakhlite petrogenesis. *Geochimica et Cosmochimica Acta*, *190*(Nature 294 1981), 191–212. https://doi.org/10.1016/j.gca.2016.06.032

Jones, J. H. (2015). Various aspects of the petrogenesis of the Martian shergottite meteorites. *Meteoritics & Planetary Science*, *50*(4), 674–690. https://doi.org/10.1111/maps.12421

Ketcham, R. A. (2005). Three-dimensional grain fabric measurements using high-resolution X-ray computed tomography. *Journal of Structural Geology*, *27*(7), 1217–1228. https://doi.org/10.1016/j.jsg.2005.02.006

Kieffer, H. H., Neugebauer, G., Munch, G., Chase, S. C., & Miner, E. (1972). Infrared thermal mapping experiment: The Viking Mars orbiter. *Icarus*, *16*(1), 47–56. https://doi.org/10.1016/0019-1035(72)90136-4

Kizovski, T. V., Tait, K. T., Cecco, V. E. D., White, L. F., & Moser, D. E. (2019). Detailed mineralogy and petrology of highly shocked poikilitic shergottite Northwest Africa 6342. *Meteoritics & Planetary Science*, *54*(4), 768–784. https://doi.org/10.1111/maps.13255

Koch, J., & Günther, D. (2011). Review of the State-of-the-Art of Laser Ablation Inductively Coupled Plasma Mass Spectrometry. *Applied Spectroscopy*, *65*(5), 155A-162A. https://doi.org/10.1366/11-06255

Kring, D. A., Gleason, J. D., Swindle, T. D., Nishiizumi, K., Caffee, M. W., Hill, D. H., et al. (2003). Composition of the first bulk melt sample from a volcanic region of Mars: Queen Alexandra Range 94201. *Meteoritics & Planetary Science*, *38*(12), 1833–1848. https://doi.org/10.1111/j.1945-5100.2003.tb00018.x

Jaret, S. J., Woerner, W. R., Phillips, B. L., Ehm, L., Nekvasil, H., Wright, S. P., & Glotch, T. D. (2015). Maskelynite formation via solid-state transformation: Evidence of infrared and X-ray anisotropy. *Journal of Geophysical Research: Planets*, *120*(3), 570–587. https://doi.org/10.1002/2014je004764

Lanari, P., Vho, A., Bovay, T., Airaghi, L., & Centrella, S. (2019). Quantitative compositional mapping of mineral phases by electron probe micro-analyser. *Geological Society, London, Special Publications*, *478*(1), 39-63.

Lane, M. D., & Bishop, J. L. (2019). Mid-infrared (thermal) emission and reflectance spectroscopy. *Remote Compositional Analysis: Techniques for Understanding Spectroscopy*, 42-67.

Lapen, T. J., Righter, M., Andreasen, R., Irving, A. J., Satkoski, A. M., Beard, B. L., et al. (2017). Two billion years of magmatism recorded from a single Mars meteorite ejection site. *Science Advances*, *3*(2), e1600922. https://doi.org/10.1126/sciadv.1600922

Lawson, C. L., & Hanson, R. J. (1974). Linear least squares with linear inequality constraints. *Solving least squares problems*, 158-173.

Lin, Y., Guan, Y., Wang, D., Kimura, M., & Leshin, L. A. (2005). Petrogenesis of the new lherzolitic shergottite Grove Mountains 99027: Constraints of petrography, mineral chemistry, and rare earth elements. *Meteoritics & Planetary Science*, *40*(11), 1599–1619. https://doi.org/10.1111/j.1945-5100.2005.tb00134.x

MacArthur, J. L., Bridges, J. C., Hicks, L. J., Burgess, R., Joy, K. H., Branney, M. J., et al. (2018). Mineralogical Constraints on the Thermal History of Martian Regolith Breccia Northwest Africa 8114. *Geochimica et Cosmochimica Acta*, *246*(J. Geophys. Res. Planets 110 2005), 267–298. https://doi.org/10.1016/j.gca.2018.11.026

McCoy, T. J., Taylor, G. J., & Keil, K. (1992). Zagami: Product of a two-stage magmatic history. *Geochimica et Cosmochimica Acta*, *56*(9), 3571–3582. https://doi.org/10.1016/0016-7037(92)90400-d

McCubbin, F. M., Elardo, S. M., Shearer, C. K., Smirnov, A., Hauri, E. H., & Draper, D. S. (2013). A petrogenetic model for the comagmatic origin of chassignites and nakhlites: Inferences from chlorine-rich minerals, petrology, and geochemistry. *Meteoritics & Planetary Science*, *48*(5), 819–853. https://doi.org/10.1111/maps.12095

McCubbin, F. M., Boyce, J. W., Novák-Szabó, T., Santos, A. R., Tartèse, R., Muttik, N., et al. (2016). Geologic history of Martian regolith breccia Northwest Africa 7034: Evidence for hydrothermal activity and lithologic diversity in the Martian crust. *Journal of Geophysical Research: Planets*, *121*(10), 2120–2149. https://doi.org/10.1002/2016je005143

McKay, D. S., Gibson, E. K., Thomas-Keprta, K. L., Vali, H., Romanek, C. S., Clemett, S. J., ... & Zare, R. N. (1996). Search for past life on Mars: Possible relic biogenic activity in Martian meteorite ALH84001. *Science*, *273*(5277), 924-930.

McSween, H. Y., Eisenhour, D. D., Taylor, L. A., Wadhwa, M., & Crozaz, G. (1996). QUE94201 shergottite: Crystallization of a Martian basaltic magma. *Geochimica et Cosmochimica Acta*, *60*(22), 4563–4569. https://doi.org/10.1016/s0016-7037(96)00265-7

Mees, F., Swennen, R., Van Geet, M., & Jacobs, P. (2003). Applications of X-ray computed tomography in the geosciences. *Geological Society, London, Special Publications*, *215*(1), 1-6.

Mikouchi, T., & Kurihara, T. (2008). Mineralogy and petrology of paired lherzolitic shergottites Yamato 000027, Yamato 000047, and Yamato 000097: Another fragment from a Martian "lherzolite" block. *Polar Science*, *2*(3), 175–194. https://doi.org/10.1016/j.polar.2008.06.003

Mittlefehldt, D. W. (1994). ALH84001, a cumulate orthopyroxenite member of the Martian meteorite clan. *Meteoritics*, *29*(2), 214-221.

Nyquist, L. E., Bogard, D. D., Shih, C.-Y., Greshake, A., Stöffler, D., & Eugster, O. (2001). Ages and Geologic Histories of Martian Meteorites. *Space Science Reviews*, *96*(1/4), 105–164. https://doi.org/10.1023/a:1011993105172

Owen, T., Biemann, K., Rushneck, D. R., Biller, J. E., Howarth, D. W., & Lafleur, A. L. (1977). The composition of the atmosphere at the surface of Mars. *Journal of Geophysical Research*, *82*(28), 4635–4639. https://doi.org/10.1029/js082i028p04635

Peters, T. J., Simon, J. I., Jones, J. H., Usui, T., Moriwaki, R., Economos, R. C., et al. (2015). Tracking the source of the enriched martian meteorites in olivine-hosted melt inclusions of two depleted shergottites, Yamato 980459 and Tissint. *Earth and Planetary Science Letters*, *418*(Earth Planet. Sci. Lett. 224 2004), 91–102. https://doi.org/10.1016/j.epsl.2015.02.033

Rahib, R. R., Udry, A., Howarth, G. H., Gross, J., Paquet, M., Combs, L. M., et al. (2019). Mantle source to near-surface emplacement of enriched and intermediate poikilitic shergottites in Mars. *Geochimica et Cosmochimica Acta*, *266*, 463–496. https://doi.org/10.1016/j.gca.2019.07.034

Ramsey, M. S., & Christensen, P. R. (1998). Mineral abundance determination: Quantitative deconvolution of thermal emission spectra. *Journal of Geophysical Research: Solid Earth*, *103*(B1), 577–596. https://doi.org/10.1029/97jb02784

Riches, A. J. V., Liu, Y., Day, J. M. D., Puchtel, I. S., Rumble, D., McSween, H. Y., et al. (2011). Petrology and geochemistry of Yamato 984028: a cumulate lherzolitic shergottite with affinities to Y 000027, Y 000047, and Y 000097. *Polar Science*, *4*(4), 497–514. https://doi.org/10.1016/j.polar.2010.04.009

Rogers, A. D., & Christensen, P. R. (2007). Surface mineralogy of Martian low-albedo regions from MGS-TES data: Implications for upper crustal evolution and surface alteration. *Journal of Geophysical Research: Planets (1991–2012)*, *112*(E1). https://doi.org/10.1029/2006je002727

Rogers, A. D., & Aharonson, O. (2008). Mineralogical composition of sands in Meridiani Planum determined from Mars Exploration Rover data and comparison to orbital measurements. *Journal of Geophysical Research: Planets (1991–2012)*, *113*(E6). https://doi.org/10.1029/2007je002995

Sabol Jr, D. E., Adams, J. B., & Smith, M. O. (1992). Quantitative subpixel spectral detection of targets in multispectral images. *Journal of Geophysical Research: Planets*, *97*(E2), 2659-2672.

Salisbury, J. W., & Eastes, J. W. (1985). The effect of particle size and porosity on spectral contrast in the mid-infrared. *Icarus*, *64*(3), 586-588.

Salisbury, J. W., Walter, L. S., & Vergo, N. (1987). Mid-infrared (2 l25 pm) spectra of minerals (lst edition). *U.S. Geological Survey OpenFile Report* 87 -263, 356 p.

Salisbury, J. W., Wald, A., & D'Aria, D. M. (1994). Thermal-infrared remote sensing and Kirchhoff's law: 1. Laboratory measurements. *Journal of Geophysical Research: Solid Earth*, *99*(B6), 11897-11911.

Sarbadhikari, A. B., Day, J. M. D., Liu, Y., Rumble, D., & Taylor, L. A. (2009). Petrogenesis of olivine-phyric shergottite Larkman Nunatak 06319: Implications for enriched components in martian basalts. *Geochimica et Cosmochimica Acta*, *73*(7), 2190–2214. https://doi.org/10.1016/j.gca.2009.01.012

Shaheen, R., Niles, P. B., Chong, K., Corrigan, C. M., & Thiemens, M. H. (2015). Carbonate formation events in ALH 84001 trace the evolution of the Martian atmosphere. *Proceedings of the National Academy of Sciences*, *112*(2), 336-341.

Siesler, H. W., Ozaki, Y., Kawata, S., & Heise, H. M. (Eds.). (2008). *Near-infrared spectroscopy: principles, instruments, applications*. John Wiley & Sons.

Smith, J. V., & Hervig, R. L. (1979). SHERGOTTY METEORITE: MINERALOGY, PETROGRAPHY AND MINOR ELEMENTS. *Meteoritics*, *14*(1), 121–142. https://doi.org/10.1111/j.1945-5100.1979.tb00486.x

Stuart, B. H. (2005). Infrared Spectroscopy: Fundamentals and Applications. *Analytical Techniques in the Sciences*, 137–165. https://doi.org/10.1002/0470011149.ch7

Taylor, L. A., Nazarov, M. A., Shearer, C. K., McSween, H. Y., Cahill, J., Neal, C. R., et al. (2002). Martian meteorite Dhofar 019: A new shergottite. *Meteoritics & Planetary Science*, *37*(8), 1107–1128. https://doi.org/10.1111/j.1945-5100.2002.tb00881.x

Thompson, C. S., & Wadsworth, M. E. (1957). Determination of the Composition of Plagio-Clase Feldspars by Means of Infrared Spectroscopy. *American Mineralogist: Journal of Earth and Planetary Materials*, *42*(5-6), 334-341.

Treiman, A. H. (2005). The nakhlite meteorites: Augite-rich igneous rocks from Mars. *Chemie Der Erde - Geochemistry*, *65*(3), 203–270. https://doi.org/10.1016/j.chemer.2005.01.004

Treiman, A. H., Dyar, M. D., McCanta, M., Noble, S. K., & Pieters, C. M. (2007). Martian Dunite NWA 2737: Petrographic constraints on geological history, shock events, and olivine color. *Journal of Geophysical Research: Planets (1991–2012)*, *112*(E4). https://doi.org/10.1029/2006je002777

Treiman, A. H., & Filiberto, J. (2015). Geochemical diversity of shergottite basalts: Mixing and fractionation, and their relation to Mars surface basalts. *Meteoritics & Planetary Science*, *50*(4), 632–648. https://doi.org/10.1111/maps.12363

Udry, A., Howarth, G. H., Lapen, T. J., & Righter, M. (2017). Petrogenesis of the NWA 7320 enriched martian gabbroic shergottite: Insight into the martian crust. *Geochimica et Cosmochimica Acta*, *204*(Science 339 2013), 1–18. https://doi.org/10.1016/j.gca.2017.01.032

Udry, A., & Day, J. M. D. (2018). 1.34 billion-year-old magmatism on Mars evaluated from the co-genetic nakhlite and chassignite meteorites. *Geochimica et Cosmochimica Acta*, *238*, 292–315. https://doi.org/10.1016/j.gca.2018.07.006

Udry, A., Howarth, G. H., Herd, C. D. K., Day, J. M. D., Lapen, T. J., & Filiberto, J. (2020). What Martian Meteorites Reveal About the Interior and Surface of Mars. *Journal of Geophysical Research: Planets*, *125*(12). https://doi.org/10.1029/2020je006523

Usui, T., McSween, H. Y., & Floss, C. (2008). Petrogenesis of olivine-phyric shergottite Yamato 980459, revisited. *Geochimica et Cosmochimica Acta*, *72*(6), 1711–1730. https://doi.org/10.1016/j.gca.2008.01.011

Usui, T., Sanborn, M., Wadhwa, M., & McSween, H. Y. (2010). Petrology and trace element geochemistry of Robert Massif 04261 and 04262 meteorites, the first

examples of geochemically enriched lherzolitic shergottites. *Geochimica et Cosmochimica Acta*, *74*(24), 7283–7306. https://doi.org/10.1016/j.gca.2010.09.010

Usui, T., Alexander, C. M. O., Wang, J., Simon, J. I., & Jones, J. H. (2012). Origin of water and mantle–crust interactions on Mars inferred from hydrogen isotopes and volatile element abundances of olivine-hosted melt inclusions of primitive shergottites. *Earth and Planetary Science Letters*, *357*(Nature 461 2009), 119–129. https://doi.org/10.1016/j.epsl.2012.09.008

Walton, E. L., & Spray, J. G. (2003). Mineralogy, microtexture, and composition of shock-induced melt pockets in the Los Angeles basaltic shergottite. *Meteoritics & Planetary Science*, *38*(12), 1865–1875. https://doi.org/10.1111/j.1945-5100.2003.tb00020.x

Warren, P. H., Greenwood, J. P., & Rubin, A. E. (2004). Los Angeles: A tale of two stones. *Meteoritics & Planetary Science*, *39*(1), 137–156. https://doi.org/10.1111/j.1945-5100.2004.tb00054.x

Yamaguchi, Y., Kahle, A. B., Tsu, H., Kawakami, T., & Pniel, M. (1998). Overview of advanced spaceborne thermal emission and reflection radiometer (ASTER). *IEEE Transactions on geoscience and remote sensing*, *36*(4), 1062-1071.

Chapter 3: Geochemical and Mineralogical Classification of Four New Shergottites: NWA 10441, NWA 10818, NWA 11043 and NWA 12335

1.1 Introduction

Martian meteorites are extremely rare, comprising less than 0.5% (~300 out of ~65,000) of the total number of confirmed meteorites in the world (Meteoritical Bulletin Database). Therefore, the discovery of new meteorites from Mars represents an exciting opportunity to expand our understanding of the only samples of the Martian surface available on Earth. Aside from NWA 7034 and its pairs, Martian meteorites are predominantly igneous and can be split up into three main groups (not including the single orthopyroxenite, ALH 84001): shergottites, nakhlites and chassignites. The nakhlites and chassignites, which are compositionally clinopyroxenites and dunites, respectively, are the least abundant groups (constituting <15% of Martian meteorites combined). Based on geochemical similarities, cosmic ray exposure and crystallization ages, nakhlites and chassignites are thought to be comagmatic, possibly ejected from the same source crater (McCubbin et al., 2013). Shergottites are the most common group of Martian meteorite, and can be broadly classified into three sub-groups based on composition, mineralogy and texture: basaltic, olivine-phyric and poikilitic (e.g., McSween and Treiman, 1998).

The largest group, the basaltic shergottites, are, as the name implies, mafic rocks containing pyroxene (pigeonite and augite) and plagioclase (often shocked to form the diaplectic glass maskelynite) (e.g., Bridges and Warren, 2006). According to the Mars Meteorite Compendium (https://www-curator.jsc.nasa.gov/antmet/mmc/index.cfm), they can be divided into textural sub-groups (fine-grained, diabasic and gabbroic) based on their varying grain size. Fine-grained and diabasic shergottites are interpreted to form in near-surface intrusive and/or surface extrusive lava flows with varying abundances of cumulate crystals in the magma (e.g., McSween and McLennan, 2014). In contrast, gabbroic shergottites, only recently characterised (<5-10 years, e.g., Filiberto et al., 2014; Udry et al., 2017), are partially crystallised cumulates thought to have formed in the feeder hypabyssal system of the fine-grained and diabasic

shergottites which erupted onto the Martian surface (e.g., Udry et al., 2017; Filiberto et al., 2018).

Olivine-phyric shergottites, similarly, are mafic rocks, but primarily comprise euhedral to subhedral olivine phenocrysts surrounded by a fine-grained basaltic groundmass (Goodrich 2003). The olivine phenocrysts crystallised at depth, and subsequently the magma followed a multi-stage crystallisation sequence during ascension up through the Martian crust until the magma was finally shallowly emplaced or erupted onto the surface (e.g., Usui et al. 2008).

Poikilitic shergottites are ultramafic to mafic rocks that contain characteristic bimodal texture (e.g., Walton et al., 2012). Poikilitic regions in these rocks are composed of pyroxene (pigeonite core, augite rim) oikocrysts enclosing smaller olivine and chromite chadacrysts (e.g., Udry et al., 2020). Non-poikilitic regions are composed of smaller olivine, pyroxene (pigeonite and augite) and maskelynite grains. The relative ratio of poikilitic and non-poikilitic textures varies between the different samples of this group. Similarly to the olivine-phyric shergottites, it is thought that the poikilitic shergottites started crystallising at depth and then followed a polybaric crystallisation path (Howarth et al., 2014). The poikilitic areas crystallised first and non-poikilitic regions formed as the magma ascended and the interstitial melts accumulated and crystallised. Unlike the other shergottites, poikilitic shergottites do not appear to have erupted onto the surface but were likely emplaced in a dike or sill near the surface (e.g., Combs et al., 2019).

The shergottites are further classified geochemically based on chondrite (CI) normalized bulk rare-earth element (REE) composition. They are designated as enriched, intermediate or depleted based on the relative abundance of light REE (LREE; La, Ce, Pr, Nd and Sm) and heavy REE (HREE; Eu, Gd, Tb, Dy, Ho, Er, Tm, Yb and Lu) (e.g., Borg and Draper, 2003). In this case, enriched refers to a flat REE profile and depleted profiles are characterized by a lower abundance of LREE relative to HREE. The REE and, isotopic (from systems such as Rb-Sr, Sm-Nd, Lu-Hf and Re-Os), signature of a shergottite relates directly to its magmatic source, reflecting either

a heterogeneous mantle with enriched and depleted reservoirs or a homogenous depleted mantle where enrichment was caused by crustal contamination (e.g., McSween, 2015).

In this paper, we present mineralogical and geochemical data on four new Martian meteorites (all shergottites), all discovered in Northwest Africa (NWA) in the past 5 years: NWA 10441, NWA 10818, NWA 11043, and NWA 12335 (Bouvier et al., 2017a; Bouvier et al., 2017b; Gattacceca et al., 2019; Gattacceca et al., 2020). We confirm the preliminary classifications of these meteorites and assess whether a suite of non-destructive analytical approaches can be used to provide comprehensive geochemical analysis while preserving the bulk of the meteoritic material.

1.2 Samples and Methods

The Institute of Meteoritics at the University of New Mexico supplied ~0.5g chips of each meteorite: NWA 10441, NWA 10818, NWA 11043 and NWA 12335. These chips were first scanned by high-resolution X-ray computed tomography, then cut to create both a thick section and a 1-inch epoxy mount.

Northwest Africa 10441 and 12335 were provisionally classified as basaltic shergottites in the diabasic textural sub-group (Bouvier et al., 2017a; Gattacceca et al., 2020). Northwest Africa 10441 is thought to be one of the pairs of NWA 8656, which has previously been verified as an enriched basaltic shergottites (Cao et al., 2018; Howarth et al., 2018). Northwest Africa 10818 and 11043 were provisionally classified as poikilitic shergottites (Bouvier et al., 2017b; Gattacceca et al., 2019). Northwest Africa 11043 was classified as an enriched poikilitic shergottite (Rahib et al., 2019), though terrestrial weathering may have played a role in altering the CI-normalized REE profile (e.g., Crozaz et al., 2003).

1.2.1 High-resolution X-Ray Computed Tomography (HRXCT)

Before any sample preparation, the chips were scanned in 3D using high-resolution X-ray computed tomography (HRXCT) with a Zeiss Versa XRM520 X-ray microscope

fitted with a flat panel detector and installed at the Australian Resources Research Centre (ARRC), CSIRO Mineral Resources in Kensington, Western Australia. The instrument was set-up to maximise phase contrast between the different rock forming minerals. Analyses were acquired with beam conditions of 160 kV, 10 W and a voxel size of 12 µm with a total of 1601 projections recorded over a 360º rotation. Each greyscale volume was segmented to provide statistics on pyroxene, olivine and maskelynite using workflows similar to that described in Godel (2013) and to compute 3D modal mineralogy.

1.2.2 Tescan Integrated Mineral Analyser (TIMA)

Prior to quantitative analysis, all thin sections and epoxy round mounts were polished and coated with ~10 nm thick film of carbon. Samples were analysed using a Tescan Integrated Mineral Analyser (TIMA) in the John de Laeter Centre at Curtin University. The TIMA is a specifically designed scanning electron microscope (SEM) that semi-quantitatively maps thin and thick sections in addition to grain mounts, using four energy dispersive X-ray (EDS) detectors. This allows mineral phase, back-scattered electron (BSE) and element X-ray maps to be collected simultaneously and quickly at a very small step size. The analyses were run in high-resolution mode with 3 µm step size at a 15 mm working distance. The beam current was controlled with a 70 nm spot size at 25 kV accelerating voltage. The maps were post-processed using the TIMA-supplied software, in which phase maps of each sample were created and specific element maps extracted (Al, Ca, Cr, Fe, K, Mg, Na, P, Si, S, and Ti). These element maps were then combined into RGB images using Adobe Photoshop to inspect mineral phase relationships and distributions.

Using the combined RGB images, the modal mineralogy was determined using the pixel-counting method described in Ford et al. (2008). Briefly, the image map (Fig. 3.1) shows different mineral phases based on how elements combine. The phases are identified and selected, using the wand feature in Adobe Photoshop, to count the number of pixels. Each phase is checked multiple times to account for any automatic selection bias, from which a mean modal abundance and subsequent standard deviation is determined. These averages are verified visually. This allows an accurate

determination of modal abundances of all phases including variations in pyroxene compositions. We also compare the modal abundance of the major phases to the calculations derived by HRXCT. Thin section and HRXCT modal abundances can vary. Thin section modal abundances represent that singular surface. How applicable those abundances are to the true modal abundances of the whole sample in 3D depends on the sample. For NWA 10818, the coarse grain size of the oikocrysts reduces the accuracy of modal abundance determination of a singular surface being a true representation. A similar situation occurs with NWA 12335. Small samples of coarse-grained rocks can lead to inaccuracies when it comes to modal abundance. The XCT provides a much clearer picture of abundance throughout the samples.

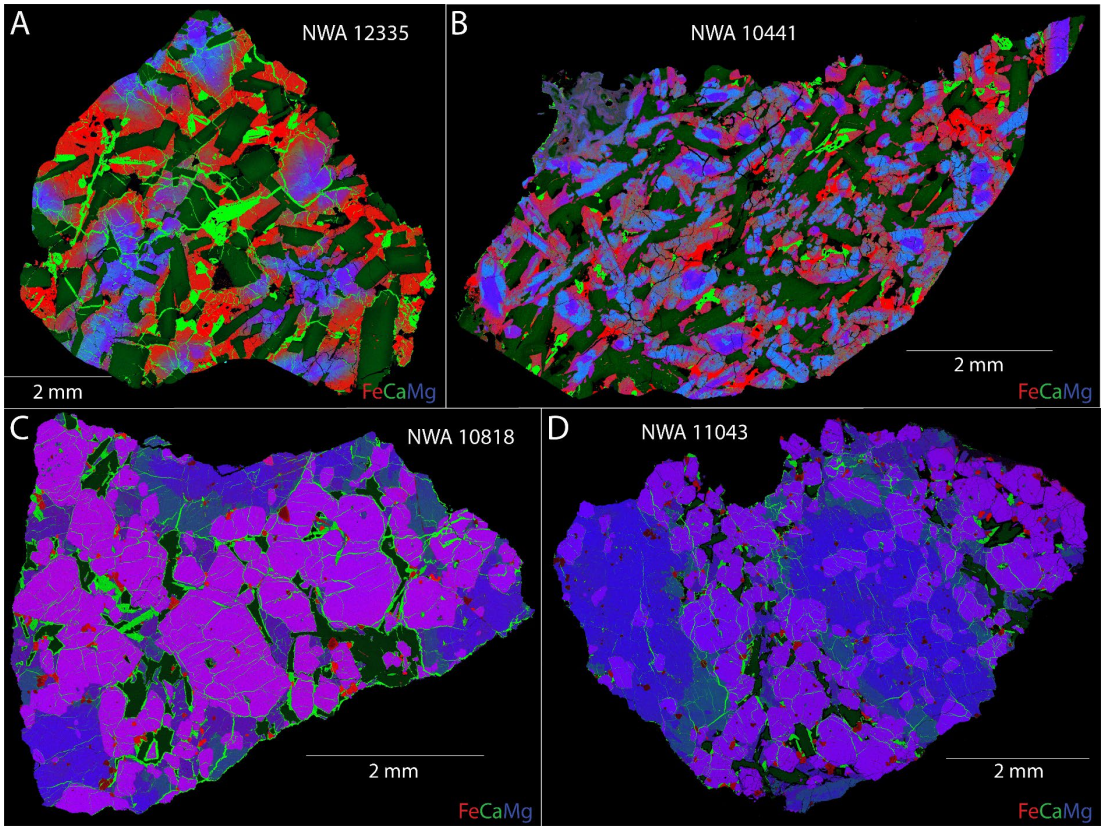

Figure 3.1 *Combined elemental distribution maps, Fe = red, Ca = green and Mg = blue. A-B: The diabasic shergottites composed primarily of maskelynite (dark green) and pyroxene (red, blue, purple). C-D: The poikilitic shergottites composed primarily of olivine (purple)), maskelynite (dark green) and pyroxene (blue, blue-green). Carbonate veining (bright green) is pervasive through NWA 12335, NWA 10818 and NWA 11043 but only slightly visible in NWA 10441.*

1.2.3 Electron Probe Micro-Analyser (EPMA)

Quantitative abundances of major and minor elements were acquired *in situ* using wavelength-dispersive analysis (WDS) spectrometry with the JEOL 8530F Plus electron probe micro-analyser (EPMA) at the Centre of Microscopy, Characterisation

and Analysis in the University of Western Australia. The majority of analyses were carried out using Probe Software's Probe for EPMA software in Quant Mapping mode with a 15 kV accelerating voltage, 40 nA beam current, 40 ms pixel dwell time and with a 2x2 µm pixel size. Maskelynite and phosphate were acquired using spot analysis. A 10 µm defocused beam, at 15 kV and 15 nA was used for maskelynite. The phosphate analysis was conducted using a focused beam (there were too many fractures for a defocused beam) with otherwise similar conditions to maskelynite. A combination of silicate and metal standards were analysed with standard ZAF corrections applied. Detection limits were typically <0.01% for Al, Ca, K, Mg, Si and <0.03% for Na, Mn, Cr, Fe and Ti. Post-processing was performed using Probe Software's CalcImage software, where the specific quant data was extracted from user-defined polygon areas of interest. Each map acquired data across an area of ~2.4 mm^2, which generated in excess of 2.5 million individual compositional analyses per map. Given this large number of analyses, totals between 98.5% and 101%, along with individual elemental abundances, were used to ensure extraction of only the target mineral during data reduction. Similar techniques were applied during line profile extraction. Data manipulation and presentation was achieved using WaveMetrics Igor Pro version 8 plotting software.

1.2.4 Electron Back-Scattered Diffraction (EBSD)

EBSD requires a very finely polished surface, therefore the epoxy mounts were polished for 4 hours on a Buehler Vibromet II Polisher with 500 nm colloidal silica in a NaOH solution. They were then coated with a thin (~5 nm) layer of carbon. EBSD analyses were carried out on all epoxy mounts using a Tescan Mira3 VP-FESEM (variable pressure field emission scanning electron microscope) with an Oxford Instruments Symmetry CMOS detector at the John de Laeter Centre, Curtin University. The analyses were acquired using a 1.5-2 µm step size, at 20 mm working distance with a 20 kV accelerating voltage and 16 beam intensity. The samples were tilted to 70˚ from the normal position for optimum kikuchi pattern collection. The data were gathered using the Oxford Instruments AZtec EDS/EBSD software and post-processed using the Oxford Instruments HKL Channel 5.12 software with the Tango and Mambo modules. Noise reduction was carried out following established procedures from previous studies (e.g., Forman et al., 2019). This enabled greater grain

definition (indexing) and more accurate grain determination (identification of grain boundaries) without generating significant artefacts within the data.

1.2.5 Laser Ablation Inductively Coupled Mass Spectrometry (LA-ICP-MS)

In situ trace element analysis was conducted by LA-ICP-MS using a RESOlution-SE excimer laser and an Agilent 8900 QQQ ICP-MS at the GeoHistory Facility, John de Laeter Centre, Curtin University. Following two cleaning pulses, analyses were conducted with a beam diameter of 50 μm with a 40s ablation followed by 45s of total background count rate acquisition. The laser was operated at a frequency rate of 4 Hz and a fluence of 2.7 J cm^{-2}. The primary reference material was NIST610 using ^{29}Si as the internal reference isotope for silica-bearing phases (plagioclase, olivine, pyroxene and glass), and ^{43}Ca as the internal reference for phosphate (merrillite and chlorapatite). International reference glasses NIST612, GSD-1G, GSE-1G, BCR-2G, and BHVO-2G were interspersed with the samples and treated as secondary standards to assess accuracy. Analytical accuracy for NIST612 was better than 5% for most elements (Ti <10%). The Iolite software package (e.g., Paton et al., 2011) was used for data reduction. REE profiles were normalised to the optimised CI carbonaceous chondrite composition listed by Lodders and Fegley (1998).

1.3 Results

1.3.1 Mineralogy, Petrology and Geochemistry

We report results by textural grouping, first describing NWA 10818 and NWA 11043, and then NWA 10441 and NWA 12335 (Fig. 3.1). Comparing these two groups offers an effective approach to illustrate the range of geology that exists on Mars. The overall geological composition and texture of the new meteorites will be presented first, followed by mineral specific results. Broadly, NWA 10441 and NWA 12335 contain 40-50% pyroxene, 35-38% maskelynite, with the remainder composed of accessory minerals such as phosphates (3-6%), oxides (3-5.5%) and sulfides (0.6-1.2%). On the other hand, NWA 10818 and NWA 11043 contain 30-40% pyroxene, 5-15% maskelynite and 44-48% olivine. A small abundance of accessory minerals are also present, such as chromites (1-2%) and phosphates (0.6-2.1%). The modal mineralogy (Table 3.1) was used to infer the bulk composition of the meteorites (Table 3.2), based

on the major element compositions of the mineralogy (e.g., Walton et al., 2012). Northwest Africa 10818 and 11043 have high Mg#'s of 65.9 and 67.4, respectively. The Mg# of NWA 11043 is slightly elevated compared to NWA 11043 (Mg# 62.2) measured by Rahib et al. (2019). Much lower Mg#'s were calculated for NWA 10441 and NWA 12335, at 38.5 and 23.9, respectively. Northwest Africa 10441 has a similar Mg# to its potential pair, NWA 8657 (Mg# 40.3) (Howarth et al., 2018). We can also compare these new meteorites with the Total Alkali Silica (TAS) diagram, which can illustrate the similarities and differences between different sets of volcanic rocks (Fig. 3.2). Northwest Africa 10818 and NWA 11043 plot in the picrobasalt field, whereas NWA 10818 plots on the edge of the known shergottite field. In contrast, NWA 10441 and 12335 both plot in the basalt field, though NWA 12335 is slightly more alkaline.

Table 3.1 *Average modal mineralogy of NWA 10441, NWA 12335, NWA 10818 and NWA 11043 (standard deviations are <1%). Average modal abundances of diabasic and poikilitic shergottites also shown for comparison.*

Thin section	NWA	NWA	NWA	NWA	Average	Average
Point Counting	10441	12335	10818	11043	Diabasic[a]	Poikilitic[b]
Pigeonite	26.7	10.5	19.6	32.3	52.7*	26.8
Augite	24.3	11.5	9.7	10.2	-	12.5
Pyroxferroite	n.d.	19.6	n.d.	n.d.	-	-
Olivine	n.d.	n.d.	44.3	47.5	-	45.2
Maskelynite	38	34.6	15.1	5.7	35.5	11.7
K-Si-Glass	tr.	2.4	n.d.	n.d.	-	-
Phosphates	3.3	6.1	2.1	0.6	2.2	1.1
Oxides	2.8	5.5	0.5	0.2	2	0.2
Sulphides	1.2	0.6	0.5	0.4	0.5	0.3
Chromites	0.3	0.4	1.9	0.8	-	1.2
Silica	3.4	1.5	n.d.	n.d.	1.8	-
Carbonate veins	tr.	7.2	6.3	2.3	-	-
Total	100	100	100	100	94.7	99
XCT	NWA 10441	NWA 12335	NWA 10818	NWA 11043		
Pyroxene	66.9	56.7	27.7	34.5		
Olivine	n.d.	n.d.	64.9	51.7		
Maskelynite	29	41	6.6	13.5		
Holes (vesicles)	2.2	n.d.	n.d.	n.d.		
Other	1.9	2.3	0.8	0.3		
Total	100	100	100	100		

* Total pyroxene, n.d. = not detected, tr. = trace (<0.1%)

[a] Barrat et al. (2002), Harvey et al. (1996), Hui et al. (2011), Irving et al. (2010), Mikouchi and Barrat (2009), Roszjar et al. (2012), Rubin et al. (2000), Stöffler et al. (1986), Warren et al. (2004), Xirouchakis et al. (2002).

[b] Combs et al. (2019), Howarth et al. (2014), Howarth et al. (2015), Lin et al. (2005), Rahib et al. (2019), Treiman et al. (1994), Usui et al. (2010).

1.3.2 Poikilitic Shergottites

Northwest Africa 10818 displays classic (in the terrestrial sense) poikilitic and non-poikilitic textures (Fig. 3.1). The poikilitic regions are composed of large pyroxene (2-4 mm) oikocrysts surrounding smaller olivine (<1 mm) and chromite (<200 μm) chadacrysts. The non-poikilitic regions are composed of subhedral to euhedral olivine (<1.5 mm), pyroxene (<1 mm) and anhedral maskelynite (<1 mm). Accessory phases in the non-poikilitic regions include merrillite, chromite, ilmenite and pyrrhotite (see Table 1 for specific modal mineralogy). Pervasive terrestrial weathering, as evidenced by carbonate veins, are also present throughout the sample. These veins have preferentially formed in the calcic-rich phases of augite and phosphates.

Table 3.2 *Inferred bulk major element compositions of NWA 10818, NWA 10441, NWA 11043 and NWA 12335. Previous results for NWA 11043 and the potential pair of NWA 10441, NWA 8657, are included for comparison.*

Bulk	Poikilitic			Basaltic		
oxide wt%	NWA 10818	NWA 11043	NWA 11043[a]	NWA 10441	NWA 12335	NWA 8657[b]
SiO_2	40.77	42.76	41.9	49.18	48.53	50.8
TiO_2	0.29	0.23	0.52	0.56	0.81	0.92
Al_2O_3	2.43	4.26	3.05	8.2	11.13	7.55
Cr_2O_3	0.43	0.28	0.97	0.13	0.04	-
MgO	25.99	24.07	22.8	6.65	3.51	7.5
FeO	23.95	20.72	24.6	18.97	19.93	19.7
MnO	0.6	0.49	0.5	0.54	0.5	0.51
CaO	3.82	5.05	4.75	11.64	10.45	10.9
Na_2O	0.51	0.9	0.22	1.77	2.47	1.46
K_2O	0.07	0.07	0.1	0.17	0.14	0.17
P_2O_5	0.47	0.48	0.58	0.98	0.91	0.53
Total	99.33	99.3	100	98.79	98.42	100
Mg#	65.91	67.44	62.2	38.46	23.9	40.3

[a] Rahib et al., 2019

[b] Howarth et al., 2018

Northwest Africa 11043 was recently described by Rahib et al. (2019). As our results are consistent with their mineralogical and petrological findings (Table 3.3), we will only report on new *in situ* trace element compositions of the mineralogy in NWA 11043. But we include elemental maps and our modal mineralogies for completeness.

1.3.2.1 Pyroxene

The poikilitic pyroxene oikocrysts in both meteorites are chemically zoned, from pigeonite ($En_{67\pm3.4}Wo_{8\pm2.6}Fs_{25\pm2.1}$) cores to augite ($En_{47\pm3}Wo_{36\pm3.8}Fs_{17\pm2.8}$) rims (Table 3.4, Fig. 3.3). The pigeonite core accounts for up to ~70% of the total grain area. The augite (rim) forms a distinct boundary with the pigeonite. Non-poikilitic pyroxenes grains are also composed of pigeonite and augite with similar sharp transitions.

In contrast, zoning in the non-poikilitic pyroxene is more interstitial with no obvious core and rim relationship. Non-poikilitic pigeonite and augite have compositions of $En_{60\pm3.1}Wo_{11\pm3.6}Fs_{29\pm2.6}$ and $En_{45\pm3}Wo_{37\pm4.7}Fs_{18\pm2.9}$, respectively, and, although within error, there is a slight trend to more Fs-rich compositions. The Mg# of poikilitic pigeonite (72.6±2.4) and augite (73.7±3.5) is higher than that of the non-poikilitic pigeonite (68±2.5) and augite (71.7±3.1), with the larger difference shown in pigeonite.

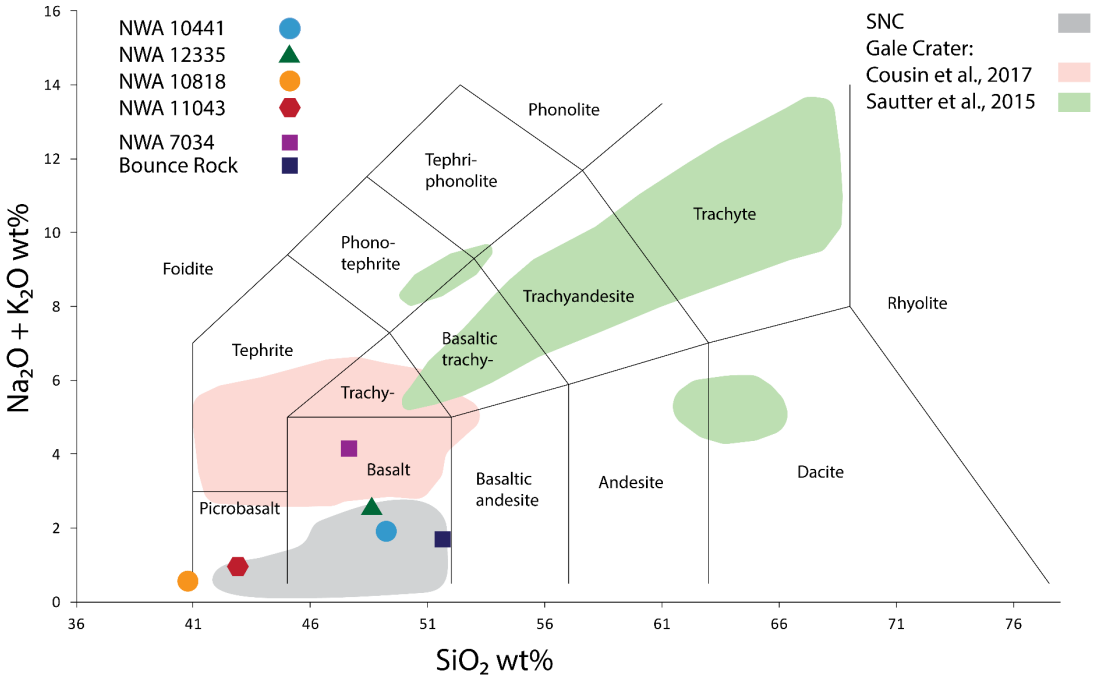

Figure 3.2 *Total alkali silica classification of the new shergottites compared to other Martian igneous rocks for reference: SNC (grey), NWA 7034 (a volcanic-derived polymict regolith breccia, Agee et al., 2013) Gale Crater float rocks (red, Cousin et al., 2017 and green, Sautter et al., 2015), Bounce Rock (Meridiani igneous sample, Zipfel et al., 2011). Figure modified from McSween, 2015.*

Table 3.3 Representative major element compositions of the mineralogy in NWA 11043.

NWA 11043	Poikilitic		Non-Poikilitic		Poikilitic	Non-Poikilitic	Non-Poikilitic		Poikilitic	Non-Poikilitic	
oxide wt%	Pigeonite core	Augite rim	Pigeonite	Augite	Olivine		Maskelynite	Merrillite	Chromite	Chromite	Ilmenite
SiO_2	52.09	50.36	50.73	49.56	35.93	35.4	53.65	1.39	2.5	2.64	1.32
TiO_2	0.19	0.33	0.54	0.73	0.09	0.09	0.08	-	3.14	9.64	51.29
Al_2O_3	0.88	1.65	1.38	1.97	0.2	0.3	27.22	0.7	8.16	6.88	0.55
Cr_2O_3	0.45	0.73	0.39	0.59	0.1	0.08	0.01	-	47.88	34.39	1.12
MgO	24.36	17.61	21.24	16.24	33.76	31.46	0.14	3.46	5.55	4.65	4.66
FeO	15.95	10.39	17.63	10.85	28.54	31.16	0.62	1.03	31.01	39.99	38.89
MnO	0.55	0.41	0.61	0.42	0.57	0.63	0.01	0.18	0.54	0.59	0.73
CaO	4.8	17.64	6.63	18.52	0.27	0.31	11.14	44.88	0.47	0.36	0.67
Na_2O	0.24	0.55	0.37	0.78	0.11	0.12	5.09	1.73	0.21	0.31	0.23
K_2O	0.05	0.04	0.05	0.05	0.03	0.04	0.24	-	0.06	0.09	0.06
P_2O_5	-	-	-	-	-	-	-	43.76	-	-	-
Total	99.56	99.71	99.55	99.71	99.61	99.59	98.2	97.13	99.51	99.56	99.52
Fo					66.13	62.61					
An							53.95				
Ab							44.65				
Or							1.4				
Wo	9.39	35.1	13.27	37.35							
En	66.27	48.76	59.17	45.57							
Fs	24.34	16.14	27.55	17.08							

***Table 3.4** Representative major element compositions of the mineralogy in NWA 10818.*

NWA 10818	Poikilitic		Non-Poikilitic		Poikilitic	Non-Poikilitic	Non-Poikilitic		Poikilitic	Non-Poikilitic	
oxide wt%	Pigeonite core	Augite rim	Pigeonite	Augite	Olivine		Maskelynite	Merrillite	Chromite	Chromite	Ilmenite
SiO_2	52.73	51.77	51.48	49.92	35.91	36.29	53.94	2.08	3.54	1.22	1.69
TiO_2	0.19	0.42	0.5	0.74	0.1	0.09	0.08	-	1.76	13.64	52.89
Al_2O_3	0.85	1.86	1.2	1.94	0.31	0.39	27.3	1.3	7.39	6	0.45
Cr_2O_3	0.44	0.77	0.33	0.61	0.19	0.09	0.01	-	50.55	28.12	1.12
MgO	24.23	16.28	21.1	15.99	33.88	29.15	0.14	3.51	5.73	4.22	4.38
FeO	16.22	10.41	18.29	11.32	28.18	32.32	0.58	1.12	28.92	44.99	37.79
MnO	0.59	0.52	0.68	0.47	0.54	0.8	0.01	0.36	0.55	0.66	0.82
CaO	3.99	17.18	5.64	17.88	0.27	0.32	11.08	44.35	0.74	0.38	0.33
Na_2O	0.2	0.38	0.27	0.66	0.11	0.11	4.99	1.66	0.22	0.19	0.16
K_2O	0.08	0.07	0.06	0.05	0.05	0.07	0.25	-	0.08	0.05	0.07
P_2O_5	-	-	-	-	-	-	-	42.65	-	-	-
Total	99.52	99.66	99.54	99.6	99.53	99.62	98.38	97.04	99.49	99.46	99.71
Fo					67.47	60.76					
An							54.33				
Ab							44.22				
Or							1.44				
Wo	7.97	35.81	11.46	36.5							
En	66.88	47.24	59.55	45.44							
Fs	25.15	16.95	28.99	18.07							

All analysed pyroxenes in NWA 10818 display a depletion in LREE (Table 3.5, Fig. 3.4). Augites, in both textures, are slightly more enriched, having $[La/Lu]_{CI}$ of 0.033 and 0.039, respectively, than pigeonite ($[La/Lu]_{CI}$ of 0.004 and 0.008, respectively). Non-poikilitic pigeonite is more enriched in LREE than the poikilitic pigeonite whereas REE patterns for both forms of augite overlap within uncertainty (Fig. 4). Overall, pigeonite displays a positive Eu anomaly ($[Eu/Eu^* = Eu_{CI}/(Sm_{CI}*Gd_{CI})^{1/2}]$ = >1) compared to augite, which displays a negative Eu anomaly (Eu/Eu* = <1). Average REE concentrations in NWA 10818 pyroxenes are ~0.1 times CI in the LREE and ~4 times CI in the HREE (Fig. 3.5).

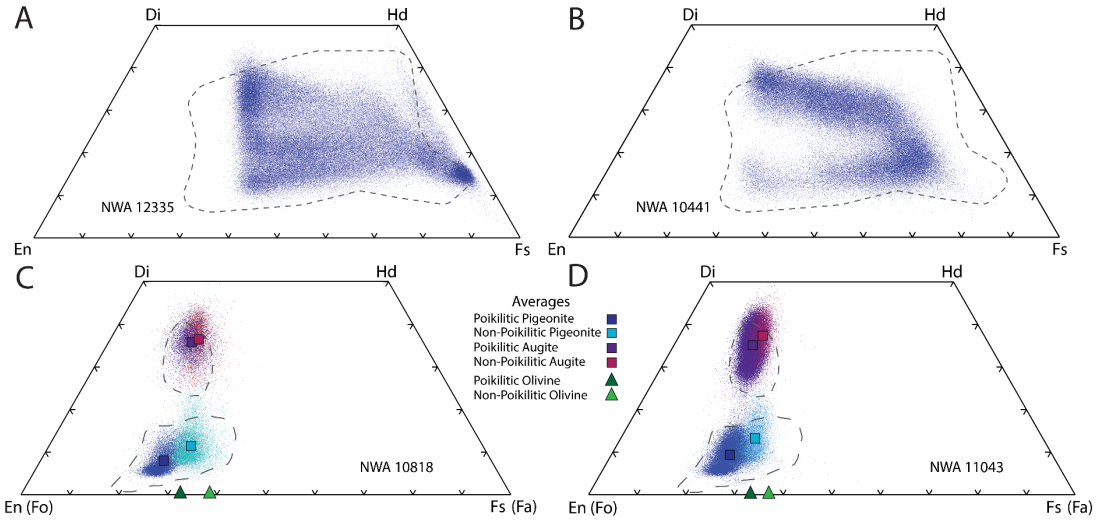

Figure 3.3 *Pyroxene quadrangle (Di = diopside, Hd = hedenbergite, En = enstatite, Fs = ferrosilite). Pyroxene and olivine compositions of (A) NWA 12335, (B) NWA 10441, (C) NWA 10818 and (D) NWA 11043. Note the difference in compositional range between the diabasic (A and B) and poikilitic shergottite (C and D) pyroxenes. The grey dashed lines represent pyroxene compositions from other basaltic (Filiberto et al., 2018 and references therein) and poikilitic (Rahib et al., 2019 and references therein) shergottites.*

Pyroxenes in NWA 11043 behave similarly to those in NWA 10818 and average REE concentrations are ~0.4 times CI for LREE and 4 times CI for HREE (Table 3.6). The poikilitic pigeonite is least abundant in REE with poikilitic augite and non-poikilitic pigeonite having similar, but slightly higher abundances. Non-poikilitic augite has the highest abundance of REE (Fig. 3.4). With the exception of the poikilitic augite, pyroxene shows an enrichment in La and a depletion in Ce. This LREE pattern was similarly reported in the bulk composition of NWA 11043 (Rahib et al., 2019). The pyroxene grains also display similar Eu anomalies as those in NWA 10818, with

pigeonite having a slightly positive (Eu/Eu* = >1) and augite having a slightly negative (Eu/Eu* = <1) Eu anomaly.

1.3.2.2 Olivine

The poikilitic olivine chadacrysts are anhedral with small inclusions of chromite (<50 µm) and basaltic melt (<100 µm), while non-poikilitic olivine is euhedral to subhedral with similar size chromite and basaltic melt inclusions. The average forsterite content of poikilitic olivine ($Fo_{66\pm2.3}$) is higher than that of non-poikilitic olivine ($Fo_{60\pm2.4}$) (Fig. 3.3). No chemical zoning is observed in any olivine grain.

Although olivine is not a major host of REE, abundances determined in this study are generally above the limit of detection (LOD). In NWA 10818, olivine in both textures show a depleted LREE pattern with a $[La/Lu]_{CI}$ of 0.142 and 0.006, respectively, and poikilitic grains more enriched than non-poikilitic (Fig. 3.6). In NWA 11043, non-poikilitic olivine shows a relative enrichment of LREE compared to poikilitic olivine, $[La/Lu]_{CI}$ = 1.3 and 1.087, respectively. Both poikilitic and non-poikilitic olivine in NWA 10818 and NWA 11043 have a positive Eu anomaly. Due to the low abundance of REE (<1_{CI}) in NWA 10818, some LREE were below the detection limit for non-poikilitic olivine.

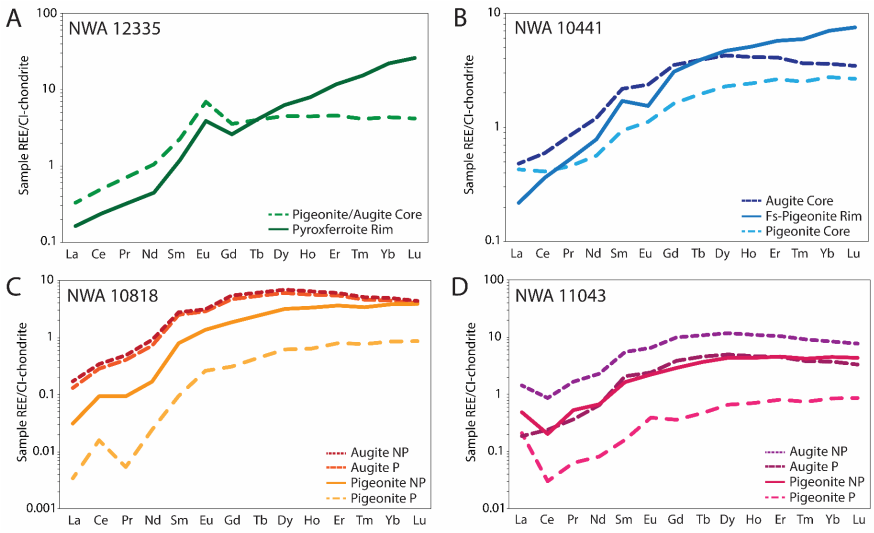

Figure 3.4 *Chondrite-normalised pyroxene REE profiles from augite and pigeonite zones. A/B: diabasic shergottites average pigeonite, augite and pyroxferroite rim REE profiles. Note due to the complexity of pigeonite and augite zoning in NWA 12335, the average of both has been shown. C/D: the poikilitic shergottites showing pigeonite and augite REE distribution in poikilitic (P) and non-poikilitic (NP) areas.*

1.3.2.3 Maskelynite

In both meteorites, plagioclase has been fully converted to maskelynite glass due to impact-related shock processes. The maskelynite morphology (based on the original plagioclase shape) is generally anhedral, only partially retaining the plagioclase lath crystal structure, with grains up to 1 mm long. Maskelynite occurs exclusively in non-poikilitic regions, though some maskelynite occurs on the rims of the pyroxene oikocrysts. The average composition of maskelynite in NWA 10818 is $An_{50.7\pm7.3}Ab_{47.3\pm7.1}Or_{1.9\pm0.9}$, which just fits into the labradorite field, though with some variation into andesine.

Table 3.5 *Representative REE abundance (ppm) in minerals from NWA 10818.*

NWA 10818	Poikilitic	Non-Poikilitic	Poikilitic		Non-Poikilitic		Non-Poikilitic	
	Olivine		Pigeonite core	Augite rim	Pigeonite	Augite	Phosphate	Maskelynite
n	5	17	11	7	8	5	9	10
La	0.017	0.001	0.001	0.031	0.007	0.04	32.349	0.115
Ce	0.064	0.011	0.01	0.177	0.058	0.214	81.349	0.245
Pr	0.003	b.d.	0.001	0.038	0.009	0.046	12.697	0.029
Nd	0.022	b.d.	0.012	0.334	0.077	0.422	76.601	0.16
Sm	0.004	b.d.	0.016	0.376	0.119	0.417	45.404	0.067
Eu	0.032	0.01	0.015	0.163	0.078	0.179	16.462	0.683
Gd	0.016	0.002	0.062	0.93	0.369	1.085	85.011	0.101
Tb	0.003	0.001	0.016	0.199	0.09	0.228	15.384	0.021
Dy	0.03	0.02	0.155	1.508	0.789	1.713	103.348	0.166
Ho	0.008	0.006	0.036	0.316	0.187	0.363	20.664	0.029
Er	0.035	0.03	0.128	0.878	0.578	0.971	55.684	0.114
Tm	0.006	0.006	0.019	0.115	0.085	0.128	7.187	0.012
Yb	0.065	0.072	0.137	0.715	0.612	0.791	43.358	0.07
Lu	0.012	0.015	0.022	0.101	0.097	0.109	5.908	0.01

b.d. below detection limit

The REE pattern of maskelynite shows that it is relatively enriched in the LREE with a $[La/Lu]_{CI}$ of 1.22 for NWA 10818 (Fig. 3.6). In NWA 11043, HREE (Tm-Lu) abundances were below LOD. Maskelynite in both NWA 10818 and NWA 11043 exhibits a positive Eu anomaly (Eu/Eu* = 25.19 and 123.93, respectively), with the anomaly being an order of magnitude larger in NWA 11043.

1.3.2.4 Chromite

Chromite grains in NWA 10818 are generally an- to subhedral and <200 µm in size. They are observed in both poikilitic and non-poikilitic areas. In thin section, the

poikilitic chromite grains can be inclusions in olivine chadacrysts, or form chadacrysts themselves, enclosed by the larger pyroxene oikocrysts. In non-poikilitic areas, chromite exists as inclusions in pyroxene and olivine, but also as distinct grains interstitial to pyroxene and olivine. Poikilitic chromite has higher average Mg# (atomic Mg/Mg+Fe) and Cr# (atomic Cr/Cr+Al) than non-poikilitic chromite (Mg# 22.8±3.5 and Cr# 82.9±3.3 vs Mg# 12.8±2.8 and Cr# 75.7±5.2, respectively). Some of the non-poikilitic chromite is zoned, with high Cr_2O_3 and low TiO_2 cores and the opposite trend in rims. Compositionally, the poikilitic chromite is Spinel $(Spn)_{15.3\pm2.7}$ Chromite $(Chr)_{74.6\pm5.7}$ Ulvöspinel $(Ulv)_{4.9\pm3.2}$ Magnetite $(Mag)_{5.2\pm3.3}$, while non-zoned non-poikilitic chromite is $Spn_{12.3\pm2.4}$ $Chr_{39.8\pm10.2}$ $Ulv_{36.6\pm10.2}$ $Mag_{11.4\pm5}$ and zoned non-poikilitic chromite is $Spn_{11.2\pm2}Chr_{58.6\pm14.6}Ulv_{24.1\pm13.1}Mag_{6\pm4.9}$. The poikilitic grains have a much tighter compositional range than the non-poikilitic chromites, trending to ulvöspinel compositions.

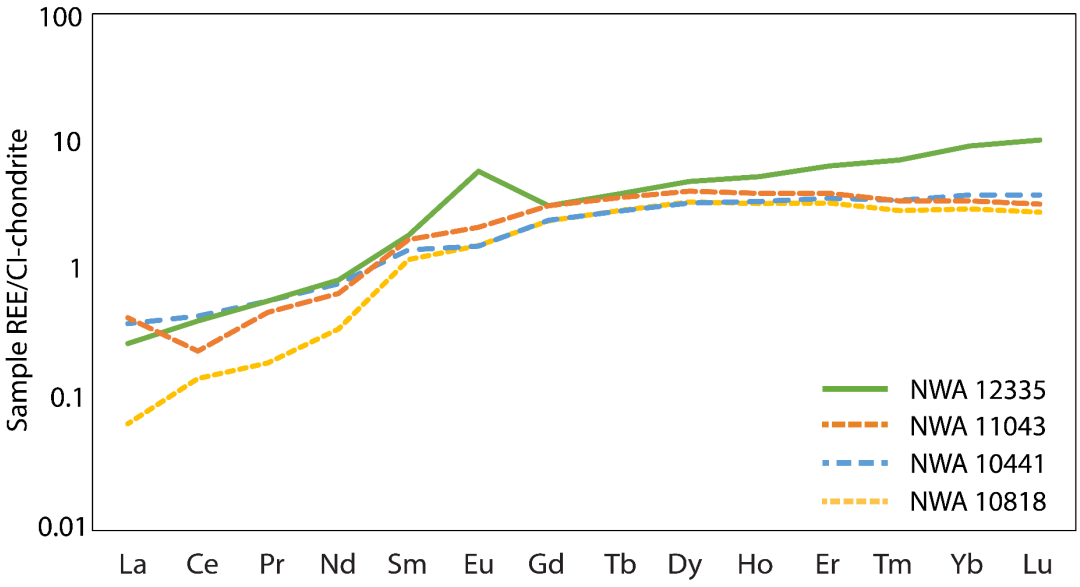

Figure 3.5 *Chondrite-normalized average REE profiles of all the pyroxenes in NWA 10441, NWA 10818, NWA 11043 and NWA 12335. This is the weighted average used in the bulk REE calculations.*

1.3.2.5 Phosphates

In NWA 10818, phosphate grains (merrillite) are anhedral and can be up to 500 µm long. The majority of the grains are observed in non-poikilitic areas, with <5% occurring as inclusions in olivine or pyroxene. Some phosphate grains are found in poikilitic areas, generally towards the rims of the pyroxene oikocrysts or as inclusions in olivine chadacrysts.

In both NWA 10818 and 11043, phosphates are the major host phase of REE, with abundances that are >100 times those in CI. The REE profiles of merrillite in NWA 10818 and NWA 11043 are very similar (Fig. 3.6). Both show a relative depletion in LREE with a $[La/Lu]_{CI}$ of 0.582 and 0.66, respectively. However, similar to REE profiles in other minerals from NWA 11043, there is an enrichment in La and slight depletion in Ce. There is also a slight negative Eu anomaly [Eu/Eu*] of ~0.8 in NWA 10818 and NWA 11043. In NWA 11043, there is variation among the phosphate analyses with two analyses displaying a relative LREE enrichment compared to the others, as discussed below.

Table 3.6 *Representative REE abundance (ppm) in minerals from NWA 11043.*

NWA 11043	Poikilitic	Non-Poikilitic	Poikilitic		Non-Poikilitic		Non-Poikilitic	
	Olivine		Pigeonite core	Augite rim	Pigeonite	Augite	Phosphate	Maskelynite
n	13	18	15	11	11	6	11	11
La	0.115	0.202	0.05	0.044	0.114	0.336	46.456	0.061
Ce	0.081	0.086	0.019	0.148	0.125	0.538	97.443	0.112
Pr	0.009	0.059	0.006	0.034	0.05	0.158	16.656	0.012
Nd	0.042	0.231	0.037	0.298	0.307	1.061	97.634	0.06
Sm	0.006	0.057	0.024	0.311	0.245	0.834	55.73	0.011
Eu	0.03	0.04	0.022	0.137	0.127	0.372	20.525	0.565
Gd	0.019	0.074	0.072	0.781	0.583	2.003	102.411	0.019
Tb	0.002	0.011	0.018	0.17	0.136	0.398	18.516	0.002
Dy	0.024	0.071	0.165	1.246	1.086	2.935	123.389	0.013
Ho	0.007	0.016	0.04	0.261	0.244	0.618	24.546	0.001
Er	0.03	0.055	0.129	0.721	0.733	1.685	66.258	0.001
Tm	0.006	0.009	0.019	0.095	0.105	0.228	8.49	b.d.
Yb	0.051	0.083	0.135	0.597	0.726	1.341	50.901	b.d.
Lu	0.011	0.017	0.022	0.083	0.11	0.194	6.884	b.d.

b.d. below detection limit

1.3.2.6 Accessory Phases

In NWA 10818 and NWA 11043, ilmenite is observed as subhedral to anhedral grains, <200 μm in diameter, and occurs in non-poikilitic areas. It contains 52.9±7.4 wt% TiO_2 and 37.8±4 wt% FeO. Pyrrhotite is also found in non-poikilitic regions, as anhedral grains that are <100 μm. Both ilmenite and pyrrhotite occur as inclusions in pyroxene and olivine, and also as distinct grains embedded in the matrix.

1.3.3 Diabasic Shergottites

Northwest Africa 10441 and 12335 are both coarse-grained with maskelynite and pyroxene (the major mineralogy) grain sizes between 1-5 mm and 2-3 mm, respectively. They are both of basaltic composition, composed primarily of pyroxene and similar to the poikilitic shergottites discussed above, all the plagioclase has been converted to maskelynite (see Table 3.1 for modal abundances). Accessory minerals include phosphate (chlorapatite and merrillite), ilmenite, magnetite and chromite. Both samples contain silica, with NWA 12335 containing K-Si-glass, similar to that found in Los Angeles (Warren et al., 2004). As with NWA 10818 and NWA 11043, NWA 12335 also contains carbonate veins most likely emplaced during terrestrial weathering.

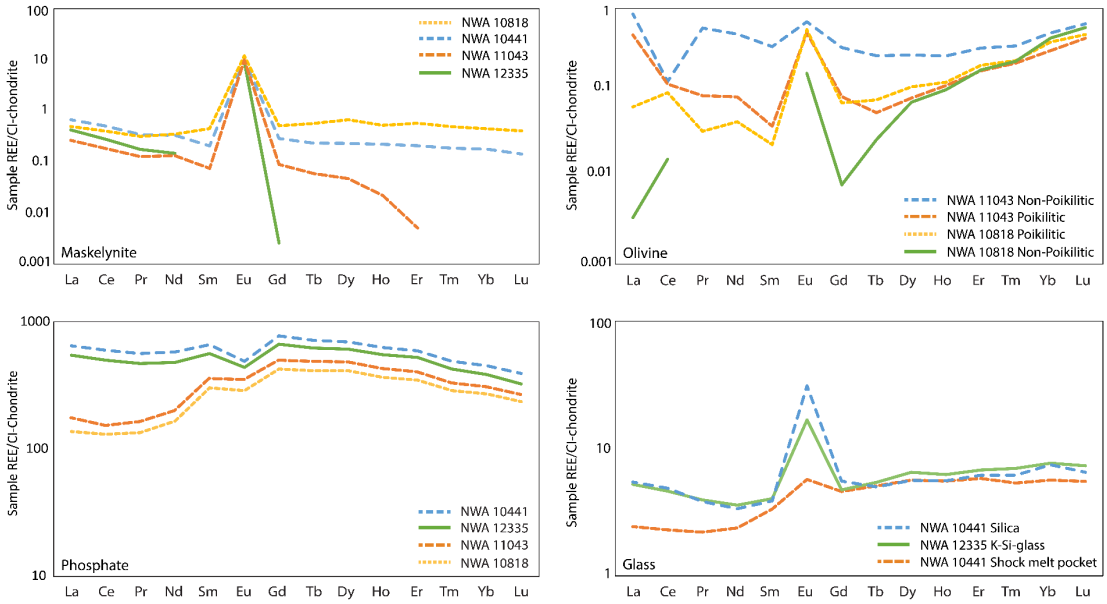

Figure 3.6 *Chondrite-normalized REE profiles of maskelynite, olivine, phosphate and glass in NWA 10818, NWA 10441, NWA 11043 and NWA 12335. Olivine is only present in NWA 10818 and NWA 11043. Both poikilitic and non-poikilitic olivine are displayed. Missing REE data is due to those analyses being below the detection limit of the instrument.*

1.3.3.1 Pyroxene

The pyroxene grains are texturally different in both samples. In NWA 10441, the pyroxene can be extremely elongate with length:width (L:W) ratios of up to 50:4, while in NWA 12335 the pyroxene is more anhedral. There is significant zoning (in Ca, Mg and Fe) in pyroxene from both samples. In NWA 12335 the zoning is complex (Fig. 3.7), but there is a general trend from high-Mg cores (pigeonite and/or augite) to high-Fe rims (pyroxferroite in the case of NWA 12335). Augite (high-Ca pyroxene)

and pigeonite (low-Ca pyroxene) occur interstitially throughout the grains (Fig. 3.8). In NWA 10441, the zoning is much more distinct having both augite and pigeonite cores, with a similar trend from high-Mg in the cores to high-Fe in the rims. Extensive exsolution lamellae (<1 to 8 μm) are observed between the augite and pigeonite in both meteorites (Fig. 3.9). In NWA 10441, pigeonite has an average composition of $En_{27.8\pm10.1}Wo_{17.2\pm3.6}Fs_{55.1\pm9}$ while augite has an average composition of $En_{31.2\pm7.9}Wo_{32.1\pm3.8}Fs_{36.7\pm10.2}$ (Table 3.7). In NWA 12335, high-Mg cores (both pigeonite and augite) have an average composition of $En_{31.9\pm10.8}Wo_{26.1\pm7.5}Fs_{42\pm13}$ while the high-Fe rims (pyroxferroite) have an average composition of $En_{5\pm1.5}Wo_{17.9\pm5.7}Fs_{77.2\pm6.1}$ (Table 3.8).

Table 3.7 *Representative major element compositions of the mineralogy in NWA 10441.*

NWA 10441								
oxide wt%	Pigeonite	Augite	Maskelynite	Merrillite	Apatite	Silica	Titanomagnetite	Ilmenite
SiO_2	47.66	48.7	55.58	0.03	0.5	93.92	0.14	0.19
TiO_2	0.46	0.43	0.04	-	-	0.26	27.18	45.7
Al_2O_3	0.65	1	25.68	0	0.01	2.52	1.68	0.59
Cr_2O_3	0.13	0.28	0	-	-	0.06	0.38	0.27
MgO	9.29	10.74	0.08	1.47	0.05	0.05	0.33	0.47
FeO	32.41	22.22	0.86	4.21	1.05	0.38	69	51.44
MnO	0.9	0.68	0.01	0.17	0.12	0.11	0.56	0.59
CaO	7.89	15.29	10.02	46.47	53.33	0.46	0.09	0.12
Na_2O	0.2	0.3	5.31	1.34	0.17	1.38	0.17	0.16
K_2O	0.04	0.04	0.48	-	-	0.53	0.03	0.03
P_2O_5	-	-	-	46.88	41.86	-	-	-
F	-	-	-	0.07	2.73	-	-	-
Cl	-	-	-	-	1.66	-	-	-
Total	99.64	99.67	98.06	100.64	101.47	99.67	99.56	99.55
An			49.34					
Ab			47.73					
Or			2.93					
Wo	17.16	32.08						
En	27.76	31.24						
Fs	55.08	36.68						

The pyroxenes in both NWA 10441 and 12335 show LREE-depleted REE profiles (Tables 3.9-10, Fig. 3.4). However, the patterns are different between the (pigeonite and augite) cores and the (Fs-pigeonite and pyroxferroite) rims. In NWA 10441, both the pigeonite and augite cores are enriched in LREE ($[La/Lu]_{CI}$ = 0.162 and 0.14, respectively) relative to the Fs-pigeonite rims ($[La/Lu]_{CI}$ = 0.029), which show an increased abundance in the HREE. A similar pattern is seen in NWA 12335, with $[La/Lu]_{Ci}$ of 0.079 for pigeonite/augite cores compared to 0.006 for pyroxferroite rims.

Pyroxene in NWA 12335 has a positive Eu anomaly (Eu/Eu* = >2) compared to a slightly negative Eu anomaly in NWA 10441 pyroxene (Eu/Eu* = <1).

1.3.3.2 Maskelynite

Maskelynite in both samples retains the original plagioclase subhedral to euhedral (up to 2-3 mm) morphology. More obvious in NWA 12335 but also noted in NWA 10441, maskelynite typically has the lath crystal shape of plagioclase. There is core to rim zoning of high-Ca (An) cores with high-K (Or) and -Na (Ab) rims. In both samples, but more extensively in NWA 12335, on the edges of the maskelynite grains, K-Si-glass has formed at the expense of the maskelynite. This has given the maskelynite an almost 'cubic' appearance (Fig. 3.7). Maskelynite regions have a compositional range of $An_{44.2\pm7.8}Ab_{52.8\pm6.8}Or_{3.1\pm4}$ (in NWA 12335) and $An_{46.9\pm6.1}$ $Ab_{49.5\pm5.4}Or_{3.5\pm2.5}$ (in NWA 10441). The large standard deviations, especially in the orthoclase component, reflect potassium zoning within the grains, which is more prominent in NWA 12335. In NWA 10441, maskelynite is enriched in the LREE with $[La/Lu]_{CI} = 4.72$ and also has a positive Eu anomaly (Eu/Eu* = 41.09) (Fig. 3.6). In NWA 12335, Sm and the HREE from Tm-Lu are below LOD, although a positive Eu anomaly might be inferred (Fig. 3.6).

Table 3.8 *Representative major element compositions of the mineralogy in NWA 12335. Note, pyroxene core is an average of both augite and pigeonite.*

NWA 12335									
oxide wt%	Pyroxene Core	Pyroxferroite Rim	Maskelynite	Merrillite	Apatite	Chlorapatite	Silica	Titanomagnetite	Ilmenite
SiO_2	48.27	45.07	55.17	0.22	0.91	0.98	92.72	0.3	0.47
TiO_2	0.39	0.36	0.03	-	-	-	0.19	25.9	49.28
Al_2O_3	1.06	0.65	25.92	0.07	0.06	0.06	2.8	1.76	0.38
Cr_2O_3	0.09	0.05	0	-	-	-	0.06	0.07	0.06
MgO	10.66	1.55	0.08	0.61	0.03	0.03	0.04	0.17	0.24
FeO	26.66	42.84	0.61	5.69	1.22	1.12	0.45	70.48	48.23
MnO	0.76	1.04	0	0.15	0.14	0.08	0.08	0.67	0.69
CaO	11.35	7.76	9.99	45.14	51.61	51.16	0.47	0.12	0.18
Na_2O	0.32	0.21	5.61	1.34	0.21	0.33	2.03	0.18	0.18
K_2O	0.04	0.06	0.27	-	-	-	0.72	0.06	0.07
P_2O_5	-	-	-	44.09	40.15	39.77	-	-	-
F	-	-	-	0.12	1.27	0.34	-	-	-
Cl	-	-	-	0.01	2.51	3.82	-	-	-
Total	99.6	99.59	97.68	97.43	98.12	97.68	99.58	99.71	99.76
An			48.83						
Ab			49.62						
Or			1.55						
Wo	26.07	17.87							
En	31.91	4.97							
Fs	42.02	77.16							

1.3.3.3 Phosphates

The phosphates are up to 1 mm long in NWA 10441 and up to 3 mm long in NWA 12335, with an abundance of 3% and 6%, respectively. The phosphate grains are anhedral, elongate crystals, generally found in the interstices between pyroxene and maskelynite. Northwest Africa 10441 and NWA 12335 contain both merrillite and chlorapatite with the latter representing ~1/3 of the phosphate in both meteorites. As is normal for phosphate minerals, REE abundances in both meteorites are extremely high (>300$_{CI}$). The REE profile of phosphates in NWA 10441 and NWA 12335 is relatively flat, both showing an enrichment in the LREE ([La/Lu]$_{CI}$ = 1.66 and 1.68, respectively). They also have a slightly negative Eu anomaly (Eu/Eu* = ~0.7).

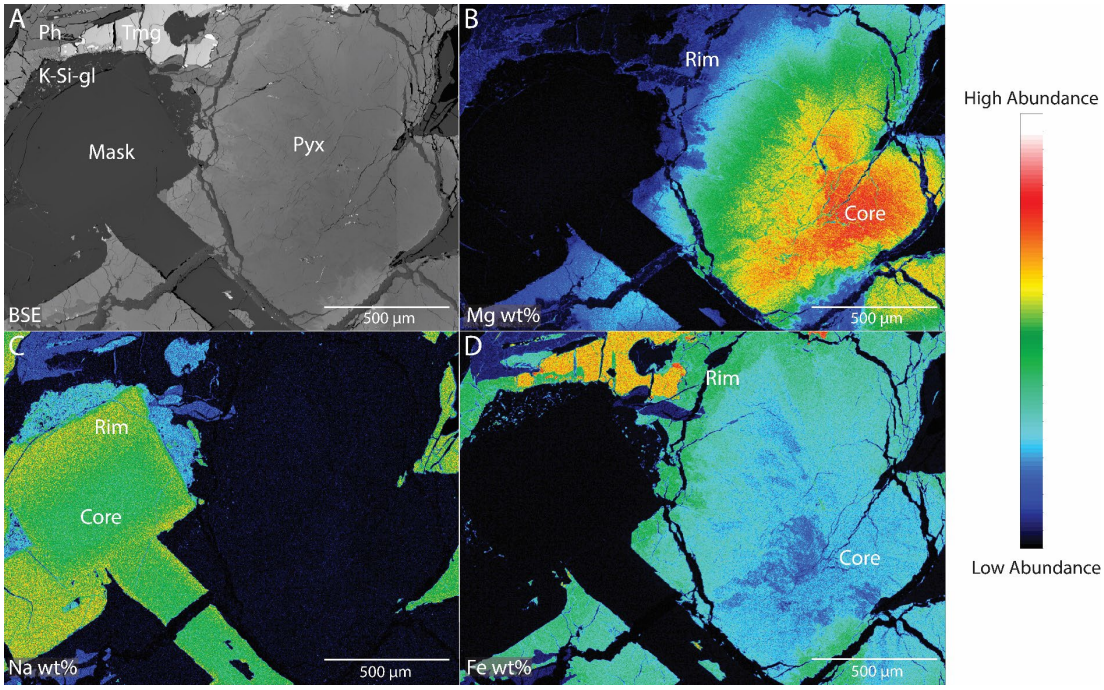

Figure 3.7 *EPMA quantitative element wt% maps of NWA 12335. A: BSE map displaying the mineralogy. B: Mg wt% map showing the trend in pyroxene from a Mg-rich core to a Mg-poor rim. C: Na wt% map showing compositional zoning in maskelynite. D: Fe wt% map showing the complex zoning within the pyroxene grain. There are no distinct boundaries between augite and pigeonite. Pyroxferroite forms as the rim of the pyroxene. Ph = phosphate, Tmg = titanomagnetite, K-S-gl = K-Si-glass, Mask = maskelynite and Pyx = pyroxene.*

1.3.3.4 Accessory Phases

Accessory phases in the diabasic shergottites contribute ~8% of the mineralogy for both NWA 10441 and NWA 12335. Titanomagnetite grains can be up to 0.5 mm long. The majority of the grains (>90%) also contain crosscutting exsolved ilmenite, which can be up to 20 µm thick. Chromite is near-absent, with very small <10 µm grains present. Pyrrhotite is present with grain sizes <300 µm. Silica is observed in both NWA 10441 and NWA 12335, with grain sizes ~300 µm. Throughout NWA 12335,

K-Si-glass is also present (Fig. 3.10). The glass has an irregular boundary with the surrounding pyroxene grains, and has entrained small elongate (<200 μm) pyroxene grains. This has been similarly observed in Los Angeles and is thought to be shock-derived (e.g., Xirouchakis et al., 2002). The REE profile of silica in NWA 10441 is relatively flat with $[La/Lu]_{CI}$ of 0.8. K-Si-glass in NWA 12335 has a similar flat REE profile with $[La/Lu]_{CI}$ 0.7 (Fig. 3.6). Significant positive Eu anomalies are present in NWA 10441 silica ($[Eu/Eu^*]_{CI}$ of 6.6) and NWA 12335 Ki-Si-glass ($[Eu/Eu^*]_{CI}$ of 3.9). The large shock melt pocket (see below) in NWA 10441 also has a slight positive Eu anomaly with $[Eu/Eu^*]_{CI}$ of 1.5. Unlike the glass, the shock melt pocket has an overall LREE-depleted profile with $[La/Lu]_{CI}$ of 0.4.

1.3.4 Bulk REE

Understanding and defining the source of the shergottites is important to understanding the magmatic history of Mars and, therefore, the evolution of the planet. The REE signatures of the shergottites likely reflect their corresponding source reservoirs.

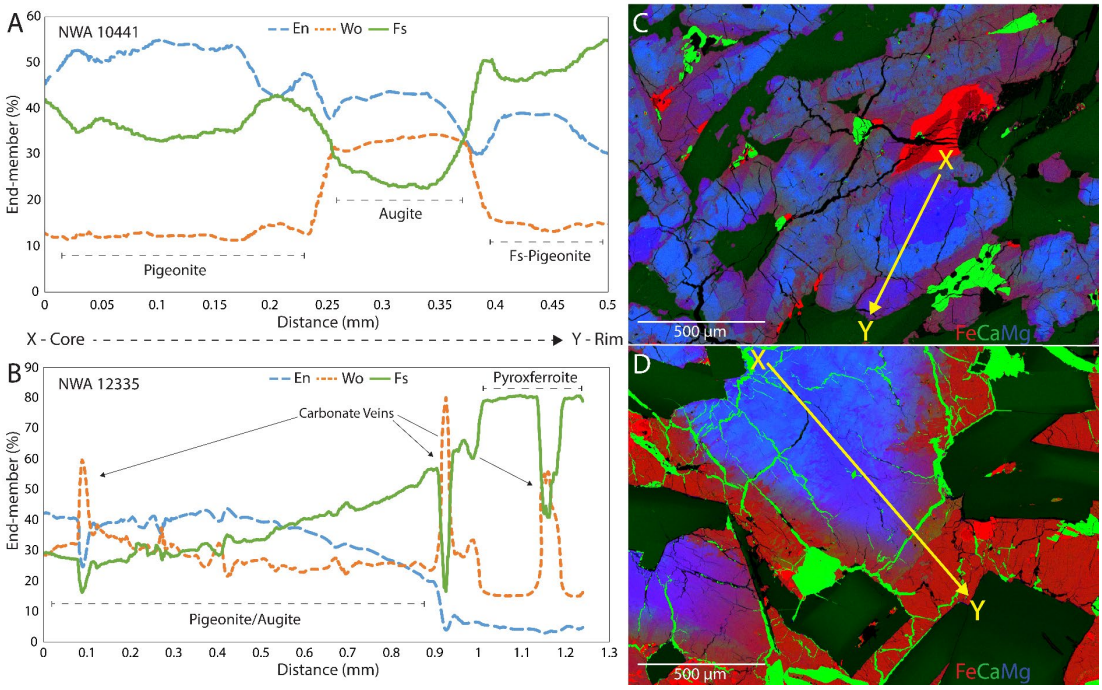

Figure 3.8 *Line profiles through combined EPMA quant maps in NWA 10441 and NWA 12335. A-B: Line profiles showing relative proportions of En, Wo and Fs in the pyroxenes. C-D: Combined quant maps with X-Y line profiles indicated. Fe = red, Ca = green and Mg = blue.*

Due to the fact that we had only thick and thin sections of the samples to work with, we determined chondrite-normalized REE profiles by combining *in situ* REE data of

compatible minerals with modal mineralogy (e.g., Howarth et al., 2018). Two separate sets of bulk REE profiles were calculated based on the two methods used to determine modal mineralogy; thin-section image point counting and 3D image analysis using HRXCT results. Modal mineralogy derived from HRXCT was restricted to pyroxene, olivine and maskelynite. Phosphate grains could not be distinguished from pyroxene or olivine grains at the spatial resolution used for analyses. In addition, the density of phosphate is very similar to the silicates (3.13g/cc vs ~3.3g/cc) making it difficult to determine. This is significant as phosphates are the main carrier of the REE budget in these rocks. Therefore, to account for this discrepancy as well as provide a calibration for our calculations, we compared our average modal mineralogy to published datasets of basaltic and poikilitic shergottites. If the olivine and pyroxene modal abundances were similar for our thin section/HRXCT abundances compared to published values, we assumed we could justifiably determine the best estimate of phosphate modal abundances of basaltic (2.2 ±1.4%) and poikilitic (1.1 ±0.5%) shergottites to use for our samples (Stöffler et al., 1986; McCoy et al., 1992; Treiman et al., 1994; Harvey et al., 1998; Rubin et al., 2000; Mikouchi, 2001; Barrat et al., 2002b; Jambon et al., 2002; Xirouchakis et al., 2002; Lin et al., 2005; Ikeda et al., 2006; Wittke et al., 2006; Usui et al., 2010; Hui et al., 2011; Llorca et al., 2013; Herd et al., 2017; Udry et al., 2017; Rahib et al., 2019). This abundance was then subtracted from the HRXCT modal abundance of pyroxene and olivine based on their relative proportions.

Table 3.9 *Representative REE abundance (ppm) in minerals from NWA 10441.*

NWA 10441	Pigeonite core	Augie core	Fs-Pigeonite rim	Phosphate	Maskelynite	Shock Melt	Silica
n	17	11	8	14	12	6	6
La	0.101	0.114	0.051	153.373	0.156	0.571	1.279
Ce	0.255	0.368	0.225	370.81	0.31	1.421	3.024
Pr	0.043	0.08	0.05	53.158	0.032	0.207	0.36
Nd	0.26	0.556	0.361	267.09	0.152	1.095	1.543
Sm	0.141	0.325	0.255	99.144	0.037	0.503	0.581
Eu	0.063	0.135	0.088	27.94	0.563	0.325	1.768
Gd	0.322	0.703	0.613	155.95	0.062	0.92	1.108
Tb	0.072	0.143	0.144	26.633	0.009	0.188	0.184
Dy	0.572	1.066	1.168	174.83	0.057	1.414	1.404
Ho	0.135	0.231	0.284	35.196	0.012	0.31	0.313
Er	0.421	0.655	0.912	95.383	0.033	0.932	0.987
Tm	0.063	0.091	0.148	12.214	0.005	0.134	0.154
Yb	0.441	0.577	1.119	72.577	0.028	0.905	1.19
Lu	0.066	0.086	0.188	9.827	0.004	0.138	0.162

Comparing the results of HRXCT modal mineralogy against the numbers derived from thin section is important for accuracy evaluation. Aside from phosphates, we can ignore the accessory phases as their REE contribution is negligible. Taking heterogeneity within samples into account, the relative HRXCT abundances of maskelynite, olivine and pyroxene in all the meteorites are similar to thin section abundances (within ~15%). The most significant discrepancy is olivine abundance in NWA 10818, with XCT of ~65 vol% and thin section of ~44 vol%. Due to the poikilitic texture and size of the sample, the thin section slice is less likely to be a true representation of the modal amount. Furthermore, due to the low overall abundance of REE in the major mineralogy compared to phosphate, these differences will not have a significant impact on the bulk REE profiles.

Using thin section-derived modal mineralogy bulk REE, NWA 10441 and NWA 12335 display an enriched REE profile, with a flat REE pattern. Northwest Africa 10818 and NWA 11043 display an intermediate profile, with a depletion in LREE relative to HREE. Northwest Africa 12335 has the highest overall bulk abundance of REE, while NWA 11043 is least abundant, with a slight enrichment in La.

Using the HRXCT derived modal mineralogy, we observe similar overall REE profiles for the meteorites, though their relative abundance of REE has changed (Table 3.11, Fig. 3.11). Although the overall REE abundances of NWA 10441 and 12335 have decreased compared to thin-section derived bulk REE, their profiles are more in line with other enriched shergottites (e.g., He et al., 2015; Cao et al., 2018). The REE profile of NWA 10441 is closer to the ‘measured’ bulk REE profile of suggested pair NWA 8657 (Howarth et al., 2018). Similarly, HRXCT-derived bulk REE of NWA 10818 and NWA 11043 are more typical of intermediate shergottites (e.g., Riches et al., 2011; Filiberto et al., 2012).

Table 3.10 *Representative REE abundance (ppm) in minerals from NWA 12335.*

NWA 12335	Pyroxene core	Pyroxferroite rim	Phosphate	Maskelynite	K-Si-Glass
n	31	13	20	14	9
La	0.077	0.038	128.686	0.098	1.227
Ce	0.308	0.146	310.17	0.17	2.867
Pr	0.067	0.03	44.356	0.016	0.371
Nd	0.481	0.205	221.921	0.067	1.653
Sm	0.338	0.178	84.368	b.d.	0.604
Eu	0.395	0.222	25.072	0.522	0.957
Gd	0.715	0.516	133.764	0.001	0.944
Tb	0.149	0.152	23.139	b.d.	0.201
Dy	1.134	1.554	153.352	b.d.	1.628
Ho	0.248	0.448	30.867	b.d.	0.35
Er	0.734	1.873	83.886	b.d.	1.086
Tm	0.103	0.382	10.64	b.d.	0.175
Yb	0.697	3.51	62.06	b.d.	1.223
Lu	0.105	0.646	8.146	b.d.	0.183

b.d. below detection limit

1.4 Discussion

This study reinforces and expands on the preliminary classifications of these meteorites (MetBull 104-107). Below we discuss the crystallization history, shock evidence and weathering, and how these processes have impacted the geochemical composition of these rocks.

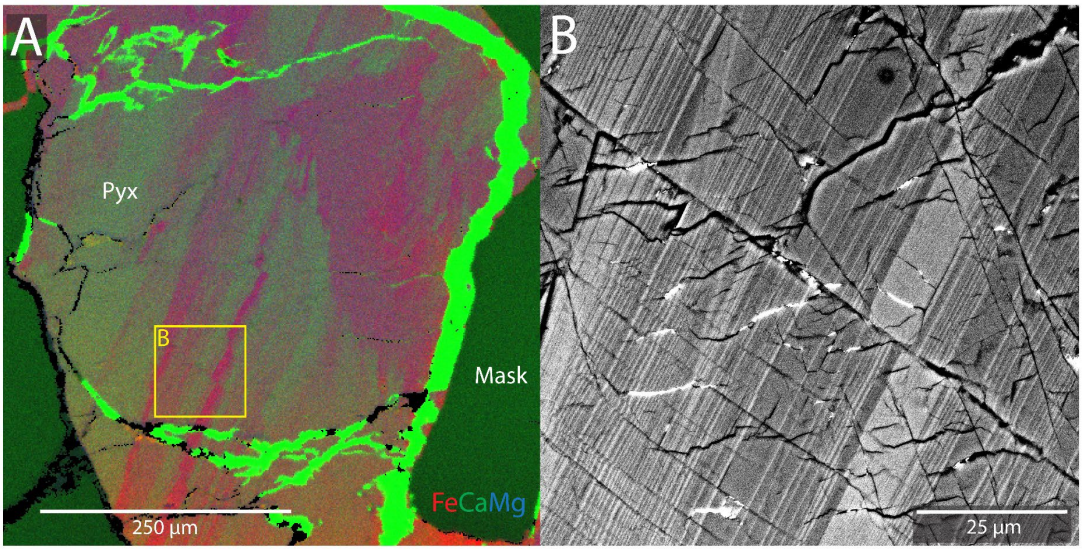

Figure 3.9 *Exsolution lamellae between augite and pigeonite in NWA 12335. A: Combined element map of a pyroxene grain showing lamellae and offsetting. Red = Fe, green = Ca, blue = Mg. Pyx = pyroxene, Mask = maskelynite, bright green = carbonate veining. B: BSE map (yellow box in A denotes location) of lamellae offset by a series of micro-faults.*

1.4.1 Crystallization History: Extrusive vs Intrusive

The poikilitic shergottites, NWA 10818 and NWA 11043, appear to have experienced similar crystallisation histories to other poikilitic shergottites (e.g., Riches et al., 2011;

Walton et al., 2012; Howarth et al., 2014; Rahib et al., 2019). The high-Fo olivines together with high-Mg#, high-Cr# chromites are consistent with these minerals being first to crystallize in the melt, followed by low-Ca pyroxene (pigeonite). The pyroxene enclosed the smaller olivine and chromite chadacrysts, forming large pyroxene oikocrysts. The presence of elemental zoning, suggests high-Ca pyroxene (augite) crystallized as overgrowths on the pigeonite oikocrysts. As interstitial melt accumulated, the cumulate oikocrysts and olivine (not enclosed by pyroxene) were entrained in the rising magma. From these interstitial melts, non-poikilitic pyroxene (pigeonite and augite) and plagioclase co-crystallized. The accessory phases also started to crystallize from the evolved melt. The poikilitic regions are more primitive than the non-poikilitic regions with higher Mg#, Fo% and Cr# (pyroxene, olivine and chromite, respectively). Based on the Ti/Al ratios of the poikilitic pyroxene (pigeonite and augite) in NWA 10818 and NWA 11043, the poikilitic regions crystallised first, most likely in the lower Martian crust close to the upper mantle boundary (Filiberto et al., 2010; Rahib et al., 2019). The non-poikilitic regions crystallised as melt accumulated during magma ascent up through the crust with final emplacement in a hypabyssal system near the surface (e.g., Lin et al., 2013).

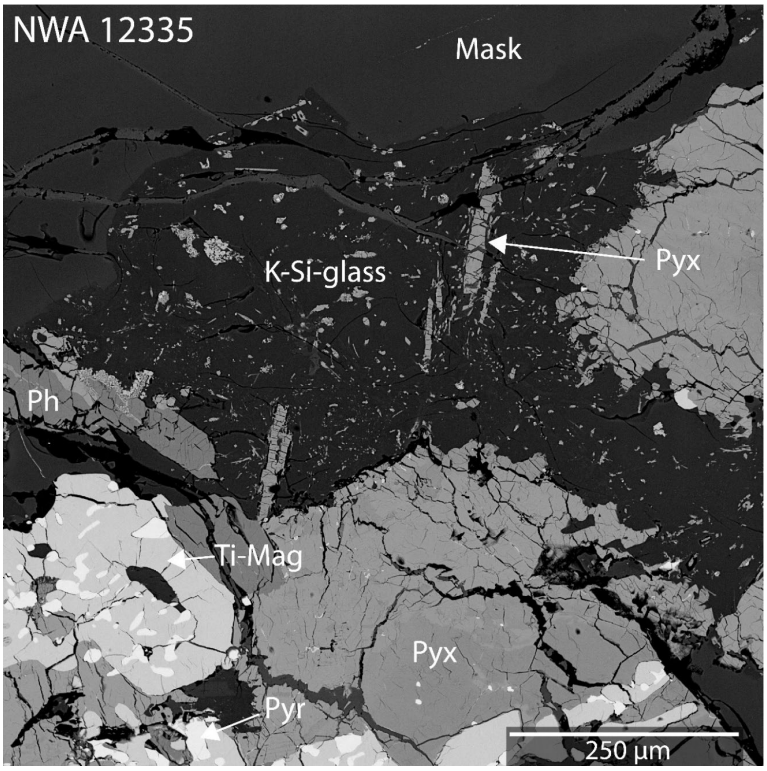

Figure 3.10 *BSE map of NWA 12335 showing the textural relationships of K-Si-glass. Note the pyroxene grains inside the glass and the irregular boundary between the glass and pyroxene grains. Ph = phosphate, Mask = maskelynite, Pyx = pyroxene, Ti-Mag = titanomagnetite, Pyr = pyrrhotite.*

The diabasic shergottites (NWA 10441 and NWA 12335) each had a slightly different petrogenesis, but their overall genesis was similar to other basaltic shergottites (e.g., McCoy et al., 1992; McSween et al., 1996; Barret et al., 2002b). Like most other basaltic shergottites, olivine is not present. Combined with the low Mg#'s of the pyroxene, NWA 10441 and NWA 12335 must have crystallized from an evolved melt. This melt has been suggested to have already experienced olivine fractionation (e.g., Treiman and Filiberto, 2015). In NWA 10441, the distinct Mg-rich augite and pigeonite cores were first to crystallize in the melt. These grains were then entrained in magma as it ascended towards the surface. As the magma rose, more Fe-rich augite and pigeonite started to form mantles around the cores. Fs-pigeonite (in the forbidden zone) rims were last to crystallize, forming as a result of extrusion of the magma onto the Martian surface. Fe-rich pyroxene compositions are metastable at pressures <10 kbar (Lindsley and Burnham, 1970), so crystallization without subsequent breakdown requires extremely rapid cooling, conducive to an eruption or extrusion of lava onto the surface.

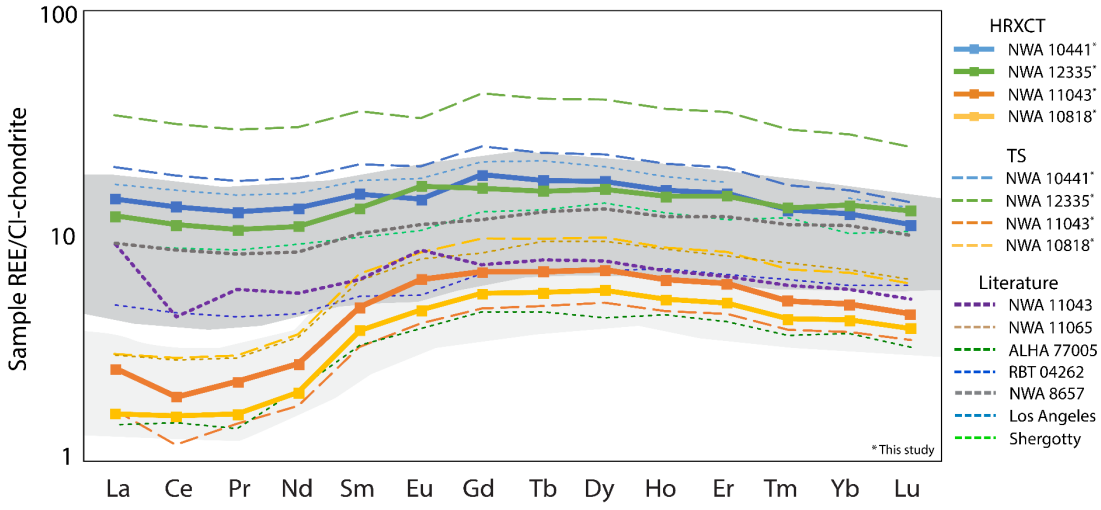

Figure 3.11 *Chondrite-normalized HRXCT and TS (thin-section) calculated bulk REE profiles of the new shergottites compared against other enriched and intermediate, basaltic and poikilitic, shergottites (Lodders, 1998; Jambon et al., 2002; Anand et al., 2008; Howarth et al., 2018; Rahib et al., 2019). Dark grey = enriched, light grey = intermediate.*

This also applies to pigeonite. NWA 10441 shows evidence of a two-stage crystallization history, with Mg-rich pyroxene cores crystallizing at depth, developing into more Fe-rich pyroxene as the magma ascended. A multi-stage crystallization doesn't necessarily require an open magmatic system. Similar shergottites to NWA

10441, such as NWA 5298 and Zagami, have been suggested to have been formed in a closed system, with sudden magma movement (i.e. eruption) initiating the final stage of crystallization (McCoy et al., 1992; Hui et al., 2011). This could also be the case for NWA 10441, however further petrological investigation is required to fully constrain the magmatic evolution.

Northwest Africa 12335 has a slightly different crystallisation history. The zoning in the pyroxene is much more complex and is similar to that of Los Angeles and Queen Alexander Range (QUE) 94201 (e.g., McSween et al., 1996; Mikouchi et al., 1998; Kring et al., 2003; Warren et al., 2004). Mg-rich pyroxene cores initially crystallized. As the magma ascended to the surface, there is a trend toward more Fe-rich pyroxene crystallization. Unlike NWA 10441, there are no sharp boundaries between augite and pigeonite zoning. The interstitial growth of compositionally different pyroxenes implies that Ca-rich and Ca-poor pyroxene co-crystallized, forming compositionally heterogeneous pyroxene grains. Ca-rich pyroxene only stopped crystallizing at the onset of plagioclase crystallization, as Ca would be preferentially incorporated into plagioclase over pyroxene. Prior to plagioclase crystallization, the melt was becoming enriched in Fe. Similar to NWA 10441, Fs-pyroxene compositions crystallized towards the rims of the pyroxene grains. However, in NWA 12335, due to very high-Fe enrichment, pyroxferroite was the final phase to crystallize on the rims of the pyroxene grains. Pyroxferroite (and plagioclase) must have crystallized rapidly as the magma cooled on eruption onto the Martian surface. As previously stated, these high-Fe rich pyroxene phases (and pigeonite itself) are metastable at low temperature and pressure. Pyroxferroite rims have been reported on a number of Martian and lunar meteorites, suggesting that these conditions are prevalent on these bodies (e.g., McSween et al., 1996; Liu et al., 2009). The crystallization sequence of NWA 12335 suggests the melt crystallized in a closed system, similar to QUE 94201 (e.g., Kring et al., 2003). This is interpreted to represent continuous crystallization instead of multi-stage crystallization (e.g., McSween et al., 1996).

Table 3.11 *Calculated bulk (using HRXCT) REE abundances (ppm) in NWA 10441, NWA 10818, NWA 11043 and NWA 12335.*

Bulk	NWA 10441	NWA 10818	NWA 11043	NWA 12335
La	3.434	0.38	0.6	2.869
Ce	8.32	0.975	1.192	6.944
Pr	1.199	0.151	0.21	1
Nd	6.082	0.925	1.237	5.063
Sm	2.305	0.569	0.722	1.99
Eu	0.829	0.265	0.365	0.947
Gd	3.728	1.108	1.381	3.264
Tb	0.652	0.206	0.257	0.585
Dy	4.366	1.432	1.757	4.02
Ho	0.896	0.292	0.356	0.839
Er	2.471	0.806	0.98	2.409
Tm	0.325	0.106	0.128	0.333
Yb	1.995	0.675	0.792	2.187
Lu	0.279	0.097	0.112	0.322

1.4.2 Rare Earth Element Determination

Although thin section-derived bulk REE profiles indicate which REE/incompatible trace element group these new shergottites belong to, the overall REE abundance is off. The modal mineralogy seems to overestimate phosphate abundance (and hence REE abundance) for NWA 10441, NWA 10818 and NWA 12335, and underestimates the amount of phosphate in NWA 11043. This is most likely due to the inherent heterogeneity of phosphate distribution at these scales within these samples. On the other hand, HRXCT-derived bulk REE profiles using inferred phosphate abundances, are more representative of the whole rock. Hence, HRXCT is the preferred technique for bulk compositions, as the distribution of mineralogy can be more comprehensively determined. Thin-section modal abundances, especially for small samples that contain large grains (poikilitic shergottites), can be inaccurate.

Using the HRXCT-modal abundance, the calculated REE profile of NWA 11043 is different to previously reported results for NWA 11043 (Rahib et al., 2019). We don't observe the same relative enrichment in LREE, though we observe very similar HREE abundances and the same La enrichment and Ce depletion pattern. Rahib et al. (2019) reported a $[La/Lu]_{CI}$ of 1.76 for NWA 11043, compared to a $[La/Lu]_{CI}$ of 0.57 using the HRXCT calculated REE profile. To understand the discrepancy between the

different results, we modelled the bulk REE profile with varying abundances of minerals using our *in situ* LA-ICP-MS REE results.

Since phosphate is the primary carrier of REE, small changes in the modal abundance will have a larger effect on the bulk. In addition to the abundance of phosphate, we note that out of the eleven phosphate analyses we have reported, two show a different pattern in the LREE (Fig 3.12). If these two phosphate compositions are the only analyses used in the calculations, we can create a inferred REE profile that is closer to the measured bulk REE (Rahib et al., 2019) using ~20% pyroxene, ~50% olivine, ~30% maskelynite and ~1.3% phosphate (Fig. 3.12). This approach raises the question of how representative the individual phosphate compositions are compared to the whole rock. Either REE were not evenly distributed in the phosphates during crystallisation or phosphate abundances throughout the rock are heterogeneous and therefore even measured bulk REE of chips (generally <1.5 g) may not be representative of the whole rock. Alternatively, secondary processes may be responsible, such as shock processes and geochemical weathering, for the heterogeneous phosphate REE abundances in NWA 11043.

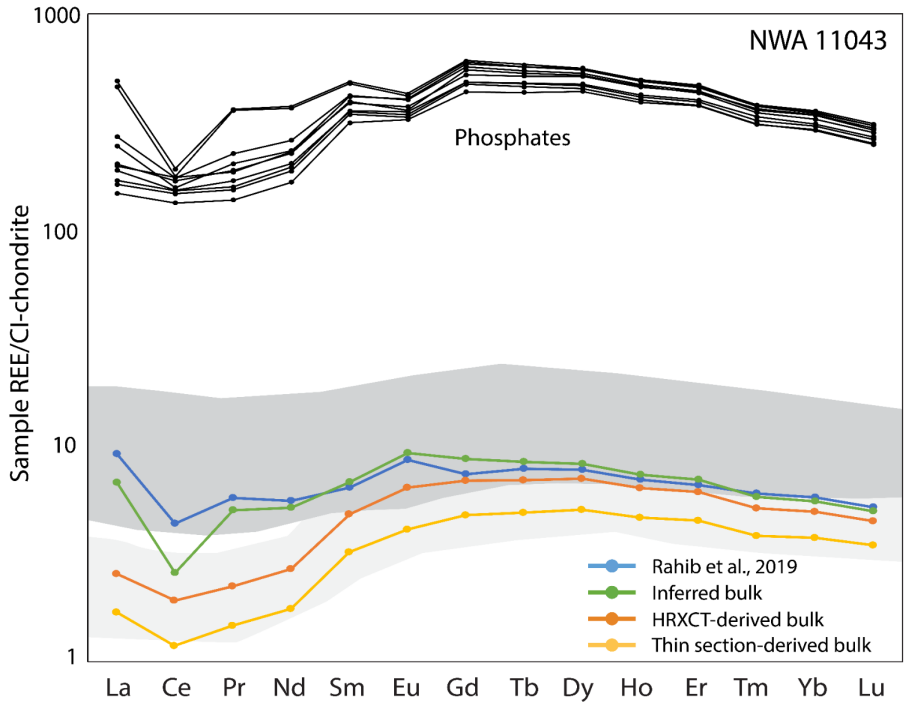

Figure 3.12 *LREE enrichment in NWA 11043. All of the in situ (this study) phosphate analyses are displayed. Note the two analyses with a relative LREE enrichment. The measured bulk spectra (Rahib et al., 2019) is compared against an inferred bulk (only including the two LREE enriched phosphate analyses) and the HRXCT- and thin section-derived bulk REE profiles (not including the two LREE enriched phosphates). Note the shift from enriched (dark grey) to intermediate (light grey) depends on which phosphates are used in the calculated bulk REE profiles.*

1.4.3 Shock Deformation Features

Shock deformation in meteorites is an extremely important process that can cause immediate and wide ranging deformational changes to the mineralogy and texture of the meteorites. Understanding and characterising the effects of shock is important to reconstructing the history of these meteorites, and also to identifying the difference between primary and secondary features. With only a few exceptions (NWA 8159, e.g., Herd et al., 2017), most shergottites have experienced significant levels of shock (e.g., El Goresy et al., 2013). Shergottite shock features likely relate to the meteorite's liberation from Mars (e.g., Fritz et al., 2005). Ejection from the Martian surface requires a powerful impact to induce the 5 km/s escape velocity (Artemieva and Ivanov, 2004). An impact crater diameter of 3 km has been purported as the minimum size of an impact event for successful ejection of rock fragments and their subsequent encounter with Earth (Head et al., 2002). Evidence of these impacts are often recorded as shock deformation in the Martian rock fragments recovered on Earth.

The most obvious shock feature in the studied shergottites is the shock metamorphosis of plagioclase to diaplectic glass, maskelynite. According to Stöffler et al. (2018) diaplectic glass forms in plagioclase from 24/34 GPa (increasing from anorthite to albite) to ~45 GPa. Maskelynite in NWA 10441 (~An_{47}) and NWA 12335 (~An_{44}) has an average andesine composition, while in NWA 10818 (~An_{50}) and NWA 11043 (~An_{57}), maskelynite has an average labradorite composition. If taking account of the maskelynite zoning in NWA 10441 and NWA 12335, a similar minimum shock pressure of ~30 GPa could be ascribed to all.

Pervasive fracturing can be seen throughout the samples, with varying degrees of severity. The basaltic shergottites (NWA 10441 and NWA 12335) have irregular and sub-planar fracturing (concentrated in the pyroxene grains), with increased fracturing on the rims of the pyroxene grains (Fig. 3.13). The poikilitic shergottites (NWA 10818 and NWA 11043) exhibit a higher degree of fracturing. Extensive planar fractures are observed in both pyroxene and olivine. In pyroxene, not all the fracturing is the result of shock. Some of the observed fracturing will be related to cleavage, though as planes of weakness, these 'cleavage fractures' would be more pronounced. According to

Stöffler et al. (2018), planar fractures in olivine and pyroxene are caused by a minimum shock pressure of 5-10 GPa.

In all of the studied shergottites, mechanical twinning in pyroxene is observed. The most pronounced twins are found in NWA 11043, where a pyroxene oikocryst has twinning in the (100) plane (Fig. 3.14). In the other pyroxene oikocryst in NWA 11043, no twinning is observed. These oikocrysts have different crystallographic orientations and consequently the grains may have reacted differently to the shock wave as it propagated through the rock, causing a heterogeneous distribution of mechanical twins. The twins in NWA 11043 are much wider than the twins in the other shergottites (up to 20 µm compared to <5 µm, respectively) and they are also much longer (up to 150 µm compared to <20 µm, respectively). However, mechanical twinning in pyroxene can form at pressures from 5-70 GPa, so they cannot be used as a reliable pressure indicator (Stöffler et al., 2018).

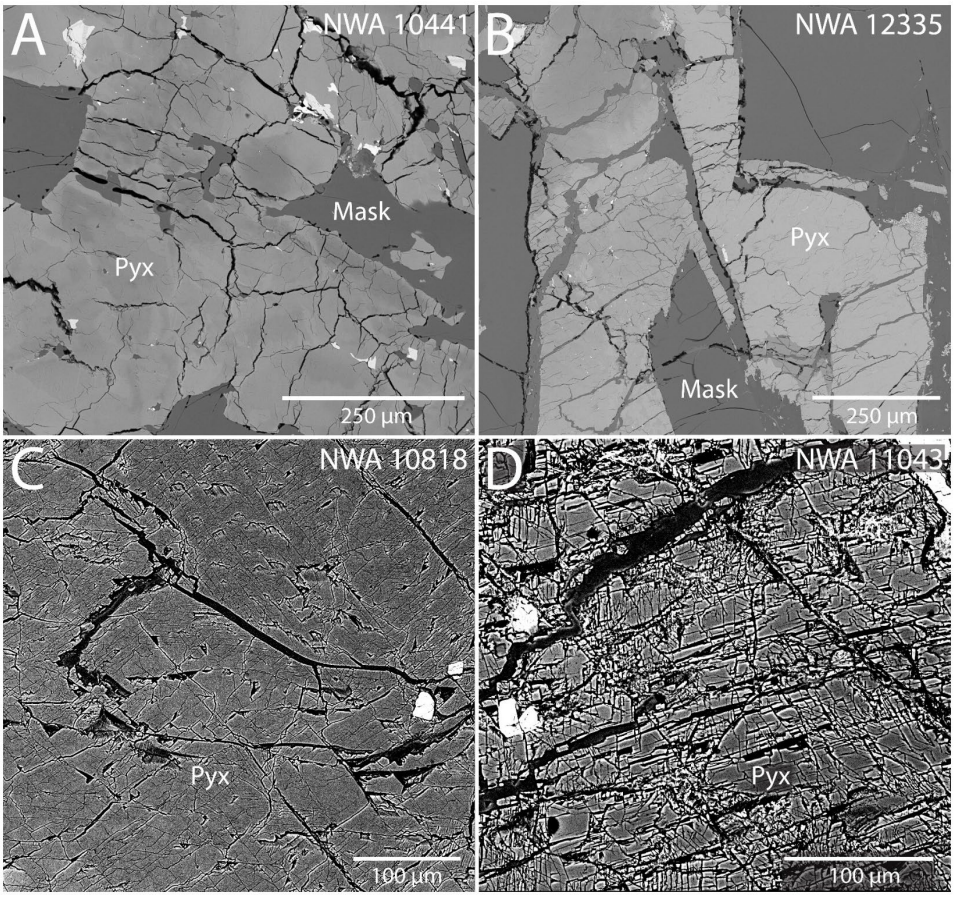

Figure 3.13 *BSE maps showing distribution and intensity of fracturing. A-B: the diabasic shergottites with irregular to sub-planar fracturing in pyroxene and little fracturing in maskelynite. C-D: pyroxene oikocryst grains in the poikilitic shergottites displaying irregular and planar fracturing. Images were stretched to highlight extent of fracturing. NWA 11043 has a higher degree of fracturing compared to NWA 10818. Pyx = pyroxene, Mask = maskelynite.*

Northwest Africa 10441 contains shock melt pockets throughout the sample, the largest being nearly 2 mm wide (Fig. 3.15). On the rim of the large shock melt pocket, there is an obvious zone where the pyroxene grains recrystallized into smaller grains within their original host grains. EBSD orientation analysis highlighted the finer recrystallised grains in the relict larger pyroxene grains. The zone of recrystallization extends to ~200 μm from the shock melt pocket. The boundary between this zone and the shock melt pocket is sharp, with the pyroxene and maskelynite grains inside the shock melt pocket becoming interwoven (Fig. 3.15). Shock melt pockets have also been reported in the suggested pair to NWA 10441, NWA 8657 (Howarth et al., 2018). Higher pressures and temperatures within the shock melt pocket have instigated partial melting of the pyroxene and maskelynite. Heterogeneous elemental distribution within the melt pocket suggests only partial integration of pyroxene and maskelynite grains into a melt glass. Due to the mafic polymineralic nature of NWA 10441, there is a large range in shock impedance of the major mineralogy (plagioclase and pyroxene). During shock wave propagation, this impedance range encourages localised melting where peak shock pressures can be much higher than the equilibrium shock pressure of the whole meteorite (e.g., Sharp and DeCarli, 2006). These pressures, likely exceeding ~70 GPa (Stöffler et al., 2018), caused high shock-induced temperatures which triggered partial melting of the rock. The minimum temperature for melting non-porous basalt is 1600ºC (Stöffler, 1984). The temperatures and pressure, therefore, represent the minimum conditions required to induce shock melting. Similar results were reported for Los Angeles where shock melt pockets were estimated to have formed at 60-80 GPa and at 1600-2000ºC (Walton and Spray, 2003). Due to these high temperatures, neocrystallization of the surrounding pyroxenes through thermal metamorphism occurred, forming a rim round the shock melt pocket. Similar localised shock effects are not observed in all the basaltic shergottites. This may be because (1) shock pressures will vary between the rocks and (2) heterogeneity in the rocks and small sample sizes could be hiding these features. Based on the evidence observed, NWA 10441 experienced higher shock pressures than the other basaltic shergottite NWA 12335.

The shock pressure estimates for these shergottites are similar to other basaltic and poikilitic shergottites (e.g., Hui et al., 2011; Walton et al., 2012). All the meteorites experienced at least ~30 GPa, with an upper limit of ~45 GPa for NWA 10818 and

NWA 11043, and <45 GPa for NWA 10441 and NWA 12335. Northwest Africa 10441 experienced the highest peak shock pressure of ~70 GPa, which caused localised melting. Based on the proposed stages of shock metamorphism by Stöffler et al. (2018), these shergottites are all in the S4 (mafic) shock stage, potentially pushing into S5. More investigation is required to further constrain shock pressures.

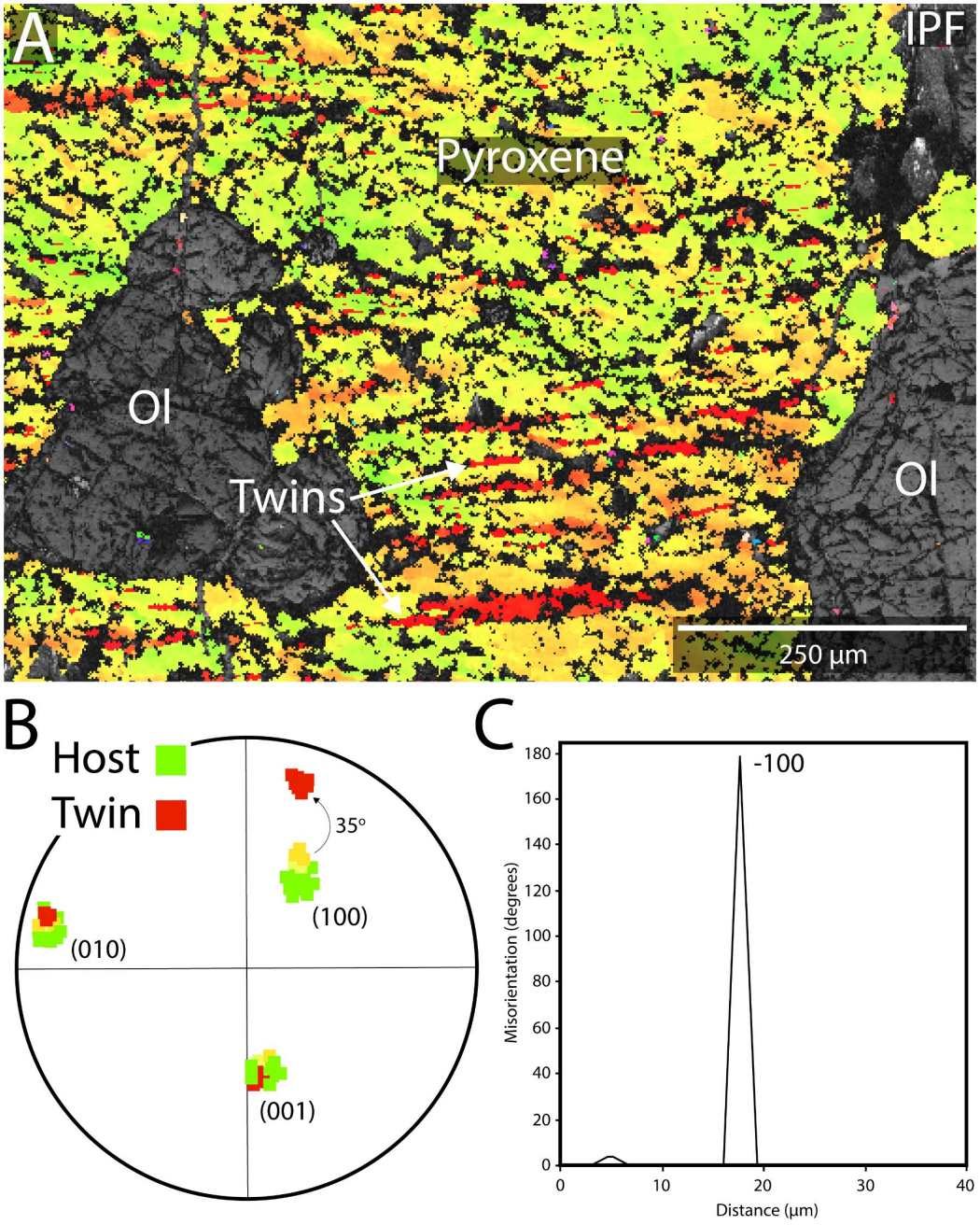

Figure 3.14 *Pyroxene shock twins in NWA 11043. A: EBSD orientation map, with an inverse pole figure (IPF) color scheme, of a pyroxene oikocryst displaying (100) shock twins (in red). The black features are fractures that did not index during EBSD analysis. Ol = olivine. B: Pole figure of the host pyroxene and shock twin orientations. The stereonet is an equal-area, lower hemisphere projection plotted in sample reference frame. C: Misorientation profile of a pyroxene (100) shock twin in a pyroxene host grain.*

1.4.4 Geochemical Weathering in NWA 11043

Once meteorites land on Earth, terrestrial weathering will start to cause alteration within the rocks, the type and extent of which will differ depending on landing site. All these new shergottites were found in 'Northwest Africa', most likely in a desert environment. Therefore, they have all experienced (to different degrees) hot desert climate weathering. Weathering has the potential to create localised REE compositional effects within the rock (Crozaz and Wadhwa, 2001; Crozaz et al., 2003).

The introduction of a terrestrial REE component can lead to a LREE enrichment profile (Crozaz et al., 2003). The distribution of the terrestrial REE component can be very heterogeneous, as it will be localised to areas that are proximal to fractures and veins, which would have facilitated the REE redistribution. *In situ* analysis of minerals allows for a deeper understanding of the effects of this weathering process. The susceptibility of the REE abundance in minerals to be altered via this process is dependent on the mineral in question. Low REE abundance carriers are more likely to be affected. Olivine and pyroxene (overall REE abundance of <1x CI and ~1x CI, respectively) both display a relative enrichment in the LREE. Maskelynite is not generally affected, as the similar REE profile of NWA 11043 compared to the other new shergottites demonstrates. Phosphates, as the main carrier of REE should not be affected by a small enrichment in LREE, as their REE abundances are >100x CI. However, in NWA 11043, we observe a variation in phosphate REE profiles, with 2 out of a total of 11 analyzed grains displaying an enrichment in LREE. This suggests that terrestrial input was significant enough to alter the REE profile of the phosphates, but heterogeneously. Interestingly, we do not observe the same LREE enrichment in the other new shergottites. Though displaying similar terrestrial weathering products, the REE profiles of the minerals do not show a terrestrial signature. This implies that NWA 11043 is more weathered than the other studied shergottites, which suggests it has had a longer terrestrial exposure time. However, longer exposure doesn't necessarily equate to increased level of alteration. Initial weathering is the most significant as the porosity of the meteorite will decrease over time due to alteration, which in turn, slows down the alteration process as there is less pore space (i.e. cracks) for alteration products to infill (Bland et al., 1996). Therefore, to explain the weathering differences we have to turn to shock processes, where differences might lead to variable alteration of rocks over the same amount of time.

All the meteorites display cracks and veins, but to different levels. NWA 11043 is the most heavily fractured, based on BSE mapping (Fig. 3.13). So much so, that the traditionally mafic crystalline rock with little to no porosity had been transformed to a rock with a high degree of 'shock induced porosity' (e.g., Rae et al., 2019). This substantial increase in porosity relative to the other meteorites, would have encouraged more extensive alteration. This could explain why NWA 11043 has mineral LREE enrichment signatures and the other meteorites do not. At which exact point a weathered meteorite, for example NWA 10818, develops a terrestrial REE signature similar to NWA 11043 is not obvious. Further work would be required to constrain the requisite conditions which is beyond the scope of this paper.

Thus, by not 'measuring' the bulk REE abundance of NWA 11043, and, instead, 'calculating' the bulk REE abundance from *in situ* analysis we can avoid terrestrially altered minerals, and just attempt to include the most 'Martian' REE abundances. We also avoid including all the veins in the bulk calculation as these will be the main carriers of the terrestrial REE, and their inclusion is unavoidable during bulk analyses. Therefore, we propose that in highly weathered meteorites, combining the 3D major modal mineralogy derived from HRXCT (or other high resolution techniques), and an average phosphate abundance derived from most of the poikilitic shergottites with *in situ* REE analyses of specific target grains yields a more accurate bulk REE profile than measured bulk powdered analyses as weathering products can be avoided

This being the case, we conclude NWA 11043 has an intermediate REE profile, and is not enriched as suggested by Rahib et al. (2019). The intermediate profile still bears a terrestrial weathering signature, with an enrichment in La and depletion in Ce, but overall fits in the intermediate field.

1.4.5 Is NWA 10441 paired with NWA 8657?

Northwest Africa 10441 is suggested to be a pair of NWA 8657 (Bouvier et al., 2017). Both meteorites were recovered in 'Northwest Africa' in 2015 and 2014, respectively. A meteorite pair by definition is a part of the original meteorite that either fragmented during decent through Earth's atmosphere or was eroded and transported via terrestrial processes away from the host meteorite (e.g., Benoit et al., 2000). Both of these

meteorites were initially reported to comprise numerous stones. The locations of these stones in relation to each other is not reported, therefore it is unknown if they were all found in the same place, or strewn across an area. If the latter, the original meteorite must have had multiple stages of fragmentation during its disintegration descending through the atmosphere (e.g., Babadzhanov, 2002). Once the meteorites have landed, terrestrial weathering can occur. As previously stated, NWA 10441 contains very little evidence of terrestrial alteration. On the other hand, NWA 8657 is reported to contain pervasive carbonate weathering throughout the meteorite with positive Ba anomalies usually associated with hot desert weathering (Howard et al., 2018). The meteorites could also have landed in areas with different weathering rates. Therefore, weathering differences may not be indicative of pairing or lack thereof.

Geologically speaking, both meteorites exhibit typical basaltic shergottite textures and compositions (Howarth et al., 2018). They contain euhedral pyroxene and maskelynite grains that are both geochemically zoned. The pyroxenes have pigeonite or augite cores, surrounded by ferrosilite-rich rims, with overlapping compositions between the meteorites. The maskelynite has high-An cores with high-Ab/Or rims. Accessory phases include phosphates, primarily merrillite, and oxides (pyrrhotite, ilmenite, titanomagnetite). Shock melt pockets and the presence of vesicles are observed throughout both meteorites (Howarth et al., 2018). Although very similar, other basaltic shergottites display similar characteristics making it inconclusive to ascribe pairing based on mineralogy and petrological evidence alone (e.g., Udry et al., 2020 and references therein).

The REE geochemistry of shergottites can also be used to test pairing. If they are paired, then their REE profile should be comparable. The HRXCT-derived REE profile of NWA 10441 is slightly more enriched in LREE, with a $[La/Lu]_{CI}$ of 1.31, compared to NWA 8657 which has a relatively flat REE profile with a $[La/Lu]_{CI}$ of 0.92. Northwest Africa 10441 also has a slight negative $[Eu/Eu^*]_{CI}$ anomaly of 0.86 compared to the flat 1.03 for NWA 8657. Even with minor differences, both NWA 10441 and NWA 8657 are enriched shergottites displaying similar REE distributions. As previously discussed, heterogeneity with the meteorites themselves, especially in relation to phosphates, creates a situation where minor differences are most likely not significant. For a conclusive match, the geochronological and ejection ages (cosmic

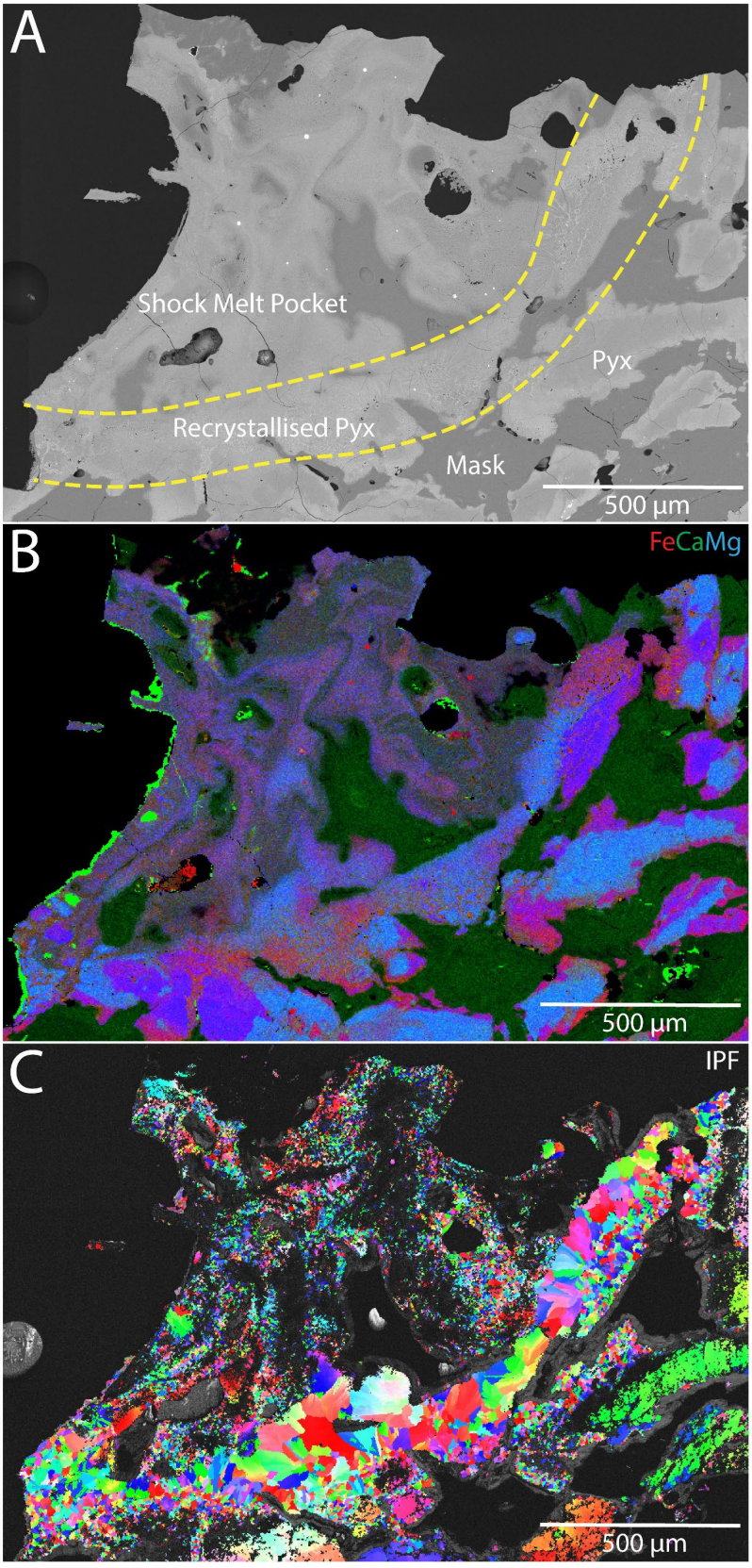

Figure 3.15 *Shock melt pocket in NWA 10441. A: BSE map of the shock melt pocket. Pyx = pyroxene, Mask = maskelynite. Yellow dashed lines indicate rim of recrystallized pyroxene. Black 'blobs' are gas vesicles. B: combined elemental distribution map, Fe = red, Ca = green and Mg = blue. C: EBSD-derived IPF (inverse pole figure) coloured map showing the recrystallized zone around the shock melt pocket. The colours represent different crystallographic orientations of the pyroxene grains which also indicates grain boundaries.*

ray exposure plus terrestrial age) of the meteorites would need to be investigated. As pairs, they would have the same or very similar corresponding ages. Without these ages, and given the previously stated evidence, NWA 8657 and NWA 10441 are likely meteorite pairs that landed in slightly different locations, producing variable weathering patterns.

1.5 Conclusions

In this study we conducted a number of geochemical and mineralogical analyses to classify four new shergottites. We confirm that NWA 10818 and NWA 11043 are intermediate poikilitic shergottites. In contrast to Rahib et al. (2019), we find that NWA 11043 has an intermediate REE pattern. This is likely because it experienced significant terrestrial weathering, encouraged by extensive shock-induced fracturing, which caused enrichment in LREE, affecting its classification based on bulk analysis. By conducting *in situ* analyses of NWA 11043, we concluded that by avoiding terrestrially altered analyses we could discern the altered vs unaltered pattern visible in the REE abundances. The crystallisation history of NWA 10818 and NWA 11043 is similar to other poikilitic shergottites. The poikilitic areas crystallized first at depth, then the non-poikilitic areas started to crystallize as the magma started to ascend towards the surface. Emplacement occurred in a hypabyssal system such as in a dike or sill near the surface.

We also confirmed that NWA 10441 and NWA 12335 are enriched basaltic (diabasic) shergottites. NWA 10441 is very similar to its proposed pair NWA 8657 (Howarth et al., 2018), though definitive confirmation would require ejection (combined cosmic-ray exposure and terrestrial age) and geochronological ages. The crystallization histories of NWA 10441 and NWA 12335 are slightly different. NWA 10441 represents multi-stage crystallization, where pyroxenes became entrained in an ascending basaltic magma. NWA 12335 represents continuous crystallization of pyroxenes until final extrusion. Both shergottites finally erupted onto the Martian surface as lavas, evidenced by the meta-stable Fs-pigeonite and pyroxferroite rims which are only preserved during rapid cooling. These new shergottites add to the consistent story of basaltic shergottites erupting as lavas onto the surface and poikilitic shergottites being emplaced hypabyssaly near the surface. Combining new methods

such as HRXCT and EBSD with traditional methods, we can examine these rocks non-destructively in ever greater detail. We have demonstrated that the combination of these techniques can be very effective, and sometimes more suitable than destructive techniques, especially with regard to highly weathered samples.

1.6 References

Agee, C. B., Wilson, N. V., McCubbin, F. M., Ziegler, K., Polyak, V. J., Sharp, Z. D., et al. (2013). Unique Meteorite from Early Amazonian Mars: Water-Rich Basaltic Breccia Northwest Africa 7034. *Science*, *339*(6121), 780–785. https://doi.org/10.1126/science.1228858

Anand, M.; James, S.; Greenwood, R. C.; Johnson, D.; Franchi, I. A. and Grady, M. M. (2008). Mineralogy and Geochemistry of Shergottite RBT 04262. *Lunar and Planetary Science Conference XXXIX*, (abs) 2173.

Artemieva, N., and Ivanov, B. (2004). Launch of martian meteorites in oblique impacts. *Icarus* 171:84–101.

Barrat, J. A., Gillet, P., Sautter, V., Jambon, A., Javoy, M., Göpel, C., Lesourd, M., Keller, F., Petit, E. (2002a). Petrology and chemistry of the basaltic shergottite North West Africa 480. *Meteoritics and Planetary Science* 37:487–499.

Barrat, J. A., Jambon, A., Bohn, M., Gillet, P., Sautter, V., Göpel, C., Lesourd, M., Keller, F. (2002b). Petrology and chemistry of the Picritic Shergottite North West Africa 1068 (NWA 1068). *Geochimica et Cosmochimica Acta* 66:3505-3518

Babadzhanov, P. B. (2002). Fragmentation and densities of meteoroids. *Astronomy & Astrophysics* 384:317-321.

Benoit P. h, Sears D. w g, Akridge J. m c, Bland P. a, Berry F. j, and Pillinger C. t. (2000). The non-trivial problem of meteorite pairing. *Meteoritics & Planetary Science* 35:393–417.

Bland, P. A., Berry, F. J., Smith, T. B., Skinner, S. J., Pillinger, C. T. (1996). The flux of meteorites to the Earth and weathering in hot desert ordinary chondrite finds. *Geochimica et Cosmochimica Acta* 60:2053-2059.

Borg, L. E., and Draper, D. S. (2003). A petrogenetic model for the origin and compositional variation of the martian basaltic meteorites. *Meteoritics & Planetary Science* 38:1713-1731.

Bouvier, A., Gattacceca, J., Agee, C., Grossman, J. and Metzler, K. (2017a). The Meteoritical Bulletin, No. 104. *Meteoritics & Planetary Science* 52:2284.

Bouvier, A., Gattacceca, J., Grossman, J. and Metzler, K. (2017b). The Meteoritical Bulletin, No. 105. *Meteoritics & Planetary Science* 52:2411.

Bridges, J. C., and Warren, P. H. (2006). The SNC meteorites: basaltic igneous processes on Mars. *Journal of the Geological Society* 163:229-251.

Cao, T., He, Q., Xue, Z. Q. (2018). Petrogenesis of basaltic shergottite NWA 8656. *Earth and Planetary Physics* 2:384-397.

Combs, L. M., Udry, A., Howarth, G. H., Righter, M., Lapen, T. J., Gross, J., Ross, D. K., Rahib, R. R., Day, J. M. D. (2019). Petrology of the enriched poikilitic shergottite Northwest Africa 10169: Insight into the martian interior. *Geochimica et Cosmochimica Acta* 266:435-462.

Cousin, A., Sautter, V., Payré, V., Forni, O., Mangold, N., Gasnault, O., et al. (2017). Classification of igneous rocks analyzed by ChemCam at Gale crater, Mars. *Icarus*, *288*, 265–283. https://doi.org/10.1016/j.icarus.2017.01.014

Crozaz, G., and Wadhwa, M. (2001). The terrestrial alteration of Saharan shergottites Dar al Gani 476 and 489: a case study of weathering in a hot desert environment. *Geochimica et Cosmochimica Acta* 65:971-977.

Crozaz, G., Floss, C., Wadhwa, M. (2003). Chemical alteration and REE mobilization

in meteorites from hot and cold deserts. *Geochimica et Cosmochimica Acta* 67:4727-4741.

El Goresy, A., Gillet, Ph., Miyahara, M., Ohtani, E., Ozawa, S., Beck, P., Montagnac, G. (2013). Shock-induced deformation of Shergottites: Shock-pressures and perturbations of magmatic ages on Mars. *Geochimica et Cosmochimica Acta* 101:233-262.

Filiberto, J., Mussel White, D. S., Gross, J., Burgess, K., LE, L., & Treiman, A. H. (2010). Experimental petrology, crystallization history, and parental magma characteristics of olivine-phyric shergottite NWA 1068: Implications for the petrogenesis of "enriched" olivine-phyric shergottites. *Meteoritics & Planetary Science*, *45*(8), 1258–1270. https://doi.org/10.1111/j.1945-5100.2010.01080.x

Filiberto J., Chin E., Day J. M. D., Franchi I. A., Greenwood R. C., Gross J., Penniston-Dorland S. C., Schwenzer S. P., and Treiman A. H. (2012). Geochemistry of intermediate olivine-phyric shergottite Northwest Africa 6234, with similarities to basaltic shergottite Northwest Africa 480 and olivine-phyric shergottite Northwest Africa 2990. *Meteoritics & Planetary Science* 47:1256–1273.

Filiberto J., Gross J., Trela J., and Ferré E. C. (2014). Gabbroic Shergottite Northwest Africa 6963: An intrusive sample of Mars. *American Mineralogist* 99:601–606.

Filiberto, J., Gross, J., Udry, A., Trela, J., Wittmann, A., Cannon, K. M., Penniston-Dorland, S., Ash, R., Hamilton, V. E., Meado, A. L., Carpenter, P., Jolliff, B., Ferré, E. C. (2018). Shergottite Northwest Africa 6963: A Pyroxene-Cumulate Martian Gabbro. *Journal of Geophysical Research: Planets* 123:1823-1841.

Forman, L. V., Timms, N. E., Bland, P. A., Daly, L., Benedix, G. K., Trimby, P. W. (2019). A morphologic and crystallographic comparison of CV chondrite matrices. *Meteoritics & Planetary Science* 54:2633-2651.

Fritz, J., Artemieva, N., Greshake, A. (2005). Ejection of Martian meteorites. *Meteoritics & Planetary Science* 40:1393-1411.

Gattacceca, J., Bouvier, A., Grossman, J., Metzler, K. and Uehara, M. (2019). The Meteoritical Bulletin, No. 106. *Meteoritics & Planetary Science* 54:469-471.

Gattacceca, J., McCubbin, F. M., Bouvier, A. and Grossman, J. (2020). The Meteoritical Bulletin, No. 107. *Meteoritics & Planetary Science* 55:460-462.

Godel, B. (2013). High-Resolution X-Ray Computed Tomography and Its Application to Ore Deposits: From Data Acquisition to Quantitative Three-Dimensional Measurements with Case Studies from Ni-Cu-PGE Deposits. *Economic Geology* 108:2005-2019.

Goodrich, C. A., Herd, C. D. K., Taylor, L. A. (2003). Spinels and oxygen fugacity in olivine-phyric and lherzolitic shergottites. *Meteoritics & Planetary Science* 38:1773-1792.

Harvey, R. P., McCoy, T. J., Leshin, L. A. (1996) Shergottite QUE94201: Texture, mineral compositions, and comparison with other basaltic Shergottites. *Lunar Planetary Science XXVII* (abs) 497-498.

He Q., Xiao L., Balta J. B., Baziotis I. P., Hsu W., and Guan Y. (2015). Petrography and geochemistry of the enriched basaltic shergottite Northwest Africa 2975. *Meteoritics & Planetary Science* 50:2024–2044.

Head J. N., Melosh H. J., and Ivanov B. A. (2002). Martian Meteorite Launch: High-Speed Ejecta from Small Craters. *Science* 298:1752–1756.

Herd, C. D. K., Walton, E. L., Agee, C. B., Muttik, N., Ziegler, K., Shearer, C. K., Bell, A. S., Santos, A. R., Burger, P. V., Simon, J. I., Tappa, M. J., McCubbin, F. M., Gattacceca, J., Lagroix, F., Sanborn, M. E., Yin, Q. Z., Cassata, W. S., Borg, L. E., Lindvall, R. E., Kruijer, T. S., Brennecka, G. A., Kleine, T., Nishiizumi, K., Caffee, M. W. (2017). The Northwest Africa 8159 martian meteorite: Expanding the martian sample suite to the early Amazonian. *Geochimica et Cosmochimica Acta* 218:1-26.

Howarth, G. H., Pernet-Fisher, J. F., Balta, J. B., Barry, P. H., Bodnar, R. J., Taylor, L. A. (2014). Two-stage polybaric formation of the new enriched, pyroxene-oikocrystic, lherzolitic shergottite, NWA 7397. *Meteoritics & Planetary Science* 49:1812-1830.

Howarth, G. H., Pernet-Fisher, J. F., Bodnar, R. J., Taylor, L. A. (2015). Evidence for the exsolution of Cl-rich fluids in martian magmas: Apatite petrogenesis in the enriched lherzolitic shergottite Northwest Africa 7755. *Geochimica et Cosmochimica Acta* 166:234-248.

Howarth, G. H., Udry, A., Day, J. M. D. (2018). Petrogenesis of basaltic shergottite Northwest Africa 8657: Implications for fO2 correlations and element redistribution during shock melting in shergottites. *Meteoritics & Planetary Science* 53:249-267.

Hui, H., Peslier, A. H., Lapen, T. J., Shafer, J. T., Brandon, A. D., Irving, A. J. (2011). Petrogenesis of basaltic shergottite Northwest Africa 5298: Closed-system crystallization of an oxidized mafic melt. *Meteoritics & Planetary Science* 46:1313-1328.

Ikeda, Y., Kimura, M., Takeda, H., Shimoda, G., Kita, N. T., Morishita, Y., Suzuki, A., Jagoutz, E., Dreibus, G. (2006). Petrology of a new basaltic shergottite: Dhofar 378. *Antarctic Meteorite Research* 19:20-44.

Irving A.J., Kuehner S.M., Herd C.D.K., Gellissen M., Rumble D., Lapan T.J., Ralew S. and Altmann M. (2010). Olivine-bearing diabasic Shergottite Northwest Africa 5990: Petrology and composition of a new type of depleted Martian igneous rock. *41st Lunar and Planetary Science Conference,* abs#1833.

Jambon, A., Barrat, J. A., Sautter, V., Gillet, Ph., Göpel, C., Javoy, M., Joron, J. L., Lesourd, M. (2002). The basaltic shergottite Northwest Africa 856: Petrology and chemistry. *Meteoritics & Planetary Science* 37:1147-1164.

Kring, D. A., Gleason, J. D., Swindle, T. D., Nishiizumi, K., Caffee, M. W., Hill, D.H., Jull, A. J. T., Boynton, W. V., (2003). Composition of the first bulk melt sample from a volcanic region of Mars: Queen Alexandra Range 94201. *Meteoritics & Planetary Science* 38:1833–1848.

Lin, Y., Guan, Y., Wang, D., Kimura, M., Leshin, L. A. (2005). Petrogenesis of the new lherzolitic shergottite Grove Mountains 99027: Constraints of petrography, mineral chemistry, and rare earth elements. *Meteoritics & Planetary Science* 40:1599-1619.

Lin, Y., Hu, S., Miao, B., Xu, L., Liu, Y., Xie, L., Feng, L., Yang, J. (2013). Grove Mountains 020090 enriched lherzolitic shergottite: A two-stage formation model. *Meteoritics & Planetary Science* 48:1572-1589.

Lindsley, D. H., and Burnham, C. W. (1970). Pyroxferroite: Stability and X-ray Crystallography of Synthetic $Ca_{0.15}Fe_{0.85}SiO_3$ Pyroxenoid. *Science* 168:364-367.

Liu Y., Floss C., Day J. M. D., Hill E., and Taylor L. A. (2009). Petrogenesis of lunar mare basalt meteorite Miller Range 05035. *Meteoritics & Planetary Science* 44:261–284.

Llorca, J., Roszjar, J., Cartwright, J. A., Bischoff, A., Ott, U., Pack, A., Merchel, S., Rugel, G., Fimiani, L., Ludwig, P. and Casado, J. V. (2013). The Ksar Ghilane 002 shergottite—the 100th registered Martian meteorite fragment. *Meteoritics & Planetary Science* 48:493-513.

Lodders, K. (1998). A survey of shergottite, nakhlite and chassigny meteorites whole-rock compositions. *Meteoritics & Planetary Science*, *33*(S4), A183–A190. https://doi.org/10.1111/j.1945-5100.1998.tb01331.x

McCoy, T. J., Taylor, G. J., Keil, K. (1992). Zagami: Product of a two-stage magmatic history. *Geochimica et Cosmochimica Acta* 56:3571-3582.

McCubbin, F. M., Elardo, S. M., Shearer, C. K., Smirnov, A., Hauri, E. H., Draper, D. S. (2013). A petrogenetic model for the comagmatic origin of chassignites and nakhlites: Inferences from chlorine-rich minerals, petrology, and geochemistry. *Meteoritics & Planetary Science* 48:819-853.

McSween, H. Y., Eisenhour, D. D., Taylor, L. A., Wadhwa, M., Crozaz, G. (1996). QUE94201 shergottite: Crystallization of a Martian basaltic magma. *Geochimica et Cosmochimica Acta* 60:4563-4569.

McSween, H. Y., and Treiman, A. H., (1998). Martian meteorites, In Planetary Materials, Reviews in Mineralogy, edited by Papike, J. J: *Mineralogical Society of America* 36:6-1–6-53.

McSween, H. Y., and McLennan, S. M. (2014). Mars, In Treatise on Geochemistry 2nd ed., edited by Heinrich D. Holland, Karl K. Turekian: *Elsevier* 251-300.

McSween, H. Y. (2015). Petrology on Mars. *American Mineralogist* 100:2380-2395.

Mikouchi T., Miyamoto M., and McKay G. A. (1998). Mineralogy of Antarctic basaltic shergottite Queen Alexandra Range 94201: Similarities to Elephant Moraine A79001 (Lithology B) martian meteorite. *Meteoritics & Planetary Science* 33:181–189.

Mikouchi, T., Miyamoto, M., McKay, G. A. (2001). Mineralogy and petrology of the Dar al Gani 476 martian meteorite: Implications for its cooling history and relationship to other shergottites. *Meteoritics & Planetary Science* 36:531-548.

Mikouchi, T., and Barrat, J.A. (2009). NWA 5029 basaltic shergottites: A clone of NWA 480/1460? *Meteoritics and Planetary Science Supplement, 72,* p.5344.

Paton, C., Hellstrom, J., Paul, B., Woodhead, J., Hergt, J. (2011). Iolite: Freeware for the visualisation and processing of mass spectrometric data. *Journal of Analytical Atomic Spectrometry* 26:2508-2518.

Rae, A. S. P., Collins, G. S., Morgan, J. V., Salge, T., Christeson, G. L., Leung, J., Lofi, J., Gulick, S. P. S., Poelchau, M., Riller, U., Gebhardt, C., Grieve, R. A. F., Osinski, G. R., IODP-ICDP Expedition 364 Scientists. (2019). Impact-Induced Porosity and Microfracturing at the Chicxulub Impact Structure. *Journal of Geophysical Research: Planets* 124:1960–1978.

Rahib, R. R., Udry, A., Howarth, G. H., Gross, J., Paquet, M., Combs, L. M., Laczniak, D. L., Day, J. M. D. (2019). Mantle source to near-surface emplacement of enriched and intermediate poikilitic shergottites in Mars. *Geochimica et Cosmochimica Acta* 266:463-496.

Riches, A. J. V., Liu, Y., Day, J. M. D., Puchtel, I. S., Rumble, D., III., McSween, H. Y., Walker, R. J., Taylor, L. A. (2011). Petrology and geochemistry of Yamato 984028: a cumulate lherzolitic shergottite with affinities to Y 000027, Y 000047, and Y 000097. *Polar Science* 4:497-514.

Roszjar, J., Bischoff, A., Llorca, J. and Pack, A. (2012). Ksar Ghilane 002 (KG 002)---A New Shergottite: Discovery, Mineralogy, Chemistry and Oxygen Isotopes. *Lunar Planetary Science XLIII* 43.

Rubin, A. E., Warren, P. H., Greenwood, J. P., Verish, R. S., Leshin, L. A., Hervig, R. L., Clayton, R. N., Mayeda, T. K. (2000). Los Angeles: The most differentiated basaltic martian meteorite. *Geology* 28:1011-1014.

Sautter, V., Toplis, M. J., Wiens, R. C., Cousin, A., Fabre, C., Gasnault, O., et al. (2015). In situ evidence for continental crust on early Mars. *Nature Geoscience*, *8*(8), 605–609. https://doi.org/10.1038/ngeo2474

Sharp, T. G., and DeCarli, P. S. (2006). Shock effects in meteorites. *Meteorites and the early solar system II* 943:653-677.

Stöffler, D. (1972). Deformation and transformation of rock-forming minerals by natural and experimental shock processes. I. Behavior of minerals under shock compression. *Fortschritte der Mineralogie* 49:50-113.

Stöffler, D. (1984). Glasses formed by hypervelocity impact. *Journal of Non-Crystalline Solids* 67:465-502.

Stöffler, D., Ostertag, R., Jammes, C., Pfannschmidt, G., Gupta, P. R., Simon, S. B., Papike, J. J., Beauchamp, R. H. (1986). Shock metamorphism and petrography of the Shergotty achondrite. *Geochimica et Cosmochimica Acta* 50:889-903.

Stöffler, D., Hamann, C., Metzler, K. (2018). Shock metamorphism of planetary silicate rocks and sediments: Proposal for an updated classification system. *Meteoritics & Planetary Science* 53:5-49.

Treiman, A. H., McKay, G. A., Bogard, D. D., Mittlefehldt, D. W., Wang, M. S., Keller, L., Lipschutz, M. E., Lindstrom, M. M., Garrison, D. (1994). Comparison of the LEW88516 and ALHA77005 martian meteorites: Similar but distinct. *Meteoritics* 29:581-592.

Treiman A. H., and Filiberto J. (2015). Geochemical diversity of shergottite basalts: Mixing and fractionation, and their relation to Mars surface basalts. *Meteoritics & Planetary Science* 50:632–648.

Udry, A., Howarth, G. H., Lapen, T. J., Righter, M. (2017). Petrogenesis of the NWA 7320 enriched martian gabbroic shergottite: Insight into the martian crust. *Geochimica et Cosmochimica Acta* 204:1-18.

Udry, A., Howarth, G. H., Herd, C. D. K., Day, J. M. D., Lapen, T. J., & Filiberto, J. (2020). What Martian Meteorites Reveal About the Interior and Surface of Mars. *Journal of Geophysical Research: Planets*, *125*(12). https://doi.org/10.1029/2020je006523

Usui, T., McSween, H. Y., Floss, C. (2008). Petrogenesis of olivine-phyric shergottite Yamato 980459, revisited. *Geochimica et Cosmochimica Acta* 72:1711-1730.

Usui, T., Sanborn, M., Wadhwa, M., McSween, H. Y. (2010). Petrology and trace

element geochemistry of Robert Massif 04261 and 04262 meteorites, the first examples of geochemically enriched lherzolitic shergottites. *Geochimica et Cosmochimica Acta* 74:7283-7306.

Walton, E. L., and Spray, J. G. (2003). Mineralogy, microtexture, and composition of shock-induced melt pockets in the Los Angeles basaltic shergottite. *Meteoritics & Planetary Science* 38:1865-1875.

Walton, E. L., Irving, A. J., Bunch, T. E., Herd, C. D. K. (2012). Northwest Africa 4797: A strongly shocked ultramafic poikilitic shergottite related to compositionally intermediate Martian meteorites. *Meteoritics & Planetary Science* 47:1449-1474.

Warren, P. H., Greenwood, J. P., Rubin, A. E. (2004). Los Angeles: A tale of two stones. *Meteoritics & Planetary Science* 39:137-156.

Wittke, J. H., Bunch, T. E., Irving, A. J., Farmer, M. and Strope, J. (2006). Northwest Africa 2975: An evolved basaltic shergottite with vesicular glass pockets and trapped melt inclusions. *Lunar Planetary Science XXXVII* 37.

Xirouchakis, D., Draper, D. S., Schwandt, C. S., Lanzirotti, A. (2002). Crystallization conditions of Los Angeles, a basaltic Martian meteorite. *Geochimica et Cosmochimica Acta* 66:1867-1880.

Zipfel, J., Schröder, C., Jolliff, B. L., Gellert, R., Herkenhoff, K. E., Rieder, R., et al. (2011). Bounce Rock—A shergottite-like basalt encountered at Meridiani Planum, Mars. Meteoritics & Planetary Science, 46(1), 1–20. https://doi.org/10.1111/j.1945-5100.2010.01127.x

Chapter 4: Application of μ-FTIR Spectroscopy to the Measurement of Pigeonite in Martian Shergottites

4.1 Introduction

Thermal infrared (TIR) spectroscopy is a powerful remote sensing tool that is used to determine compositions of target, especially planetary, surfaces. Infrared spectrometers have been onboard a number of major missions into deep space. Mars has been the objective of the majority of these missions, and has been extensively, globally and locally, mapped with infrared spectrometers at ever-higher spatial resolutions. The Viking mission (launched in 1975) contained the first infrared spectrometer called the Mars Infrared Thermal Mapper (IRTM), operating four TIR bands: 6.1-8.3, 8.3-9.8, 9.8-12.5 and 17.7-24 μm (e.g., Kieffer et al., 1972; Kieffer et al., 1976; Kieffer et al., 1977). Mars Global Surveyor arrived in orbit around Mars in 1997. Onboard was the Thermal Emission Spectrometer (TES), a 3x6 km/pixel TIR spectrometer operating in the 6-50 μm wavelength range (Christensen et al., 2001). This was the first hyperspectral, TIR instrument to globally map the Martian surface, confirming its largely mafic (basaltic) composition (e.g., Bandfield et al., 2000). Another TIR spectrometer, the Thermal Emission Imaging System (THEMIS) onboard the 2001 Mars Odyssey orbiter also globally mapped the Martian surface at 100 m/pixel, operating seven bands used for surface science in the 6 – 15 μm wavelength range (Christensen et al., 2004a). THEMIS provided much higher spatial resolution but with lower spectral resolution than TES. Combining the spectral resolution of TES and the spatial resolution of THEMIS has been an effective approach to unravelling the complex geology of the Martian surface (e.g., Milam et al., 2004; Christensen et al., 2005; Rogers et al., 2005; Tornabene et al., 2008; Rogers and Bandfield, 2009). Furthermore, the Mars Exploration Rovers (MERs) had Miniature Thermal Emission Spectrometers (Mini-TES) onboard, providing in-situ analyses of the Martian surface (Christensen et al., 2003). In addition to its own surface science results, Mini-TES proved vital in calibrating and verifying satellite observations (e.g., Christensen et al., 2004b; McSween et al., 2004; Fergason et al., 2006; Rogers and Aharonson, 2008; Hamilton and Ruff, 2012).

To interpret the Martian surface spectra acquired from these missions, the spectra must be compared against known mineral and/or rock spectra from a spectral library using linear least squares modelling (Ramsey and Christensen, 1998; Rogers and Aharonson, 2008). In the mid-infrared (5-50 μm), a bulk or average spectrum of an area is typically the linear combination of its constituents in proportion to their abundance. Therefore, the modal mineralogy of a bulk or average spectrum can be linearly modelled using a spectral library to find a 'best-fit'. This process relies heavily on having a spectral library that represents all of the components in the mixture. The output is only as good as the input. For planetary bodies, the available mid-infrared mineral spectra that can be used for modelling are terrestrially derived (e.g., Christensen et al., 2000. The use of various spectral libraries has yielded valuable insights into Martian geology. We know the Martian surface is primarily basaltic, comprised of mafic minerals such as pyroxene, olivine and plagioclase similar to terrestrial basalts (e.g., Bandfield et al., 2000; Christensen et al., 2000; Rogers et al., 2007; Koeppen and Hamilton, 2008). The Martian meteorites, especially shergottites, which are the most abundant and diverse type of Martian meteorite, have thus far yet to be clearly identified in the dust free regions of the Martian surface (e.g., Hamilton et al., 2003). The shergottites are mafic rocks that can be broadly split up into three groups: basaltic, olivine-phyric and poikilitic (Fig. 4.1). All three groups are comprised, in different relative proportions, of pyroxene, olivine and plagioclase. Olivine and plagioclase are well represented in the current extant spectral libraries and other laboratory sources. The currently available pyroxene spectra in the various libraries include numerous clino- and orthopyroxene compositions and a synthetic pigeonite ($Wo_{10}En_{36}Fs_{54}$ 33,34, Hamilton, 2000). However, the composition of pyroxene in the shergottites is primarily 'inter-end member' augite and pigeonite with minor orthopyroxene (Fig. 4.2) (e.g., Bridges and Warren, 2006). Therefore, aside from some orthopyroxene compositions, shergottites show a greater range in pyroxene compositions, especially towards Fe-rich compositions, than the pyroxene mineral spectra in the terrestrial libraries.

From previous studies, pyroxene spectra vary based on geochemistry and crystal system (orthorhombic vs monoclinic) (Hamilton et al., 2000 and references therein). Therefore, ensuring the right composition pyroxenes are used is important for linear deconvolution of rocks and/or Martian surface spectra. Previous studies have

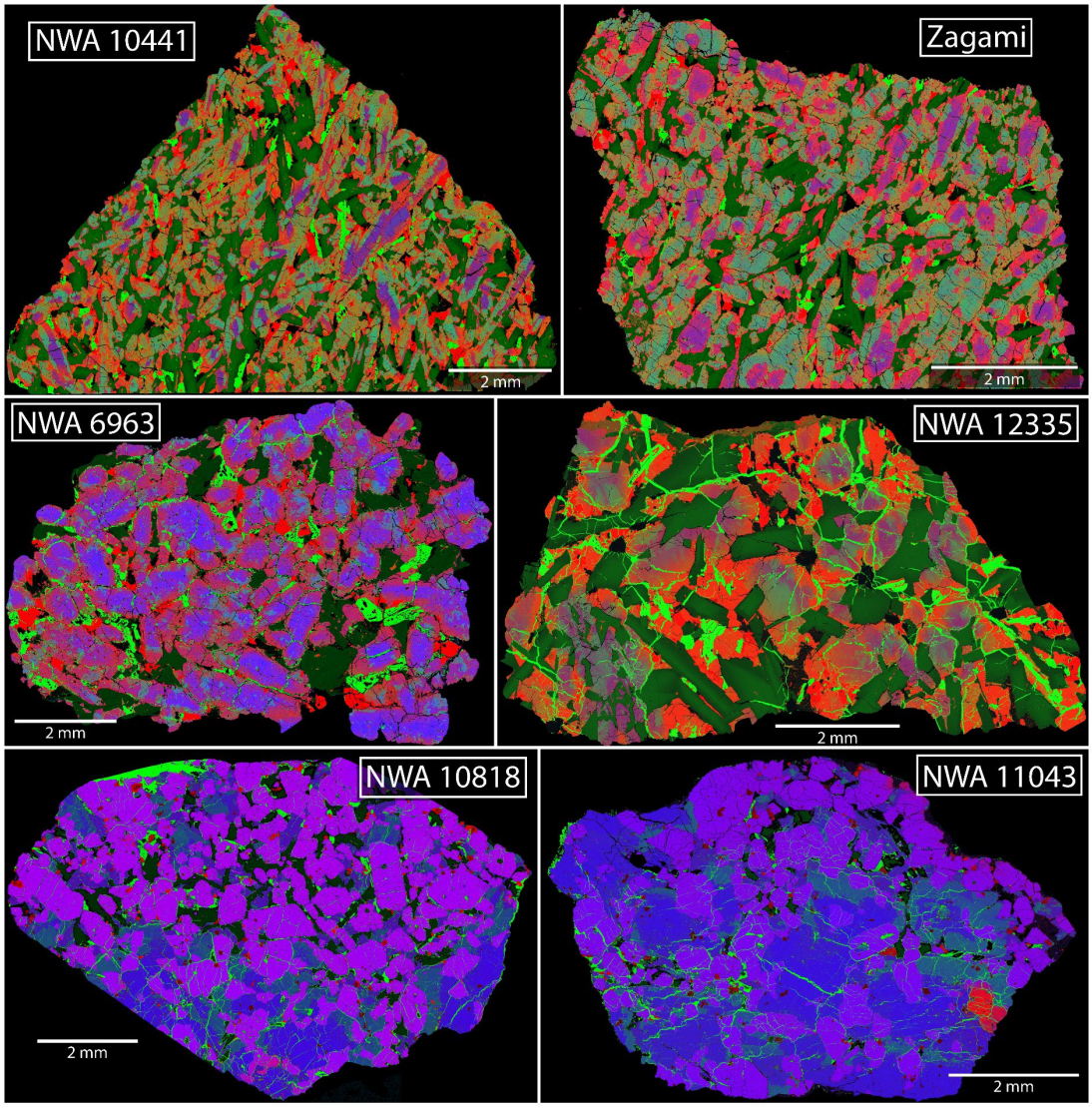

Figure 4.1 *Element distribution maps of the six shergottites used in this study. Note the different textures. The basaltic shergottites (NWA 6963, NWA 10441, NWA 12335 and Zagami) contain pyroxene (red-purple-light green) and maskelynite (dark green). The variation in colour in the pyroxene grains represents extensive geochemical zoning. The poikilitic shergottites (NWA 10818 and NWA 11043) contain olivine (purple), pyroxene (blue and light green) and maskelynite (dark green). Fe = red, Ca = green and Mg = blue.*

attempted to model a range of Martian meteorites with a spectral library of terrestrial minerals (e.g., Hamilton et al., 1997; Hamilton et al., 2010). The early modelling by Hamilton et al. (1997) met with mixed success. The modal abundance determination of the Martian meteorites was relatively accurate but the spectral fit, especially for Zagami (basaltic shergottite), suggested the composition of the meteorites was not fully represented in the mineral spectral library (lack of a pigeonite spectrum was suggested as a source of error). Hamilton et al. (2010) improved on modelling olivine-bearing Martian meteorites with a significantly expanded spectral library: 75 mineral spectra were used including an expanded range of olivine compositions and a single synthetic pigeonite spectrum (Wo10En36Fs54 33,34). These mineral compositions

were more representative of the Martian meteorites, and therefore, produced better spectral fits. However, the modal abundance determination of pyroxene was grouped together. Thus, we cannot assess which pyroxene compositions were included in the final spectral fits, for example pigeonite.

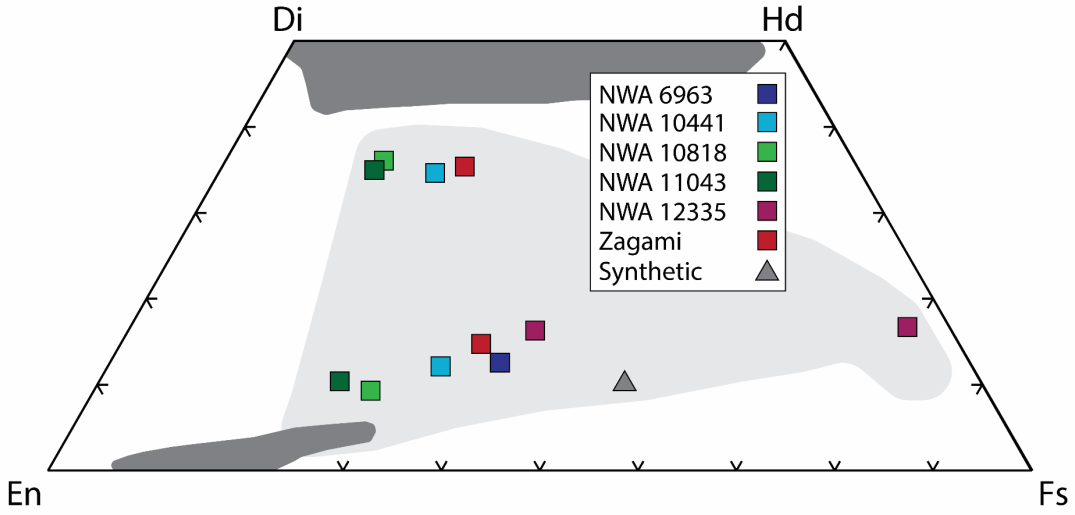

Figure 4.2 *The pyroxene quadrangle (Di = diopside, Hd = hedenbergite, En = enstatite, Fs = ferrosilite) displaying the composition of the new Martian pyroxene spectra based on their host meteorite. Light grey = shergottite pyroxene compositions. Dark grey = terrestrial pyroxenes from Christensen et al. (2000) and Hamilton et al. (2000). Synthetic = synthetic pigeonite spectrum (Wo10En36Fs54 33,34) from Hamilton (2000). Note the differences between the shergottite and terrestrial pyroxene compositions.*

The traditional technique for acquiring a mineral spectrum is to locate a natural occurrence and disaggregate it into several different particulate sizes. Analysing such a sample produces a generic spectrum, one devoid of preferred crystallographic orientation effects, which are similar to how polarised light can vary with orientation in a microscope. The method of using a particulate sample ensures measurement of the average spectrum for a given mineral at all orientations. Although this approach has been effective for many terrestrially derived minerals, there are fundamentally two major issues associated with acquiring pyroxene spectra that match the Martian meteorites. The most obvious is that creating a particulate of Martian meteorite derived minerals is undesirable due to the rarity of the samples and the destructive nature of the disaggregation. Therefore, in acquiring Martian mineral spectra a less destructive method would be preferable. Secondly, the 'inter-end member' augite and pigeonite themselves are a problem. Pigeonite exists here on Earth, but not in 'pure' form. Pigeonite is only stable at high temperatures (>~900ºC) (Lindsley, 1983), and therefore becomes unstable as the pigeonite-bearing magma rises to the surface and cools. If the magma does not rapidly cool, pigeonite will exsolve augite lamellae then

invert from monoclinic Ca-poor clinopyroxene into orthorhombic orthopyroxene at the micron scale. In effect, slow cooling totally removes pigeonite from the rock. On the other hand, if the pigeonite-bearing magma rises fast to the surface and is rapidly cooled (e.g., eruption as a lava), it will not invert to orthorhombic orthopyroxene. Pigeonite will either not exsolve (based on composition) forming 'clearly zoned' pigeonite grains (e.g. in the poikilitic shergottites) or will just exsolve augite lamellae (e.g. in the basaltic shergottites) (e.g., Leroux et al., 2004). Even if pigeonite still exists in the rock, physically separating the mineral from other pyroxenes in its current exsolved or zoned state is almost impossible. Therefore, a high spatial resolution technique would be required to access the pigeonite at this micron scale. In an effort to avoid these issues, a number of pigeonite mineral samples have been synthesised and subsequently spectrally analysed (Hamilton, 2000; Lindsley et al., 2019). Although these pigeonite compositions are closer to those in Martian meteorites, they still do not capture the full range of augite and pigeonite chemistries measured. Hence, a new approach is required that can leverage pyroxene spectra with the right composition.

Microscopic Fourier Transform Infrared Spectroscopy (μ-FTIR) enables infrared spectra to be acquired from meteorite thin sections, non-destructively. A number of studies have used this technique to characterise a variety of geological samples, including Martian meteorites (e.g., Jaret et al., 2015; Hamilton and Santos, 2017; Morlok et al., 2017; Filiberto et al., 2018). However, extracting pigeonite spectra specifically has not been a target. This is because μ-FTIR is only part of the answer. Before any pigeonite (mineral) measured from thin sections can be applied to the modelling of remote sensing data, it must represent a random orientation and a known geochemistry. To obtain a spectrum representative of a randomly oriented sample with a given composition, we need to: (1) acquire spectra from at least three different crystallographically axis-oriented grains and average them together and (2) measure the geochemistry, equal to the spot size of the infrared spectra, of those same grains. To meet these requirements, we use electron backscatter diffraction (EBSD) to assess the orientation and an electron probe micro-analyser (EPMA) to quantitatively map the geochemistry of the mineral grains. This enables accurate mineral spectra to be measured from Martian meteorites non-destructively while maintaining the necessary requirements so they can be used in linear modelling of Martian surface spectra (Fig.

4.3). Although bulk Martian meteorite spectra have been used for modelling Mars' surface, there has been, as yet, no individual mineral spectra sourced from other planetary bodies used in linear deconvolution modelling (e.g., Hamilton et al., 1997; Hamilton et al., 2003).

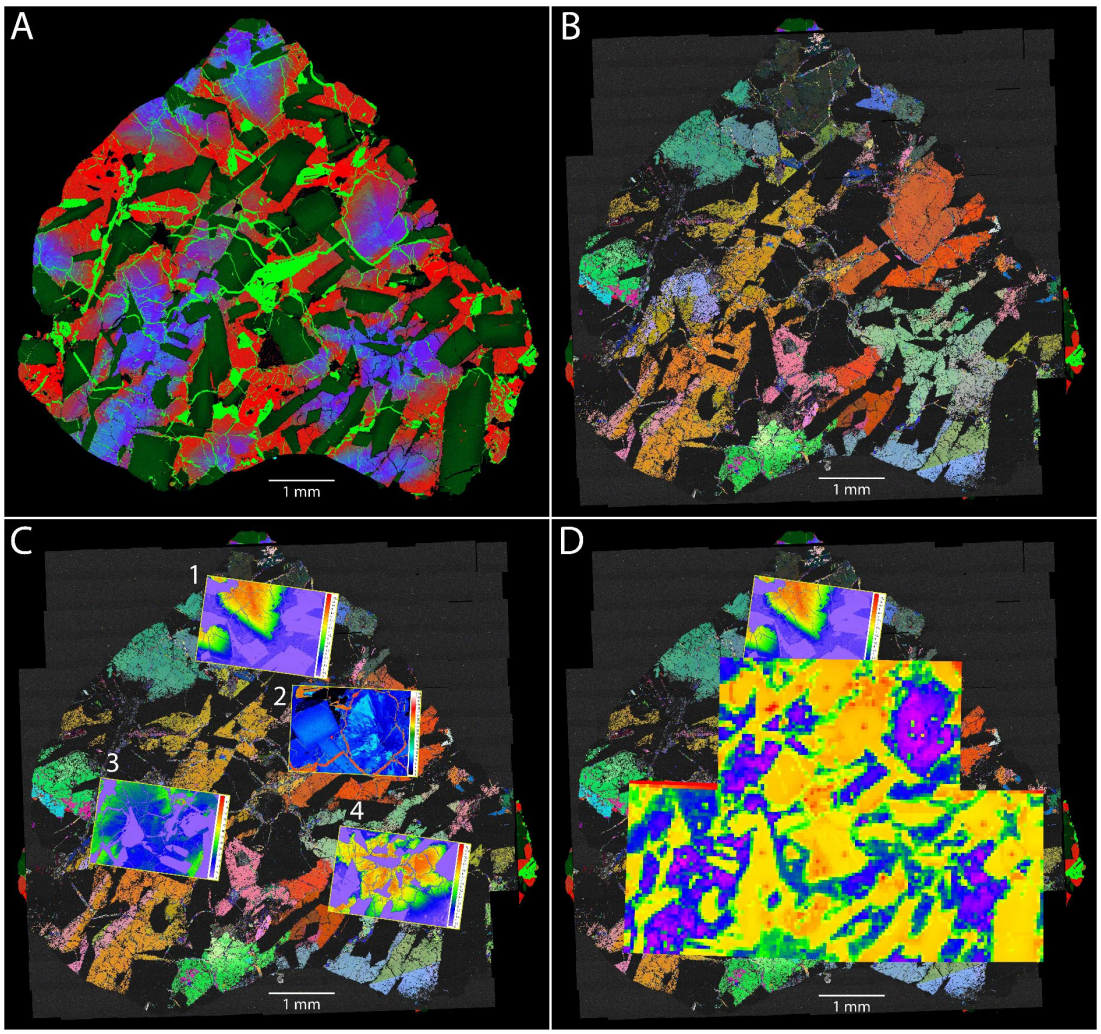

Figure 4.3 *Example of the analytical process to extract randomly oriented spectra with a known geochemistry from a thin-section. Images are of NWA12335 (a diabasic basaltic shergottite). A: TIMA combined RGB element map of the whole sample. Red = Fe, green = Ca, blue = Mg. B: EBSD crystallographic Euler orientation map. The different colours represent different crystallographic orientations of the pyroxene. The black areas are maskelynite, which does not index in EBSD mapping due to its glassy nature. C: EPMA quant maps overlaid on the EBSD map. 1 = Mg wt%, 2 = Ca wt%, 3 = Fe wt%, 4 = Mg%. D: µFTIR spectral maps display reflectance at 873 cm^{-1}, used to illustrate the distribution of maskelynite and pyroxene in the sample. Blue/purple = pyroxene, orange/yellow = maskelynite.*

We present eleven new augite and pigeonite spectra derived from four basaltic shergottites (NWA 6963, NWA 10441, NWA 12335 and Zagami) and two poikilitic shergottites (NWA 10818 and NWA 11043). These spectra represent, for the first time, that relevant pyroxene spectra can be derived from Martian meteorites.

4.1.1 Pigeonite on Mars

The predominance of pigeonite (and 'inter-end member' augite) in the shergottites suggests that the conditions for pigeonite formation and preservation are prevalent in Martian geological processes, at least in the last 600 Ma, based on the absolute ages of the shergottites. Several factors could influence pigeonite formation on Mars. Compared to Earth, the Martian mantle is Fe-rich relative to Mg (Earth has an Fe:Mg ratio of ~0.2 compared to ~0.6 on Mars) (Wänke and Dreibus, 1994; McDonough and Sun, 1995; Halliday et al., 2001; Yoshizaki and McDonough, 2020). We know from experimental phase relations that pigeonite is stable at lower temperatures with increasing Fe-content (Lindsley, 1983). Even though Mars is, on average, cooler than Earth due to its smaller size, because of its Fe-rich composition, pigeonite can be stable at these conditions. From the geochemistry of basaltic shergottites, we know that a large proportion of them crystallized from Fe-rich magmas (e.g., McSween, 2007). In some cases, the Fe content in the magma was high enough to crystallize pyroxferroite (e.g., McSween et al., 1996; Warren et al., 2004; Orr et al., *in review*). This suggests the role of Fe should not be understated. Further experimental studies on magma crystallization from a Fe-rich 'Martian equivalent melt' might elucidate the role of Fe in preferential crystallization of pigeonite.

For pigeonite preservation on or near the surface of Mars, magma needs to cool rapidly, as slow cooling encourages pigeonite to invert to orthopyroxene and augite (the prevailing condition on Earth). Rapid cooling commonly is associated with eruption of lava and requires fast magma ascent (to reduce slow cooling time). In the basaltic shergottites, augite has exsolved from pigeonite suggesting a certain level of cooling. However, this occurs at quite high temperatures (>900ºC), suggesting this occurred on eruption (Leroux et al., 2014). The poikilitic shergottites contain 'pure' pigeonite with no augite exsolution. Suggested to have crystallised at hypabyssal depths, pressure likely played an essential role in preserving pigeonite during the cooling of these rocks (e.g., Rahib et al., 2019).

The shergottites themselves indicate volcanic activity very late in Martian history. Unlike Earth, an active, multi-plate tectonic regime does not exist on Mars, and therefore traditional avenues for magma eruption do not exist. The drivers for melting and volcanism rely on long-lived mantle plumes (as in the case for Olympus Mons),

especially for late-history volcanic activity (e.g., Kiefer et al., 2015). Over Martian history, volcanic activity has decreased, primarily due to thickening of the lithosphere, often associated with stagnant lid planets. On Earth, 90% of continental magma is intrusive, as the magma gets 'stuck' on ascension (Crisp, 1984). With a thickening lithosphere, we can expect a similar situation with Mars. However, through lithospheric growth, the mantle of Mars has cooled inefficiently. Even though Mars is much smaller than Earth, Mars' mantle temperature is not that much lower than Earth's (Baratoux et al., 2011), with even a large proportion still molten (Duncan et al., 2018). These temperatures (>1700ºC for the shergottite source region) will lead to melting and periodic volcanic activity as magma ascends through the lithosphere. Mars' lithosphere thickness is variable, with >300 km thickness estimated for the North Pole (Phillips et al., 2008) and only ~50 km thick for Tharsis Montes (Grott and Breuer, 2010). As a likely source candidate for the shergottites, the relatively thin lithosphere under Tharsis (Late-Amazonian surface age) and hot mantle will increase likelihood of continued volcanic activity (Lagain et al., *in prep*).

Shergottite lavas are a product of continued volcanic activity on Mars, likely through melting of a residual high-temperature Fe-rich mantle. There is evidence to suggest that Martian geological conditions favour pigeonite formation in Late-Amazonian melts. As young Martian rocks, interpreted to comprise surface and near surface lavas, shergottites in theory should contribute significantly to satellite remote observations of the Martian surface. However, there are a number of issues associated with remote sensing of Mars, such as dust cover, especially over regions like Tharsis (e.g., Hamilton et al., 2003). Although the application of our work to Mars will not be simple, acquiring infrared spectra that are representative of the shergottites, especially the 'inter-end member' compositions of augite and pigeonite, may provide new data to aid our understanding of Martian surface geology.

4.2 Samples and Methods

4.2.1 Samples

The University of New Mexico (UNM) supplied the ~0.5g chips of all the Martian meteorites used in this study, including the basaltic shergottites Northwest Africa

(NWA) 6963, NWA 10441, NWA 12335 and Zagami, and the poikilitic shergottites NWA 10818 and NWA 11043.

The basaltic shergottites are the largest group of shergottites, composed primarily of, in most cases, maskelynite (shock-metamorphosed plagioclase) and pyroxene (augite and pigeonite). NWA 10441 and Zagami are both comprised of roughly equal proportions of maskelynite, augite and pigeonite (e.g., McCoy et al., 1992; Orr et al., *in review)*. The pyroxene grains are geochemically zoned from core to rim. Both augite and pigeonite cores are present, with the rims of the pyroxene grains trending towards Fe-rich pigeonite. Extensive micron-scale exsolution is present throughout the pyroxene grains. The maskelynite also contains minor core (Ca) to rim (Na) zoning. NWA 12335 is composed of complexly zoned augite and pigeonite grains surrounded by pyroxferroite rims with Ca-core to Na-rim maskelynite (Orr et al., *in review*). NWA 6963 is a gabbroic shergottite, comprised of anhedral pigeonite grains (with minor augite) and a small proportion of maskelynite (e.g., Filiberto et al., 2017). The pigeonite grains again are zoned from Mg-rich cores to Fe-rich rims. All the samples contain a number of accessory minerals in various abundances (e.g. oxides, sulphides and phosphates).

The poikilitic shergottites (NWA 10818 and NWA 11043) are comprised of maskelynite, olivine and pyroxene (augite and pigeonite) (e.g., Rahib et al., 2019; Orr et al., *in review*). They contain two distinct regions. The poikilitic areas are comprised of large, zoned pyroxene (pigeonite core and augite rim) oikocrysts surrounding smaller olivine and chromite chadacrysts. The non-poikilitic areas comprise fine-grained interstitial maskelynite, olivine and pyroxene (augite and pigeonite). Unlike the basaltic shergottites, the pyroxene in the poikilitic shergottites does not display extensive exsolution or complex zoning. The augite and pigeonite are distinct. Both NWA 10818 and NWA 11043 contain accessory minerals in the non-poikilitic areas (e.g. chromite and phosphate).

These meteorite samples were cut and made into 1-inch round polished epoxy mounts and then carbon coated with ~10 nm thickness for the electron probe techniques described below. We applied the same analysis workflow to each sample, ensuring maximum comparability.

4.2.2 Tescan Integrated Mineral Analyzer (TIMA)

For initial inspection and mineral determination, the samples were analysed using a Tescan Integrated Mineral Analyser (TIMA) in the John de Laeter Centre at Curtin University. The TIMA is a specially designed scanning-electron microscope (SEM) that maps samples with four EDS (Energy Dispersive) X-ray detectors. This produces element and phases maps of the samples. The analyses were acquired with a 70 nm spot size (proxy for beam current), 3 μm (some samples were also mapped at 1 μm) step size, 15 mm working distance (WD) and at 25 kV accelerating voltage. The maps were post-processed using the Tescan TIMA software, where element maps were extracted, and phase maps created. The element maps were then further processed using Adobe Photoshop and combined to create RGB maps to illustrate mineral phase distributions and ion relationships.

4.2.3 Electron Back-Scattered Diffraction (EBSD)

After TIMA, the sections were re-polished using a Buehler Vibromet II Polisher with 500 nm colloidal silica in a NaOH solution for 4 hours, ensuring a very fine polished surface. Lastly, the samples were carbon coated with ~5 nm thickness in preparation for electron microscopic analysis. Mapping was conducted using electron back-scattered diffraction (EBSD) with the Oxford Instruments Symmetry CMOS detector attached to a Tescan Mira3 VP-FESEM (variable pressure field emission scanning electron microscope) in the John de Laeter Centre, Curtin University. The EBSD technique is commonly used to determine the crystallographic orientation of the mineral grains (e.g., Daly et al., 2019). The analyses were run at 1-2 μm step size (depending on the meteorite), 20 mm working distance and with a 20 kV accelerating voltage. Samples were tilted 70^0 from the normal position for optical kikuchi pattern collection. The data were collected using Oxford Instruments AZtec EDS/EBSD software. Post-processing was done using Oxford Instruments HKL Channel 5.12 software, with the Tango and Mambo modules. Noise reduction was carried out using previously established procedures (e.g., Forman et al., 2019), enabling increased grain identification and determination without generating significant artefacts.

4.2.4 Electron Probe Micro-Analyzer (EPMA)

Quantitative major and minor element geochemistry of individual minerals was determined using a JEOL 8530F Plus electron probe micro-analyser (EPMA) in the Centre of Microscopy, Characterisation and Analysis, University of Western Australia. The data were collected using Probe Software's Probe for EPMA software in the Quant Mapping Mode, using 15 kV accelerating voltage, 40 nA beam current, 40 ms pixel time and with a 2x2 µm pixel size. Both silicate and metal standards were used with standard ZAF corrections applied. Detection limits were <0.01% for Al, Ca, K, Mg, Si and <0.03% for Na, Mn, Si, Cr, Fe and Ti. Post-processing was primarily undertaken using Probe Software's CalcImage. CalcImage enabled user-defined polygon areas (equivalent size to the spot size of µ-FTIR maps) for quant map extraction. Each quant map acquired in excess of 2.5 million individual compositional spot analyses. Even extracting small areas (~100 µm) produces thousands of data points. To ensure accuracy and reliability of the data, quality control filters were essential. These included limiting data to between 98.5% and 101% totals, in addition to filters on individual element abundances, thus avoiding extracting anomalous data. Golden Software's Surfer 16 and WaveMetrics Igor Pro Version 8 programs were utilized for data manipulation and presentation as ternary diagrams.

4.2.5 Micro-Fourier Transform Infrared Spectroscopy (µ-FTIR)

Mid-infrared spectral maps were collected using micro-Fourier transform infrared (µ-FTIR) spectroscopy. The samples were analysed using a Thermo Scientific Nicolet iN10MX infrared imaging microscope at Curtin University. A liquid-nitrogen cooled MCT/A (mercury cadmium telluride) detector was used, operating in the 4000-675 cm^{-1} (5-15 µm) range. The infrared spectra were measured in reflection, which allows effective emissivity to be calculated using Kirchhoff's Law (E = 1 – R) (e.g., Hamilton, 2010). Orbiting satellites and surface rovers measure emissivity when mapping the surface of Mars (e.g., Christensen et al., 2001; Christensen et al., 2004a; Christensen et al., 2004b). Therefore, for direct comparisons to be possible, laboratory data needs to be presented in emissivity (e.g., Hamilton et al., 2003). Effective emissivity is relative and not absolute, therefore explicit quantification comparison between band depths would not be accurate. Mapping was conducted using Thermo Fischer's OMNIC Picta software. Spectra were acquired using 50-100 µm step and spot sizes (sample grain size dependent, 50 µm for basaltic and 100 µm for poikilitic

shergottites), 64 scans, 4 cm^{-1} spectral resolution (2 cm^{-1} sampling). These conditions were determined to produce the smallest step size, best signal to noise, fastest acquisition with the optimal number of scans. A polished gold reflectance standard was used as background, which was analysed once before each map acquisition under the same conditions. Maps generally took ~20 hours (~3300 infrared spectra were measured). Post-processing of the spectral maps relied on CytoSpec® for data validation and the open source Davinci program (http://davinci.asu.edu/) for data manipulation. We used WaveMetrics Igor Pro Version 8 to statistically analyse the pyroxene spectra for critical absorption (see below) wavenumber locations.

4.2.6 Extracting spectra from a thin section

The TIMA qualitative element maps of the samples were used to explore the distribution of, the relationships between, as well as compositional zoning within individual mineral grains (Fig. 4.3). This provided essential context to constraining target mineral grains. As the infrared spectrum of a mineral in thin section is dependent on the crystal orientation, we determined grains that were oriented on or close to a specific crystallographic axis, by using EBSD. Clinopyroxene (both augite and pigeonite) is monoclinic, and has 3 principal axes, <a> {100} and <b> {010} (the short axes), and <c> {001} (the long axis). By combining spectra from grains that are specifically oriented on each of these principal axes, we can create an 'artificial' randomly oriented spectrum (Fig. 4.4) which can then be compared to spectra of randomly oriented particulate minerals, assuming such a sample would not be biased towards any single axis due to crystallographic elongation (e.g., Christensen et al., 2000). To validate this approach, a similar method to Benedix et al. (2016) and Hamilton (2018) was applied. Olivine spectra measured from grains (in NWA 11043) oriented on the three principal axes were averaged, and then compared against terrestrial olivine spectra of similar composition (Fig. 4.5). The Martian olivine spectrum demonstrates clear similarities to the terrestrial olivine. The only observable difference is the shape of band 3 (~915 cm^{-1}), which is similar to differing crystallite size in the sample (Hamilton et al., 2020). Given the relative similarity of the spectra, we are confident in the proposed methodology in measuring randomly oriented spectra from thin sections. Due to the pervasive nature of zoning and exsolution within the pyroxene (primarily in the basaltic shergottites), some of the measured infrared spectra

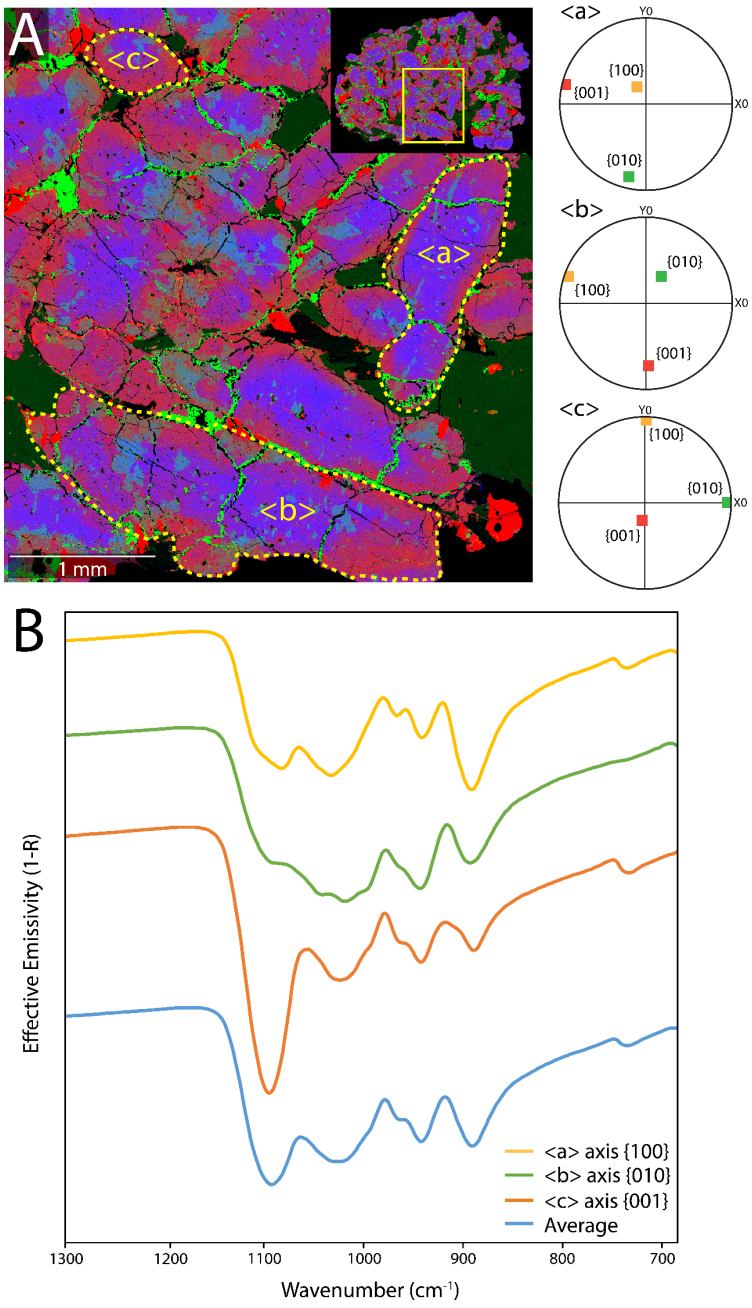

Figure 4.4 *Axis-oriented pigeonite grains from NWA 6963. A: FeCaMg (RGB) of NWA 6963, with specific <a> {100}, <b> {010} and <c> {001} pigeonite grains highlighted with their corresponding pole figures. The pole figures represent the orientation of that specific grain in {100}, {010} and {001}. These grains were chosen due to one particular orientation being proximal to the centre of the pole figure, thereby are oriented on a specific axis. B: Infrared spectra of the axis-oriented pigeonite grains. The <a>, <b> and <c> axis spectra were equally combined to create the 'randomly' oriented average spectrum. Spectra offset for clarity.*

included exsolution lamellae. This potentially could pose a problem, as the whole purpose of this study is to extract the purest pigeonite spectra possible. To mitigate against the possibility that for example, augite lamellae could be included in the pure pigeonite spectra, we can rely on two factors. (1) In the mid-infrared, a spectrum of any area is equal to the linear combination of its constituents (e.g., Ramsey and Christensen, 1998). Therefore, if the area of a measured spectrum comprised of mostly

pigeonite also contains minor augite lamellae, the spectrum will represent that composition. (2) We can depend on this principle to ensure the reliability of the acquired spectra, by utilizing the quantitative element maps acquired with the EPMA. Extracting upwards of a thousand geochemical spot analyses from the same target area of the infrared spectrum provides a means to test the true composition of that spectrum. If the average composition of that area is pigeonite, even containing augite lamellae, we can confidently state that the resulting spectrum will reflect that pigeonite composition. Furthermore, contamination analysis of mixing augite and pigeonite spectra at different abundances show that only at contamination of >20% are band position (minor) changes observable (Fig. 4.6). Due to the nature of augite and pigeonite spectra, <20% contamination only produces relative spectral contrast changes, again minor. To be clear, none of the acquired spectra contained a high level of contamination (<5%). This is to explain that although it would be impossible to acquire 'pure' spectra of either mineral using these rocks, the very minor contamination has no real effect. This was not the case for the poikilitic derived pyroxenes, as they do not contain exsolution. Therefore, by combining a number of advanced microscopic techniques, we can extract mineral, in this case pyroxene, spectra from Martian meteorites non-destructively, with a random orientation and a specific geochemistry.

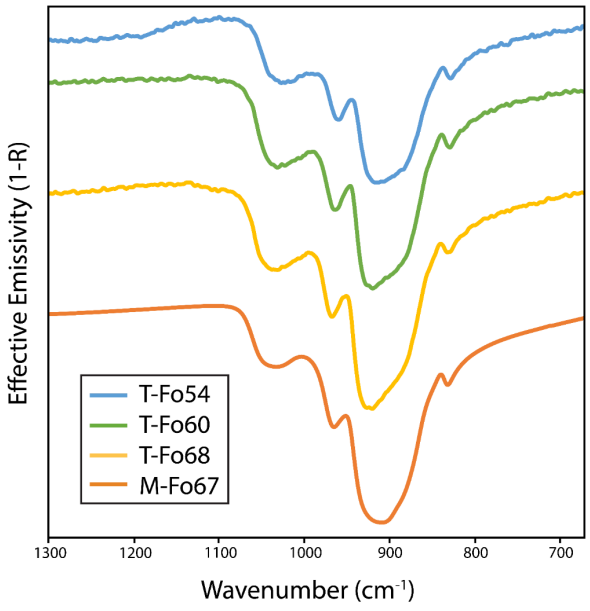

Figure 4.5 *Terrestrial olivine spectra (Hamilton, 2010) compared to a randomly oriented Martian olivine spectrum measured from a thin section (NWA 11043). The Martian spectrum display a similar spectral profile to its terrestrial counterpart, providing a validation for creating a randomly oriented spectrum from a thin section. T = terrestrial. M = Martian. Fo = forsterite content. Spectra offset for clarity.*

Compared to particulate-derived spectra, the polished surfaces of thin sections produce significantly more signal during spectral analysis. This equates to an increase in band depth of the resulting spectra. Particulate-derived spectra tend to have a more subdued band depth and Martian surface spectra even more so. Direct comparisons between these different sample groups are possible because (1) the band centre positions do not change between solid and coarse (>~65-125 µm) particulates and (2) utilizing a blackbody spectrum mitigates these effects (e.g., Hamilton et al., 1997). Used in comparisons or linear deconvolution, blackbody spectra can uniformly reduce or increase spectral contrast across the spectra, in effect, removing spectral contrast differences from the different spectral datasets, thereby allowing for direct comparisons.

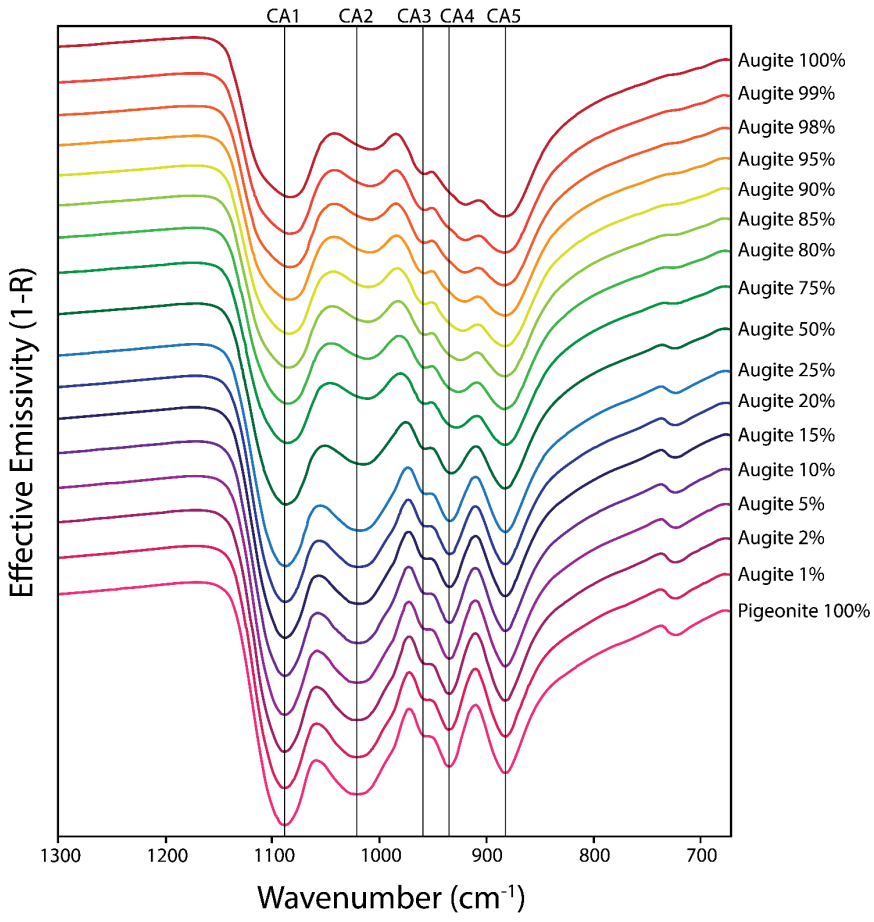

Figure 4.6 *Contamination analysis of pigeonite. Although only the purest areas were analysed with infrared spectroscopy, due to the extensive zoning/lamellae in the shergottites (especially the basaltic shergottites), some contamination of augite may be present. However, only at 20% or greater contamination are there minor observable changes to band centre positions, for example CA2. Below 20%, the spectral shape (and contrast) is the only variable that is experiencing change. Below 10%, there is little observable change. Phase contamination in all the measured spectra is likely below 5%, with the poikilitic shergottite spectra having the least contamination due to their sharp zoning. Compositional variation in the pigeonite is also accounted for through averaging the geochemistry of the infrared spectra spots. The distinct spectral profiles of augite and pigeonite suggest contamination is at a minimum.*

4.3 Results

Pyroxene spectra were extracted from four basaltic and two poikilitic shergottites. These include four augite spectra, six pigeonite spectra and a single pyroxferroite (technically, a pyroxenoid) spectrum (Fig. 4.7). Although pigeonite is structurally a clinopyroxene, it shares spectral characteristics with the orthopyroxenes, which have relatively similar chemistries. To be classified as a pigeonite, the pyroxene must have a Wo value between 5 and 20 wt%. Above 20 wt% Wo, augite is the prevalent phase. The 5 wt% Wo line also marks the assumed structural transformation line from orthorhombic to monoclinic: orthopyroxene (defined by having an orthorhombic crystal system) has the space group Pbca, pigeonite is monoclinic with the space group $P2_1/c$, and clinopyroxene has the space group C2/c. In the mid-infrared, the vibrational frequencies caused by stretching and bending modes of Si-O bonds in the mineral interacting with light determine the resulting infrared spectrum, varying with either/both the composition and structure of the mineral. Given this, these Martian pyroxene spectra display distinct spectral profiles. We also present orientation and geochemical data of the pyroxene spectra and compare these new spectra to examples of terrestrial pyroxene spectra using quantitative band centre analysis.

4.3.1 Crystallographic Orientation

The orientation of a single crystal can have a significant effect on the spectral profile of a mineral (Fig. 4.4). In pyroxene, the <a> and <b> axes are both short axes, while the <c> axis is the long axis of the pyroxene grain. Orientation effects observed are either broadening/shortening or deepening/shallowing of the band minima. The Christiansen Feature (CF) maintains the same wavelength position in all axes. The major differences between the <a> and <b> axes are ~1090 cm^{-1} and ~960 cm^{-1}; along the <b> axis, spectral features are both shallower and band centres more subtle. The band centre ~1020 cm^{-1} is broader in <b> axis than <a> axis spectra. Along the <c> axis, the most significant orientation effect is the deepening and sharpening of the ~1090 cm^{-1} band. This deep band centre (relative to the other spectra) in <c> axis spectra is the most prominent orientation-dependent spectral feature out of all the crystallographically oriented spectra. Although it is important to recognise how different axes can affect infrared spectra, the purpose of this study is to nullify those effects.

4.3.2 Pyroxene Geochemistry

The pyroxene geochemistry reported is that of the specific pyroxenes whose spectra were measured and may not be representative of the whole meteorite. For a more comprehensive description of the geochemistry of shergottites, please see the following references: McCoy et al. (1992); Filiberto et al. (2014); Filiberto et al. (2018); Rahib et al. (2019); Orr et al. (*in review)*.

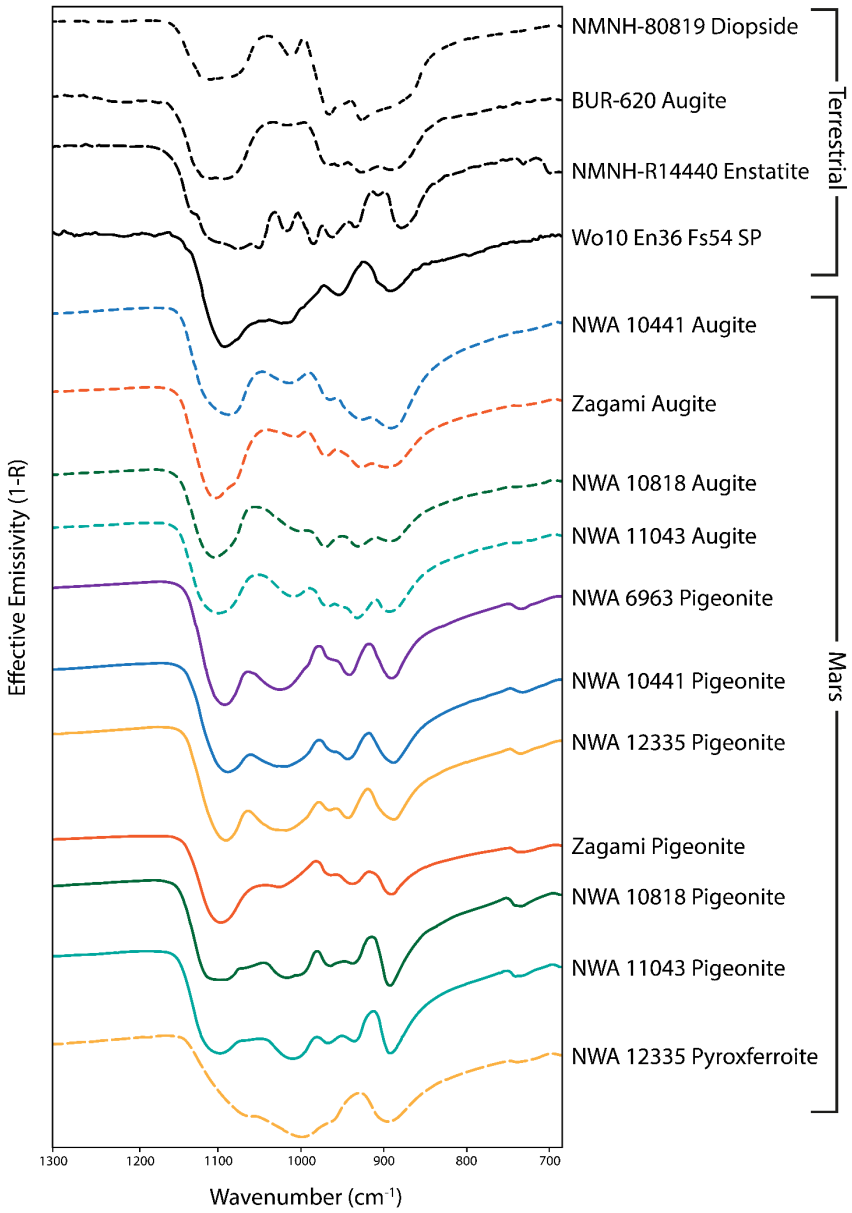

Figure 4.7 *Randomly oriented Martian augite, pigeonite and pyroxferroite spectra from this study compared against those of terrestrial pyroxenes (diopside, augite, enstatite and synthetic pigeonite (SP)). Note the differences in spectral profile between the terrestrial and Martian spectra. Line patterns are matched between mineral types. Terrestrial pyroxene spectra taken from ASU spectral library (Christensen et al., 2000; Hamilton, 2000). Synthetic pigeonite (Wo10En36Fs54 33,34) from Hamilton (2000). Spectra offset for clarity.*

Pyroxene across the basaltic shergottite samples have large geochemical ranges relative to the poikilitic shergottite samples (Tables 4.1-3). The augite spectra were measured from the rims of the pyroxene oikocrysts in both NWA 10818 and NWA 11043, with compositions of Enstatite $(En)_{48-50}$ Wollastonite $(Wo)_{34-36}$ Ferrosilite $(Fs)_{16}$. Similarly, the pigeonite spectra were measured from the cores of the pyroxene oikocrysts of NWA 10818 and NWA 11043 with compositions of En_{63-65} Wo_{9-10} Fs_{24-28}. In contrast, pyroxene zoning in the basaltic shergottites is much more complex. Hence, the range of augite and pigeonite spectra compositions are greater than in the poikilitic shergottites. Only a single pigeonite spectrum was measured from NWA 6963 with an average composition of $En_{47.8\pm4}$ $Wo_{12.4\pm4.1}$ $Fs_{39.8\pm3.4}$. Although augite is present in NWA 6963 (as zones in the pyroxene grains), the augite bearing areas are not large or clearly distinct enough to extract an accurate augite spectrum. NWA 10441 and Zagami contain similar pyroxene zoning, with relatively distinct augite and pigeonite zones. Augite compositions were En_{40-43} Wo_{34} Fs_{22-25}. Pigeonite compositions were $En_{48-55}Wo_{12-15}$ Fs_{33-38}. On the other hand, pyroxene zoning in NWA 12335 is much more complex as augite is intermixed with pigeonite. Therefore, similarly to NWA 6963, no augite spectrum was measured. The pigeonite spectrum extracted has a composition of $En_{41.7\pm5.6}$ $Wo_{16.4\pm3.4}$ $Fs_{41.9\pm3.2}$. In all the basaltic shergottites analysed, the pyroxenes have Fe-rich pigeonite rims. In NWA 12335, the rims and even some whole grains are composed of pyroxferroite (spectrum composition of $En_{4.5\pm1.1}$ $Wo_{16.9\pm2.8}$ $Fs_{78.6\pm3.4}$), so we measured the spectrum of that as well.

Table 4.1 *Major element compositions of pigeonite, from which the infrared spectra were measured.*

Oxide wt%	NWA 6963	*SD*	NWA 10441	*SD*	NWA 10818	*SD*	NWA 11043	*SD*	NWA 12335	*SD*	Zagami	*SD*
SiO_2	49.65	*1.38*	49.97	*1.31*	53.11	*1.61*	52.04	*1.38*	49.92	*1.87*	51.1	*1.56*
TiO_2	0.33	*0.35*	0.29	*0.35*	0.38	*0.37*	0.24	*0.28*	0.31	*0.32*	0.19	*0.25*
Al_2O_3	0.91	*0.98*	0.82	*0.53*	1.03	*0.69*	0.88	*0.57*	0.81	*0.32*	0.79	*0.87*
Cr_2O_3	0.3	*0.25*	0.28	*0.23*	0.37	*0.27*	0.45	*0.29*	0.08	*0.12*	0.36	*0.26*
FeO	23.36	*2*	24.03	*2.54*	17.41	*2.52*	15.94	*1.47*	25.41	*1.84*	19.77	*2.32*
MnO	0.67	*0.32*	0.69	*0.37*	0.72	*0.72*	0.56	*0.28*	0.81	*0.46*	0.64	*0.3*
MgO	15.71	*1.54*	16.65	*1.85*	21.84	*2.73*	23.88	*1.72*	14.17	*2.14*	18.77	*2.13*
CaO	5.67	*1.18*	6.63	*1.54*	4.46	*1.98*	5.31	*1.34*	7.77	*1.63*	5.51	*1.12*
Na_2O	0.46	*0.81*	0.23	*0.47*	0.16	*0.21*	0.25	*0.24*	0.25	*0.27*	0.37	*0.99*
K_2O	0.06	*0.27*	0.05	*0.08*	0.09	*0.14*	0.03	*0.05*	0.05	*0.07*	0.04	*0.23*
Total	97.12	*0.72*	99.62	*0.73*	99.57	*0.7*	99.59	*0.7*	99.58	*0.69*	97.54	*0.73*
Wo	12.39	*4.15*	14.14	*3.17*	9.21	*4.23*	10.42	*2.76*	16.42	*3.45*	11.71	*2.5*
En	47.77	*3.97*	47.5	*4.37*	62.74	*5.53*	65.18	*3.62*	41.67	*5.59*	55.5	*4.17*
Fs	39.84	*3.41*	38.37	*4.46*	28.06	*4.36*	24.41	*2.2*	41.91	*3.16*	32.79	*3.62*

4.3.3 Quantitative Band Centre Analysis

To describe the quantitative variations between the spectra, we adopted the approach used by Hamilton (2000). In that study, identification of critical absorptions (CA) as a proxy for band centres allowed for direct quantitative comparison between the pyroxene spectra. Band centre positions can change based on composition and structure of the mineral, thus providing information on how those factors influence the spectral profile of minerals. In that study, CA classification depended on: (1) the band minima (centres) having a change in emissivity ($\Delta\varepsilon$) >20% of the total spectral contrast of that spectrum, (2) a band being observed in all similar pyroxene spectra and (3) a band being observable at lower spectral resolutions (e.g., at TES resolutions of 10 cm^{-1} and 2 cm^{-1}). Based on these criteria, Hamilton (2000) identified three CAs in the 1300-675 cm^{-1} range for monoclinic pyroxene (clinopyroxene) and four in orthorhombic pyroxene (orthopyroxene). Primarily due to compositional differences (which can lead to different numbers of CAs) we identified five CAs in our Martian augite and pigeonite spectra, and four CAs in pyroxferroite (Table 4.4, Fig. 4.8). By comparing the centre positions of the CAs (five were identified, thus CA1 to CA5) and the Christiansen Feature (CF), where the refractive index of a mineral is close to unity (often observed as emissivity maxima in spectra), we can describe (quantify) the compositional and structural effects on the Martian pyroxene spectra in relation to the terrestrial pyroxene compositions. The purpose of comparing CA positions is to provide context and increase confidence of the validity the Martian pyroxene spectra rather than explain their spectral profiles.

Table 4.2 *Major element compositions of augite, from which the infrared spectra were measured.*

Oxide wt%	NWA 10441	*SD*	NWA 10818	*SD*	NWA 11043	*SD*	Zagami	*SD*
SiO_2	49.79	*1.21*	51.9	*1.69*	50.58	*1.02*	50.83	*1.08*
TiO_2	0.26	*0.29*	0.33	*0.3*	0.29	*0.31*	0.27	*0.29*
Al_2O_3	1.25	*1.13*	1.72	*0.72*	1.49	*0.54*	1.18	*0.39*
Cr_2O_3	0.46	*0.29*	0.82	*0.4*	0.81	*0.42*	0.63	*0.34*
FeO	16.09	*2.82*	10	*1.45*	10.46	*1.47*	13.46	*1.86*
MnO	0.56	*0.48*	0.46	*0.48*	0.41	*0.25*	0.46	*0.27*
MgO	14.09	*1.4*	16.68	*1.26*	18.04	*1.23*	14.59	*1.02*
CaO	16.78	*1.94*	17.37	*1.25*	17.09	*2.37*	16.04	*1.14*
Na_2O	0.39	*0.38*	0.39	*0.31*	0.5	*0.32*	0.71	*0.53*
K_2O	0.05	*0.06*	0.06	*0.1*	0.04	*0.05*	0.03	*0.1*
Total	99.71	*0.72*	99.73	*0.72*	99.7	*0.71*	98.19	*0.71*
Wo	34.28	*4.15*	35.9	*2.44*	33.94	*4.68*	34.24	*2.15*
En	40.06	*3.53*	47.97	*2.27*	49.85	*3.06*	43.32	*2.38*
Fs	25.66	*4.71*	16.13	*2.25*	16.21	*2.22*	22.43	*3.18*

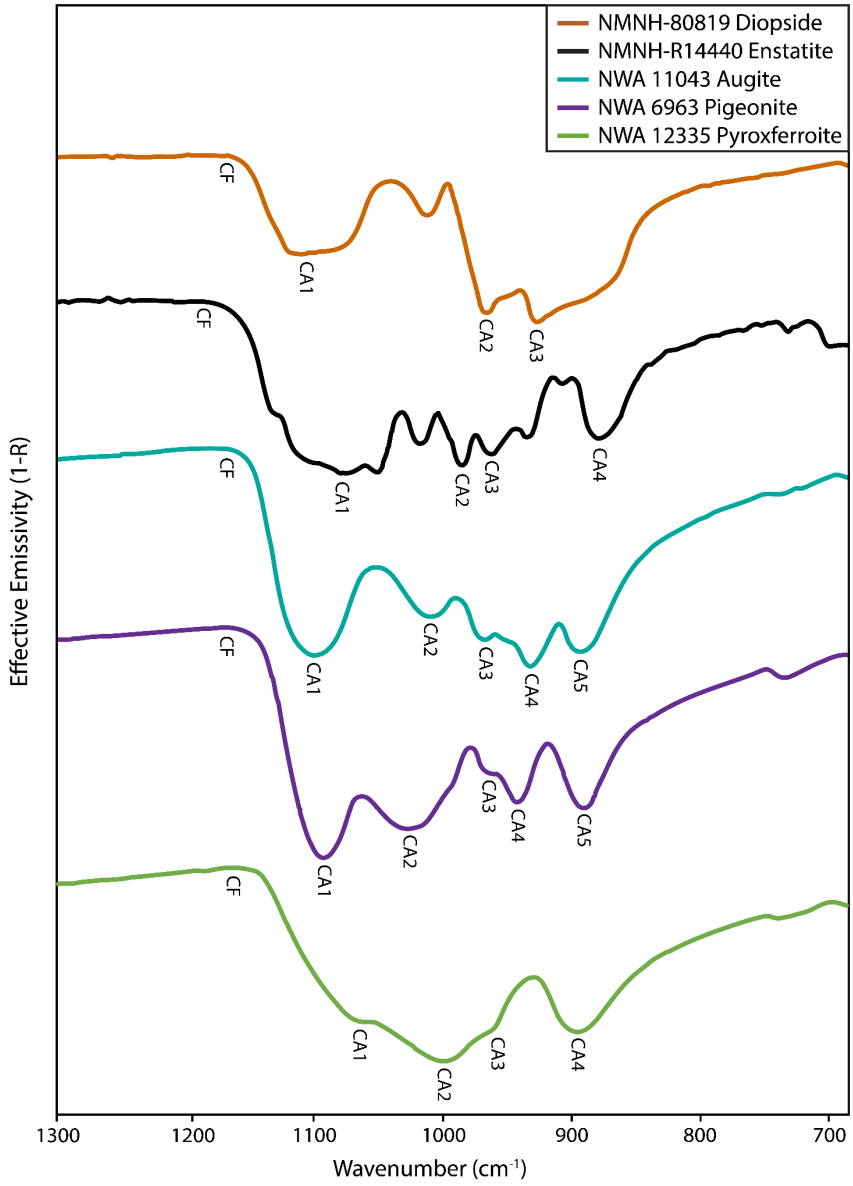

Figure 4.8 *Terrestrial and Martian pyroxene spectra with their Christiansen Feature (CF) and critical absorptions (CA) labelled. CAs for diopside and enstatite taken from Hamilton et al. (2000). Diopside and enstatite spectra taken from ASU spectral library (Christensen et al., 2000; Hamilton, 2000). Spectra offset for clarity.*

4.3.4 Augite and Pigeonite

Figure 4.8 illustrates the locations of the CAs in terrestrial diopside and enstatite (as per their identification in Hamilton et al., 2000) compared to average spectra (simulating measurements of randomly oriented coarse particles) of augite from NWA 11043, pigeonite from NWA 6963 and pyroxferroite from NWA 12335. Broadly, the pigeonite spectrum, being closer in composition to enstatite but similarly monoclinic to diopside, displays CAs that resemble both terrestrial spectra. For example, the CF position in pigeonite (1173 cm^{-1}) is similar to that of diopside (~1170 cm^{-1}), with enstatites CF at ~1190 cm^{-1}. CA1 in pigeonite (1090 cm^{-1}) is similar to CA1 in diopside

(1104 cm^{-1}) but not CA1 in enstatite (1071 cm^{-1}). However, CA5 in pigeonite (883 cm^{-1}) is similar to CA4 in enstatite (872 cm^{-1}) but not CA3 in diopside (920 cm^{-1}). The Martian augite spectra (Fig. 4.8, NWA 11043 Augite) behave overall in a very similar manner as to the pigeonite spectra, relative to terrestrial pyroxene. When the Martian augite spectra are compared solely to the Martian pigeonite spectra, differences start to emerge. The major location differences in terms of CAs are CA2-CA4, with CA1 and CA5 being within 2-3 cm^{-1} of each other. CA2-CA4 are >5 cm^{-1} from each other, with the position of CA2 in the augite and pigeonite spectra displaying the greatest relative difference of 23 cm^{-1}.

4.3.5 Pyroxferroite

The single pyroxferroite spectrum measured in NWA 12335 displays a slightly different spectral profile than that of augite and pigeonite (and the terrestrial pyroxene) (Fig. 4.8)**.** Unlike augite and pigeonite, only four CAs were observed. CA1 at 1059 cn^{-1} is closer in position to CA1 in enstatite 1071 cm^{-1}. Compared to the Martian pyroxene spectra, CA1 and CA3 are present (though subtly), and between ~1100-900 cm^{-1} there is a very broad CA2 (~990 cm^{-1}). Instead of the CA4 observed in augite and pigeonite a broad peak is observed. To make comparisons easier between the Martian pyroxene spectra, pyroxferroite's technical '4th' CA is labelled as CA5, with no CA4 being observed. Unlike the other pyroxenes, pyroxferroite has a broad CA5 at ~887 cm^{-1}.

Table 4.3 *Major element compositions of pyroxferroite, from which the infrared spectra were measured.*

Oxide wt%	Martian NWA 12335	*SD*	Lunar Apollo 11	Terrestrial CS-1329 (2)	HS-325.4B Pyroxmangite	WAR-6894 Pyroxmangite
SiO_2	44.76	*0.93*	46.8	47.47	46.18	45.36
TiO_2	0.35	*0.35*	0.5	-	-	-
Al_2O_3	0.56	*0.61*	0.3	0.27	0.11	0.19
Cr_2O_3	0.05	*0.1*	-	0.31	-	-
FeO	43.86	*1.98*	44.6	32.17	0.11	0.32
MnO	1	*0.37*	0.8	10.81	50.59	51.21
MgO	1.4	*0.34*	0.8	4.04	0.4	0.38
CaO	7.35	*1.29*	6	3.89	1.75	0.92
Na_2O	0.18	*0.23*	tr.	0.35	0.01	-
K_2O	0.04	*0.07*	-	-	0.01	-
Total	99.54	*0.68*	99.8	99.31	99.15	98.38

Apollo 11 sample taken from Chao et al. (1970)

Terrestrial pyroxferroite taken from Shchipalkina et al. (2016)

Both pyroxmangite taken from Christensen et al. (2000).

4.4 Discussion

As this study represents the first time Martian in-situ mineral spectra have been measured for the purpose of interpreting remote sensing data, contextualising these results is imperative to establishing their reliability. By investigating the newly measured thin section pyroxene spectra behaviour in the infrared we can develop our understanding of how they relate to other clino- and orthopyroxenes. Similarly, how pyroxferroite relates to other examples and its solid solution end member pyroxmangite is important to address.

Table 4.4 *Wavenumber positions of the Christiansen Feature (CF) and critical absorptions (CA) in the pyroxene spectra.*

Sample	Pyroxene	Wavenumber (cm^{-1})					
		CF	CA1	CA2	CA3	CA4	CA5
NWA 10441	Augite	1173	1084	1011	958	920	883
NWA 10818	Augite	1176	1101	995	964	922	883
NWA 11043	Augite	1176	1093	1001	962	926	885
Zagami	Augite	1180	1099	1001	962	920	889
NWA 10441	Pigeonite	1173	1086	1016	955	937	881
NWA 10818	Pigeonite	1176	1090	1012	958	930	885
NWA 11043	Pigeonite	1176	1093	1005	960	930	885
NWA 12335	Pigeonite	1167	1086	1014	960	937	879
NWA 6963	Pigeonite	1173	1090	1024	958	935	883
Zagami	Pigeonite	1174	1093	1026	958	931	885
NWA 12335	Pyroxferroite	1159	1059	993	958		887

4.4.1 Band Centre Comparison

We can evaluate the representativeness of the Martian pyroxene spectra, and by extension the methodology we applied in acquiring the spectra, through composition comparisons using CAs (band centres). It is well established that there are trends in spectral band centre positions in pyroxene spectra based on composition (e.g., Hamilton et al., 2000 and references therein; Hamilton, 2003). We can compare the Martian to the terrestrial spectra through CA wavenumber positions based on Mg# (Mg/Mg+Fe) (Fig. 4.9). Mg# is used as we can directly compare the effects of Mg and Fe together, without interference from Ca (largely used to distinguish between phases). Encouragingly, there are some clear and obvious trends in spectral band centres based on composition from the terrestrial orthopyroxene, our low-Ca pigeonite and high-Ca augite all the way to terrestrial clinopyroxene. The CF position of the thin section

pyroxene spectra shifts based on the Fe:Mg ratio. As Fe content increases (and Mg decreases), the CF shifts to lower wavenumbers. CA1 and CA3 display a similar trend. On the other hand, CA2, CA4 and CA5 display an opposite trend, as Mg content increases the band centres shift to lower wavenumbers. Deciphering the true cause of these observable trends is not an easy task. A number of studies have attempted to explain the infrared behaviour (spectral profile) of pyroxenes based on composition and the effect of cation substitution, in M1 and M2 sites, on the tetrahedral-oxygen (T-O) bond character of the mineral (e.g., Hamilton et al., 2000; Hamilton, 2003; Arnold et al., 2014; Lane and Bishop, 2019). The results suggest composition plays a significant role in the spectral character of pyroxene, but establishing predictable patterns is a bit more elusive. However, discerning the impact of cation size and charge on infrared spectra can be challenging to isolate. Although out of the scope of this study, measuring the infrared spectra of crystallographically oriented pyroxene grains (from thin sections) and then comparing their band centre positions based on composition may yield more answers.

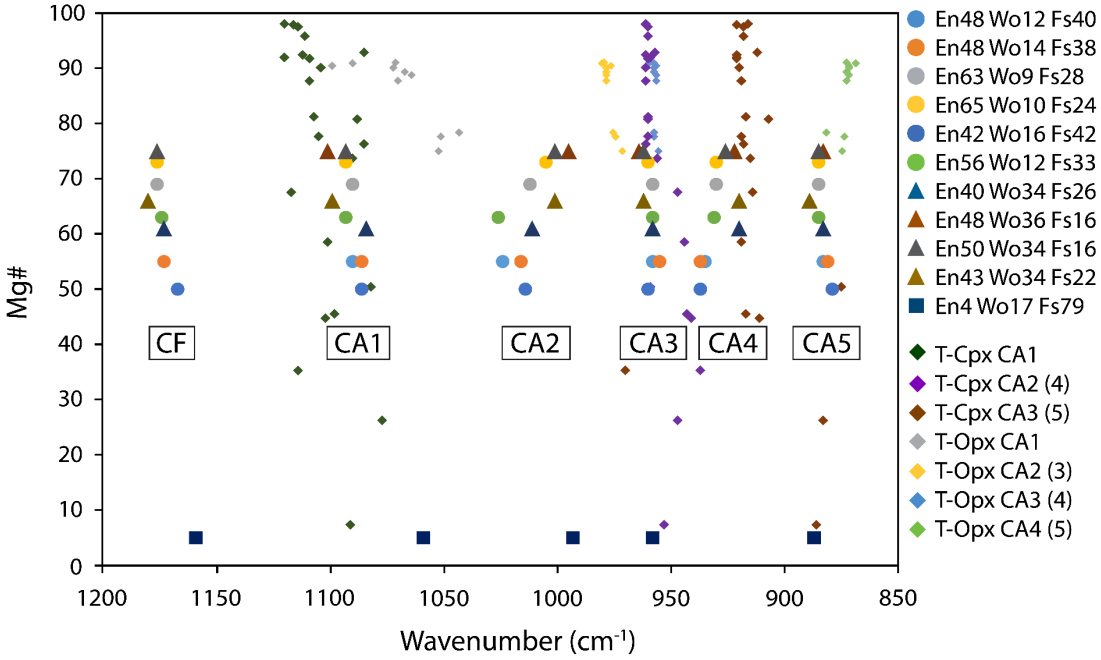

Figure 4.9 *Wavenumber positions of the Christiansen Feature (CF) and critical absorptions (CA) in both terrestrial and Martian pyroxene spectra based on Mg# (Mg/Mg+Fe). Martian spectra: circles = pigeonite, triangles = augite, square = pyroxferroite. T-Cpx = terrestrial clinopyroxene. T-Opx = terrestrial orthopyroxene. The terrestrial pyroxenes are grouped as CA's rather than individual samples. The numbers in brackets are denoting the corresponding Martian CA if different to those identified by Hamilton (2000). Note the slight trends in CA wavelength position based on composition. Includes all available quadrilateral pyroxene spectra taken from the ASU spectral library, with a quality flag of 1 (pure, with no obvious inclusions). See Christensen et al. (2000) for details.*

Overall, we have averaged individual crystallographically oriented pyroxene spectra to create single spectra which effectively mimics the spectrum of randomly oriented

particulate samples. The resulting Martian pyroxene spectra display the expected infrared behaviour as a function of composition, indicating that our overall approach is sound.

4.4.2 Additional Pigeonite Spectral Feature

The spectral features of minerals are the unique qualifiers that are used to identify the minerals in the infrared. In the pigeonite spectra, outside of the CAs previously highlighted, there is an additional spectral feature ~750 cm^{-1}. This feature is a slight decrease in emissivity across ~20 cm^{-1} of the spectral profile of pigeonite. There is also a slight hint of this feature in pyroxferroite, but it is not observed in the augite spectra. Interestingly, it is also observed in synthetic pigeonite spectra (Lindsley et al., 2019). This suggests it is not the result of instrument or atmospheric interference but is a genuine spectral feature of pigeonite. It doesn't, however, seems to be uniformly observed across the major crystallographic orientations. In Figure 4.4, this spectral feature is observed in both the <a> and <c> axis oriented spectra, but not in the <b> axis. In pyroxene the <a> and <b> axes are both short axes. Though why the <b> axis doesn't display the spectral feature and the <a> axis does is not clear. The <c> axis, or long axis, spectrum displays a relatively stronger feature than the <a> axis spectrum. This is more predictable as <c> axis spectra tend to exhibit stronger spectral features. The feature seems to be composition dependent, as it is not observed in the terrestrial clinopyroxene, but is (to a lesser extent) observed in terrestrial orthopyroxene. This suggests Ca (Wo%) content may be responsible. Therefore, higher-Ca content probably decreases the likelihood of the feature being observed, though if it is a gradual or sharp boundary remains unknown. Nevertheless, if observed in an average or bulk spectrum of a rock, this would suggest the presence of pigeonite, or at least low-Ca pyroxene.

4.4.3 Pyroxferroite

Pyroxferroite ($(Fe^{2+},Ca)SiO_3$) is a pyroxenoid (triclinic structure) that exhibits solid solution with pyroxmangite ($MnSiO_3$) (Chao et al., 1970). Pyroxferroite is very rare, reported in only a handful of lunar basalts and Martian shergottites, with only a few terrestrial examples (e.g., McSween et al., 1996; Mancini et al., 2000; Lui et al., 2009; Shchipalkina et al., 2016). It is a late-stage crystallisation mineral formed during rapid

cooling of an Fe-enriched lava, although on Earth it can form in magmatic, metamorphic and metasomatic environments (Lindsley and Burnham, 1970; Shchipalkina et al., 2016). Importantly, the composition of pyroxferroite in the Martian shergottites (and lunar rocks) is different to pyroxferroite found on Earth. Martian and lunar pyroxferroite comprise ~45 wt% FeO compared to ~20-33 wt% FeO (and much higher MnO) in terrestrial samples (Chao et al., 1970; Shchipalkina et al., 2016; Orr et al., in review). This significant compositional difference underscores the necessity for infrared analysis of pyroxferroite. The rarity of pyroxferroite is primarily because it is metastable at low pressure (<10 kbar) and temperature (<1040^{o}C), and therefore likely to break down during cooling (Lindsley and Burnham, 1970). Even in the shergottites, we see evidence of breakdown products. Pyroxferroite-breakdown material (PBM) is a combination of fayalite, ferroan augite and silica, and forms when the lava does not cool fast enough, instigating the breakdown of pyroxferroite (e.g., Warren et al., 2004). In Los Angeles, the modal abundance of PBM is ~10% in stone 1 and 25% in stone 2 (Warren et al., 2004). In NWA 12335, there is limited PBM, but ~20% pyroxferroite (Orr et al., *in* review). Therefore, pyroxferroite and its products represent a significant portion of some shergottites. Based on compositional and structural differences, pyroxferroite exhibits a distinct infrared spectrum compared to quadrilateral pyroxene spectra (Fig. 4.8). Figure 4.10 shows how the pyroxferroite spectrum compares to pyroxmangite spectra from Christensen et al. (2000) with a Martian pigeonite spectrum for reference. The CA4 band in pyroxferroite is the only band consistently observed in all the spectra. The Martian pyroxferroite, being an extremely Fe-rich end member, has a unique spectral profile compared to pyroxmangite. Comparisons to other pyroxene (orthopyroxene and clinopyroxene) may not be suitable given the diverging composition and structure. However, measuring the pyroxferroite spectrum supplements available data with another rare, but relevant, Martian mineral spectrum.

4.5 Conclusions

Measuring Martian pyroxenes in thin section utilizing a number of microscopic techniques has opened up a new, non-destructive approach to calculating infrared spectra having effectively random crystallographic orientation for mineral compositions not previously available. Utilizing TIMA for element mapping, EBSD to identify crystallographically oriented grains and EPMA to acquire equal area

geochemistry to the μ-FTIR spot size enabled us to extract accurate Martian pyroxene spectra. Both basaltic and poikilitic pyroxene spectra were measured, representing the compositional range in the shergottites. Our in-situ augite and pigeonite spectra fill in the compositional gap between available data in the literature and the shergottites, the spectral profiles of which are distinct from the current terrestrial ortho- and clinopyroxene spectra. Our spectra display band centre wavenumber positions that are consistent with known trends in pyroxene spectra as a function of chemistry and structure, indicating the approach is robust. The single pyroxferroite spectrum has a spectral profile distinct from the other pyroxene spectra we analyzed. Although it is not a quadrilateral pyroxene, pyroxferroite is an important mineral in the growing number of Fe-rich basaltic meteorites. Supplementing the currently available pyroxene spectra with shergottite pyroxene compositions should support the evaluation of Martian surface spectra.

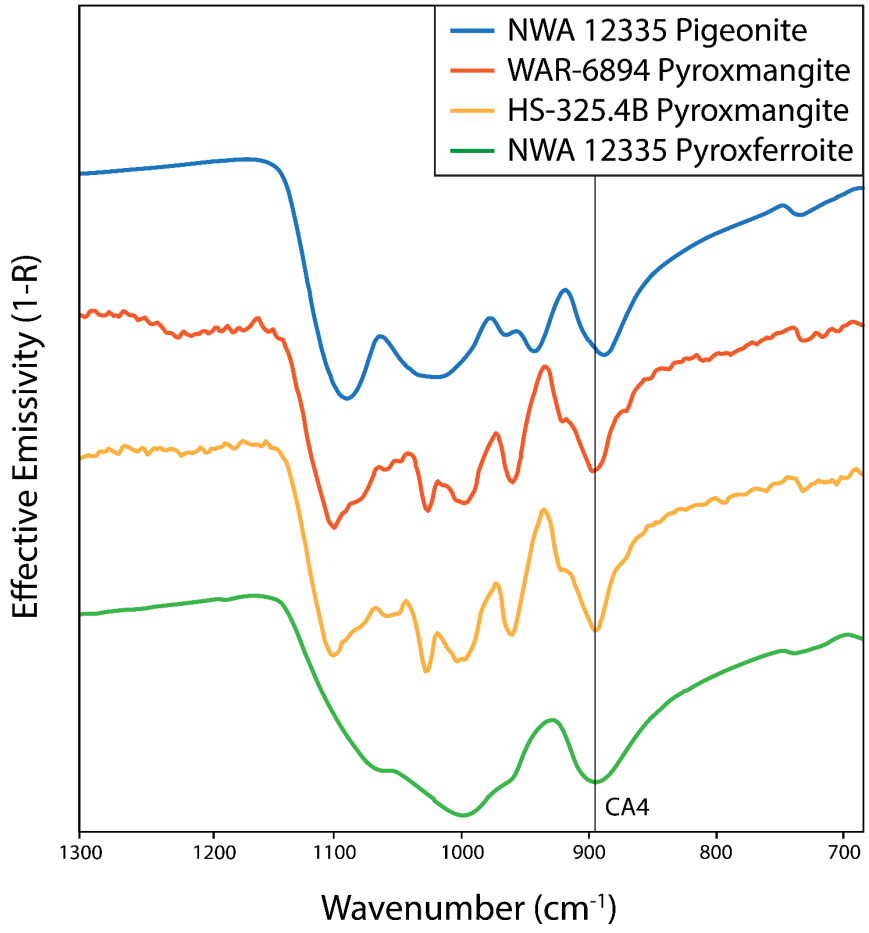

Figure 4.10 *Triclinic pyroxferroite and pyroxmangite spectra with a Martian pigeonite spectrum for reference. Pyroxmangite spectra taken from ASU spectral library (Christensen et al., 2000). The Mn-rich pyroxmangite display distinct spectral profiles compared to the Fe-rich pyroxferroite spectrum. Only the CA4 band centre is consistent through all the spectra. Spectra offset for clarity.*

4.6 References

Arnold, J. A., Glotch, T. D., & Plonka, A. M. (2014). Mid-infrared optical constants of clinopyroxene and orthoclase derived from oriented single-crystal reflectance spectra. *American Mineralogist*, *99*(10), 1942-1955.

Bandfield, J. L., Hamilton, V. E., & Christensen, P. R. (2000). A Global View of Martian Surface Compositions from MGS-TES. *Science*, *287*(5458), 1626–1630. https://doi.org/10.1126/science.287.5458.1626

Bandfield, J. L., Rogers, D., Smith, M. D., & Christensen, P. R. (2004). Atmospheric correction and surface spectral unit mapping using Thermal Emission Imaging System data. *Journal of Geophysical Research: Planets (1991–2012)*, *109*(E10). https://doi.org/10.1029/2004je002289

Baratoux, D., Toplis, M. J., Monnereau, M., & Gasnault, O. (2011). Thermal history of Mars inferred from orbital geochemistry of volcanic provinces. *Nature*, *472*(7343), 338–341. https://doi.org/10.1038/nature09903

Benedix, G. K., Hamilton, V. E. and Reddy, S. M. (2016). μ-FTIR spectroscopy and electron backscatter diffraction of Martian shergottite Robert Massif 04262. *47th Lunar and Planetary Science Conference,* Abs#: 1903.

Bridges, J. C., & Warren, P. H. (2006). The SNC meteorites: basaltic igneous processes on Mars. *Journal of the Geological Society*, *163*(2), 229–251. https://doi.org/10.1144/0016-764904-501

Cassata, W. S., Cohen, B. E., Mark, D. F., Trappitsch, R., Crow, C. A., Wimpenny, J., et al. (2018). Chronology of martian breccia NWA 7034 and the formation of the martian crustal dichotomy. *Science Advances*, *4*(5), eaap8306. https://doi.org/10.1126/sciadv.aap8306

Chao, E. C. T., Minkin, J. A., Frondel, C., Klein, C., Drake, J. C., Fuchs, L., Tani, B., Smith, J. V., Anderson, A. T., Moore, P. B., Zechman, G. R., Traill, R. J., Plant., A.

G., Douglas, J. A. V., Dence, M. R. (1970). Pyroxferroite, a new calcium-bearing iron silicate from Tranquillity Base. *Proceedings of the Apollo 11 Lunar Science Conference, 1,* 65-79.

Chevrel, M. O., Baratoux, D., Hess, K.-U., & Dingwell, D. B. (2014). Viscous flow behavior of tholeiitic and alkaline Fe-rich martian basalts. *Geochimica et Cosmochimica Acta*, *124*, 348–365. https://doi.org/10.1016/j.gca.2013.08.026

Christensen, P. R., Bandfield, J. L., Hamilton, V. E., Howard, D. A., Lane, M. D., Piatek, J. L., et al. (2000). A thermal emission spectral library of rock-forming minerals. *Journal of Geophysical Research: Planets*, *105*(E4), 9735–9739. https://doi.org/10.1029/1998je000624

Christensen, P. R., Mehall, G. L., Silverman, S. H., Anwar, S., Cannon, G., Gorelick, N., et al. (2003). Miniature Thermal Emission Spectrometer for the Mars Exploration Rovers. *Journal of Geophysical Research: Planets (1991–2012)*, *108*(E12). https://doi.org/10.1029/2003je002117

Christensen, P. R., Jakosky, B. M., Kieffer, H. H., Malin, M. C., Jr, H. Y. M., Nealson, K., et al. (2004a). The Thermal Emission Imaging System (THEMIS) for the Mars 2001 Odyssey Mission. *Space Science Reviews*, *110*(1/2), 85–130. https://doi.org/10.1023/b:spac.0000021008.16305.94

Christensen, P. R., Wyatt, M. B., Glotch, T. D., Rogers, A. D., Anwar, S., Arvidson, R. E., et al. (2004b). Mineralogy at Meridiani Planum from the Mini-TES Experiment on the Opportunity Rover. *Science*, *306*(5702), 1733–1739. https://doi.org/10.1126/science.1104909

Christensen, P. R., McSween, H. Y., Bandfield, J. L., Ruff, S. W., Rogers, A. D., Hamilton, V. E., et al. (2005). Evidence for magmatic evolution and diversity on Mars from infrared observations. *Nature*, *436*(7050), 504–509. https://doi.org/10.1038/nature03639

Corrigan, C. M., Velbel, M. A., & Vicenzi, E. P. (2015). Modal abundances of pyroxene, olivine, and mesostasis in nakhlites: Heterogeneity, variation, and implications for nakhlite emplacement. *Meteoritics & Planetary Science*, *50*(9), 1497–1511. https://doi.org/10.1111/maps.12492

Crisp, J. A. (1984). Rates of magma emplacement and volcanic output. *Journal of Volcanology and Geothermal Research*, *20*(3–4), 177–211. https://doi.org/10.1016/0377-0273(84)90039-8

Daly, L., Piazolo, S., Lee, M. R., Griffin, S., Chung, P., Campanale, F., et al. (2019). Understanding the emplacement of Martian volcanic rocks using petrofabrics of the nakhlite meteorites. *Earth and Planetary Science Letters*, *520*, 220–230. https://doi.org/10.1016/j.epsl.2019.05.050

Duncan, M. S., Schmerr, N. C., Bertka, C. M., & Fei, Y. (2018). Extending the Solidus for a Model Iron-Rich Martian Mantle Composition to 25 GPa. *Geophysical Research Letters*, *45*(19), 10,211-10,220. https://doi.org/10.1029/2018gl078182

Ferdous, J., Brandon, A. D., Peslier, A. H., & Pirotte, Z. (2017). Evaluating crustal contributions to enriched shergottites from the petrology, trace elements, and Rb-Sr and Sm-Nd isotope systematics of Northwest Africa 856. *Geochimica et Cosmochimica Acta*, *211*(Science 339 2013), 280–306. https://doi.org/10.1016/j.gca.2017.05.032

McSween, H. Y., Arvidson, R. E., Bell, J. F., Blaney, D., Cabrol, N. A., Christensen, P. R., et al. (2004). Basaltic Rocks Analyzed by the Spirit Rover in Gusev Crater. *Science*, *305*(5685), 842–845. https://doi.org/10.1126/science.3050842

Filiberto, J., Gross, J., Trela, J., & Ferré, E. C. (2014). Gabbroic Shergottite Northwest Africa 6963: An intrusive sample of Mars. *American Mineralogist*, *99*(4), 601–606. https://doi.org/10.2138/am.2014.4638

Filiberto, J., Gross, J., Udry, A., Trela, J., Wittmann, A., Cannon, K. M., et al. (2018). Shergottite Northwest Africa 6963: A Pyroxene-Cumulate Martian Gabbro. *Journal*

of Geophysical Research: Planets, *123*(7), 1823–1841. https://doi.org/10.1029/2018je005635

Forman, L. V., Timms, N. E., Bland, P. A., Daly, L., Benedix, G. K., & Trimby, P. W. (2019). A morphologic and crystallographic comparison of CV chondrite matrices. *Meteoritics & Planetary Science*, *54*(11), 2633–2651. https://doi.org/10.1111/maps.13380

Grott, M., & Breuer, D. (2010). On the spatial variability of the Martian elastic lithosphere thickness: Evidence for mantle plumes? *Journal of Geophysical Research: Planets (1991–2012)*, *115*(E3). https://doi.org/10.1029/2009je003456

Halliday, A. N., Wänke, H., Birck, J.-L., & Clayton, R. N. (2001). The Accretion, Composition and Early Differentiation of Mars. *Space Science Reviews*, *96*(1–4), 197–230. https://doi.org/10.1023/a:1011997206080

Hamilton, V. E., Christensen, P. R., & McSween, H. Y. (1997). Determination of Martian meteorite lithologies and mineralogies using vibrational spectroscopy. *Journal of Geophysical Research: Planets*, *102*(E11), 25593–25603. https://doi.org/10.1029/97je01874

Hamilton, V. E. (2000). Thermal infrared emission spectroscopy of the pyroxene mineral series. *Journal of Geophysical Research: Planets*, *105*(E4), 9701–9716. https://doi.org/10.1029/1999je001112

Hamilton, V. E., Christensen, P. R., McSween, H. Y., & Bandfield, J. L. (2003). Searching for the source regions of martian meteorites using MGS TES: Integrating martian meteorites into the global distribution of igneous materials on Mars. *Meteoritics & Planetary Science*, *38*(6), 871–885. https://doi.org/10.1111/j.1945-5100.2003.tb00284.x

Hamilton, V. E. (2010). Thermal infrared (vibrational) spectroscopy of Mg–Fe olivines: A review and applications to determining the composition of planetary

surfaces. *Chemie Der Erde - Geochemistry*, *70*(1), 7–33. https://doi.org/10.1016/j.chemer.2009.12.005

Hamilton, V. E., & Ruff, S. W. (2012). Distribution and characteristics of Adirondack-class basalt as observed by Mini-TES in Gusev crater, Mars and its possible volcanic source. *Icarus*, *218*(2), 917–949. https://doi.org/10.1016/j.icarus.2012.01.011

Herd, C. D. K., Walton, E. L., Agee, C. B., Muttik, N., Ziegler, K., Shearer, C. K., et al. (2017). The Northwest Africa 8159 martian meteorite: Expanding the martian sample suite to the early Amazonian. *Geochimica et Cosmochimica Acta*, *218*(Science 339 2013), 1–26. https://doi.org/10.1016/j.gca.2017.08.037

Howarth, G. H., Pernet-Fisher, J. F., Balta, J. B., Barry, P. H., Bodnar, R. J., & Taylor, L. A. (2014). Two-stage polybaric formation of the new enriched, pyroxene-oikocrystic, lherzolitic shergottite, NWA 7397. *Meteoritics & Planetary Science*, *49*(10), 1812–1830. https://doi.org/10.1111/maps.12357

Jambon, A., Sautter, V., Barrat, J.-A., Gattacceca, J., Rochette, P., Boudouma, O., et al. (2016). Northwest Africa 5790: Revisiting nakhlite petrogenesis. *Geochimica et Cosmochimica Acta*, *190*(Nature 294 1981), 191–212. https://doi.org/10.1016/j.gca.2016.06.032

Kereszturi, A., & Chatzitheodoridis, E. (2016). Searching for the Source Crater of Nakhlite Meteorites. *Origins of Life and Evolution of Biospheres*, *46*(4), 455–471. https://doi.org/10.1007/s11084-016-9498-x

Kieffer, H. H., Neugebauer, G., Munch, G., Chase, S. C., & Miner, E. (1972). Infrared thermal mapping experiment: The Viking Mars orbiter. *Icarus*, *16*(1), 47–56. https://doi.org/10.1016/0019-1035(72)90136-4

Kieffer, H. H., Chase, S. C., Miner, E. D., Palluconi, F. D., Munch, G., Neugebauer, G., & Martin, T. Z. (1976). Infrared Thermal Mapping of the Martian Surface and Atmosphere: First Results. *Science*, *193*(4255), 780–786. https://doi.org/10.1126/science.193.4255.780

Kieffer, H. H., Martin, T. Z., Peterfreund, A. R., Jakosky, B. M., Miner, E. D., & Palluconi, F. D. (1977). Thermal and albedo mapping of Mars during the Viking primary mission. *Journal of Geophysical Research*, *82*(28), 4249–4291. https://doi.org/10.1029/js082i028p04249

Kiefer, W. S., Filiberto, J., Sandu, C., & Li, Q. (2015). The effects of mantle composition on the peridotite solidus: Implications for the magmatic history of Mars. *Geochimica et Cosmochimica Acta*, *162*, 247–258. https://doi.org/10.1016/j.gca.2015.02.010

Koeppen, W. C., & Hamilton, V. E. (2008). Global distribution, composition, and abundance of olivine on the surface of Mars from thermal infrared data. *Journal of Geophysical Research: Planets (1991–2012)*, *113*(E5). https://doi.org/10.1029/2007je002984

Lagain, A., Benedix, G. K., Servis, K., Baratoux, D., Bland, P. A., Rajšić, A., Devillepoix, H. A. R., Norman, C., Towner, M., Samson, E. K., Anderson, S. (in prep). 90 million craters on Mars: the key to finding the source locations of the meteorites.

Lane, M., & Bishop, J. (2019). Mid-infrared (Thermal) Emission and Reflectance Spectroscopy: Laboratory Spectra of Geologic Materials. In J. Bishop, J. Bell III, & J. Moersch (Eds.), *Remote Compositional Analysis: Techniques for Understanding Spectroscopy, Mineralogy, and Geochemistry of Planetary Surfaces* (Cambridge Planetary Science, pp. 42-67). Cambridge: Cambridge University Press. doi:10.1017/9781316888872.005

Lapen, T. J., Righter, M., Andreasen, R., Irving, A. J., Satkoski, A. M., Beard, B. L., et al. (2017). Two billion years of magmatism recorded from a single Mars meteorite ejection site. *Science Advances*, *3*(2), e1600922. https://doi.org/10.1126/sciadv.1600922

Leroux, H., Devouard, B., Cordier, P., & Guyot, F. (2004). Pyroxene microstructure in the Northwest Africa 856 martian meteorite. *Meteoritics & Planetary Science*, *39*(5), 711–722. https://doi.org/10.1111/j.1945-5100.2004.tb00114.x

Lindsley, D. H., & Burnham, C. W. (1970). Pyroxferroite: Stability and X-ray Crystallography of Synthetic Ca0.15Fe0.85SiO3 Pyroxenoid. *Science*, *168*(3929), 364–367. https://doi.org/10.1126/science.168.3929.364

Lindsley, D. H. (1983). Pyroxene thermometry. *American Mineralogist, 68*(5-6), 477-493.

Lindsley, D. H., Nekvasil, H., & Glotch, T. D. (2019). Synthesis of pigeonites for spectroscopic studies. *American Mineralogist*, *104*(4), 615–618. https://doi.org/10.2138/am-2019-6869ccbyncnd

Liu, Y., Floss, C., Day, J. M. D., Hill, E., & Taylor, L. A. (2009). Petrogenesis of lunar mare basalt meteorite Miller Range 05035. *Meteoritics & Planetary Science*, *44*(2), 261–284. https://doi.org/10.1111/j.1945-5100.2009.tb00733.x

Mancini, F., Alviola, R., Marshall, B., Satoh, H., & Papunen, H. (2000). THE MANGANESE SILICATE ROCKS OF THE EARLY PROTEROZOIC VITTINKI GROUP, SOUTHWESTERN FINLAND: METAMORPHIC GRADE AND GENETIC INTERPRETATIONS. *The Canadian Mineralogist*, *38*(5), 1103–1124. https://doi.org/10.2113/gscanmin.38.5.1103

McCoy, T. J., Taylor, G. J., & Keil, K. (1992). Zagami: Product of a two-stage magmatic history. *Geochimica et Cosmochimica Acta*, *56*(9), 3571–3582. https://doi.org/10.1016/0016-7037(92)90400-d

McDonough, W. F., & Sun, S. (1995). The composition of the Earth. *Chemical Geology*, *120*(3–4), 223–253. https://doi.org/10.1016/0009-2541(94)00140-4

McSween, H. Y., Eisenhour, D. D., Taylor, L. A., Wadhwa, M., & Crozaz, G. (1996). QUE94201 shergottite: Crystallization of a Martian basaltic magma. *Geochimica et*

Cosmochimica Acta, *60*(22), 4563–4569. https://doi.org/10.1016/s0016-7037(96)00265-7

McSween, H. Y., Arvidson, R. E., Bell, J. F., Blaney, D., Cabrol, N. A., Christensen, P. R., et al. (2004). Basaltic Rocks Analyzed by the Spirit Rover in Gusev Crater. *Science*, *305*(5685), 842–845. https://doi.org/10.1126/science.3050842

Milam, K. A., McSween, H. Y., Hamilton, V. E., Moersch, J. M., & Christensen, P. R. (2004). Accuracy of plagioclase compositions from laboratory and Mars spacecraft thermal emission spectra. *Journal of Geophysical Research: Planets (1991–2012)*, *109*(E4). https://doi.org/10.1029/2003je002097

Mittlefehldt, D. W. (1994). ALH84001, a cumulate orthopyroxenite member of the martian meteorite clan. *Meteoritics*, *29*(2), 214–221. https://doi.org/10.1111/j.1945-5100.1994.tb00673.x

Morlok, A., Bischoff, A., Patzek, M., Sohn, M., & Hiesinger, H. (2017). Chelyabinsk – a rock with many different (stony) faces: An infrared study. *Icarus*, *284*(Remote Sens. Environ. 113 2009), 431–442. https://doi.org/10.1016/j.icarus.2016.11.030

Ody, A., Poulet, F., Quantin, C., Bibring, J.-P., Bishop, J. L., & Dyar, M. D. (2015). Candidates source regions of martian meteorites as identified by OMEGA/MEx. *Icarus*, *258*, 366–383. https://doi.org/10.1016/j.icarus.2015.05.019

Orr, K. J., Forman, L. V., Rankenburg, K., Evans, N. J., McDonald, B. J., Godel, B., Benedix. G. K. (in review). Geochemical, Mineralogical and Spectral Classification of Four New Shergottites. *Meteoritics and Planetary Science.*

Phillips, R. J., Zuber, M. T., Smrekar, S. E., Mellon, M. T., Head, J. W., Tanaka, K. L., et al. (2008). Mars North Polar Deposits: Stratigraphy, Age, and Geodynamical Response. *Science*, *320*(5880), 1182–1185. https://doi.org/10.1126/science.1157546

Rahib, R. R., Udry, A., Howarth, G. H., Gross, J., Paquet, M., Combs, L. M., et al. (2019). Mantle source to near-surface emplacement of enriched and intermediate

poikilitic shergottites in Mars. *Geochimica et Cosmochimica Acta*, *266*, 463–496. https://doi.org/10.1016/j.gca.2019.07.034

Ramsey, M. S., & Christensen, P. R. (1998). Mineral abundance determination: Quantitative deconvolution of thermal emission spectra. *Journal of Geophysical Research: Solid Earth*, *103*(B1), 577–596. https://doi.org/10.1029/97jb02784

Rogers, A. D., Christensen, P. R., & Bandfield, J. L. (2005). Compositional heterogeneity of the ancient Martian crust: Analysis of Ares Vallis bedrock with THEMIS and TES data. *Journal of Geophysical Research: Planets (1991–2012)*, *110*(E5). https://doi.org/10.1029/2005je002399

Rogers, A. D., Bandfield, J. L., & Christensen, P. R. (2007). Global spectral classification of Martian low-albedo regions with Mars Global Surveyor Thermal Emission Spectrometer (MGS-TES) data. *Journal of Geophysical Research: Planets (1991–2012)*, *112*(E2). https://doi.org/10.1029/2006je002726

Rogers, A. D., & Aharonson, O. (2008). Mineralogical composition of sands in Meridiani Planum determined from Mars Exploration Rover data and comparison to orbital measurements. *Journal of Geophysical Research: Planets (1991–2012)*, *113*(E6). https://doi.org/10.1029/2007je002995

Rogers, A. D., & Bandfield, J. L. (2009). Mineralogical characterization of Mars Science Laboratory candidate landing sites from THEMIS and TES data. *Icarus*, *203*(2), 437–453. https://doi.org/10.1016/j.icarus.2009.04.020

Ruggiu, L. K., Gattacceca, J., Devouard, B., Udry, A., Debaille, V., Rochette, P., et al. (2020). Caleta el Cobre 022 Martian meteorite: Increasing nakhlite diversity. *Meteoritics & Planetary Science*. https://doi.org/10.1111/maps.13534

Salisbury, J. W., D'Aria, D. M., & Jarosewich, E. (1991). Midinfrared (2.5–13.5 μm) reflectance spectra of powdered stony meteorites. *Icarus*, *92*(2), 280–297. https://doi.org/10.1016/0019-1035(91)90052-u

Santos, A. R., Agee, C. B., McCubbin, F. M., Shearer, C. K., Burger, P. V., Tartèse, R., & Anand, M. (2015). Petrology of igneous clasts in Northwest Africa 7034: Implications for the petrologic diversity of the martian crust. *Geochimica et Cosmochimica Acta*, *157*(Science 339 2013), 56–85. https://doi.org/10.1016/j.gca.2015.02.023

Shchipalkina, N. V., Aksenov, S. M., Chukanov, N. V., Pekov, I. V., Rastsvetaeva, R. K., Schäfer, C., et al. (2016). Pyroxenoids of pyroxmangite–pyroxferroite series from xenoliths of Bellerberg paleovolcano (Eifel, Germany): Chemical variations and specific features of cation distribution. *Crystallography Reports*, *61*(6), 931–939. https://doi.org/10.1134/s1063774516060146

Smith, M. D., Bandfield, J. L., & Christensen, P. R. (2000). Separation of atmospheric and surface spectral features in Mars Global Surveyor Thermal Emission Spectrometer (TES) spectra. *Journal of Geophysical Research: Planets*, *105*(E4), 9589–9607. https://doi.org/10.1029/1999je001105

Tornabene, L. L., Moersch, J. E., McSween, H. Y., Hamilton, V. E., Piatek, J. L., & Christensen, P. R. (2008). Surface and crater-exposed lithologic units of the Isidis Basin as mapped by coanalysis of THEMIS and TES derived data products. *Journal of Geophysical Research: Planets (1991–2012)*, *113*(E10). https://doi.org/10.1029/2007je002988

Usui, T., Sanborn, M., Wadhwa, M., & McSween, H. Y. (2010). Petrology and trace element geochemistry of Robert Massif 04261 and 04262 meteorites, the first examples of geochemically enriched lherzolitic shergottites. *Geochimica et Cosmochimica Acta*, *74*(24), 7283–7306. https://doi.org/10.1016/j.gca.2010.09.010

Wänke, H., & Dreibus, G. (1994). Chemistry and accretion history of Mars. *Philosophical Transactions of the Royal Society of London. Series A: Physical and Engineering Sciences*, *349*(1690), 285–293. https://doi.org/10.1098/rsta.1994.0132

Warren, P. H., Greenwood, J. P., & Rubin, A. E. (2004). Los Angeles: A tale of two

stones. *Meteoritics & Planetary Science*, *39*(1), 137–156. https://doi.org/10.1111/j.1945-5100.2004.tb00054.x

Wilson, L., Mouginis-Mark, P. J., Tyson, S., Mackown, J., & Garbeil, H. (2009). Fissure eruptions in Tharsis, Mars: Implications for eruption conditions and magma sources. *Journal of Volcanology and Geothermal Research*, *185*(1–2), 28–46. https://doi.org/10.1016/j.jvolgeores.2009.03.006

Yoshizaki, T., & McDonough, W. F. (2020). The composition of Mars. *Geochimica et Cosmochimica Acta*, *273*, 137–162. https://doi.org/10.1016/j.gca.2020.01.011

Chapter 5: Linear Modelling of Basaltic Shergottites using Martian Composition-Specific Mineral Spectra

5.1 Introduction

A cornerstone of space exploration is the use of infrared spectroscopy to determine the physical characteristics and surface composition of planetary bodies (e.g., Bandfield et al., 2000; Christensen et al., 2000b, 2001, 2003a, 2003b; Hamilton et al., 2001, 2003; Bandfield et al., 2002; Rogers et al., 2007; Koeppen and Hamilton, 2008; Tornabene et al., 2008; Pan et al., 2015). Infrared spectroscopy can be split up into two types of spectrometers, near-infrared (0.7 to 3.0 μm wavelengths), used largely for locating hydrated minerals and can also be used for silicate minerals (Hunt, 1977; Aines and Rossman, 1984; Murchie et al., 2007; Poulet et a., 2007; Mustard et al., 2008; Carter et al., 2013), and mid-infrared (MIR), used to determine silicate modal mineralogy of geological units (e.g., Vincent et al., 1975; Bandfield et al., 2002; Rogers et al., 2007b). Across the mid-infrared wavelengths (5-50μm), the bulk spectrum of a rock or surface, is a linear combination of the constituent components in proportion to their abundance (e.g., Thomson and Salisbury, 1993). This allows a determination of the modal mineralogy of a bulk spectrum (an averaged spectrum of an area) (Ramsey and Christensen, 1998; Rogers and Aharonson, 2008). To accurately determine the mineralogy of a bulk spectrum, one commonly applied method is to linearly model the spectrum using a well-characterised spectral library. This spectral library should, as closely as possible, resemble the true mineralogical makeup of that bulk spectrum, as the resulting modal mineralogy will only be as good as the end-member library used to determine it. This is significant for determining the geology of Mars, especially when attempting to locate areas on the surface that are similar to the mineralogy of the shergottites (or other meteorites we know come from Mars). Traditional techniques (though not always), when measuring spectral end-members, use a large enough sample of a single mineral composition to crush into smaller particles (e.g., Christensen et al., 2000a; Johnson et al., 2002; Johnson et al., 2003). Particulate samples are desirable as calibration points because of the randomly oriented particles, which better mimic a planetary surface. Crystallographically oriented crystals have specific spectral patterns and geologically, it is more likely that crystals generally settle in a random manner. Analysing mineral particulates in this way has proved successful

in producing a wide range of mineral spectra to be used in linear modelling (e.g., Christensen et al., 2000).

The shergottites, the most abundant group of Martian meteorites (representing more than 90% of the ~150 unique specimens), are ultramafic to mafic basaltic rocks that crystallised as intrusive magma or as extrusive lava (Udry et al., 2020 and references therein). The major mineralogy of the shergottites is similar to terrestrial ultramafic to mafic rocks, comprised of olivine, plagioclase and pyroxene (e.g., Goodrich, 2002; McSween et al., 1996; Bridges and Warren, 2006; Gross et al., 2011; Filiberto et al., 2018; Rahib et al., 2019). However, many of the pyroxene compositions of the shergottites are rare in terrestrial lithologies. Pyroxene is a solid solution series mineral, therefore not only is the final composition based on the composition of the parental melt, but it is dependent on temperature and pressure. Shergottites are predominantly composed of pigeonite (and inter-end member augite), a rare high temperature pyroxene which only remains stable in rapidly cooling magma (Lindsley, 1983; Lindsley and Anderson, 1983; Bertka and Holloway, 1993). Typical abundances in the basaltic shergottites of pigeonite and augite range from 15-60% and 13-55%, respectively (Table 5.1). Total pyroxene is generally over 60% of the meteorite. On Earth, magma tends to cool too slowly to retain stable pigeonite, therefore pigeonite commonly inverts into orthopyroxene with lamellae of augite. In the shergottites, rapid cooling has preserved pigeonite, but typically the pigeonite is complexly zoned with augite and/or contains augite lamellae (e.g., Jambon et al., 2002; Leroux et al., 2004; Warren et al., 2004; Orr et al., submitted). Due to these zoning issues, both in terrestrial and Martian samples, only synthetic pigeonite (in particulate form) has been used to deconvolve Martian surface and meteorite spectra to date (e.g., Hamilton et al., 2000; Rogers et al., 2007; Hamilton, 2010). Synthetic samples are a useful addition to spectral libraries, but the pigeonites produced so far do not fully represent the range of shergottite compositions (Lindsley et al., 2019). To resolve the lack of representative Martian pyroxene compositional spectra, Orr et al. (in prep, Part 1) extracted more than 10 pyroxene (augite, pigeonite and a single pyroxferroite) spectra, measured from shergottite thin sections (both basaltic and poikilitic shergottites). Using a high-resolution, non-destructive methodology, these Martian pyroxene spectra were acquired with both a random orientation and a known geochemistry. The purpose of this study is to use these Martian mineral spectra to linearly model Martian meteorite

spectra, as a means of validating their applicability and determining whether they produce statistically better results than available pyroxene spectra.

Previous studies (e.g., Hamilton et al., 1997; Hamilton, 2010) linearly modelled Martian meteorite spectra using terrestrial minerals with mixed success at reproducing the measured bulk. Hamilton (2010) improved on the earlier modelling by using a much-expanded mineral spectral library. This included a wide range of olivine compositions, that were more representative of Martian meteorite compositions, and a single synthetic pigeonite spectrum (Hamilton, 2000). Using a 75-strong mineral spectral library, Hamilton (2010) modelled a range of olivine- and pyroxene-bearing Martian meteorites, demonstrating better matches between the modelled and measured mineral abundances of the meteorites. In this paper, we demonstrate that even better model results are achieved with a more complete representation of pyroxene, focussing on pigeonite. This is particularly relevant to the basaltic shergottites because their major mineralogy is maskelynite and pyroxene.

5.2 Samples and Methods

To cover the range and diversity of compositions in these rocks, we modelled nine basaltic shergottites in this study. The Institute of Meteoritics at the University of New Mexico supplied 0.5g chips of the following samples: Los Angeles, Northwest Africa (NWA) 856, NWA 6963, NWA 10068, NWA 10441, NWA 12335 and Zagami. NIPR (National Institute of Polar Research) supplied <0.2g chips of the following samples: Yamato- (Y) 002192 and Y-002712. All the chips were cut and made into thin-sections and/or 1-inch round thick sections. These were polished and coated with carbon (~2 nm thickness) for modal mineralogical and crystallographic analyses that are described in Orr et al. (*in prep*, Part 1). Here we present the details of modal mineralogy measurement along with bulk spectral analysis.

5.2.1 Basaltic Shergottites

The shergottites can be subdivided based on their mineralogy and texture into three broad groups: basaltic, olivine-phyric and poikilitic (Fig. 5.1). We will focus on basaltic shergottites in this study. This group is mafic in composition, comprising extensively zoned pyroxene (augite, pigeonite and in some cases pyroxferroite) and

maskelynite with a number of minor accessory phases. They can be further split based upon texture. The fine-grained basaltic shergottites (NWA 856, NWA 10068, and Zagami) contain euhedral pyroxene and maskelynite grains, with more clearly defined geochemical zoning in the pyroxene (McCoy et al., 1992; Jambon et al., 2002; He et al., 2015). The diabasic basaltic shergottites (NWA 10441, NWA 12335, and Los Angeles) comprise more anhedral grains with complexly zoned pyroxene and in some cases, contain pyroxferroite (Fe-rich triclinic pyroxenoid) (Warren et al., 2004; Howarth et al., 2018; Orr et al., submitted). Unlike the other diabasic shergottites, Y-002192 and Y-002712 are predominantly composed of augite (Mikouchi and Takenouchi, 2016). The fine-grained and diabasic groups are not mutually exclusive, rather representing slight shifts in composition and texture. On the other hand, the gabbroic basaltic shergottites, of which we have one sample, NWA 6963, are a distinct group, comprised of sub–anhedral pyroxene (predominantly pigeonite with minor augite) and maskelynite (Filiberto et al., 2018). Unlike the other groups, these gabbroic meteorites are defined by their plutonic texture. Accessory minerals in the basaltic shergottites include magnetite, pyrrhotite, phosphates, silica, and ilmenite.

5.2.2 Tescan Integrated Mineral Analyser (TIMA)

For modal abundance determination, we analyzed the samples with a Tescan Integrated Mineral Analyser (TIMA) at the John de Laeter Centre, Curtin University. With four EDS (Energy Dispersive) X-ray detectors, the TIMA is a specifically designed scanning electron microscope (SEM) that maps the elemental composition of the samples. Analysis produces phase and individual element maps of the samples. Map acquisition used the ‘high resolution’ mode which indicates a specific analytical set up of a 3 μm spot and step size, 15 mm working distance and at 25 kV accelerating voltage. We post-processed the data using the TIMA software to extract element maps, from which we created RGB (red-green-blue) images using Adobe Photoshop. Our calculation of modal abundances utilized the pixel counting technique in Adobe Photoshop (references and details in Orr et al., submitted; Table 5.1).

In the basaltic shergottites, pyroxenes are complexly zoned, and in some of the meteorites, micron-scale augite-pigeonite exsolution lamellae are dominant; these appear as brown pixels (mixtures) in our RGB maps because they are smaller than our TIMA measurement step size of 3 μm (Fig. 5.2). Although pixel counting is generally

an effective approach to determining mineral modes, resolutions counted in nanometres are required to map features such as exsolution lamellae. Given this condition, when determining the modal abundance of these rocks, we assigned the brown pixels to augite. Sources of error in this method of analysis is primarily related to the ability to positively identify minerals based on the RGB combinations. Due to the complex nature of the augite/pigeonite exsolution intergrowths, the exact proportions of these minerals are difficult to extract.

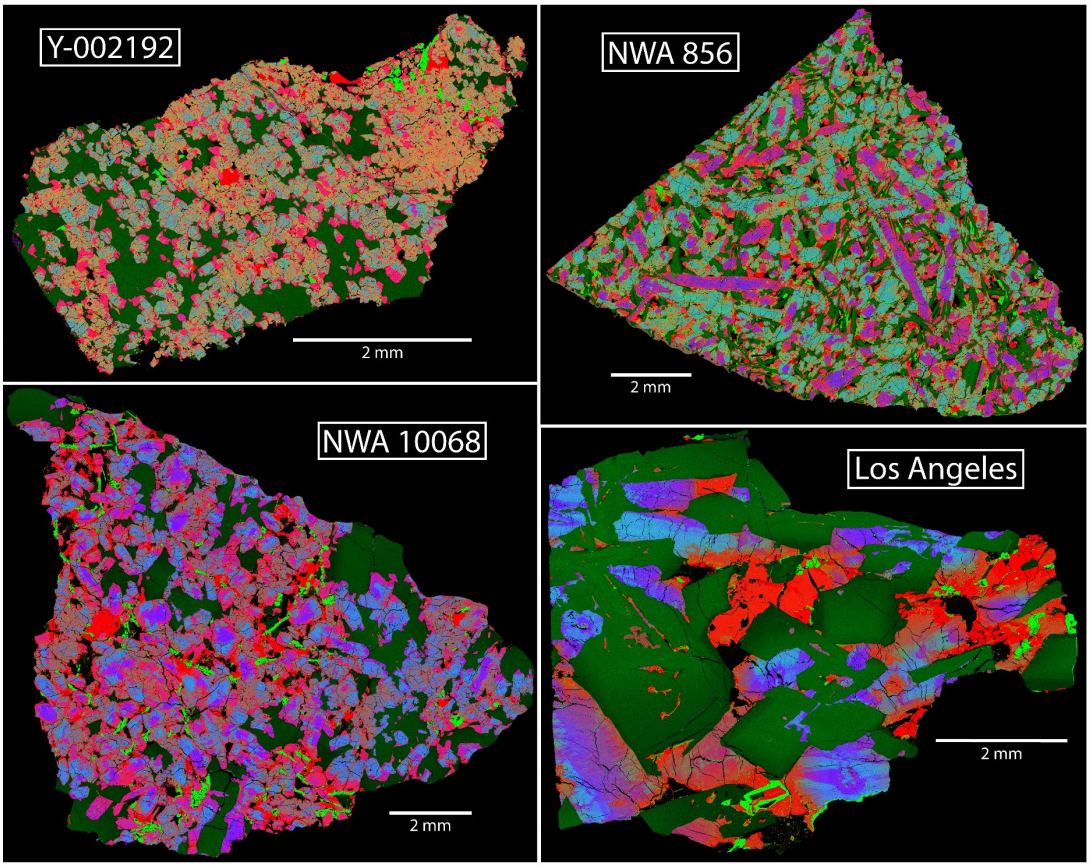

Figure 5.1 *Elemental distribution maps of some of the basaltic shergottites in this study. Fe = red, Ca = green, Mg = blue. Pigeonite = red-purple-blue, augite = light blue-green, maskelynite = dark green. For similar maps of NWA 6963, NWA 10441, NWA 12335 and Zagami please see Orr et al. (in prep). As mostly composed of pyroxene and maskelynite, these rocks are largely different based on texture and geochemical zoning in pyroxene. The zoning can be relatively distinct in NWA 856, to complex in Los Angeles.*

5.2.3 Micro-Fourier Transform Infrared Spectroscopy (µ-FTIR)

To acquire bulk mid-infrared spectra, we measured the Martian meteorites using micro-Fourier Transform Infrared Spectroscopy (µ-FTIR). We used a Thermo Scientific Nicolet iN10MX infrared imaging microscope at Curtin University with a liquid-nitrogen cooled MCT/A (Mercury Cadmium Telluride) detector, operating over the 5-15 µm (4000-675 cm^{-1}) wavelength range. Data acquisition used on Thermo

Fisher's OMNIC Picta software with analytical conditions of 400 µm step and spot sizes, 2 scans with 4 cm^{-1} spectral resolution. Background signal was calibrated using a polished gold reflectance standard, which was measured occurred before every analysis under the same acquisition parameters. The open source Davinci program (http://davinci.asu.edu) was used for post processing spectral analysis and deconvolution (see below). Averaging all the spectra from each sample map is equal to the bulk spectrum of that sample (Hanna et al., 2020; Hamilton et al., 2021).

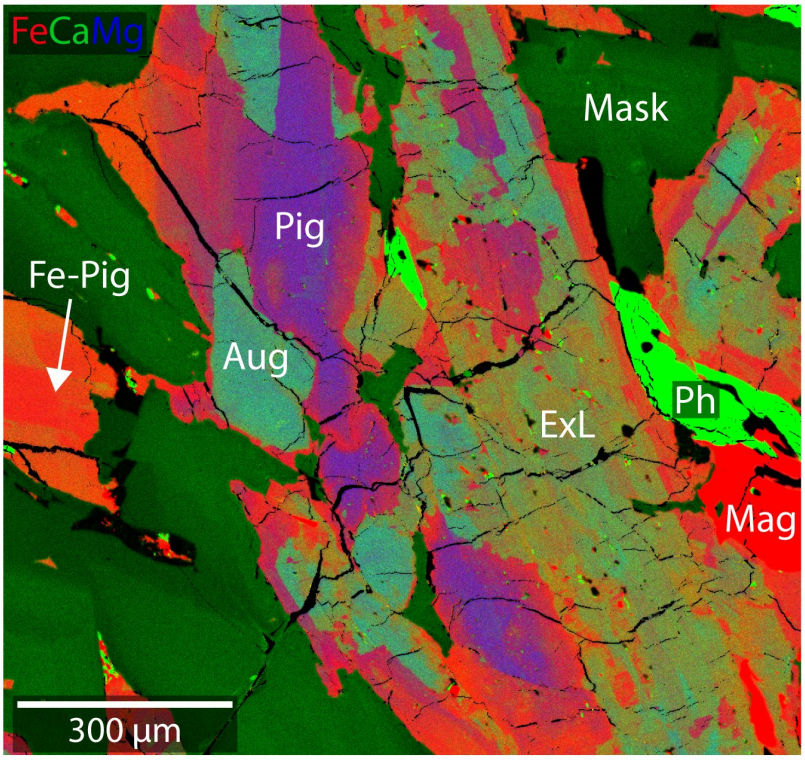

Figure 5.2 *Elemental distribution map of a small area in NWA 10441. Fe = red, Ca = green, Mg = blue. Complex geochemical zoning between augite and pigeonite (and Fe-rich pigeonite) can be observed. The mottled brown regions are comprised of exsolution lamellae of augite and pigeonite. The lamellae are generally too small to pick out for modal abundance determination. In the case for these meteorites, the exsolution lamellae regions appear to be geochemically in the middle of augite and pigeonite, in the forbidden zone of the pyroxene quadrangle. Mineralogy: Aug = augite, ExL = exsolution lamellae, Mag = magnetite, Mask = maskelynite, Ph = phosphate, Pig = pigeonite, Fe-Pig = Fe-rich pigeonite.*

Along with the various other measurements, orbiting satellites and rovers examining Mars measure the emissivity (e.g., Christensen et al., 2001) of the surface. A commonly used spectral library for the analysis of Martian remote sensing data contains emissivity spectra (e.g., Christensen et al., 2000a) of terrestrial rocks and minerals. To allow for direct comparisons between those data and our reflectance measurements, we must convert our spectra to emissivity. Measurement of laboratory spectra used bi-directional reflection, which using Kirchhoff's Law (Emissivity = 1 –

Reflection) allows for 'effective emissivity' to be calculated (e.g., Hamilton, 2010). Effective emissivity will be treated as equal to emissivity with an additional caveat. Due to greater signal from the polished surfaces of the samples, a blackbody spectrum will be used to mitigate against any disparity in spectral contrast. A blackbody spectrum is equal to unit emissivity at all wavelengths and, thus, will uniformly moderate any contrast differences automatically during the deconvolution analysis in Davinci, allowing for accurate comparisons between differently 'sourced' infrared spectra (e.g., Hamilton et al.., 1997; 2003).

5.2.4 Linear Modelling

In the mid infrared wavelength range (5-50 μm), for particle sizes >65 μm, the spectrum of an area (or rock) is the linear combination of its constituents (minerals), proportional to their relative areal abundances. With similar sized particulate spectral end members, this linearity can continue down to 10-20 μm particle sizes (Ramsey and Christensen, 1998). By using this principle, we can apply a deconvolution algorithm to a bulk spectrum, in this case a Martian meteorite, to unravel its mineralogy using a spectral library of known end members (e.g., Hamilton et al., 1997). We have used the non-negative least squares algorithm (NNLS) (Rogers and Aharonson, 2008), which takes as inputs the library and target spectra, and returns a modelled bulk spectrum, including the uncertainty on each end member.

End member selection is the most important step in linear modelling, as the result will only be as good as the end member input. In this study, we know the composition of the target meteorites and are using compositions from those specific meteorites in the deconvolution studies, which therefore is a potential bias. Although the modelling does not represent a typical real-world application, it should demonstrate associated improvements or differences of using shergottite composition specific pyroxene spectral end members. Although many different end member combinations may model a bulk spectrum precisely, they may not necessarily make geological sense. Therefore, it is important to have a good understanding of likely compositions of the bulk spectra prior to attempting linear modelling. The purpose of this paper is to assess the accuracy of using Martian mineral spectra to model bulk Martian meteorite spectra, however, to minimise error, accessory mineral spectra will be included. In theory, this should

decrease the error of the modelling in proportion to the total accessory mineral abundance, (4-10%, Table 5.1). However, when model results include end members with low abundance (1-2%), the confidence that those specific end members are 'true' constituents of the rock is generally very low. In modelling TES spectra, the detection limit is ~10% (Christensen et al., 2000c). Using laboratory resolutions, this will likely be lower, but at 1-2% abundances, the utility of accessory mineral spectra is to improve the overall spectral fit (Hamilton, 2010).

Table 5.1 *Measured modal abundances of the shergottites compared to linear modelling using different libraries. Measured data derived from TIMA element maps, point counted using Photoshop (see text). All values are percentages, rounded to nearest integer. Measured errors are ±1-2% for major mineralogy and ±1% for accessory minerals total. RMS also percentages.*

Library	*Sample*	*Augite*	*Pigeonite*	*Pyroxferroite*	*Orthopyroxene*	*Total Pyroxene*	*Maskelynite*	*Accessory Minerals*	*Total*	*RMS*
	Los Angeles	14	27	6	-	47	48	5	100	-
	NWA 856	41	30	-	-	71	24	5	100	-
	NWA 6963	15	59	-	-	74	16	10	100	-
	NWA 10068	48	25	-	-	73	18	9	100	-
Measured	NWA 10441	29	31	-	-	60	34	7	100	-
	NWA 12335	14	25	16	-	55	35	10	100	-
	Y-002192	52	18	-	-	68	27	4	100	-
	Y-002712	57	15	-	-	72	20	9	100	-
	Zagami	44	28	-	-	72	23	5	100	-
	Los Angeles	32 (3)	55 (4)	-	2 (1)	89	9 (0)	2 (0)	100	0.72
	NWA 856	39 (2)	52 (3)	-	3 (1)	94	4 (0)	1 (0)	99	1.03
	NWA 6963	14 (2)	80 (4)	-	1 (2)	95	4 (0)	1 (0)	100	1.59
	NWA 10068	31 (2)	57 (4)	-	5 (2)	93	5 (0)	2 (0)	100	1.37
	NWA 10441	33 (2)	50 (4)	-	8 (2)	91	7 (0)	2 (0)	100	1.43
Terrestrial	NWA 12335	11 (2)	69 (4)	-	10 (2)	90	9 (0)	-	99	1.74
	Y-002192	43 (2)	48 (2)	-	2 (1)	93	4 (0)	2 (0)	99	0.74
	Y-002712	46 (2)	46 (3)	-	4 (1)	96	3 (0)	2 (0)	101	0.77
	Zagami	25 (2)	68 (3)	-	<1 (1)	94	4 (0)	2 (0)	100	1.18
	Los Angeles[a]	31 (2)	50 (3)	-	8 (1)	89	9 (0)	3 (0)	101	0.32
	Zagami[b]	23 (2)	65 (5)	-	7 (2)	95	2 (0)	3 (1)	100	0.33
	Los Angeles	18 (1)	26 (2)	8 (1)	-	52	44 (1)	4 (1)	100	0.29
	NWA 856	33 (0)	36 (1)	8 (1)	-	77	22 (1)	<1 (1)	100	0.29
	NWA 6963	3 (1)	65 (4)	21 (2)	-	89	8 (2)	2 (2)	99	0.67
	NWA 10068	24 (0)	34 (1)	14 (1)	-	72	18 (1)	10 (1)	100	0.4
	NWA 10441	24 (0)	23 (1)	15 (0)	-	62	29 (1)	10 (0)	101	0.31
Martian	NWA 12335	7 (1)	27 (1)	25 (1)	-	59	38 (1)	3 (1)	100	0.49
	Y-002192	42 (1)	17 (2)	16 (1)	-	75	24 (2)	-	99	0.57
	Y-002712	42 (1)	28 (2)	15 (2)	-	85	15 (2)	-	100	0.62
	Zagami	16 (1)	54 (1)	7 (1)	-	77	22 (1)	<1 (0)	100	0.34
	Los Angeles[a]	18 (1)	18 (1)	12 (1)	-	48	42 (1)	10 (1)	100	0.19
	Zagami[b]	32 (2)	27 (4)	18 (2)	-	77	10 (2)	13 (2)	100	0.22
Combined	Zagami	28 (2)	59 (3)	2 (0)	-	89	9 (0)	2 (0)	100	0.26
Terrestrial	Zagami	24 (4)	68 (8)	-	-	92	4 (1)	2 (1)	98	1.17
Martian	TES 10 cm^{-1}	16 (2)	54 (3)	6 (2)	-	76	22 (1)	1 (1)	99	0.34
Combined		28 (4)	59 (8)	2 (1)	-	89	9 (1)	2 (0)	100	0.25

[a] Hamilton et al., 2003.

[b] Hamilton et al., 1997.

Each basaltic shergottite was modelled twice; once using Martian, and again using terrestrial, end members (Table 5.2). The Martian and terrestrial libraries are labels, just used to differentiate between the different datasets, as the origin of a spectrum has no bearing on the result. Synthetic spectral end members were also included in the terrestrial end member group (Lindsley et al., 2019). The pyroxene results will be reported as end members groups i.e., augite and pigeonite, similar to the measured modal abundances (Table 5.1). Individual end member results will be available in the supplemental material.

5.2.4.1 Modelling Parameters

Setting out the modelling parameters is important to contextualise this study. The four terrestrial augite spectra used for this comparison were downloaded from the Arizona State University (ASU) spectral library (Christensen et al., 2000a) and are characterized by Hamilton (2000). Included in the terrestrial end member group are the pigeonites synthesized by Lindsley et al. (2019). As the Martian mineral spectra from Orr et al. (*in prep*, Part 1) have a wavelength range of 5-15 μm, the terrestrial end member group had to be resampled to that range (Fig. 5.3). This constrains the spectral information we can use for linear modelling mainly to the 8-12 μm Reststrahlen band region, which includes the Christiansen features (CF) of all the major minerals (the models were run between the 1300-675 cm^{-1} wavenumber range). Any end members that have obvious spectral inclusions will not be used for deconvolution. Using the quality standards of the ASU spectral library, only end members with a quality of 1 (high purity, with no inclusions) were used (refer to Christensen et al., 2000a). All the Martian meteorites in this study contain maskelynite (plagioclase shocked to form diaplectic glass). To reduce the number of variables we include only our maskelynite spectra (Orr et al., 2021, in prep) in both the Martian and terrestrial end member groups. This allows us to focus primarily on the effect of change pyroxene composition.

In the terrestrial end member group, pyroxene end members that are closest to the actual composition of the basaltic meteorites will be used. From the ASU library, augite will represent the high-Ca pyroxene and orthopyroxene the low-Ca. Combined with synthetic pigeonite (Lindsley et al., 2019), they represent the pyroxene compositional range using in the terrestrial modelling. As mentioned, maskelynite will

be included in the terrestrial group. The linear modelling algorithm should select the best-fitting spectra. The Martian end member group comprises solely of thin/thick section-derived pyroxene spectra from basaltic shergottites discussed by Orr et al., 2021 (*in prep,* Part 1). Due to extensive geochemical zoning in the meteorites analysed here, all pyroxene compositions will be included in the modelling. Pyroxferroite, although technically a pyroxenoid, is also included all the modelling, acting as a Fe-rich pigeonite proxy for the meteorites that do not technically contain pyroxferroite. It should be noted that we model some meteorites with end members directly measured from them. This does not introduce bias because how well a mineral end member models a rock is purely based on its composition. The origin of a spectrum is not important. A Martian pyroxene is the same as a terrestrial pyroxene. Furthermore, the basaltic shergottite pyroxenes are extensively geochemically zoned, with single grains comprising a huge range in compositions (Orr et al., submitted). Having an end member with a singular composition in that range does not necessarily lead to a better model. The range in compositions need to be adequately accounted for, hence all the basaltic shergottite-derived spectra are used in the modelling.

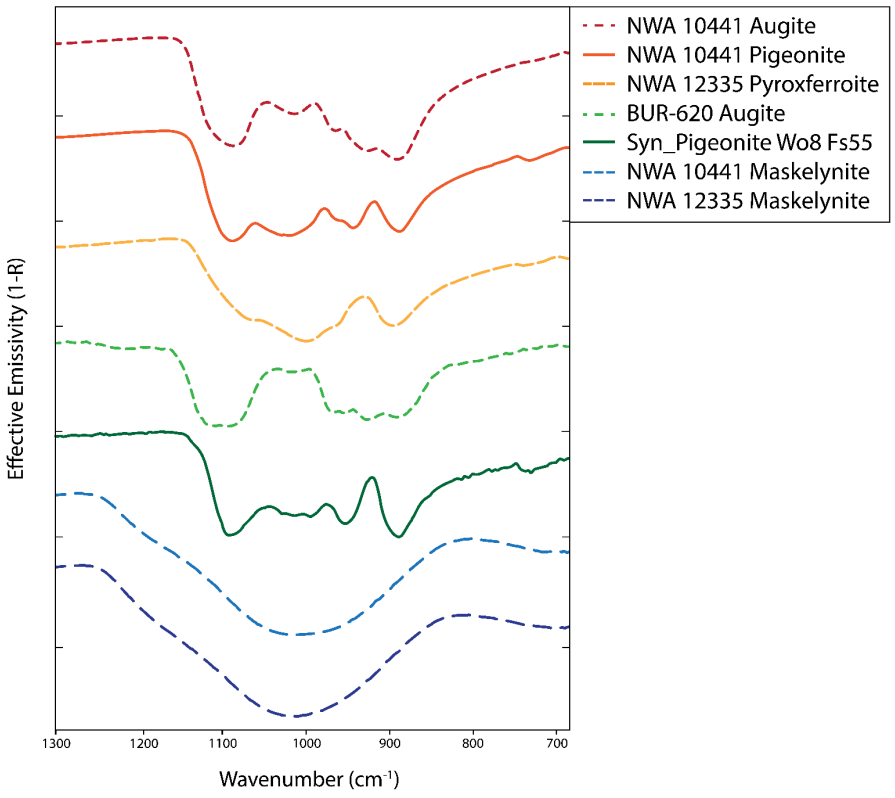

Figure 5.3 *Examples of the mineral spectra that will be used to model the basaltic shergottites. NWA 10441 and NWA 12335 pyroxene spectra (Orr et al., in prep) are part of the Martian library. BUR-620 (Christensen et al., 2000a; Hamilton, 2000) and the synthetic pigeonite (Lindsley et al., 2019) are part of the terrestrial library. The maskelynite spectra are included in both sets of libraries.*

5.2.4.2 Error Evaluation

To assess the error or 'goodness of fit' of the linear modelling, we can utilize a number of tools. The residual error of the modelling is the relative difference in emissivity between the measured spectra and the modelled spectra across all wavelengths. These differences are illustrated as lines in the modelling results, where any increase or decrease in emissivity represents regions where deviation has occurred. These relative differences or similarities can be expressed as a singular number in the form of the root-mean-square (RMS) of the modelling (Ramsey and Christensen, 1998). The RMS represents mathematically, the 'goodness of fit' of the modelling. Values can range from 0 to 1, where the closer to 0 equals a better fit. However, RMS cannot be compared across different samples, only for different fits of a sample. Therefore, RMS will only be used for comparison between a Martian or terrestrial modelling run of the same sample. The average difference in RMS of all the samples will also be calculated. Additionally, each identified end member in the modelling will have an associated uncertainty to its suggested modal abundance. These errors are larger for end members that are similar to each other and smaller for spectrally distinct end members. Lastly, we can compare the measured modal abundance of the mineralogy to the modal abundance suggested by the modelling. Although the measured modal abundance may not be representative of the whole meteorite (thin sections may not necessarily capture the true mineralogical distribution of whole samples), we are linearly modelling the same thin sections in the infrared that we used to determine the mineralogy of the samples we have. Hence, the averaged infrared spectra of the meteorites should be representative of our measured mineral modal abundances. Therefore, to assess the geological error of the modelling, we can compare the calculated modal abundance to the measured modal abundance of the meteorites. Overall, a model is deemed accurate if the mathematical RMS is close to 0 and the suggested modal abundance is close to the measured modal abundance. Both mathematical and geological error will be used in tandem, to fully evaluate the linear modelling.

5.3 Results

Linear modelling using both Martian and terrestrial end member libraries was compared to assess how accurately we can reproduce shergottite bulk spectra. The results are presented based on basaltic shergottite compositional groups, i.e., diabasic,

fine-grained and gabbroic. Firstly, however, we present the averaged spectra of the basaltic shergottites, to observe any obvious differences and similarities across the different basaltic groups.

Table 5.2 *End-member list used in the linear modelling.*

Model	*Sample*	*End Member*	*Composition*
Martian	NWA 10441	Augite	$En_{40.1}\ Wo_{34.3}\ Fs_{25.7}$
	Zagami	Augite	$En_{43.3}\ Wo_{34.2}\ Fs_{22.4}$
	NWA 6963	Pigeonite	$En_{47.8}\ Wo_{12.4}\ Fs_{39.8}$
	NWA 10441	Pigeonite	$En_{47.5}\ Wo_{14.1}\ Fs_{38.4}$
	NWA 12335	Pigeonite	$En_{41.7}\ Wo_{16.4}\ Fs_{41.9}$
	Zagami	Pigeonite	$En_{55.5}\ Wo_{11.7}\ Fs_{32.8}$
	NWA 12335	Pyroxferroite	$En_{4.5}\ Wo_{16.9}\ Fs_{78.6}$
Terrestrial	Wo8 Fs20	Syn Pigeonite	$En_{74.8}\ Wo_{7.6}\ Fs_{17.6}$
	Wo10 Fs20	Syn Pigeonite	$En_{73.6}\ Wo_{9.7}\ Fs_{16.6}$
	Wo8 Fs30	Syn Pigeonite	$En_{65.9}\ Wo_{7.3}\ Fs_{26.7}$
	Wo10 Fs30	Syn Pigeonite	$En_{64.7}\ Wo_{9.6}\ Fs_{25.7}$
	Wo8 Fs40	Syn Pigeonite	$En_{54.8}\ Wo_{7.7}\ Fs_{37.5}$
	Wo10 Fs40	Syn Pigeonite	$En_{55.5}\ Wo_{9.3}\ Fs_{35.2}$
	Wo8 Fs55	Syn Pigeonite	$En_{42.9}\ Wo_{7.1}\ Fs_{50}$
	HS-119.4B	Augite	$En_{34.1}\ Wo_{49.5}\ Fs_{16.4}$
	BUR-620	Augite	$En_{23.6}\ Wo_{48.1}\ Fs_{28.3}$
	NMNH-119197	Augite	$En_{41.6}\ Wo_{48.7}\ Fs_{9.6}$
	DSM-AUG01	Augite	$En_{42.9}\ Wo_{43.7}\ Fs_{13.4}$
	BUR-1920	Bronzite	$En_{77.1}\ Wo_{1.5}\ Fs_{21.4}$
	NMNH-119793	Bronzite	$En_{86}\ Wo_{2}\ Fs_{12.1}$
	NMNH-93527	Bronzite	$En_{75.3}\ Wo_{3}\ Fs_{21.8}$
	NMNH-C2368	Bronzite	$En_{71.8}\ Wo_{4.2}\ Fs_{24}$
	HS-9.4B	Enstatite	$En_{88.9}\ Wo_{1.2}\ Fs_{9.8}$
	DSM-ENS01	Enstatite	$En_{90}\ Wo_{0.5}\ Fs_{9.8}$
	NMNH-34669	Enstatite	$En_{90.7}\ Wo_{0.2}\ Fs_{9.1}$
Both	NWA 10441	Maskelynite	$An_{49.3}\ Ab_{47.7}\ Or_{2.9}$
	NWA 12335	Maskelynite	$An_{48.8}\ Ab_{49.6}\ Or_{1.5}$
	P2	Apatite	-
	Coesite	Coesite	-
	K-rich Glass	K-rich Glass	-

Syn = synthetic

Synthetic pigeonite spectra taken from Lindsley et al. (2019).

Terrestrial augite, bronzite, enstatite, apatite, coesite and K-rich glass taken from Christensen et al. (2000).

5.3.1 Averaged Basaltic Shergottite Spectra

Bulk spectra of the basaltic shergottites in this study are shown in Fig. 4. The primary mineralogy is maskelynite and pyroxene, therefore, the composition and modal

abundance of these minerals will dominate the bulk meteorite spectra. The spectral shapes are different for both minerals, given the difference in their compositions and structures. Both maskelynite and pyroxene have distinct CF, which can be observed in the meteorite spectra (Fig. 5.4), however, maskelynite, being a diaplectic glass, has a much simpler emissivity pattern, which is best described as a single, wide absorption band (e.g., Jaret et al., 2015). The maskelynite CF is commonly observed at ~1240 cm^{-1} (i.e., NWA 856 and NWA 12335). The spectral profile begins to gently slope in emissivity as wavenumber decreases with a band centre just above 1000 wavenumbers. The CF, and corresponding decrease in emissivity, is the most obvious example in an averaged spectrum of its presence in the rock. In terms of bulk spectra, Los Angeles (46% maskelynite) shows the most obvious affect, whereas in NWA 6963 (16% maskelynite), the effect is hidden and mostly notable by the position of the CF. All of the meteorites display a CF at ~1150 cm^{-1}, due to the spectral profile of pyroxene. For the rest of the wavenumbers, <1150 cm^{-1}, maskelynite is smoothing the spectral structure of pyroxene. The band centres we see in the basaltic shergottites are almost single-handedly due to pyroxene. The pyroxene band centres are related to the relative abundance of mainly augite and pigeonite.

5.3.2 Linear Modelling

5.3.2.1 Terrestrial Spectral Library

Figures 5-7 show the results of NNLS modelling using the terrestrial and Martian libraries. The spectral fits to the basaltic shergottites using the terrestrial library are commonly visibly worse than the fits obtained using the Martian library and this is supported quantitatively by the differences in the RMS errors between the two models. Due to the similarity of the basaltic shergottite spectra, all the models of the meteorites have comparable misfits (Fig. 5-7). The modelled maskelynite abundances are all quite low compared to the measured values (Table 5.1). This can be observed between the maskelynite and pyroxene CFs, where the model does not follow the measured spectra that closely. In terms of pyroxene, the model fits well the first (~1075 cm^{-1}) and last (~885 cm^{-1}) band centre of the shergottite spectra but does not fit as well in between these features. As band positions are indicative of composition and structure, these discrepancies suggest some of the pyroxenes in the meteorites are not fully represented by the terrestrial pyroxene spectra. In modal abundances, the modelling is not very

accurate compared to the measured values. Overall, augites are largely under-modelled by ~5-35 vol% (absolute), whereas pigeonite (including orthopyroxene) is over-modelled by 20-58 vol% (absolute), and maskelynite was always under-modelled by ~11-37% (absolute). These results suggest that synthetic pigeonites are not good fits to Martian pigeonites and are accommodated by decreased maskelynite abundance; this is not surprising given the broad, smooth shape of maskelynite relative to the augites. There are some positive results. The modelling of Y-002192 and Y-002712 correctly models higher abundances of augite compared to the other meteorites (Fig. 5.7 and Table 5.1). This is also the case for pigeonite in NWA 6963, where it equally modelled pigeonite (and orthopyroxene) at 81 vol% similar to the Martian library model (Fig. 5.8).

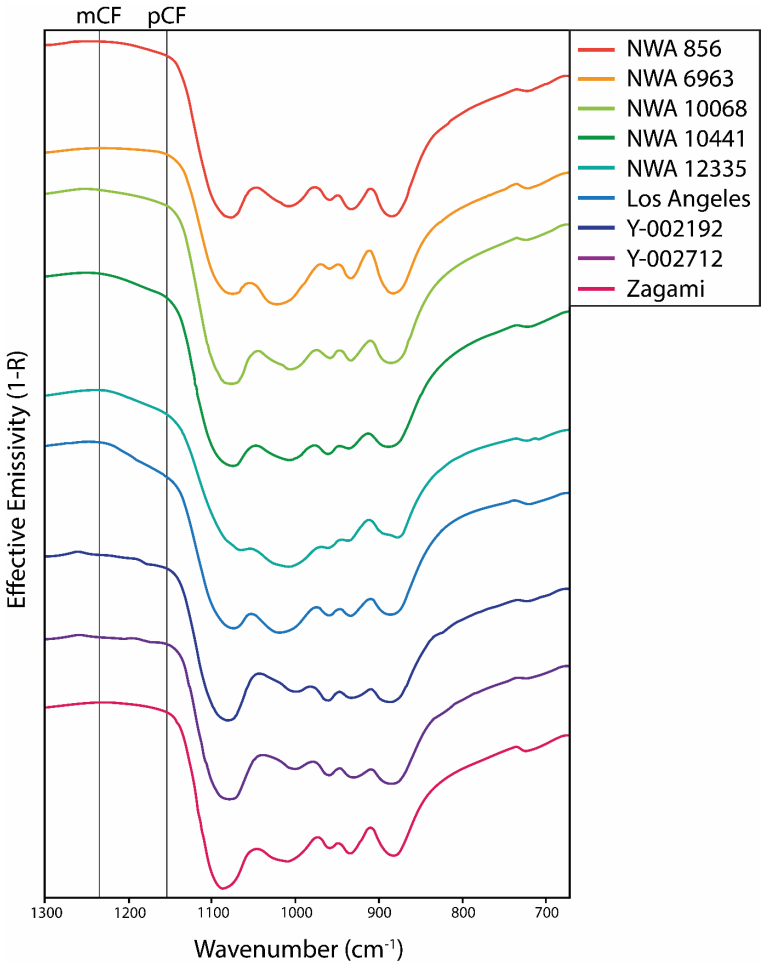

Figure 5.4 *Averaged spectra of the basaltic shergottites. The abundance and composition of maskelynite and pyroxene generally determines the relative spectral profiles of these rocks. The Christiansen Features (CF) of maskelynite (mCF, ~1240 cm-1) and pyroxene (pCF, ~1150 cm^{-1}) are highlighted to illustrate the gradual decrease in emissivity with decreasing wavenumbers between the mCF and pCF, which is based on maskelynite abundance (Orr et al., Part 1 in prep). The major bands ~1080 and ~885 cm^{-1}, (observed in all pyroxene spectra) present in the averaged spectra. The minor band region (between the major bands) can significantly change based on composition (pyroxene geochemistry), with not all bands in this region present in all pyroxene spectra. Spectra offset for clarity.*

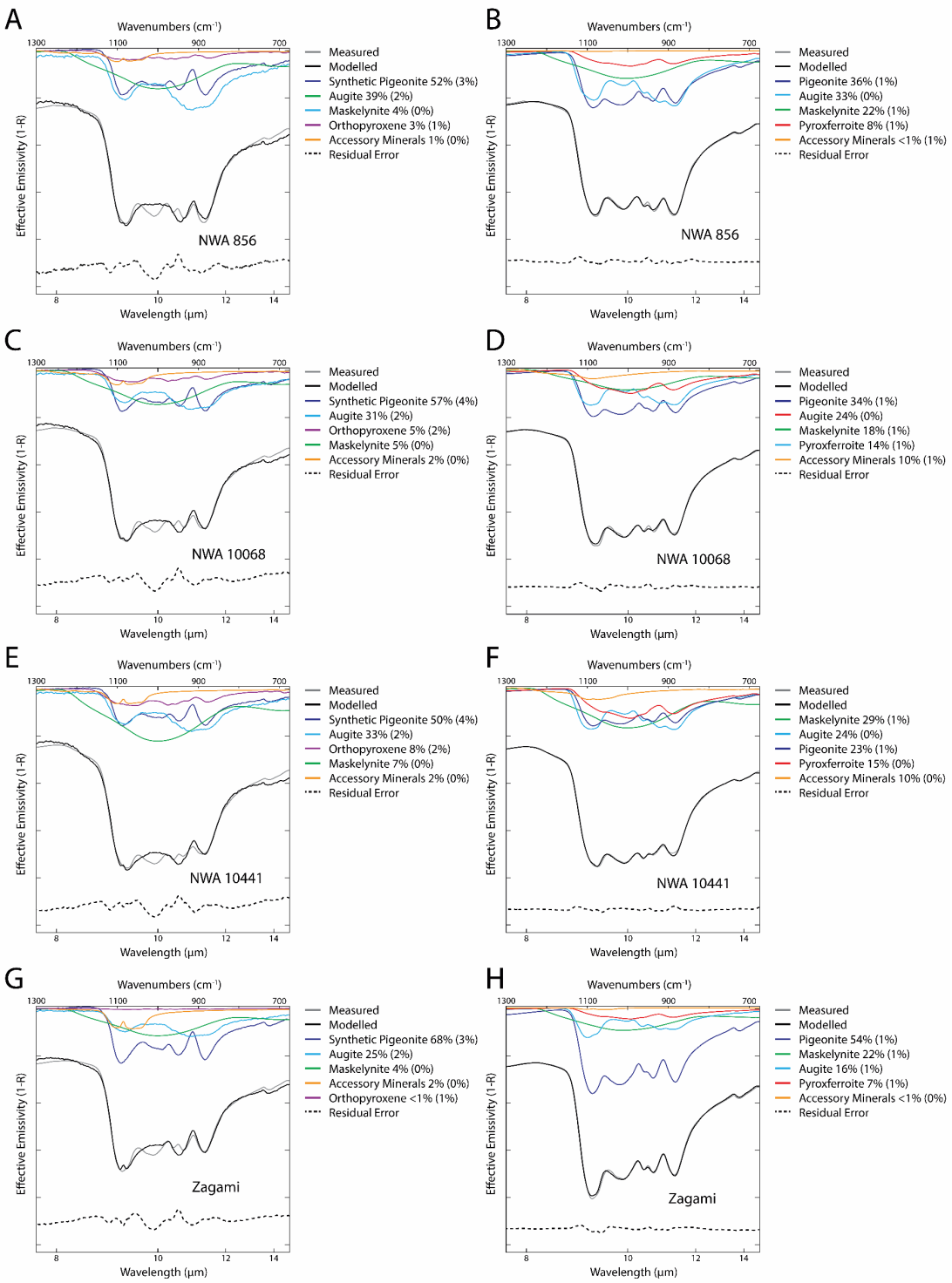

Figure 5.5 *Modelling results for NWA 856, NWA 10068, NWA 10441 and Zagami (Mars-specific composition library used on the right; terrestrial library endmembers plus maskelynite used on the left). The percentage number in brackets represents the error associated with each calculated modal abundance. Residual error is the relative difference in emissivity between the measured and modelled spectra.*

5.3.2.2 Martian Spectral Library

Overall, the Martian library produces better fits as measured by RMS (0.74% average improvement), although there are still visible misfits in the residual spectra (Fig. 5.5-

7). Maskelynite in most cases was well-represented, with accurate modal abundances (Fig. 5.5, Table 5.1). This can also be seen in the spectra. Between the maskelynite CF and pyroxene CF, the modelled spectrum closely matches the measured spectrum. In fact, all the maskelynite in the basaltic shergottites were modelled within ~5% of their measured value, except NWA 10068 where it was within 10%. Generally, all of the major spectral features of the meteorites are accounted for with the Martian library. However, some meteorite models are better matches than others. The Fe-rich shergottites NWA 12335 and Los Angeles were modelled well (Fig. 5.6). Los Angeles was modelled ±4% of its measured modal abundances of each major phase. The model for NWA 12335 correctly identifies pyroxferroite as a major spectral component as well as pigeonite. The largest discrepancy is augite, where the model is ~7% less than the measured value. Zagami and NWA 856 are both also modelled closely, with only minor differences in band fits. In terms of modal abundance, in both cases pigeonite is over-modelled relative to augite. This is also the case for NWA 10441 and NWA 10068. In Y-002192 and Y-002712 (augite-rich basalts), the models relative to the other meteorites, correctly identifies augite in higher abundance (42%), though Y-002712 over-models pigeonite by ~15% (Fig. 5.7). Pyroxferroite is identified in relative high abundance (15-16%) in both rocks, though has not been reported in these rocks. In the model of gabbroic shergottite NWA 6963, pigeonite is the dominant phase, which is correct, but augite was severely under-modelled (Fig. 5.6). Again, pyroxferroite was modelled at 21%, suggesting an Fe-rich component. Misfits between the measured and modelled spectra of the rocks suggests the full compositional range may not be fully represented by the currently available pyroxene spectra. Missing accessory phases in the modelling will also likely have a minor impact on band centre shifts.

5.4 Discussion

Linear modelling of Martian meteorites (and any other hand samples) provides the opportunity to test the efficacy of various mineral compositions in reproducing bulk rock spectra. In theory, as we know the mineralogy and composition of these hand samples, modelling them with mineral spectra should be straight forward. However, there are a lot of contributory factors to consider when modelling rock spectra. This is especially the case for Martian meteorites, as even in the basaltic shergottites with only

two major minerals, representing the range in geochemical composition in the spectral library can be challenging.

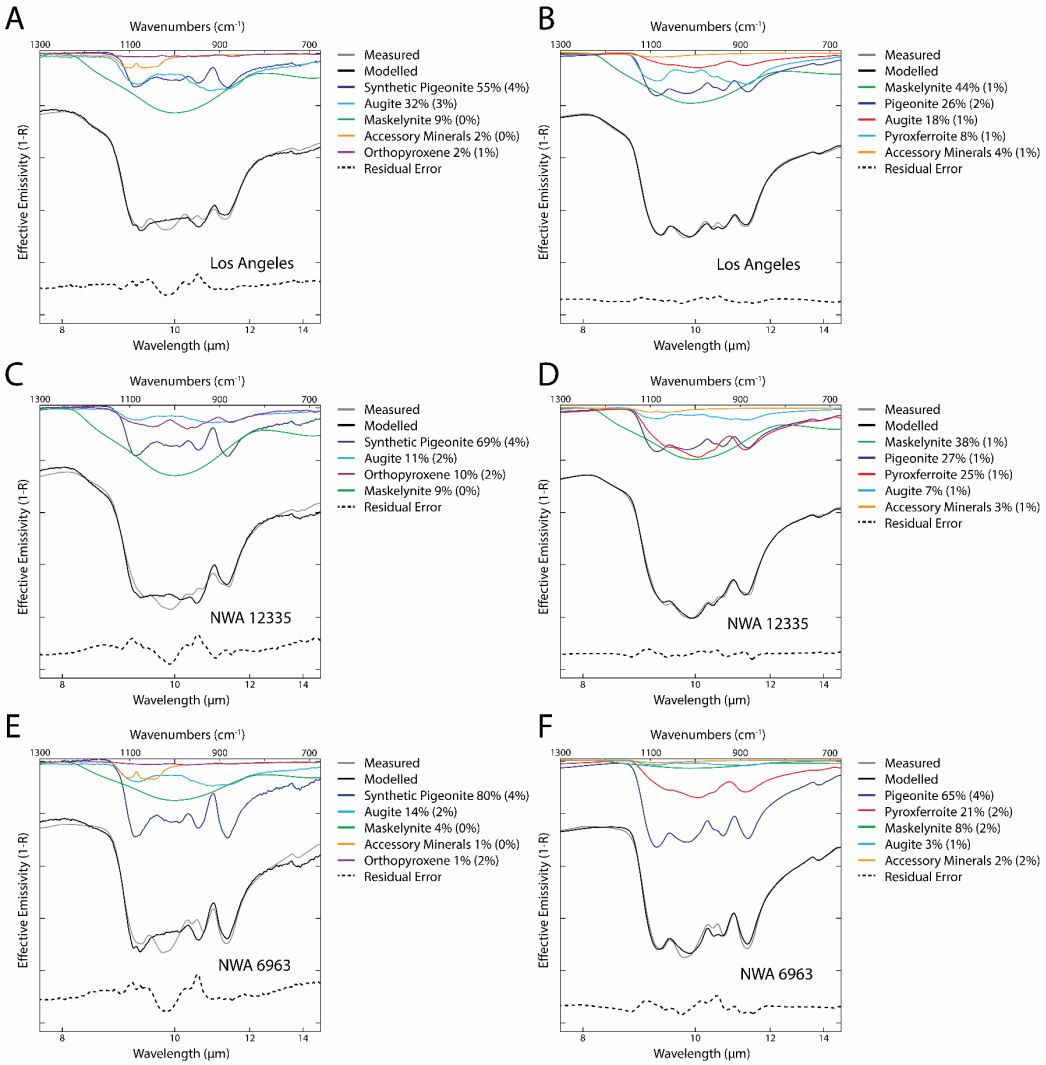

Figure 5.6 *Modelling results for pyroxferroite-bearing Los Angeles and NWA 12335 and pigeonite-rich NWA 6963. A, C, E: terrestrial library linear modelling. B, D, F: Martian library linear modelling. The percentage number in brackets represents the error associated with each calculated modal abundance. Residual error is the relative difference in emissivity between the measured and modelled spectra.*

5.4.1 Martian modelling

Our modelling of the basaltic shergottites using the Mars-derived spectral library is quite effective. The key indicator is that each spectral feature was well fit by the modelled spectra. All the models included pyroxferroite. Though not reported for most of the meteorites, pyroxferroite likely represented the Fe-rich end member pyroxene component in all the meteorites. Given the geochemical compositional range in the pyroxene, this is not surprising (Orr et al., submitted). A common feature in some of the model spectra is a slight shift in band centre position compared to the measured

spectra. From previous studies, we know the band centres of pyroxene shift based on composition (Hamilton et al., 2000; Orr et al., in prep Part 1). Therefore, these slight incompatibilities suggest that the range in pyroxene compositions was not fully represented in the spectra used for the linear modelling. In a majority of the meteorites (i.e., NWA 10441), the measured band centres, mainly CA1, have a slightly longer wavelength that the model spectra. Using the band centre compositional trends identified by Orr et al. (in prep), we can infer that the missing composition is likely an Fe-rich pyroxene, as the position of CA1 increases in wavelength with increasing Fe content of the mineral. Pyroxferroite was included to represent the Fe-rich pyroxene in the modelling. However, being an extreme Fe-rich (Fs_{79}) pyroxenoid, it likely did not fully account for intermediate Fe-rich pyroxene compositions. From the geochemistry of pyroxene in the shergottites, the likely missing pyroxene spectrum would be a $Fs_{55\text{-}75}$ pigeonite, as augite tends to not exist in such an Fe-rich form in the shergottites (Orr et al., submitted, probably need some other references here too). An Fe-pigeonite has previously been purported to be a missing component of linear modelling of Meridiani Planum (Rogers et al., 2008). A similar situation is observed in NWA 10068 with maskelynite. The major spectral feature of maskelynite is its CF, which changes position based on composition (Fig. 5.8). In the NWA 10068 model spectrum, the maskelynite CF position (as previously mentioned can be observed in the average spectra) has a slightly longer wavelength position than the same feature in the measured spectrum. This suggests the maskelynite in NWA 10068 is slightly more anorthitic (Ca-rich) than the maskelynite used in the linear modelling. From Bouvier et al. (2017), the composition of maskelynite in NWA 10068 is ~An_{55}, whereas the composition of maskelynite in NWA 12335 (from which the 35_Maskelynite spectrum was measured) is ~An_{44} (Orr et al., submitted).

5.4.2 Composition Matters

Overall, the pyroxene spectra from shergottites reproduce bulk shergottite spectra better than the terrestrial endmembers. Although there are discrepancies in the Martian modelling, they are largely minor shifts in band centre positions, which relates to compositional variation in the shergottites that is not fully accounted for. In the terrestrial modelling, the major band centres (~1075 cm^{-1} and ~885 cm^{-1}, Fig. 5.4) of the shergottite spectra are accounted for, as these are predominant in all pyroxene spectra. In the minor band regions, the terrestrial modelling does not fit the spectra as

well. This region is where the spectral shape of pyroxene shows substantial change based on composition and crystal structure (Hamilton, 2000; Orr et al., Part 1 in prep). Utilising the synthetic pigeonite spectra likely improved the modelling, especially when the shergottites are known to comprise of pigeonite (e.g., Hamilton, 2010). If only augite and orthopyroxene was included, it would likely yield a worse result (e.g., Hamilton et al., 1997). However, when compared against the Martian library modelling, it is obvious that using spectra that have similar geochemical composition to the target yields improved results over spectra that may be the right phase, but not exactly the right composition.

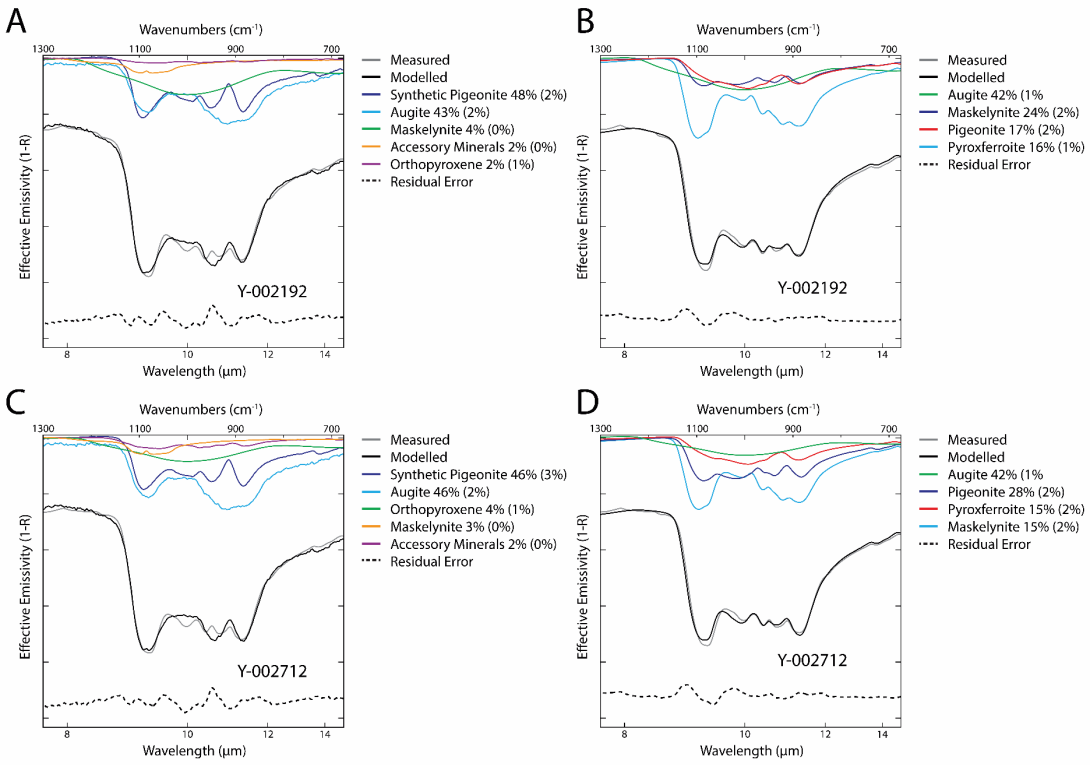

Figure 5.7 *Modelling results for augite-rich Y-002712 and Y-002192. A, C: terrestrial library linear modelling. B, D: Martian library linear modelling. The percentage number in brackets represents the error associated with each calculated modal abundance. Residual error is the relative difference in emissivity between the measured and modelled spectra.*

To keep the focus on pyroxene, Martian maskelynite was included in the terrestrial library. This was an effort to improve the modelling and reliability of direct comparison. Even with these maskelynite spectra (the Martian library modelling demonstrate that these maskelynite spectra model the maskelynite in the shergottites very well), the modelled abundance of maskelynite was always under-determined and inaccurate in the terrestrial modelling. This suggests that using pyroxene spectra with a different composition to the shergottites also impacted how maskelynite was

modelled in these rocks (e.g., Feely and Christensen, 1999). The linear least squares algorithm is only as good as the input. If a major compositional spectral end member is different to the composition of the same mineral in the target, this can severely impact on the overall model and how other major end members are modelled. Therefore, even when modelling rocks with only two major minerals (maskelynite and pyroxene), if one of those minerals is not correctly accounted for, this will likely impact the other end members and then the whole model. Although this study is focused on pyroxene, it is obvious including maskelynite with a similar composition to the shergottites significantly improved the models.

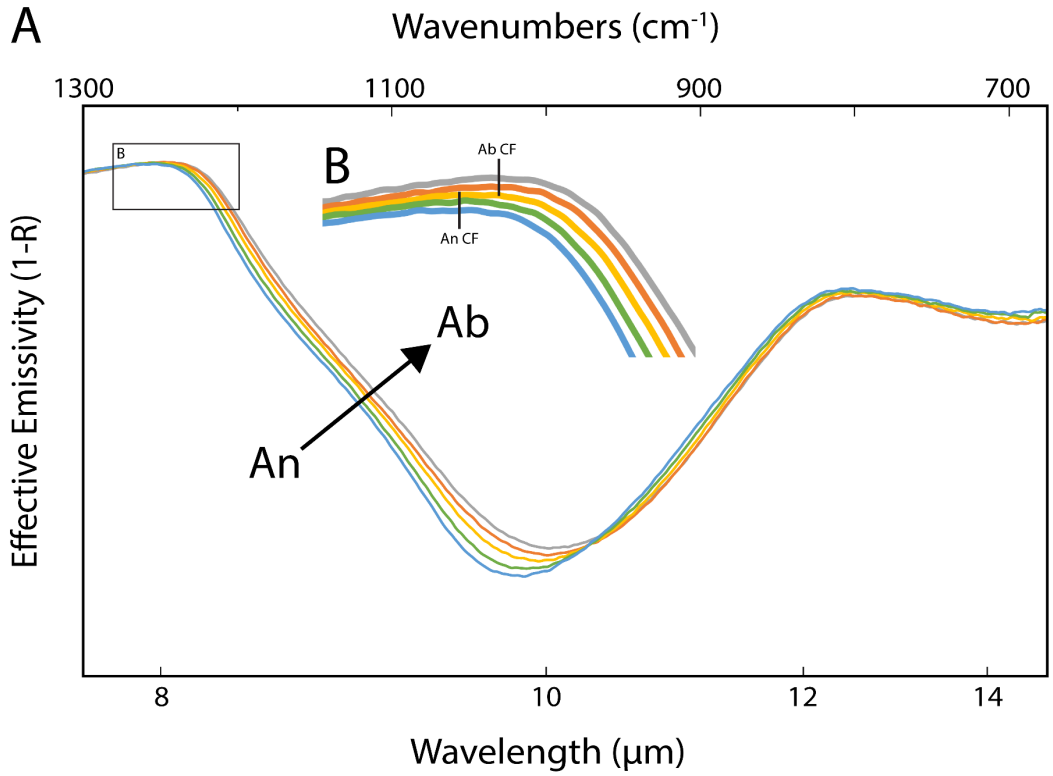

Figure 5.8 *Maskelynite spectra measured from NWA 12335. Maskelynite in this meteorite are zoned with Ca-rich (An) cores and Na-rich (Ab) rims. A: maskelynite spectra taken from the core of a grain then towards the rim. Each spectrum represents a slightly different composition, replicating the geochemical zoning seen in NWA 12335 (Orr et al., submitted). B: the same maskelynite spectra (though slightly offset to increase clarity) magnified around the CF. Increasing Ab content in the maskelynite shifts the CF position to decreasing wavenumbers.*

The basaltic shergottites, although comprising similar mineralogy, can be quite different. The modal abundances of augite, pigeonite, pyroxferroite and maskelynite are unique to the specific meteorites, and therefore their crystallisation history and evolution. Being able to distinguish between augite-rich (Y-002192 and Y-002712), pigeonite-rich (NWA 6963), maskelynite-rich (Los Angeles and NWA 12335) shergottites as well as those with similar modal abundances of augite, pigeonite and

maskelynite (NWA 856 and Zagami) enables much more information to be gleaned from the spectra. However, this can only be achieved with a very compositionally close spectral library to the measured composition of the targets. The terrestrial library struggled to model these changes in phase composition and/or abundance very well. Except for the augite-rich (Y-002192 and Y-002712) shergottites where it correctly modelled a higher modal abundance of augite, the rest were similarly modelled with a high proportion of pigeonite but little augite and maskelynite. The Martian library models, were able to make these observations, demonstrating a significant positive step in modelling basaltic shergottites. This is exemplified in the modelling of Los Angeles and Zagami spectra (measured in emissivity) from Hamilton et al. (1997; 2010) (Fig. 5.9). This Zagami spectrum is the only previously modelled basaltic shergottite (Hamilton et al., 1997). Though the original model was over a larger spectral range (1400-400 cm^{-1}), the largest spectral misfits are in the spectral range (1300-675 cm^{-1}) used in this study. The modeling of Zagami in this study has obviously improved because of a more extensive spectral library, which now includes an expanded range in clino- and orthopyroxene, synthetic pigeonite and Martian-specific augite and pigeonite. Although the difference in RMS of the Martian and terrestrial modelling is not as large as with the previous results, the suggested modal abundances for the Martian library are much closer to the measured mineralogy than the terrestrial library. Additionally, the direct emissivity Los Angeles and Zagami spectra has higher noise, which is not as easily modelled using the very low noise Martian library, thus impacting the RMS. To improve the RMS, noise would need to be introduced to the Martian-derived spectra.

To evaluate how well the new Martian spectra model together with the terrestrial library, all the end member spectra in this study were combined in a single library to model Zagami (Fig. 5.10). The combined library model resulted in the lowest RMS (Table 5.1). However, this was only a very slight improvement over the Martian library models (the RMS of the Zagami model was 0.26% compared to 0.34%, respectively). The overall improvement of the modelling compared to the terrestrial and Martian runs clearly rests with the inclusion of the Martian library. This is important, as during more realistic modelling (when a large spectral library is used for modelling of unknown surface spectra) these Martian spectra will be used to supplement the currently available library, not replace it. The fact that there is an improvement in RMS from

1.18 to 0.26% (terrestrial to combined), suggests for pyroxene, acquiring more representative pyroxene spectra is the preferred approach over trying to replicate those intermediate compositions with end member compositions.

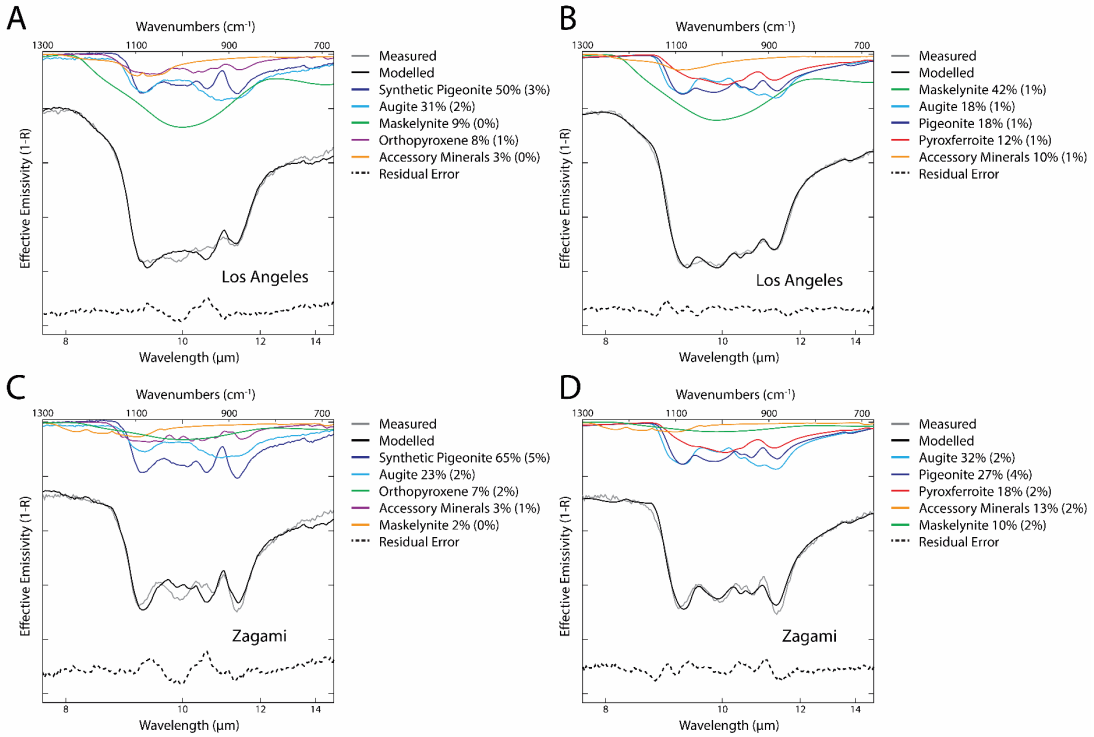

Figure 5.9 *Modelling results for Los Angeles and Zagami (Hamilton et al., 1997 and Hamilton et al., 2003) using both terrestrial (A, C) and Martian (B, D) spectral libraries. The Martian spectral library performs similarly better than the terrestrial library. The percentage number in brackets represents the error associated with each calculated modal abundance. Residual error is the relative difference in emissivity between the measured and modelled spectra.*

5.4.3 Application to Mars

The benefit of modelling the shergottites is that the mineralogy and composition are already known. This hindsight enables the right end members to be chosen for the modelling. Being able to preference certain end members or compositions over others is a major advantage. Modelling the Martian surface is generally done blind, with no detailed prior knowledge of the surface composition, the signal to noise is worse and there is lower spectral resolution. Therefore, the approach to modelling remote surfaces is slightly different. To ensure the modelling accounts for all possible compositions, spectral libraries contain a more diverse range in spectral end members. Therefore, the Martian pyroxene spectra will supplement a larger library that can model a diverse range of rock compositions. This library would best be applied to surface spectra measured by the Thermal Emission Spectrometer (TES), onboard Mars Global Surveyor (e.g., Christensen et al., 2001; Bandfield et al., 2000; Bandfield et al.,

2002; Rogers et al., 2007b). With spectral sampling of 5 or 10 cm^{-1} TES is the only hyperspectral thermal infrared instrument used to determine the surface mineralogy of Mars (e.g., Christensen et al., 2001). Fig. 5.10 shows that even at 10 cm^{-1} (replicating TES spectral resolution) the modelling is almost as accurate as at laboratory spectral resolution (4 cm^{-1}). The RMS of the Combined library modelling of Zagami at 10 cm^{-1} was 0.25% compared to 0.26% at 4 cm^{-1}. This is using spectra will very little noise, but this shows that the pyroxene spectral features are still identifiable at 10 cm^{-1}, and therefore the composition of pyroxene should still be important when modelling TES surface spectra.

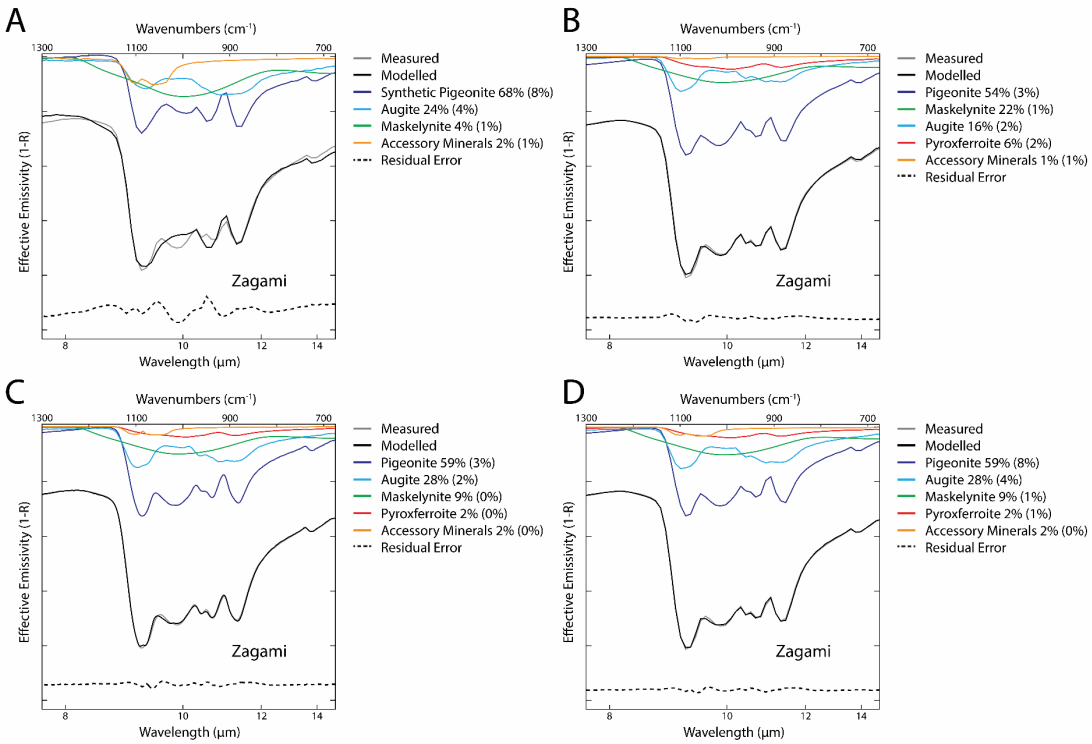

Figure 5.10 *Modelling results for Zagami. A, B: Modelling Zagami using TES 10 cm-1 spectral resolution with both the Martian and terrestrial libraries. C: Modelling laboratory Zagami using a Martian and terrestrial combined library. D: Modelling TES 10 cm-1 Zagami with the combined library. The percentage number in brackets represents the error associated with each calculated modal abundance. Residual error is the relative difference in emissivity between the measured and modelled spectra.*

Furthermore, the TES spectra will need to be run over a shorter wavelength range to match the lab-measured spectra. This study has shown, that even at a reduced wavelength range (5-15 um), similarly composed basaltic shergottites can be distinguished based on their geochemistry in infrared. However, the number of end members that can be used in the spectral library will be less than when modelling the larger spectral range due to the reduced number of channels. There are ~45 channels

available using the spectral range 1300 to ~825 cm^{-1} (this includes the Martian CO_2 absorption band cutoff ~825 cm^{-1}). Although this is roughly a third of the available channels when using the full spectral range, there are enough to model all the major mineral groups and the necessary atmospheric spectra. Furthermore, the purpose of using the reduced spectral range is to target pyroxene-rich surface rocks, not necessarily to model a wide variety of surfaces. Another consideration is to exclude spectral end members with band centres only outside of the 1300 to ~825 cm^{-1} spectral range. Figure 5.11 demonstrates using magnetite, with band centres at 555 and 340 cm^{-1}, in the linear modelling of Zagami. In the 1300 to ~825 cm^{-1} spectral range, magnetite is predominantly a featureless spectral end member and therefore has been incorrectly identified as a major mineral (39% abundance). This will likely be the case for other minerals such as haematite, but these minerals would be not the target of liner modelling using these Martian-derived mineral spectra.

As many Martian meteorites, i.e., the shergottites, are surface and/or near-surface lavas, we would expect to observe similar compositions to the shergottites on the Martian surface. Unfortunately, this has not been the case. Spectral studies searching for meteorite compositions on the Martian surface resulted in very few areas with matching spectral signatures (e.g., Hamilton et al., 2003). In this case, bulk Martian meteorite spectra were used as spectral end members. However, up to now, there has not been a study using Martian-specific, individual mineral spectra in the linear modelling. Using the Martian library, just like modelling the shergottite spectra in this study, potentially may help in finding shergottite compositions on the surface. As we have seen from this study, there are significant advantages using the pyroxene spectra measured from the meteorites over terrestrial pyroxene spectra when modelling the shergottites. However, modelling the Martian surface has its own issues that need to be taken into consideration. The particle size of the target directly influences linear mixing. Above ~60 μm grain size, infrared spectra can be linearly modelled using randomly oriented particulates (with a grain size of >200 μm). <60 μm grain sizes introduce volume scattering effects, which start to change the spectral features of the sample. Linear mixing can be extended to ~20 μm grain sizes if similar sized spectral end members are used. The assumption with Mars, is the surface geology is generally coarse than ~60 μm, therefore can be linearly modelled using end members. A significant caveat to spectrally modelling the surface is dust (Christensen et al., 2001).

Almost half of the Martian surface is covered in a thick layer of dust (bright regions), which inhibits infrared spectroscopy in those areas. The dust covered regions tend to include younger terranes such as Tharsis and Elysium, which have been postulated to be likely source terranes of the younger shergottites (600 Ma) (Mouginis-Mark et al., 1992) and was interpreted as the most likely explanation for the non-detection of shergottite spectra by Hamilton et al. (2003). Although there may be limitations to the areas we can evaluate for shergottite compositional matches, we can still use the *in situ* pyroxene spectra to model the Martian surface that is relatively dust free. This includes TES spectra and infrared rover observations, such as from the Mini-Thermal Emission Spectrometers onboard the Mars Exploration Rovers (e.g., Christensen et al., 2004; Ruff et al., 2006; Rogers et al., 2007b; Zipfel et al., 2011).

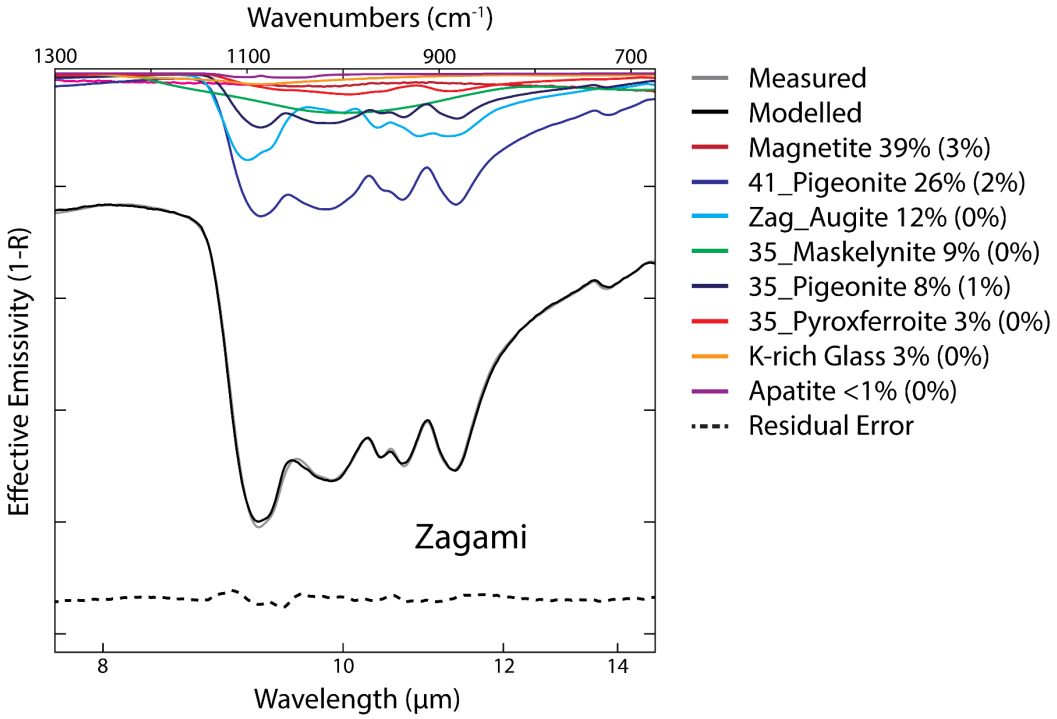

Figure 5.11 *Linear modelling using the Martian library with magnetite. Due to its featureless spectral profile in this wavelength range, magnetite has been incorrectly identified in high abundance. The end members identified are not grouped.*

5.5 Conclusions

Through linear modelling of nine basaltic shergottites with both a Martian (thin section determined) spectral library and a terrestrial spectral library, we have demonstrated that using Martian-specific compositions (Orr et al., in prep, Part 1) results in more accurate matches when modelling bulk spectra. The augite, pigeonite and pyroxferroite spectra in combination with maskelynite spectra modelled the

shergottites closely, with the ability to distinguish between compositionally similar basaltic shergottites. The terrestrial modelling struggled to model all the band centres of the shergottites, therefore missing key information about the rocks. The modelling results demonstrated even with these in-situ pyroxene spectra used in the Martian library, the range of pyroxene composition in the basaltic shergottites are still not fully represented. We found a likely key missing pyroxene spectrum to be a Fe-rich pigeonite, as this would likely account for some shifts in the model band centres relative to the measured shergottite spectra. Overall, this study has clearly demonstrated the benefit of modelling Martian meteorites with spectral end members of similar composition.

5.6 References

Aines, R. D., & Rossman, G. R. (1984). Water in minerals? A peak in the infrared. *Journal of Geophysical Research: Solid Earth*, *89*(B6), 4059-4071.

Bandfield, J. L., Hamilton, V. E., & Christensen, P. R. (2000). A Global View of Martian Surface Compositions from MGS-TES. *Science*, *287*(5458), 1626–1630. https://doi.org/10.1126/science.287.5458.1626

Bandfield, J. L. (2002). Global mineral distributions on Mars. *Journal of Geophysical Research: Planets (1991–2012)*, *107*(E6), 9-1-9–20. https://doi.org/10.1029/2001je001510

Bertka, C. M., & Holloway, J. R. (1993). Pigeonite at solidus temperatures: Implications for partial melting. *Journal of Geophysical Research: Solid Earth*, *98*(B11), 19755–19766. https://doi.org/10.1029/93jb02173

Bouvier, A., Gattacceca, J., Agee, C., Grossman, J., & Metzler, K. (2017). The Meteoritical Bulletin, No. 104. *Meteoritics & Planetary Science*, *52*(10), 2284–2284. https://doi.org/10.1111/maps.12930

Bridges, J. C., & Warren, P. H. (2006). The SNC meteorites: basaltic igneous processes on Mars. *Journal of the Geological Society*, *163*(2), 229–251. https://doi.org/10.1144/0016-764904-501

Carter, J., Poulet, F., Bibring, J. -P., Mangold, N., & Murchie, S. (2013). Hydrous minerals on Mars as seen by the CRISM and OMEGA imaging spectrometers: Updated global view. *Journal of Geophysical Research: Planets*, *118*(4), 831–858. https://doi.org/10.1029/2012je004145

Christensen, P. R., Bandfield, J. L., Clark, R. N., Edgett, K. S., Hamilton, V. E., Hoefen, T., et al. (2000a). Detection of crystalline hematite mineralization on Mars by the Thermal Emission Spectrometer: Evidence for near-surface water. *Journal of Geophysical Research: Planets*, *105*(E4), 9623–9642. https://doi.org/10.1029/1999je001093

Christensen, P. R., Bandfield, J. L., Hamilton, V. E., Howard, D. A., Lane, M. D., Piatek, J. L., et al. (2000b). A thermal emission spectral library of rock-forming minerals. *Journal of Geophysical Research: Planets*, *105*(E4), 9735–9739. https://doi.org/10.1029/1998je000624

Christensen, P. R., Bandfield, J. L., Smith, M. D., Hamilton, V. E., & Clark, R. N. (2000c). Identification of a basaltic component on the Martian surface from Thermal Emission Spectrometer data. *Journal of Geophysical Research: Planets*, *105*(E4), 9609–9621. https://doi.org/10.1029/1999je001127

Christensen, P. R., Bandfield, J. L., Hamilton, V. E., Ruff, S. W., Kieffer, H. H., Titus, T. N., et al. (2001). Mars Global Surveyor Thermal Emission Spectrometer experiment: Investigation description and surface science results. *Journal of Geophysical Research: Planets*, *106*(E10), 23823–23871. https://doi.org/10.1029/2000je001370

Christensen, P. R., Bandfield, J. L., III, J. F. B., Gorelick, N., Hamilton, V. E., Ivanov, A., et al. (2003a). Morphology and Composition of the Surface of Mars: Mars Odyssey

THEMIS Results. *Science*, *300*(5628), 2056–2061. https://doi.org/10.1126/science.1080885

Christensen, P. R., Mehall, G. L., Silverman, S. H., Anwar, S., Cannon, G., Gorelick, N., et al. (2003b). Miniature Thermal Emission Spectrometer for the Mars Exploration Rovers. *Journal of Geophysical Research: Planets (1991–2012)*, *108*(E12). https://doi.org/10.1029/2003je002117

Christensen, P. R., Wyatt, M. B., Glotch, T. D., Rogers, A. D., Anwar, S., Arvidson, R. E., et al. (2004). Mineralogy at Meridiani Planum from the Mini-TES Experiment on the Opportunity Rover. *Science, 306*(5702), 1733-1739. https://doi.org/10.1126/science.1104909

Feely, K. C., & Christensen, P. R. (1999). Quantitative compositional analysis using thermal emission spectroscopy: Application to igneous and metamorphic rocks. *Journal of Geophysical Research: Planets*, *104*(E10), 24195–24210. https://doi.org/10.1029/1999je001034

Filiberto, J., Gross, J., Udry, A., Trela, J., Wittmann, A., Cannon, K. M., et al. (2018). Shergottite Northwest Africa 6963: A Pyroxene-Cumulate Martian Gabbro. *Journal of Geophysical Research: Planets*, *123*(7), 1823–1841. https://doi.org/10.1029/2018je005635

Goodrich, C. A. (2002). Olivine-phyric martian basalts: A new type of shergottite. *Meteoritics & Planetary Science*, *37*(S12), B31–B34. https://doi.org/10.1111/j.1945-5100.2002.tb00901.x

Gross, J., Treiman, A. H., Filiberto, J., & Herd, C. D. K. (2011). Primitive olivine-phyric shergottite NWA 5789: Petrography, mineral chemistry, and cooling history imply a magma similar to Yamato-980459. *Meteoritics & Planetary Science*, *46*(1), 116–133. https://doi.org/10.1111/j.1945-5100.2010.01152.x

Hamilton, V. E., Christensen, P. R., & McSween, H. Y. (1997). Determination of Martian meteorite lithologies and mineralogies using vibrational

spectroscopy. *Journal of Geophysical Research: Planets*, *102*(E11), 25593–25603. https://doi.org/10.1029/97je01874

Hamilton, V. E. (2000). Thermal infrared emission spectroscopy of the pyroxene mineral series. *Journal of Geophysical Research: Planets*, *105*(E4), 9701–9716. https://doi.org/10.1029/1999je001112

Hamilton, V. E., Wyatt, M. B., McSween, H. Y., & Christensen, P. R. (2001). Analysis of terrestrial and Martian volcanic compositions using thermal emission spectroscopy: 2. Application to Martian surface spectra from the Mars Global Surveyor Thermal Emission Spectrometer. *Journal of Geophysical Research: Planets*, *106*(E7), 14733–14746. https://doi.org/10.1029/2000je001353

Hamilton, V. E., Christensen, P. R., McSween, H. Y., & Bandfield, J. L. (2003). Searching for the source regions of martian meteorites using MGS TES: Integrating martian meteorites into the global distribution of igneous materials on Mars. *Meteoritics & Planetary Science*, *38*(6), 871–885. https://doi.org/10.1111/j.1945-5100.2003.tb00284.x

Hamilton, V. E., Goodrich, C. A., Treiman, A. H., Connolly, H. C., Zolensky, M. E., & Shaddad, M. H. (2020). Meteoritic evidence for a Ceres-sized water-rich carbonaceous chondrite parent asteroid. *Nature Astronomy*, 1-6.

Hanna, R. D., Hamilton, V. E., Haberle, C. W., King, A. J., Abreu, N. M., & Friedrich, J. M. (2020). Distinguishing relative aqueous alteration and heating among CM chondrites with IR spectroscopy. *Icarus*, *346*, 113760.

He, Q., Xiao, L., Balta, J. B., Baziotis, I. P., Hsu, W., & Guan, Y. (2015). Petrography and geochemistry of the enriched basaltic shergottite Northwest Africa 2975. *Meteoritics & Planetary Science*, *50*(12), 2024–2044. https://doi.org/10.1111/maps.12571

Howarth, G. H., Udry, A., & Day, J. M. D. (2018). Petrogenesis of basaltic shergottite Northwest Africa 8657: Implications for fO2 correlations and element redistribution

during shock melting in shergottites. *Meteoritics & Planetary Science*, *53*(2), 249–267. https://doi.org/10.1111/maps.12999

Hunt, G. R. (1977). Spectral signatures of particulate minerals in the visible and near infrared. *Geophysics*, *42*(3), 501-513.

Jambon, A., Barrat, J. A., Sautter, V., Gillet, P., Göpel, C., Javoy, M., et al. (2002). The basaltic shergottite Northwest Africa 856: Petrology and chemistry. *Meteoritics & Planetary Science*, *37*(9), 1147–1164. https://doi.org/10.1111/j.1945-5100.2002.tb00885.x

Jaret, S. J., Woerner, W. R., Phillips, B. L., Ehm, L., Nekvasil, H., Wright, S. P., & Glotch, T. D. (2015). Maskelynite formation via solid-state transformation: Evidence of infrared and X-ray anisotropy. *Journal of Geophysical Research: Planets*, *120*(3), 570–587. https://doi.org/10.1002/2014je004764

Johnson, J. R., Hörz, F., Lucey, P. G., & Christensen, P. R. (2002). Thermal infrared spectroscopy of experimentally shocked anorthosite and pyroxenite: Implications for remote sensing of Mars. *Journal of Geophysical Research: Planets (1991–2012)*, *107*(E10), 3-1-3–14. https://doi.org/10.1029/2001je001517

Johnson, J. R., Hörz, F., & Staid, M. I. (2003). Thermal infrared spectroscopy and modeling of experimentally shocked plagioclase feldspars. *American Mineralogist*, *88*(10), 1575–1582. https://doi.org/10.2138/am-2003-1020

Koeppen, W. C., & Hamilton, V. E. (2008). Global distribution, composition, and abundance of olivine on the surface of Mars from thermal infrared data. *Journal of Geophysical Research: Planets (1991–2012)*, *113*(E5). https://doi.org/10.1029/2007je002984

Leroux, H., Devouard, B., Cordier, P., & Guyot, F. (2004). Pyroxene microstructure in the Northwest Africa 856 martian meteorite. *Meteoritics & Planetary Science*, *39*(5), 711–722. https://doi.org/10.1111/j.1945-5100.2004.tb00114.x

Lindsley, D. H. (1983). Pyroxene thermometry. *American Mineralogist*, *68*(5-6), 477-493.

Lindsley, D. H., & Andersen, D. J. (1983). A two-pyroxene thermometer. *Journal of Geophysical Research: Solid Earth*, *88*(S02), A887–A906. https://doi.org/10.1029/jb088is02p0a887

Lindsley, D. H., Nekvasil, H., & Glotch, T. D. (2019). Synthesis of pigeonites for spectroscopic studies. *American Mineralogist*, *104*(4), 615–618. https://doi.org/10.2138/am-2019-6869ccbyncnd

McCoy, T. J., Taylor, G. J., & Keil, K. (1992). Zagami: Product of a two-stage magmatic history. *Geochimica et Cosmochimica Acta*, *56*(9), 3571–3582. https://doi.org/10.1016/0016-7037(92)90400-d

McSween, H. Y., Eisenhour, D. D., Taylor, L. A., Wadhwa, M., & Crozaz, G. (1996). QUE94201 shergottite: Crystallization of a Martian basaltic magma. *Geochimica et Cosmochimica Acta*, *60*(22), 4563–4569. https://doi.org/10.1016/s0016-7037(96)00265-7

Mikouchi, T., & Takenouchi, A. (2016). Mineralogical Investigation of Yamato 002712 Basaltic Shergottite: Implications for the Redox Change During Crystallization. *47th Lunar and Planetary Science Conference*, Abs# 1903.

Minitti, M. E., & Hamilton, V. E. (2010). A search for basaltic-to-intermediate glasses on Mars: Assessing Martian crustal mineralogy. *Icarus*, *210*(1), 135–149. https://doi.org/10.1016/j.icarus.2010.06.028

Mouginis-Mark, P. J., McCoy, T. J., Taylor, G. J., & Keil, K. (1992). Martian parent craters for the SNC meteorites. *Journal of Geophysical Research: Planets, 97*(E6), 10213-10225. https://doi.org/10.1029/92jeoo612

Murchie, S., Arvidson, R., Bedini, P., Beisser, K., Bibring, J. -P., Bishop, J., et al. (2007). Compact Reconnaissance Imaging Spectrometer for Mars (CRISM) on Mars

Reconnaissance Orbiter (MRO). *Journal of Geophysical Research: Planets (1991–2012)*, *112*(E5). https://doi.org/10.1029/2006je002682

Mustard, J. F., Murchie, S. L., Pelkey, S. M., Ehlmann, B. L., Milliken, R. E., Grant, J. A., et al. (2008). Hydrated silicate minerals on Mars observed by the Mars Reconnaissance Orbiter CRISM instrument. *Nature*, *454*(7202), 305–309. https://doi.org/10.1038/nature07097

Pan, C., Rogers, A. D., & Michalski, J. R. (2015). Thermal and near-infrared analyses of central peaks of Martian impact craters: Evidence for a heterogeneous Martian crust. *Journal of Geophysical Research: Planets*, *120*(4), 662–688. https://doi.org/10.1002/2014je004676

Poulet, F., Gomez, C., Bibring, J. -P., Langevin, Y., Gondet, B., Pinet, P., et al. (2007). Martian surface mineralogy from Observatoire pour la Minéralogie, l'Eau, les Glaces et l'Activité on board the Mars Express spacecraft (OMEGA/MEx): Global mineral maps. *Journal of Geophysical Research: Planets*, *112*(E8). https://doi.org/10.1029/2006je002840

Rahib, R. R., Udry, A., Howarth, G. H., Gross, J., Paquet, M., Combs, L. M., et al. (2019). Mantle source to near-surface emplacement of enriched and intermediate poikilitic shergottites in Mars. *Geochimica et Cosmochimica Acta*, *266*, 463–496. https://doi.org/10.1016/j.gca.2019.07.034

Ramsey, M. S., & Christensen, P. R. (1998). Mineral abundance determination: Quantitative deconvolution of thermal emission spectra. *Journal of Geophysical Research: Solid Earth*, *103*(B1), 577–596. https://doi.org/10.1029/97jb02784

Rogers, A. D., Bandfield, J. L., & Christensen, P. R. (2007a). Global spectral classification of Martian low-albedo regions with Mars Global Surveyor Thermal Emission Spectrometer (MGS-TES) data. *Journal of Geophysical Research: Planets (1991–2012)*, *112*(E2). https://doi.org/10.1029/2006je002726

Rogers, A. D., & Christensen, P. R. (2007b). Surface mineralogy of Martian low-albedo regions from MGS-TES data: Implications for upper crustal evolution and surface alteration. *Journal of Geophysical Research: Planets (1991–2012)*, *112*(E1). https://doi.org/10.1029/2006je002727

Rogers, A. D., & Aharonson, O. (2008). Mineralogical composition of sands in Meridiani Planum determined from Mars Exploration Rover data and comparison to orbital measurements. *Journal of Geophysical Research: Planets (1991–2012)*, *113*(E6). https://doi.org/10.1029/2007je002995

Ruff, S. W., Christensen, P. R., Blaney, D. L., Farrand, W. H., Johnson, J. R., Michalski, J. R., ... & Squyres, S. W. (2006). The rocks of Gusev Crater as viewed by the Mini-TES instrument. *Journal of Geophysical Research: Planets*, *111*(E12).

Thomson, J. L., & Salisbury, J. W. (1993). The mid-infrared reflectance of mineral mixtures (7–14 μm). *Remote Sensing of Environment*, *45*(1), 1-13.

Tornabene, L. L., Moersch, J. E., McSween, H. Y., Hamilton, V. E., Piatek, J. L., & Christensen, P. R. (2008). Surface and crater-exposed lithologic units of the Isidis Basin as mapped by coanalysis of THEMIS and TES derived data products. *Journal of Geophysical Research: Planets (1991–2012)*, *113*(E10). https://doi.org/10.1029/2007je002988

Udry, A., Howarth, G. H., Herd, C. D. K., Day, J. M. D., Lapen, T. J., & Filiberto, J. (2020). What Martian Meteorites Reveal About the Interior and Surface of Mars. *Journal of Geophysical Research: Planets*, *125*(12). https://doi.org/10.1029/2020je006523

Vincent, R. K., Rowan, L. C., Gillespie, R. E., & Knapp, C. (1975). Thermal-infrared spectra and chemical analyses of twenty-six igneous rock samples. *Remote Sensing of Environment*, *4*, 199-209.

Warren, P. H., Greenwood, J. P., & Rubin, A. E. (2004). Los Angeles: A tale of two stones. *Meteoritics & Planetary Science*, *39*(1), 137–156. https://doi.org/10.1111/j.1945-5100.2004.tb00054.x

Zipfel, J., Schröder, C., Jolliff, B. L., Gellert, R., Herkenhoff, K. E., Rieder, R., et al. (2011). Bounce rock – A shergottite-like basalt encountered at Meridiani Planum, Mars. *Meteoritics & Planetary Science,* 46(1), 1-20. https://dio.org/10.1111/j.1945-5100.2010.01127.x

Chapter 6: Conclusions

In this PhD, I have investigated the Martian meteorites, primarily shergottites, to help improve the application of linear modelling to Martian surface mid-infrared spectra. With the number of space exploration missions increasing, fine tuning remote sensing datasets and tools has immediate applications to furthering our understanding of the solar system.

Combining an in-depth study of the mineralogy and geochemistry of the shergottites, I have shown the validity of using pyroxene spectra directly from thin sections to be used in future linear modelling of Martian surface spectra. In Chapter 2, I detailed the pipeline of analytical techniques used to solve the research questions of this PhD. Due to the rarity of the Martian meteorites, all the techniques were (mostly) non-destructive. This enabled multiple analyses to by overlapped and used in tandem, as the same surface could be analysed multiple times with different instruments. This was taken advantage of in Chapter 3, where I undertook a detailed classification of new basaltic (NWA 10441 and NWA 12335) and poikilitic (NWA 10818 and NWA 11043) shergottites. To confirm classification, I investigated multiple facets of the meteorites, from their geochemistry and texture to shock features and terrestrial weathering products. By using HRXCT, TIMA and LA-ICP-MS data, I found NWA 11043's REE pattern had been disturbed by terrestrial weathering and using *in-situ* analysis enabled weathering products to be avoided when inferring the REE pattern of the meteorite. The mineralogical and geochemical analysis of all the meteorites laid the groundwork for the infrared spectroscopic investigations in the next chapters.

Chapter 4 focused on building a database of Martian-specific mineralogy by measuring infrared spectra of the mineralogy (primarily pyroxene) of the shergottites. This was to fill a compositional hole in the currently available pyroxene spectra that are used for linear modelling of the Martian meteorites and surface. By combining element maps for target grains reconnaissance, EBSD mapping to determine crystallographic orientations, quantitative mapping of the target grains to determine geochemistry and infrared spectroscopic mapping of key areas, I produced 11 pyroxene spectra that satisfy the requirements (having a random orientation and known geochemistry) for use in linear modelling. Importantly, these spectra are now representative of previously

unknown compositions. To test if these pyroxene spectra offer any associated improvements over the previously available pyroxene spectra, I linearly modelled nine basaltic shergottites in Chapter 5. Basaltic shergottites were chosen, as their major mineralogy consists of pyroxene (augite, pigeonite and in some cases pyroxferroite) and maskelynite. As the spectral profile of maskelynite displays a smooth structure, the effective emissivity bands of the basaltic shergottite spectra would largely be due to the presence of pyroxene. By modelling these rocks in separate runs (varying the spectral end members) using a Martian-derived spectral library and a terrestrial/synthetic derived library, I could evaluate the effectiveness of the new Martian pyroxene spectra. The results of Chapter 5 demonstrated that there was a significant improvement using the compositionally representative Martian pyroxene spectra over the terrestrial/synthetic pyroxene spectra. I was able to spectrally fit to different basaltic shergottites with relatively different modal abundances of pyroxene (augite and pigeonite) while the terrestrial/synthetic library struggled to differentiate between the different shergottites. This is largely down to the composition of the pyroxene spectra, the closer it is to the true composition, the more representative the model of the measured bulk spectra will be.

Overall, modelling the basaltic shergottites has demonstrated the utility of acquiring this Martian pyroxene spectra for use in linear modelling. By using a more representative spectral library, more information can be discerned from the results. This modelling acted as a proof of concept for the effectiveness of the Martian pyroxene spectra. The next step would be to use the new spectra to supplement the currently available mineral spectra to linearly model TES surface spectra of Mars. Modelling surface spectra is quite different to modelling the Martian meteorites. Without prior knowledge of the surface and generally lower quality data to work with (i.e., lower signal-to-noise), the Martian pyroxene spectra will provide a much needed expansion to the current spectral library that covers a wide variety of mineral compositions. I would expect, given the benefit of using them for modelling the basaltic shergottites, we should see an improvement in the MIR modelling of pyroxene-rich areas of the Martian surface and they should help, in combination with other methods, to constrain the location of the source craters of the Martian meteorites.

Chapter 7: Bibliography

Adams, J. B. (1993). Imaging spectroscopy: Interpretation based on spectral mixture analysis. *Remote geochemical analysis: Elemental and mineralogical composition*, 145-166.

Agee, C. B., Wilson, N. V., McCubbin, F. M., Ziegler, K., Polyak, V. J., Sharp, Z. D., et al. (2013). Unique Meteorite from Early Amazonian Mars: Water-Rich Basaltic Breccia Northwest Africa 7034. *Science*, *339*(6121), 780–785. https://doi.org/10.1126/science.1228858

Aines, R. D., & Rossman, G. R. (1984). Water in minerals? A peak in the infrared. *Journal of Geophysical Research: Solid Earth*, *89*(B6), 4059-4071.

Ali, A., Jabeen, I., Gregory, D., Verish, R., & Banerjee, N. R. (2016). New triple oxygen isotope data of bulk and separated fractions from SNC meteorites: Evidence for mantle homogeneity of Mars. *Meteoritics & Planetary Science*, *51*(5), 981–995. https://doi.org/10.1111/maps.12640

Anand, M.; James, S.; Greenwood, R. C.; Johnson, D.; Franchi, I. A. and Grady, M. M. (2008). Mineralogy and Geochemistry of Shergottite RBT 04262. *Lunar and Planetary Science Conference XXXIX*, (abs) 2173.

Armytage, R. M. G., Debaille, V., Brandon, A. D., & Agee, C. B. (2018). A complex history of silicate differentiation of Mars from Nd and Hf isotopes in crustal breccia NWA 7034. *Earth and Planetary Science Letters*, *502*(Science 339 2013), 274–283. https://doi.org/10.1016/j.epsl.2018.08.013

Arnold, J. A., Glotch, T. D., & Plonka, A. M. (2014). Mid-infrared optical constants of clinopyroxene and orthoclase derived from oriented single-crystal reflectance spectra. *American Mineralogist*, *99*(10), 1942-1955.

Aronson, J. R., Emslie, A. G., & McLinden, H. G. (1966). Infrared spectra from fine particulate surfaces. *Science*, *152*(3720), 345-346.

Artemieva, N. & Ivanov, B. (2004) Launch of martian meteorites in oblique impacts. *Icarus 171*, 84-101. doi.org/10.1016/j.icarus.2004.05.003

Balta, J. B., Sanborn, M., McSween, H. Y., & Wadhwa, M. (2013). Magmatic history and parental melt composition of olivine-phyric shergottite LAR 06319: Importance of magmatic degassing and olivine antecrysts in Martian magmatism. *Meteoritics & Planetary Science*, *48*(8), 1359–1382. https://doi.org/10.1111/maps.12140

Bandfield, J. L., Hamilton, V. E., & Christensen, P. R. (2000). A Global View of Martian Surface Compositions from MGS-TES. *Science*, *287*(5458), 1626–1630. https://doi.org/10.1126/science.287.5458.1626

Bandfield, J. L. (2002). Global mineral distributions on Mars. *Journal of Geophysical Research: Planets (1991–2012)*, *107*(E6), 9-1-9–20. https://doi.org/10.1029/2001je001510

Bandfield, J. L., Rogers, D., Smith, M. D., & Christensen, P. R. (2004). Atmospheric correction and surface spectral unit mapping using Thermal Emission Imaging System data. *Journal of Geophysical Research: Planets (1991–2012)*, *109*(E10). https://doi.org/10.1029/2004je002289

Baratoux, D., Toplis, M. J., Monnereau, M., & Gasnault, O. (2011). Thermal history of Mars inferred from orbital geochemistry of volcanic provinces. *Nature*, *472*(7343), 338–341. https://doi.org/10.1038/nature09903

Barrat, J. A., Gillet, P., Sautter, V., Jambon, A., Javoy, M., Göpel, C., Lesourd, M., Keller, F., Petit, E. 2002a. Petrology and chemistry of the basaltic shergottite North West Africa 480. *Meteoritics and Planetary Science* 37:487–499.

Barrat, J. A., Jambon, A., Bohn, M., Gillet, P., Sautter, V., Göpel, C., Lesourd, M., Keller, F. 2002b. Petrology and chemistry of the Picritic Shergottite North West Africa 1068 (NWA 1068). *Geochimica et Cosmochimica Acta* 66:3505-3518

Barrat, J., & Bollinger, C. (2010). Geochemistry of the Martian meteorite ALH 84001, revisited. *Meteoritics & Planetary Science*, *45*(4), 495–512. https://doi.org/10.1111/j.1945-5100.2010.01042.x

Babadzhanov, P. B. 2002. Fragmentation and densities of meteoroids. *Astronomy & Astrophysics* 384:317-321.

Benedix, G. K., Hamilton, V. E. and Reddy, S. M. (2016). μ-FTIR spectroscopy and electron backscatter diffraction of Martian shergottite Robert Massif 04262. *47th Lunar and Planetary Science Conference,* Abs#: 1903.

Benoit P. h, Sears D. w g, Akridge J. m c, Bland P. a, Berry F. j, and Pillinger C. t. 2000. The non-trivial problem of meteorite pairing. *Meteoritics & Planetary Science* 35:393–417.

Bertka, C. M., & Holloway, J. R. (1993). Pigeonite at solidus temperatures: Implications for partial melting. *Journal of Geophysical Research: Solid Earth*, *98*(B11), 19755–19766. https://doi.org/10.1029/93jb02173

Bland, P. A., Berry, F. J., Smith, T. B., Skinner, S. J., Pillinger, C. T. 1996. The flux of meteorites to the Earth and weathering in hot desert ordinary chondrite finds. *Geochimica et Cosmochimica Acta* 60:2053-2059.

Bogard, D. D., & Johnson, P. (1983). Martian Gases in an Antarctic Meteorite? *Science*, *221*(4611), 651–654. https://doi.org/10.1126/science.221.4611.651

Borg, L. E., Nyquist, L. E., Wiesmann, H., & Reese, Y. (2002). Constraints on the petrogenesis of Martian meteorites from the Rb-Sr and Sm-Nd isotopic systematics of the lherzolitic shergottites ALH77005 and LEW88516. *Geochimica et Cosmochimica Acta*, *66*(11), 2037-2053.

Borg, L. E., & Draper, D. S. (2003). A petrogenetic model for the origin and compositional variation of the martian basaltic meteorites. *Meteoritics & Planetary Science*, *38*(12), 1713–1731. https://doi.org/10.1111/j.1945-5100.2003.tb00011.x

Bouvier, A., Blichert-Toft, J., & Albarède, F. (2009). Martian meteorite chronology and the evolution of the interior of Mars. *Earth and Planetary Science Letters*, *280*(1–4), 285–295. https://doi.org/10.1016/j.epsl.2009.01.042

Bouvier, A., Gattacceca, J., Agee, C., Grossman, J. and Metzler, K. 2017a. The Meteoritical Bulletin, No. 104. *Meteoritics & Planetary Science* 52:2284.

Bouvier, A., Gattacceca, J., Grossman, J. and Metzler, K. 2017b. The Meteoritical Bulletin, No. 105. *Meteoritics & Planetary Science* 52:2411.

Bridges, J. C., & Warren, P. H. (2006). The SNC meteorites: basaltic igneous processes on Mars. *Journal of the Geological Society*, *163*(2), 229–251. https://doi.org/10.1144/0016-764904-501

Cao, T., He, Q., & Xue, Z. (2018). Petrogenesis of basaltic shergottite NWA 8656. *Earth and Planetary Physics*, *2*(5), 384–397. https://doi.org/10.26464/epp2018036

Carter, J., Poulet, F., Bibring, J. -P., Mangold, N., & Murchie, S. (2013). Hydrous minerals on Mars as seen by the CRISM and OMEGA imaging spectrometers: Updated global view. *Journal of Geophysical Research: Planets*, *118*(4), 831–858. https://doi.org/10.1029/2012je004145

Cassata, W. S., Cohen, B. E., Mark, D. F., Trappitsch, R., Crow, C. A., Wimpenny, J., et al. (2018). Chronology of martian breccia NWA 7034 and the formation of the martian crustal dichotomy. *Science Advances*, *4*(5), eaap8306. https://doi.org/10.1126/sciadv.aap8306

Chabal, Y. J. (1988). Surface infrared spectroscopy. *Surface Science Reports*, *8*(5-7), 211-357.

Chao, E. C. T., Minkin, J. A., Frondel, C., Klein, C., Drake, J. C., Fuchs, L., Tani, B., Smith, J. V., Anderson, A. T., Moore, P. B., Zechman, G. R., Traill, R. J., Plant., A. G., Douglas, J. A. V., Dence, M. R. (1970). Pyroxferroite, a new calcium-bearing iron silicate from Tranquillity Base. *Proceedings of the Apollo 11 Lunar Science Conference, 1,* 65-79.

Chevrel, M. O., Baratoux, D., Hess, K.-U., & Dingwell, D. B. (2014). Viscous flow behavior of tholeiitic and alkaline Fe-rich martian basalts. *Geochimica et Cosmochimica Acta*, *124*, 348–365. https://doi.org/10.1016/j.gca.2013.08.026

Christensen, P. R., Bandfield, J. L., Clark, R. N., Edgett, K. S., Hamilton, V. E., Hoefen, T., et al. (2000a). Detection of crystalline hematite mineralization on Mars by the Thermal Emission Spectrometer: Evidence for near-surface water. *Journal of Geophysical Research: Planets*, *105*(E4), 9623–9642. https://doi.org/10.1029/1999je001093

Christensen, P. R., Bandfield, J. L., Hamilton, V. E., Howard, D. A., Lane, M. D., Piatek, J. L., et al. (2000b). A thermal emission spectral library of rock-forming minerals. *Journal of Geophysical Research: Planets*, *105*(E4), 9735–9739. https://doi.org/10.1029/1998je000624

Christensen, P. R., Bandfield, J. L., Smith, M. D., Hamilton, V. E., & Clark, R. N. (2000c). Identification of a basaltic component on the Martian surface from Thermal Emission Spectrometer data. *Journal of Geophysical Research: Planets*, *105*(E4), 9609–9621. https://doi.org/10.1029/1999je001127

Christensen, P. R., Bandfield, J. L., Hamilton, V. E., Ruff, S. W., Kieffer, H. H., Titus, T. N., et al. (2001). Mars Global Surveyor Thermal Emission Spectrometer experiment: Investigation description and surface science results. *Journal of Geophysical Research: Planets*, *106*(E10), 23823–23871. https://doi.org/10.1029/2000je001370

Christensen, P. R., Bandfield, J. L., III, J. F. B., Gorelick, N., Hamilton, V. E., Ivanov, A., et al. (2003a). Morphology and Composition of the Surface of Mars: Mars Odyssey

THEMIS Results. *Science*, *300*(5628), 2056–2061. https://doi.org/10.1126/science.1080885

Christensen, P. R., Mehall, G. L., Silverman, S. H., Anwar, S., Cannon, G., Gorelick, N., et al. (2003b). Miniature Thermal Emission Spectrometer for the Mars Exploration Rovers. *Journal of Geophysical Research: Planets (1991–2012)*, *108*(E12). https://doi.org/10.1029/2003je002117

Christensen, P. R., Jakosky, B. M., Kieffer, H. H., Malin, M. C., Jr, H. Y. M., Nealson, K., et al. (2004a). The Thermal Emission Imaging System (THEMIS) for the Mars 2001 Odyssey Mission. *Space Science Reviews*, *110*(1/2), 85–130. https://doi.org/10.1023/b:spac.0000021008.16305.94

Christensen, P. R., Wyatt, M. B., Glotch, T. D., Rogers, A. D., Anwar, S., Arvidson, R. E., et al. (2004b). Mineralogy at Meridiani Planum from the Mini-TES Experiment on the Opportunity Rover. *Science*, *306*(5702), 1733–1739. https://doi.org/10.1126/science.1104909

Christensen, P. R., McSween, H. Y., Bandfield, J. L., Ruff, S. W., Rogers, A. D., Hamilton, V. E., et al. (2005). Evidence for magmatic evolution and diversity on Mars from infrared observations. *Nature*, *436*(7050), 504–509. https://doi.org/10.1038/nature03639

Collinet, M., Charlier, B., Namur, O., Oeser, M., Médard, E., & Weyer, S. (2017). Crystallization history of enriched shergottites from Fe and Mg isotope fractionation in olivine megacrysts. *Geochimica et Cosmochimica Acta*, *207*(Philos. Trans. Roy. Soc. B: Biol. Sci. 361 2006), 277–297. https://doi.org/10.1016/j.gca.2017.03.029

Combs, L. M., Udry, A., Howarth, G. H., Righter, M., Lapen, T. J., Gross, J., et al. (2019). Petrology of the enriched poikilitic shergottite Northwest Africa 10169: Insight into the martian interior. *Geochimica et Cosmochimica Acta*. https://doi.org/10.1016/j.gca.2019.07.001

Corrigan, C. M., Velbel, M. A., & Vicenzi, E. P. (2015). Modal abundances of pyroxene, olivine, and mesostasis in nakhlites: Heterogeneity, variation, and implications for nakhlite emplacement. *Meteoritics & Planetary Science*, *50*(9), 1497–1511. https://doi.org/10.1111/maps.12492

Cousin, A., Sautter, V., Payré, V., Forni, O., Mangold, N., Gasnault, O., et al. (2017). Classification of igneous rocks analyzed by ChemCam at Gale crater, Mars. *Icarus*, *288*, 265–283. https://doi.org/10.1016/j.icarus.2017.01.014

Crisp, J. A. (1984). Rates of magma emplacement and volcanic output. *Journal of Volcanology and Geothermal Research*, *20*(3–4), 177–211. https://doi.org/10.1016/0377-0273(84)90039-8

Crozaz, G., and Wadhwa, M. 2001. The terrestrial alteration of Saharan shergottites Dar al Gani 476 and 489: a case study of weathering in a hot desert environment. *Geochimica et Cosmochimica Acta* 65:971-977.

Crozaz, G., Floss, C., Wadhwa, M. 2003. Chemical alteration and REE mobilization in meteorites from hot and cold deserts. *Geochimica et Cosmochimica Acta* 67:4727-4741.

Daly, L., Piazolo, S., Lee, M. R., Griffin, S., Chung, P., Campanale, F., et al. (2019). Understanding the emplacement of Martian volcanic rocks using petrofabrics of the nakhlite meteorites. *Earth and Planetary Science Letters*, *520*, 220–230. https://doi.org/10.1016/j.epsl.2019.05.050

Debaille, V., Yin, Q.-Z., Brandon, A. D., & Jacobsen, B. (2008). Martian mantle mineralogy investigated by the 176Lu–176Hf and 147Sm–143Nd systematics of shergottites. *Earth and Planetary Science Letters*, *269*(1–2), 186–199. https://doi.org/10.1016/j.epsl.2008.02.008

Duncan, M. S., Schmerr, N. C., Bertka, C. M., & Fei, Y. (2018). Extending the Solidus for a Model Iron-Rich Martian Mantle Composition to 25 GPa. *Geophysical Research Letters*, *45*(19), 10,211-10,220. https://doi.org/10.1029/2018gl078182

Diem, M., Roberts, G. M., Lee, O., & Barlow, A. (1988). Design and performance of an optimized dispersive infrared dichrograph. *Applied spectroscopy*, *42*(1), 20-27.

El-Dasher, B. S., & Torres, S. G. (2009). Electron Backscatter Diffraction in Materials Science, 339–344. https://doi.org/10.1007/978-0-387-88136-2_25

El Goresy, A., Gillet, Ph., Miyahara, M., Ohtani, E., Ozawa, S., Beck, P., Montagnac, G. 2013. Shock-induced deformation of Shergottites: Shock-pressures and perturbations of magmatic ages on Mars. *Geochimica et Cosmochimica Acta* 101:233-262.

Faix, O. (1992). Fourier transform infrared spectroscopy. In *Methods in lignin chemistry* (pp. 83-109). Springer, Berlin, Heidelberg.

Feely, K. C., & Christensen, P. R. (1999). Quantitative compositional analysis using thermal emission spectroscopy: Application to igneous and metamorphic rocks. *Journal of Geophysical Research: Planets*, *104*(E10), 24195–24210. https://doi.org/10.1029/1999je001034

Ferdous, J., Brandon, A. D., Peslier, A. H., & Pirotte, Z. (2017). Evaluating crustal contributions to enriched shergottites from the petrology, trace elements, and Rb-Sr and Sm-Nd isotope systematics of Northwest Africa 856. *Geochimica et Cosmochimica Acta*, *211*(Science 339 2013), 280–306. https://doi.org/10.1016/j.gca.2017.05.032

Filiberto, J., Mussel White, D. S., Gross, J., Burgess, K., LE, L., & Treiman, A. H. (2010). Experimental petrology, crystallization history, and parental magma characteristics of olivine-phyric shergottite NWA 1068: Implications for the petrogenesis of "enriched" olivine-phyric shergottites. *Meteoritics & Planetary Science*, *45*(8), 1258–1270. https://doi.org/10.1111/j.1945-5100.2010.01080.x

Filiberto, J., Chin, E., Day, J. M. D., Franchi, I. A., Greenwood, R. C., Gross, J., et al. (2012). Geochemistry of intermediate olivine-phyric shergottite Northwest Africa

6234, with similarities to basaltic shergottite Northwest Africa 480 and olivine-phyric shergottite Northwest Africa 2990. *Meteoritics & Planetary Science*, *47*(8), 1256–1273. https://doi.org/10.1111/j.1945-5100.2012.01382.x

Filiberto J., Gross J., Trela J., and Ferré E. C. 2014. Gabbroic Shergottite Northwest Africa 6963: An intrusive sample of Mars. *American Mineralogist* 99:601–606.

Filiberto, J. (2017). Geochemistry of Martian basalts with constraints on magma genesis. *Chemical Geology*, *466*(Earth Planet. Sci. Lett. 224 3-4 2004), 1–14. https://doi.org/10.1016/j.chemgeo.2017.06.009

Filiberto, J., Gross, J., Udry, A., Trela, J., Wittmann, A., Cannon, K. M., et al. (2018). Shergottite Northwest Africa 6963: A Pyroxene-Cumulate Martian Gabbro. *Journal of Geophysical Research: Planets*, *123*(7), 1823–1841. https://doi.org/10.1029/2018je005635

First, E., & Hammer, J. (2016). Igneous cooling history of olivine-phyric shergottite Yamato 980459 constrained by dynamic crystallization experiments. *Meteoritics & Planetary Science*, *51*(7), 1233–1255. https://doi.org/10.1111/maps.12659

Forman, L. V., Timms, N. E., Bland, P. A., Daly, L., Benedix, G. K., Trimby, P. W. 2019. A morphologic and crystallographic comparison of CV chondrite matrices. *Meteoritics & Planetary Science* 54:2633-2651.

Fritz, J., Artemieva, N., & Greshake, A. (2005). Ejection of Martian meteorites. *Meteoritics & Planetary Science*, *40*(9–10), 1393–1411. https://doi.org/10.1111/j.1945-5100.2005.tb00409.x

Gattacceca, J., Bouvier, A., Grossman, J., Metzler, K. and Uehara, M. 2019. The Meteoritical Bulletin, No. 106. *Meteoritics & Planetary Science* 54:469-471.

Gattacceca, J., McCubbin, F. M., Bouvier, A. and Grossman, J. 2020. The Meteoritical Bulletin, No. 107. *Meteoritics & Planetary Science* 55:460-462.

Godel, B. 2013. High-Resolution X-Ray Computed Tomography and Its Application to Ore Deposits: From Data Acquisition to Quantitative Three-Dimensional Measurements with Case Studies from Ni-Cu-PGE Deposits. *Economic Geology* 108:2005-2019.

Goldstein, J. I., Newbury, D. E., Echlin, P., Joy, D. C., Lyman, C. E., Lifshin, E., et al. (2003). Scanning Electron Microscopy and X-ray Microanalysis, Third Edition. https://doi.org/10.1007/978-1-4615-0215-9

Goodrich, C. A. (2002). Olivine-phyric martian basalts: A new type of shergottite. *Meteoritics & Planetary Science*, *37*(S12), B31–B34. https://doi.org/10.1111/j.1945-5100.2002.tb00901.x

Goodrich, C. A., Herd, C. D. K., Taylor, L. A. 2003. Spinels and oxygen fugacity in olivine-phyric and lherzolitic shergottites. *Meteoritics & Planetary Science* 38:1773-1792.

Griffiths, P. R., & De Haseth, J. A. (2007). *Fourier transform infrared spectrometry* (Vol. 171). John Wiley & Sons.

Gross, J., Treiman, A. H., Filiberto, J., & Herd, C. D. K. (2011). Primitive olivine-phyric shergottite NWA 5789: Petrography, mineral chemistry, and cooling history imply a magma similar to Yamato-980459. *Meteoritics & Planetary Science*, *46*(1), 116–133. https://doi.org/10.1111/j.1945-5100.2010.01152.x

Grott, M., & Breuer, D. (2010). On the spatial variability of the Martian elastic lithosphere thickness: Evidence for mantle plumes? *Journal of Geophysical Research: Planets (1991–2012)*, *115*(E3). https://doi.org/10.1029/2009je003456

Günther, D., & Hattendorf, B. (2005). Solid sample analysis using laser ablation inductively coupled plasma mass spectrometry. *TrAC Trends in Analytical Chemistry*, *24*(3), 255–265. https://doi.org/10.1016/j.trac.2004.11.017

Halliday, A. N., Wänke, H., Birck, J.-L., & Clayton, R. N. (2001). The Accretion, Composition and Early Differentiation of Mars. *Space Science Reviews*, *96*(1–4), 197–230. https://doi.org/10.1023/a:1011997206080

Hamid, S. H., & Prichard, W. H. (1988). Application of infrared spectroscopy in polymer degradation. *Polymer-Plastics Technology and Engineering*, *27*(3), 303-334.

Hamilton, V. E., Christensen, P. R., & McSween, H. Y. (1997). Determination of Martian meteorite lithologies and mineralogies using vibrational spectroscopy. *Journal of Geophysical Research: Planets*, *102*(E11), 25593–25603. https://doi.org/10.1029/97je01874

Hamilton, V. E. (2000). Thermal infrared emission spectroscopy of the pyroxene mineral series. *Journal of Geophysical Research: Planets*, *105*(E4), 9701–9716. https://doi.org/10.1029/1999je001112

Hamilton, V. E., Wyatt, M. B., McSween, H. Y., & Christensen, P. R. (2001). Analysis of terrestrial and Martian volcanic compositions using thermal emission spectroscopy: 2. Application to Martian surface spectra from the Mars Global Surveyor Thermal Emission Spectrometer. *Journal of Geophysical Research: Planets*, *106*(E7), 14733–14746. https://doi.org/10.1029/2000je001353

Hamilton, V. E. (2003a). Thermal infrared emission spectroscopy of titanium-enriched pyroxenes. *Journal of Geophysical Research: Planets (1991–2012)*, *108*(E8). https://doi.org/10.1029/2003je002052

Hamilton, V. E., Christensen, P. R., McSween, H. Y., & Bandfield, J. L. (2003b). Searching for the source regions of Martian meteorites using MGS TES: Integrating Martian meteorites into the global distribution of igneous materials on Mars. *Meteoritics & Planetary Science*, *38*(6), 871–885. https://doi.org/10.1111/j.1945-5100.2003.tb00284.x

Hamilton, V. E. (2010). Thermal infrared (vibrational) spectroscopy of Mg–Fe olivines: A review and applications to determining the composition of planetary

surfaces. *Chemie Der Erde - Geochemistry*, *70*(1), 7–33. https://doi.org/10.1016/j.chemer.2009.12.005

Hamilton, V. E., & Ruff, S. W. (2012). Distribution and characteristics of Adirondack-class basalt as observed by Mini-TES in Gusev crater, Mars and its possible volcanic source. *Icarus*, *218*(2), 917–949. https://doi.org/10.1016/j.icarus.2012.01.011

Hamilton, V. E., Simon, A. A., Christensen, P. R., Reuter, D. C., Clark, B. E., Barucci, M. A., et al. (2019). Evidence for widespread hydrated minerals on asteroid (101955) Bennu. *Nature Astronomy*, *3*(4), 332-340.

Hamilton, V. E., Goodrich, C. A., Treiman, A. H., Connolly, H. C., Zolensky, M. E., & Shaddad, M. H. (2020). Meteoritic evidence for a Ceres-sized water-rich carbonaceous chondrite parent asteroid. *Nature Astronomy*, 1-6.

Hanel, R., Conrath, B., Hovis, W., Kunde, V., Lowman, P., Maguire, W., et al. (1972). Investigation of the Martian environment by infrared spectroscopy on Mariner 9. *Icarus*, *17*(2), 423-442.

Hanna, R. D., Hamilton, V. E., Haberle, C. W., King, A. J., Abreu, N. M., & Friedrich, J. M. (2020). Distinguishing relative aqueous alteration and heating among CM chondrites with IR spectroscopy. *Icarus*, *346*, 113760.

Harvey, R. P., & McSween, H. Y. (1996). A possible high-temperature origin for the carbonates in the Martian meteorite ALH84001. *Nature*, *382*(6586), 49-51.

He, Q., Xiao, L., Balta, J. B., Baziotis, I. P., Hsu, W., & Guan, Y. (2015). Petrography and geochemistry of the enriched basaltic shergottite Northwest Africa 2975. *Meteoritics & Planetary Science*, *50*(12), 2024–2044. https://doi.org/10.1111/maps.12571

Head, J. N., Melosh, H. J., & Ivanov, B. A. (2002). Martian Meteorite Launch: High-Speed Ejecta from Small Craters. *Science*, *298*(5599), 1752–1756. https://doi.org/10.1126/science.1077483

Herd, C. D. K. (2003). The oxygen fugacity of olivine-phyric martian basalts and the components within the mantle and crust of Mars. *Meteoritics & Planetary Science*, *38*(12), 1793–1805. https://doi.org/10.1111/j.1945-5100.2003.tb00015.x

Herd, C. D. K., Walton, E. L., Agee, C. B., Muttik, N., Ziegler, K., Shearer, C. K., et al. (2017). The Northwest Africa 8159 martian meteorite: Expanding the martian sample suite to the early Amazonian. *Geochimica et Cosmochimica Acta*, *218*(Science 339 2013), 1–26. https://doi.org/10.1016/j.gca.2017.08.037

Herd, C. D. K., Tornabene, L. L., Bowling, T. J., Walton, E. L., Sharp, T. G., Melosh, H. J., et al. (2018, March). Linking Martian Meteorites to their Source Craters: New Insights. In *Lunar and Planetary Science Conference* (No. 2083, p. 2266).

Hook, S. J., & Kahle, A. B. (1996). The micro Fourier transform interferometer (μFTIR)—a new field spectrometer for acquisition of infrared data of natural surfaces. *Remote Sensing of Environment*, *56*(3), 172-181.

Howarth, G. H., Pernet-Fisher, J. F., Balta, J. B., Barry, P. H., Bodnar, R. J., & Taylor, L. A. (2014). Two-stage polybaric formation of the new enriched, pyroxene-oikocrystic, lherzolitic shergottite, NWA 7397. *Meteoritics & Planetary Science*, *49*(10), 1812–1830. https://doi.org/10.1111/maps.12357

Howarth, G. H., Pernet-Fisher, J. F., Bodnar, R. J., Taylor, L. A. 2015. Evidence for the exsolution of Cl-rich fluids in martian magmas: Apatite petrogenesis in the enriched lherzolitic shergottite Northwest Africa 7755. *Geochimica et Cosmochimica Acta* 166:234-248.

Howarth, G. H., Udry, A., & Day, J. M. D. (2018). Petrogenesis of basaltic shergottite Northwest Africa 8657: Implications for fO2 correlations and element redistribution during shock melting in shergottites. *Meteoritics & Planetary Science*, *53*(2), 249–267. https://doi.org/10.1111/maps.12999

Hrstka, T., Gottlieb, P., Skála, R., Breiter, K., & Motl, D. (2018). Automated mineralogy and petrology - applications of TESCAN Integrated Mineral Analyzer (TIMA). *Journal of Geosciences*, 47–63. https://doi.org/10.3190/jgeosci.250

Hui, H., Peslier, A. H., Lapen, T. J., Shafer, J. T., Brandon, A. D., Irving, A. J. 2011. Petrogenesis of basaltic shergottite Northwest Africa 5298: Closed-system crystallization of an oxidized mafic melt. *Meteoritics & Planetary Science* 46:1313-1328.

Hunt, G. R. (1977). Spectral signatures of particulate minerals in the visible and near infrared. *Geophysics*, *42*(3), 501-513.

Humayun, M., Nemchin, A., Zanda, B., Hewins, R. H., Grange, M., Kennedy, A., et al. (2013). Origin and age of the earliest Martian crust from meteorite NWA 7533. *Nature*, *503*(7477), 513–516. https://doi.org/10.1038/nature12764

Humphreys, F. J. (2004). Characterisation of fine-scale microstructures by electron backscatter diffraction (EBSD). *Scripta Materialia*, *51*(8), 771–776. https://doi.org/10.1016/j.scriptamat.2004.05.016

Ikeda, Y., Kimura, M., Takeda, H., Shimoda, G., Kita, N. T., Morishita, Y., Suzuki, A., Jagoutz, E., Dreibus, G. 2006. Petrology of a new basaltic shergottite: Dhofar 378. *Antarctic Meteorite Research* 19:20-44.

Irving A.J., Kuehner S.M., Herd C.D.K., Gellissen M., Rumble D., Lapan T.J., Ralew S. and Altmann M. 2010. Olivine-bearing diabasic Shergottite Northwest Africa 5990: Petrology and composition of a new type of depleted Martian igneous rock. *41st Lunar and Planetary Science Conference,* abs#1833.

Jambon, A., Barrat, J. A., Sautter, V., Gillet, P., Göpel, C., Javoy, M., et al. (2002). The basaltic shergottite Northwest Africa 856: Petrology and chemistry. *Meteoritics & Planetary Science*, *37*(9), 1147–1164. https://doi.org/10.1111/j.1945-5100.2002.tb00885.x

Jambon, A., Sautter, V., Barrat, J.-A., Gattacceca, J., Rochette, P., Boudouma, O., et al. (2016). Northwest Africa 5790: Revisiting nakhlite petrogenesis. *Geochimica et Cosmochimica Acta*, *190*(Nature 294 1981), 191–212. https://doi.org/10.1016/j.gca.2016.06.032

Jaret, S. J., Woerner, W. R., Phillips, B. L., Ehm, L., Nekvasil, H., Wright, S. P., & Glotch, T. D. (2015). Maskelynite formation via solid-state transformation: Evidence of infrared and X-ray anisotropy. *Journal of Geophysical Research: Planets*, *120*(3), 570–587. https://doi.org/10.1002/2014je004764

Johnson, J. R., Hörz, F., Lucey, P. G., & Christensen, P. R. (2002). Thermal infrared spectroscopy of experimentally shocked anorthosite and pyroxenite: Implications for remote sensing of Mars. *Journal of Geophysical Research: Planets (1991–2012)*, *107*(E10), 3-1-3–14. https://doi.org/10.1029/2001je001517

Johnson, J. R., Hörz, F., & Staid, M. I. (2003). Thermal infrared spectroscopy and modeling of experimentally shocked plagioclase feldspars. *American Mineralogist*, *88*(10), 1575–1582. https://doi.org/10.2138/am-2003-1020

Jones, J. H. (2015). Various aspects of the petrogenesis of the Martian shergottite meteorites. *Meteoritics & Planetary Science*, *50*(4), 674–690. https://doi.org/10.1111/maps.12421

Kereszturi, A., & Chatzitheodoridis, E. (2016). Searching for the Source Crater of Nakhlite Meteorites. *Origins of Life and Evolution of Biospheres*, *46*(4), 455–471. https://doi.org/10.1007/s11084-016-9498-x

Ketcham, R. A. (2005). Three-dimensional grain fabric measurements using high-resolution X-ray computed tomography. *Journal of Structural Geology*, *27*(7), 1217–1228. https://doi.org/10.1016/j.jsg.2005.02.006

Kieffer, H. H., Neugebauer, G., Munch, G., Chase, S. C., & Miner, E. (1972). Infrared thermal mapping experiment: The Viking Mars orbiter. *Icarus*, *16*(1), 47–56. https://doi.org/10.1016/0019-1035(72)90136-4

Kieffer, H. H., Chase, S. C., Miner, E. D., Palluconi, F. D., Munch, G., Neugebauer, G., & Martin, T. Z. (1976). Infrared Thermal Mapping of the Martian Surface and Atmosphere: First Results. *Science*, *193*(4255), 780–786. https://doi.org/10.1126/science.193.4255.780

Kieffer, H. H., Martin, T. Z., Peterfreund, A. R., Jakosky, B. M., Miner, E. D., & Palluconi, F. D. (1977). Thermal and albedo mapping of Mars during the Viking primary mission. *Journal of Geophysical Research*, *82*(28), 4249–4291. https://doi.org/10.1029/js082i028p04249

Kiefer, W. S., Filiberto, J., Sandu, C., & Li, Q. (2015). The effects of mantle composition on the peridotite solidus: Implications for the magmatic history of Mars. *Geochimica et Cosmochimica Acta*, *162*, 247–258. https://doi.org/10.1016/j.gca.2015.02.010

Kizovski, T. V., Tait, K. T., Cecco, V. E. D., White, L. F., & Moser, D. E. (2019). Detailed mineralogy and petrology of highly shocked poikilitic shergottite Northwest Africa 6342. *Meteoritics & Planetary Science*, *54*(4), 768–784. https://doi.org/10.1111/maps.13255

Koch, J., & Günther, D. (2011). Review of the State-of-the-Art of Laser Ablation Inductively Coupled Plasma Mass Spectrometry. *Applied Spectroscopy*, *65*(5), 155A-162A. https://doi.org/10.1366/11-06255

Koeppen, W. C., & Hamilton, V. E. (2008). Global distribution, composition, and abundance of olivine on the surface of Mars from thermal infrared data. *Journal of Geophysical Research: Planets (1991–2012)*, *113*(E5). https://doi.org/10.1029/2007je002984

Kring, D. A., Gleason, J. D., Swindle, T. D., Nishiizumi, K., Caffee, M. W., Hill, D. H., et al. (2003). Composition of the first bulk melt sample from a volcanic region of Mars: Queen Alexandra Range 94201. *Meteoritics & Planetary Science*, *38*(12), 1833–1848. https://doi.org/10.1111/j.1945-5100.2003.tb00018.x

Lagain, A., Benedix, G. K., Servis, K., Baratoux, D., Bland, P. A., Rajšić, A., Devillepoix, H. A. R., Norman, C., Towner, M., Samson, E. K., Anderson, S. (in prep). 90 million craters on Mars: the key to finding the source locations of the meteorites.

Lanari, P., Vho, A., Bovay, T., Airaghi, L., & Centrella, S. (2019). Quantitative compositional mapping of mineral phases by electron probe micro-analyser. *Geological Society, London, Special Publications*, *478*(1), 39-63.

Lane, M. D., & Bishop, J. L. (2019). Mid-infrared (thermal) emission and reflectance spectroscopy. *Remote Compositional Analysis: Techniques for Understanding Spectroscopy*, 42-67.

Lapen, T. J., Righter, M., Andreasen, R., Irving, A. J., Satkoski, A. M., Beard, B. L., et al. (2017). Two billion years of magmatism recorded from a single Mars meteorite ejection site. *Science Advances*, *3*(2), e1600922. https://doi.org/10.1126/sciadv.1600922

Lawson, C. L., & Hanson, R. J. (1974). Linear least squares with linear inequality constraints. *Solving least squares problems*, 158-173.

Leroux, H., Devouard, B., Cordier, P., & Guyot, F. (2004). Pyroxene microstructure in the Northwest Africa 856 martian meteorite. *Meteoritics & Planetary Science*, *39*(5), 711–722. https://doi.org/10.1111/j.1945-5100.2004.tb00114.x

Lin, Y., Guan, Y., Wang, D., Kimura, M., & Leshin, L. A. (2005). Petrogenesis of the new lherzolitic shergottite Grove Mountains 99027: Constraints of petrography, mineral chemistry, and rare earth elements. *Meteoritics & Planetary Science*, *40*(11), 1599–1619. https://doi.org/10.1111/j.1945-5100.2005.tb00134.x

Lin, Y., Hu, S., Miao, B., Xu, L., Liu, Y., Xie, L., Feng, L., Yang, J. 2013. Grove Mountains 020090 enriched lherzolitic shergottite: A two-stage formation model. *Meteoritics & Planetary Science* 48:1572-1589.

Lindsley, D. H., & Burnham, C. W. (1970). Pyroxferroite: Stability and X-ray Crystallography of Synthetic Ca0.15Fe0.85SiO3 Pyroxenoid. *Science*, *168*(3929), 364–367. https://doi.org/10.1126/science.168.3929.364

Lindsley, D. H. (1983). Pyroxene thermometry. *American Mineralogist, 68*(5-6), 477-493.

Lindsley, D. H., & Andersen, D. J. (1983). A two-pyroxene thermometer. *Journal of Geophysical Research: Solid Earth*, *88*(S02), A887–A906. https://doi.org/10.1029/jb088is02p0a887

Lindsley, D. H., Nekvasil, H., & Glotch, T. D. (2019). Synthesis of pigeonites for spectroscopic studies. *American Mineralogist*, *104*(4), 615–618. https://doi.org/10.2138/am-2019-6869ccbyncnd

Liu, Y., Floss, C., Day, J. M. D., Hill, E., & Taylor, L. A. (2009). Petrogenesis of lunar mare basalt meteorite Miller Range 05035. *Meteoritics & Planetary Science*, *44*(2), 261–284. https://doi.org/10.1111/j.1945-5100.2009.tb00733.x

Llorca, J., Roszjar, J., Cartwright, J. A., Bischoff, A., Ott, U., Pack, A., Merchel, S., Rugel, G., Fimiani, L., Ludwig, P. and Casado, J. V. 2013. The Ksar Ghilane 002 shergottite—the 100th registered Martian meteorite fragment. *Meteoritics & Planetary Science* 48:493-513.

Lodders, K. (1998). A survey of shergottite, nakhlite and chassigny meteorites whole-rock compositions. *Meteoritics & Planetary Science*, *33*(S4), A183–A190. https://doi.org/10.1111/j.1945-5100.1998.tb01331.x

MacArthur, J. L., Bridges, J. C., Hicks, L. J., Burgess, R., Joy, K. H., Branney, M. J., et al. (2018). Mineralogical Constraints on the Thermal History of Martian Regolith Breccia Northwest Africa 8114. *Geochimica et Cosmochimica Acta*, *246*(J. Geophys. Res. Planets 110 2005), 267–298. https://doi.org/10.1016/j.gca.2018.11.026

Mancini, F., Alviola, R., Marshall, B., Satoh, H., & Papunen, H. (2000). THE MANGANESE SILICATE ROCKS OF THE EARLY PROTEROZOIC VITTINKI GROUP, SOUTHWESTERN FINLAND: METAMORPHIC GRADE AND GENETIC INTERPRETATIONS. *The Canadian Mineralogist*, *38*(5), 1103–1124. https://doi.org/10.2113/gscanmin.38.5.1103

McCoy, T. J., Taylor, G. J., & Keil, K. (1992). Zagami: Product of a two-stage magmatic history. *Geochimica et Cosmochimica Acta*, *56*(9), 3571–3582. https://doi.org/10.1016/0016-7037(92)90400-d

McCubbin, F. M., Elardo, S. M., Shearer, C. K., Smirnov, A., Hauri, E. H., & Draper, D. S. (2013). A petrogenetic model for the comagmatic origin of chassignites and nakhlites: Inferences from chlorine-rich minerals, petrology, and geochemistry. *Meteoritics & Planetary Science*, *48*(5), 819–853. https://doi.org/10.1111/maps.12095

McCubbin, F. M., Boyce, J. W., Novák-Szabó, T., Santos, A. R., Tartèse, R., Muttik, N., et al. (2016). Geologic history of Martian regolith breccia Northwest Africa 7034: Evidence for hydrothermal activity and lithologic diversity in the Martian crust. *Journal of Geophysical Research: Planets*, *121*(10), 2120–2149. https://doi.org/10.1002/2016je005143

McDonough, W. F., & Sun, S. (1995). The composition of the Earth. *Chemical Geology*, *120*(3–4), 223–253. https://doi.org/10.1016/0009-2541(94)00140-4

McFadden, L. A., & Cline, T. P. (2005). Spectral reflectance of Martian meteorites: Spectral signatures as a template for locating source region on Mars. *Meteoritics & Planetary Science*, *40*(2), 151–172. https://doi.org/10.1111/j.1945-5100.2005.tb00372.x

McKay, D. S., Gibson, E. K., Thomas-Keprta, K. L., Vali, H., Romanek, C. S., Clemett, S. J., ... & Zare, R. N. (1996). Search for past life on Mars: Possible relic biogenic activity in Martian meteorite ALH84001. *Science*, *273*(5277), 924-930.

McSween, H. Y., & Stolper, E. M. (1980). Basaltic meteorites. *Scientific American*, *242*(6), 54-63.

McSween, H. Y., Eisenhour, D. D., Taylor, L. A., Wadhwa, M., & Crozaz, G. (1996). QUE94201 shergottite: Crystallization of a Martian basaltic magma. *Geochimica et Cosmochimica Acta*, *60*(22), 4563–4569. https://doi.org/10.1016/s0016-7037(96)00265-7

McSween, H. Y., and Treiman, A. H., 1998. Martian meteorites, In Planetary Materials, Reviews in Mineralogy, edited by Papike, J. J: *Mineralogical Society of America* 36:6-1–6-53.

McSween, H. Y., Arvidson, R. E., Bell, J. F., Blaney, D., Cabrol, N. A., Christensen, P. R., et al. (2004). Basaltic Rocks Analyzed by the Spirit Rover in Gusev Crater. *Science*, *305*(5685), 842–845. https://doi.org/10.1126/science.3050842

McSween, H. Y., and McLennan, S. M. 2014. Mars, In Treatise on Geochemistry 2nd ed., edited by Heinrich D. Holland, Karl K. Turekian: *Elsevier* 251-300.

McSween, H. Y. (2015). Petrology on Mars. *American Mineralogist*, *100*(11–12), 2380–2395. https://doi.org/10.2138/am-2015-5257

Mees, F., Swennen, R., Van Geet, M., & Jacobs, P. (2003). Applications of X-ray computed tomography in the geosciences. *Geological Society, London, Special Publications*, *215*(1), 1-6.

Mikouchi T., Miyamoto M., and McKay G. A. 1998. Mineralogy of Antarctic basaltic shergottite Queen Alexandra Range 94201: Similarities to Elephant Moraine A79001 (Lithology B) martian meteorite. *Meteoritics & Planetary Science* 33:181–189.

Mikouchi, T., Miyamoto, M., McKay, G. A. 2001. Mineralogy and petrology of the Dar al Gani 476 martian meteorite: Implications for its cooling history and relationship to other shergottites. *Meteoritics & Planetary Science* 36:531-548.

Mikouchi, T., & Kurihara, T. (2008). Mineralogy and petrology of paired lherzolitic shergottites Yamato 000027, Yamato 000047, and Yamato 000097: Another fragment from a Martian "lherzolite" block. *Polar Science*, *2*(3), 175–194. https://doi.org/10.1016/j.polar.2008.06.003

Mikouchi, T., and Barrat, J.A. 2009. NWA 5029 basaltic shergottites: A clone of NWA 480/1460? *Meteoritics and Planetary Science Supplement, 72,* p.5344.

Mikouchi, T., & Takenouchi, A. (2016). Mineralogical Investigation of Yamato 002712 Basaltic Shergottite: Implications for the Redox Change During Crystallization. *47th Lunar and Planetary Science Conference*, Abs# 1903.

Milam, K. A., McSween, H. Y., Hamilton, V. E., Moersch, J. M., & Christensen, P. R. (2004). Accuracy of plagioclase compositions from laboratory and Mars spacecraft thermal emission spectra. *Journal of Geophysical Research: Planets (1991–2012)*, *109*(E4). https://doi.org/10.1029/2003je002097

Minitti, M. E., & Hamilton, V. E. (2010). A search for basaltic-to-intermediate glasses on Mars: Assessing Martian crustal mineralogy. *Icarus*, *210*(1), 135–149. https://doi.org/10.1016/j.icarus.2010.06.028

Mittlefehldt, D. W. (1994). ALH84001, a cumulate orthopyroxenite member of the Martian meteorite clan. *Meteoritics*, *29*(2), 214-221.

Morlok, A., Bischoff, A., Patzek, M., Sohn, M., & Hiesinger, H. (2017). Chelyabinsk – a rock with many different (stony) faces: An infrared study. *Icarus*, *284*(Remote Sens. Environ. 113 2009), 431–442. https://doi.org/10.1016/j.icarus.2016.11.030

Mouginis-Mark, P. J., McCoy, T. J., Taylor, G. J., & Keil, K. (1992). Martian parent craters for the SNC meteorites. *Journal of Geophysical Research: Planets, 97*(E6), 10213-10225. https://doi.org/10.1029/92jeoo612

Murchie, S., Arvidson, R., Bedini, P., Beisser, K., Bibring, J. -P., Bishop, J., et al. (2007). Compact Reconnaissance Imaging Spectrometer for Mars (CRISM) on Mars Reconnaissance Orbiter (MRO). *Journal of Geophysical Research: Planets (1991–2012)*, *112*(E5). https://doi.org/10.1029/2006je002682

Mustard, J. F., Murchie, S. L., Pelkey, S. M., Ehlmann, B. L., Milliken, R. E., Grant, J. A., et al. (2008). Hydrated silicate minerals on Mars observed by the Mars Reconnaissance Orbiter CRISM instrument. *Nature*, *454*(7202), 305–309. https://doi.org/10.1038/nature07097

Nash, D. B., & Salisbury, J. W. (1991). Infrared reflectance spectra (2.2–15 μm) of plagioclase feldspars. *Geophysical Research Letters*, *18*(6), 1151-1154.

Nyquist, L. E., Bogard, D. D., Shih, C.-Y., Greshake, A., Stöffler, D., & Eugster, O. (2001). Ages and Geologic Histories of Martian Meteorites. *Space Science Reviews*, *96*(1/4), 105–164. https://doi.org/10.1023/a:1011993105172

Ody, A., Poulet, F., Quantin, C., Bibring, J.-P., Bishop, J. L., & Dyar, M. D. (2015). Candidates source regions of Martian meteorites as identified by OMEGA/MEx. *Icarus*, *258*, 366–383. https://doi.org/10.1016/j.icarus.2015.05.019

Orr, K. J., Forman, L. V., Rankenburg, K., Evans, N. J., McDonald, B. J., Godel, B., Benedix. G. K. (in review). Geochemical, Mineralogical and Spectral Classification of Four New Shergottites. *Meteoritics and Planetary Science.*

Owen, T., Biemann, K., Rushneck, D. R., Biller, J. E., Howarth, D. W., & Lafleur, A. L. (1977). The composition of the atmosphere at the surface of Mars. *Journal of Geophysical Research*, *82*(28), 4635–4639. https://doi.org/10.1029/js082i028p04635

Pan, C., Rogers, A. D., & Michalski, J. R. (2015). Thermal and near-infrared analyses of central peaks of Martian impact craters: Evidence for a heterogeneous Martian crust. *Journal of Geophysical Research: Planets*, *120*(4), 662–688. https://doi.org/10.1002/2014je004676

Paton, C., Hellstrom, J., Paul, B., Woodhead, J., Hergt, J. 2011. Iolite: Freeware for the visualisation and processing of mass spectrometric data. *Journal of Analytical Atomic Spectrometry* 26:2508-2518.

Peters, T. J., Simon, J. I., Jones, J. H., Usui, T., Moriwaki, R., Economos, R. C., et al. (2015). Tracking the source of the enriched martian meteorites in olivine-hosted melt inclusions of two depleted shergottites, Yamato 980459 and Tissint. *Earth and Planetary Science Letters*, *418*(Earth Planet. Sci. Lett. 224 2004), 91–102. https://doi.org/10.1016/j.epsl.2015.02.033

Phillips, R. J., Zuber, M. T., Smrekar, S. E., Mellon, M. T., Head, J. W., Tanaka, K. L., et al. (2008). Mars North Polar Deposits: Stratigraphy, Age, and Geodynamical Response. *Science*, *320*(5880), 1182–1185. https://doi.org/10.1126/science.1157546

Poulet, F., Gomez, C., Bibring, J. -P., Langevin, Y., Gondet, B., Pinet, P., et al. (2007). Martian surface mineralogy from Observatoire pour la Minéralogie, l'Eau, les Glaces et l'Activité on board the Mars Express spacecraft (OMEGA/MEx): Global mineral maps. *Journal of Geophysical Research: Planets*, *112*(E8). https://doi.org/10.1029/2006je002840

Rae, A. S. P., Collins, G. S., Morgan, J. V., Salge, T., Christeson, G. L., Leung, J., Lofi, J., Gulick, S. P. S., Poelchau, M., Riller, U., Gebhardt, C., Grieve, R. A. F., Osinski, G. R., IODP-ICDP Expedition 364 Scientists. 2019. Impact-Induced Porosity and Microfracturing at the Chicxulub Impact Structure. *Journal of Geophysical Research: Planets* 124:1960–1978.

Rahib, R. R., Udry, A., Howarth, G. H., Gross, J., Paquet, M., Combs, L. M., et al. (2019). Mantle source to near-surface emplacement of enriched and intermediate poikilitic shergottites in Mars. *Geochimica et Cosmochimica Acta*, *266*, 463–496. https://doi.org/10.1016/j.gca.2019.07.034

Ramsey, M. S., & Christensen, P. R. (1998). Mineral abundance determination: Quantitative deconvolution of thermal emission spectra. *Journal of Geophysical Research: Solid Earth*, *103*(B1), 577–596. https://doi.org/10.1029/97jb02784

Riches, A. J. V., Liu, Y., Day, J. M. D., Puchtel, I. S., Rumble, D., McSween, H. Y., et al. (2011). Petrology and geochemistry of Yamato 984028: a cumulate lherzolitic shergottite with affinities to Y 000027, Y 000047, and Y 000097. *Polar Science*, *4*(4), 497–514. https://doi.org/10.1016/j.polar.2010.04.009

Rogers, A. D., Christensen, P. R., & Bandfield, J. L. (2005). Compositional heterogeneity of the ancient Martian crust: Analysis of Ares Vallis bedrock with THEMIS and TES data. *Journal of Geophysical Research: Planets (1991–2012)*, *110*(E5). https://doi.org/10.1029/2005je002399

Rogers, A. D., Bandfield, J. L., & Christensen, P. R. (2007a). Global spectral classification of Martian low-albedo regions with Mars Global Surveyor Thermal Emission Spectrometer (MGS-TES) data. *Journal of Geophysical Research: Planets (1991–2012)*, *112*(E2). https://doi.org/10.1029/2006je002726

Rogers, A. D., & Christensen, P. R. (2007b). Surface mineralogy of Martian low-albedo regions from MGS-TES data: Implications for upper crustal evolution and surface alteration. *Journal of Geophysical Research: Planets (1991–2012)*, *112*(E1). https://doi.org/10.1029/2006je002727

Rogers, A. D., & Aharonson, O. (2008). Mineralogical composition of sands in Meridiani Planum determined from Mars Exploration Rover data and comparison to orbital measurements. *Journal of Geophysical Research: Planets (1991–2012)*, *113*(E6). https://doi.org/10.1029/2007je002995

Rogers, A. D., & Bandfield, J. L. (2009). Mineralogical characterization of Mars Science Laboratory candidate landing sites from THEMIS and TES data. *Icarus*, *203*(2), 437–453. https://doi.org/10.1016/j.icarus.2009.04.020

Roszjar, J., Bischoff, A., Llorca, J. and Pack, A. 2012. Ksar Ghilane 002 (KG 002)---A New Shergottite: Discovery, Mineralogy, Chemistry and Oxygen Isotopes. *Lunar Planetary Science XLIII* 43.

Rubin, A. E., Warren, P. H., Greenwood, J. P., Verish, R. S., Leshin, L. A., Hervig, R. L., Clayton, R. N., Mayeda, T. K. 2000. Los Angeles: The most differentiated basaltic martian meteorite. *Geology* 28:1011-1014.

Ruff, S. W., Christensen, P. R., Blaney, D. L., Farrand, W. H., Johnson, J. R., Michalski, J. R., ... & Squyres, S. W. (2006). The rocks of Gusev Crater as viewed by the Mini-TES instrument. *Journal of Geophysical Research: Planets*, *111*(E12).

Ruggiu, L. K., Gattacceca, J., Devouard, B., Udry, A., Debaille, V., Rochette, P., et al. (2020). Caleta el Cobre 022 Martian meteorite: Increasing nakhlite diversity. *Meteoritics & Planetary Science*. https://doi.org/10.1111/maps.13534

Sabol Jr, D. E., Adams, J. B., & Smith, M. O. (1992). Quantitative subpixel spectral detection of targets in multispectral images. *Journal of Geophysical Research: Planets*, *97*(E2), 2659-2672.

Salisbury, J. W., & Eastes, J. W. (1985). The effect of particle size and porosity on spectral contrast in the mid-infrared. *Icarus*, *64*(3), 586-588.

Salisbury, J. W., Walter, L. S., & Vergo, N. (1987). Mid-infrared (2 l25 pm) spectra of minerals (lst edition). *U.S. Geological Survey OpenFile Report* 87 -263, 356 p.

Salisbury, J. W., D'Aria, D. M., & Jarosewich, E. (1991). Midinfrared (2.5–13.5 μm) reflectance spectra of powdered stony meteorites. *Icarus*, *92*(2), 280–297. https://doi.org/10.1016/0019-1035(91)90052-u

Salisbury, J. W., Wald, A., & D'Aria, D. M. (1994). Thermal-infrared remote sensing and Kirchhoff's law: 1. Laboratory measurements. *Journal of Geophysical Research: Solid Earth*, *99*(B6), 11897-11911.

Santos, A. R., Agee, C. B., McCubbin, F. M., Shearer, C. K., Burger, P. V., Tartèse, R., & Anand, M. (2015). Petrology of igneous clasts in Northwest Africa 7034: Implications for the petrologic diversity of the martian crust. *Geochimica et*

Cosmochimica Acta, *157*(Science 339 2013), 56–85. https://doi.org/10.1016/j.gca.2015.02.023

Sarbadhikari, A. B., Day, J. M. D., Liu, Y., Rumble, D., & Taylor, L. A. (2009). Petrogenesis of olivine-phyric shergottite Larkman Nunatak 06319: Implications for enriched components in martian basalts. *Geochimica et Cosmochimica Acta*, *73*(7), 2190–2214. https://doi.org/10.1016/j.gca.2009.01.012

Sautter, V., Toplis, M. J., Wiens, R. C., Cousin, A., Fabre, C., Gasnault, O., et al. (2015). In situ evidence for continental crust on early Mars. *Nature Geoscience*, *8*(8), 605–609. https://doi.org/10.1038/ngeo2474

Shaheen, R., Niles, P. B., Chong, K., Corrigan, C. M., & Thiemens, M. H. (2015). Carbonate formation events in ALH 84001 trace the evolution of the Martian atmosphere. *Proceedings of the National Academy of Sciences*, *112*(2), 336-341.

Sharp, T. G., and DeCarli, P. S. 2006. Shock effects in meteorites. *Meteorites and the early solar system II* 943:653-677.

Shchipalkina, N. V., Aksenov, S. M., Chukanov, N. V., Pekov, I. V., Rastsvetaeva, R. K., Schäfer, C., et al. (2016). Pyroxenoids of pyroxmangite–pyroxferroite series from xenoliths of Bellerberg paleovolcano (Eifel, Germany): Chemical variations and specific features of cation distribution. *Crystallography Reports*, *61*(6), 931–939. https://doi.org/10.1134/s1063774516060146

Siesler, H. W., Ozaki, Y., Kawata, S., & Heise, H. M. (Eds.). (2008). *Near-infrared spectroscopy: principles, instruments, applications*. John Wiley & Sons.

Smith, J. V., & Hervig, R. L. (1979). SHERGOTTY METEORITE: MINERALOGY, PETROGRAPHY AND MINOR ELEMENTS. *Meteoritics*, *14*(1), 121–142. https://doi.org/10.1111/j.1945-5100.1979.tb00486.x

Smith, M. D., Bandfield, J. L., & Christensen, P. R. (2000). Separation of atmospheric and surface spectral features in Mars Global Surveyor Thermal Emission Spectrometer

(TES) spectra. *Journal of Geophysical Research: Planets*, *105*(E4), 9589–9607. https://doi.org/10.1029/1999je001105

Stöffler, D. 1972. Deformation and transformation of rock-forming minerals by natural and experimental shock processes. I. Behavior of minerals under shock compression. *Fortschritte der Mineralogie* 49:50-113.

Stöffler, D. 1984. Glasses formed by hypervelocity impact. *Journal of Non-Crystalline Solids* 67:465-502.

Stöffler, D., Ostertag, R., Jammes, C., Pfannschmidt, G., Gupta, P. R., Simon, S. B., Papike, J. J., Beauchamp, R. H. 1986. Shock metamorphism and petrography of the Shergotty achondrite. *Geochimica et Cosmochimica Acta* 50:889-903.

Stöffler, D., Hamann, C., Metzler, K. 2018. Shock metamorphism of planetary silicate rocks and sediments: Proposal for an updated classification system. *Meteoritics & Planetary Science* 53:5-49.

Stuart, B. H. (2005). Infrared Spectroscopy: Fundamentals and Applications. *Analytical Techniques in the Sciences*, 137–165. https://doi.org/10.1002/0470011149.ch7

Taylor, L. A., Nazarov, M. A., Shearer, C. K., McSween, H. Y., Cahill, J., Neal, C. R., et al. (2002). Martian meteorite Dhofar 019: A new shergottite. *Meteoritics & Planetary Science*, *37*(8), 1107–1128. https://doi.org/10.1111/j.1945-5100.2002.tb00881.x

Thompson, C. S., & Wadsworth, M. E. (1957). Determination of the Composition of Plagio-Clase Feldspars by Means of Infrared Spectroscopy. *American Mineralogist: Journal of Earth and Planetary Materials*, *42*(5-6), 334-341.

Thomson, J. L., & Salisbury, J. W. (1993). The mid-infrared reflectance of mineral mixtures (7–14 μm). *Remote Sensing of Environment*, *45*(1), 1-13.

Tornabene, L. L., Moersch, J. E., McSween, H. Y., McEwen, A. S., Piatek, J. L., Milam, K. A., & Christensen, P. R. (2006). Identification of large (2–10 km) rayed craters on Mars in THEMIS thermal infrared images: Implications for possible Martian meteorite source regions. *Journal of Geophysical Research: Planets (1991–2012)*, *111*(E10). https://doi.org/10.1029/2005je002600

Tornabene, L. L., Moersch, J. E., McSween, H. Y., Hamilton, V. E., Piatek, J. L., & Christensen, P. R. (2008). Surface and crater-exposed lithologic units of the Isidis Basin as mapped by coanalysis of THEMIS and TES derived data products. *Journal of Geophysical Research: Planets (1991–2012)*, *113*(E10). https://doi.org/10.1029/2007je002988

Treiman, A. H., McKay, G. A., Bogard, D. D., Mittlefehldt, D. W., Wang, M. S., Keller, L., Lipschutz, M. E., Lindstrom, M. M., Garrison, D. 1994. Comparison of the LEW88516 and ALHA77005 martian meteorites: Similar but distinct. *Meteoritics* 29:581-592.

Treiman, A. H. (2005). The nakhlite meteorites: Augite-rich igneous rocks from Mars. *Chemie Der Erde - Geochemistry*, *65*(3), 203–270. https://doi.org/10.1016/j.chemer.2005.01.004

Treiman, A. H., Dyar, M. D., McCanta, M., Noble, S. K., & Pieters, C. M. (2007). Martian Dunite NWA 2737: Petrographic constraints on geological history, shock events, and olivine color. *Journal of Geophysical Research: Planets (1991–2012)*, *112*(E4). https://doi.org/10.1029/2006je002777

Treiman, A. H., & Filiberto, J. (2015). Geochemical diversity of shergottite basalts: Mixing and fractionation, and their relation to Mars surface basalts. *Meteoritics & Planetary Science*, *50*(4), 632–648. https://doi.org/10.1111/maps.12363

Udry, A., Howarth, G. H., Lapen, T. J., Righter, M. 2017. Petrogenesis of the NWA 7320 enriched martian gabbroic shergottite: Insight into the martian crust. *Geochimica et Cosmochimica Acta* 204:1-18.

Udry, A., & Day, J. M. D. (2018). 1.34 billion-year-old magmatism on Mars evaluated from the co-genetic nakhlite and chassignite meteorites. *Geochimica et Cosmochimica Acta*, *238*, 292–315. https://doi.org/10.1016/j.gca.2018.07.006

Udry, A., Howarth, G. H., Herd, C. D. K., Day, J. M. D., Lapen, T. J., & Filiberto, J. (2020). What Martian Meteorites Reveal About the Interior and Surface of Mars. *Journal of Geophysical Research: Planets*, *125*(12). https://doi.org/10.1029/2020je006523

Usui, T., McSween, H. Y., & Floss, C. (2008). Petrogenesis of olivine-phyric shergottite Yamato 980459, revisited. *Geochimica et Cosmochimica Acta*, *72*(6), 1711–1730. https://doi.org/10.1016/j.gca.2008.01.011

Usui, T., Sanborn, M., Wadhwa, M., & McSween, H. Y. (2010). Petrology and trace element geochemistry of Robert Massif 04261 and 04262 meteorites, the first examples of geochemically enriched lherzolitic shergottites. *Geochimica et Cosmochimica Acta*, *74*(24), 7283–7306. https://doi.org/10.1016/j.gca.2010.09.010

Usui, T., Alexander, C. M. O., Wang, J., Simon, J. I., & Jones, J. H. (2012). Origin of water and mantle–crust interactions on Mars inferred from hydrogen isotopes and volatile element abundances of olivine-hosted melt inclusions of primitive shergottites. *Earth and Planetary Science Letters*, *357*(Nature 461 2009), 119–129. https://doi.org/10.1016/j.epsl.2012.09.008

Vincent, R. K., Rowan, L. C., Gillespie, R. E., & Knapp, C. (1975). Thermal-infrared spectra and chemical analyses of twenty-six igneous rock samples. *Remote Sensing of Environment*, *4*, 199-209.

Walton, E. L., & Spray, J. G. (2003). Mineralogy, microtexture, and composition of shock-induced melt pockets in the Los Angeles basaltic shergottite. *Meteoritics & Planetary Science*, *38*(12), 1865–1875. https://doi.org/10.1111/j.1945-5100.2003.tb00020.x

Walton, E. L., Irving, A. J., Bunch, T. E., Herd, C. D. K. 2012. Northwest Africa 4797: A strongly shocked ultramafic poikilitic shergottite related to compositionally intermediate Martian meteorites. *Meteoritics & Planetary Science* 47:1449-1474.

Wänke, H., & Dreibus, G. (1994). Chemistry and accretion history of Mars. *Philosophical Transactions of the Royal Society of London. Series A: Physical and Engineering Sciences*, *349*(1690), 285–293. https://doi.org/10.1098/rsta.1994.0132

Warren, P. H., Greenwood, J. P., & Rubin, A. E. (2004). Los Angeles: A tale of two stones. *Meteoritics & Planetary Science*, *39*(1), 137–156. https://doi.org/10.1111/j.1945-5100.2004.tb00054.x

Werner, S. C., Ody, A., & Poulet, F. (2014). The Source Crater of Martian Shergottite Meteorites. *Science*, *343*(6177), 1343–1346. https://doi.org/10.1126/science.1247282

Wilson, L., Mouginis-Mark, P. J., Tyson, S., Mackown, J., & Garbeil, H. (2009). Fissure eruptions in Tharsis, Mars: Implications for eruption conditions and magma sources. *Journal of Volcanology and Geothermal Research*, *185*(1–2), 28–46. https://doi.org/10.1016/j.jvolgeores.2009.03.006

Wittke, J. H., Bunch, T. E., Irving, A. J., Farmer, M. and Strope, J. 2006. Northwest Africa 2975: An evolved basaltic shergottite with vesicular glass pockets and trapped melt inclusions. *Lunar Planetary Science XXXVII* 37.

Xirouchakis, D., Draper, D. S., Schwandt, C. S., Lanzirotti, A. 2002. Crystallization conditions of Los Angeles, a basaltic Martian meteorite. *Geochimica et Cosmochimica Acta* 66:1867-1880.

Yamaguchi, Y., Kahle, A. B., Tsu, H., Kawakami, T., & Pniel, M. (1998). Overview of advanced spaceborne thermal emission and reflection radiometer (ASTER). *IEEE Transactions on geoscience and remote sensing*, *36*(4), 1062-1071.

Yoshizaki, T., & McDonough, W. F. (2020). The composition of Mars. *Geochimica et Cosmochimica Acta*, *273*, 137–162. https://doi.org/10.1016/j.gca.2020.01.011

Zipfel, J., Schröder, C., Jolliff, B. L., Gellert, R., Herkenhoff, K. E., Rieder, R., et al. (2011). Bounce Rock—A shergottite-like basalt encountered at Meridiani Planum, Mars. Meteoritics & Planetary Science, 46(1), 1–20. https://doi.org/10.1111/j.1945-5100.2010.01127.x

Chapter 8: Appendix

Supplemental material for Chapters 3, 4 and 5 can be found here on Research Data Australia: https://doi.org/10.25917/cmep-sz38